DYNAMICS OF LOCAL GROUP SATELLITE GALAXIES IN THE ERA OF PRECISION ASTROMETRY

by

Ekta Patel

A Dissertation Submitted to the Faculty of the

DEPARTMENT OF ASTRONOMY

In Partial Fulfillment of the Requirements
For the Degree of

DOCTOR OF PHILOSOPHY
WITH A MAJOR IN ASTRONOMY AND ASTROPHYSICS

In the Graduate College

THE UNIVERSITY OF ARIZONA

2019

THE UNIVERSITY OF ARIZONA
GRADUATE COLLEGE

As members of the Dissertation Committee, we certify that we have read the dissertation prepared by Ekta Patel, titled Dynamics of Local Group Satellite Galaxies in the Era of Precision Astrometry and recommend that it be accepted as fulfilling the dissertation requirement for the Degree of Doctor of Philosophy.

Prof. Gurtina Besla — Date: May 9, 2019

Prof. Dennis Zaritsky — Date: May 9, 2019

Prof. Peter Behroozi — Date: May 9, 2019

Prof. David Sand — Date: May 9, 2019

Dr. Jeff Carlin — Date: May 9, 2019

Final approval and acceptance of this dissertation is contingent upon the candidate's submission of the final copies of the dissertation to the Graduate College.

I hereby certify that I have read this dissertation prepared under my direction and recommend that it be accepted as fulfilling the dissertation requirement.

Date: May 9, 2019

Dissertation Director: Dr. Gurtina Besla
Assistant Professor
Department of Astronomy

ACKNOWLEDGEMENTS

I believe this journey was sparked by a very specific moment in my life that occurred in the summer of 2006. My sister, Priyam, invited me to tag along with her and two friends, Ramya and Ashwin, to watch my first meteor shower. I was enamored with the gleaming balls of light streaking across the sky and while I didn't know it then, that night was pivotal in my decision to pursue astronomy. I owe many thanks to the three of you for letting me come along then and on the many adventures that have followed.

There are so many people that have helped me push past my own fears and the obstacles that come along with pursuing this degree. I am fortunate to have such an amazing support network and am gracious to all of you.

First, I thank my parents. If it wasn't for their sacrifices and those of their parents before them, I would not have had the opportunity to not only go to the university of my choice for my undergraduate degree, but also the opportunity to continue pursuing my studies in Arizona. Mom and Dad, I know it was hard to let your youngest girl move so far away from home and I tremendously appreciate the strength you've had in supporting my decision.

I may not have made it to graduate school without my undergraduate advisor, David Hogg. Thanks for giving me the chance to see what it means to do research in astronomy and for helping me get through the grad school application process even when I wanted to give up. I also appreciate your continued support throughout graduate school. I would also like to thank my undergraduate research partner, David Mykytyn, for bringing me along to Hogg's group and for teaching me so much Python.

I owe much of the growth I have experienced as a scientist to my amazing advisor, Gurtina Besla. G, from the time your recruited me during my prospective visit, you have been a huge advocate and role model. Thank you for believing in me, for teaching me so much, and for spending so many hours of our first years at Arizona in your office going over plot after plot. Though I will never enjoy the wall of post-its, your mentoring and advising have played a huge role in seeing this degree to the end. You have helped me build a sense of confidence that I have never felt before in my scientific pursuits. Thank you for making my graduate career an extremely rewarding and fulfilling experience. Most of all, thanks for being a friend through it all.

I'd also like to thank my "little big" (academic) brother, Nicolas Garavito-Camargo. Thank you so much for always offering to chat over some code or ideas, for celebrating with me, and for being such a good friend throughout grad school. I

will dearly miss our lunches and the parties in your kitchen. Let's finally write that paper together! Thank you to Katie Chamberlain, my academic little sister. I'm so glad you decided to join our group and thank you for always bringing positive energy to our meetings. Thank you also to Myoungwon Jeon and Yumi Choi, Besla team members past and present, who I've had the pleasure of learning from.

Science happens through collaboration and I am very thankful to the collaborators I have had the opportunity to work with continuously over the last five years. Tony Sohn – you rock! Thanks for working with me on so many projects and for answering all of the silly questions I've sent your way. It's been a pleasure to have you on board. Kaisey Mandel – thanks for agreeing to work with some random student of a grad school classmate. I bet you didn't know what you were getting yourself into but I very much appreciate all that you taught me about statistics. Thank you for taking a chance on me. Roeland van der Marel – thank you for welcoming me to the HSTPROMO group. You've taught me a lot and I appreciate your guidance on many projects (and life decisions) throughout the years. Many thanks to Greg Dooley, Jeff Carlin, Erik Tollerud, Michelle Collins, and members of the HSTPROMO collaboration for working with me as well. I owe a huge thank you to Paul Torrey and Vicente Rodriguez-Gomez who have been tremendously generous with their time and in answering endless emails from me about the Illustris simulations. Many thanks to Julianne Dalcanton, Peter Behroozi, Xiaohui Fan, Nitya Kallivayalil, Raja GuhaThakurta, and my thesis committee who have been mentors and advocates throughout the years.

I've been fortunate to have such a large community of fellow graduate students at Steward Observatory. Whether we spent one year at Steward together or five, I'm thankful for the vibrant community of scientists I've had the pleasure of being a part of. I'd specifically like to thank Samantha Scibelli, Rachel Smullen, Christine O'Donnell, Yifan Zhou, Rixin Li, Rachael Amaro (and Onyx), Charity Woodrum, Evan Schneider, Justin Spilker, Wen-fai Fong, Patrick Sheehan, Adam Sutherland, Raga Pucha, Michi Baubock, Jan-Torge Schindler, Peter Senchyna, Lia Medeiros, Joseph Long, Carolyn Raithel, David Ball, Raphael Hviding, and Kevin Hainline for some wonderful memories. Thanks to my non-astronomy friends Nicole Denny and Angela Yung for keeping me sane and adventuring around Tucson with me. I'd also like to thank my bendy friends at the Circus Academy of Tucson for providing an escape from reality for a few hours each week.

My family has been the biggest and best support system I could have asked for throughout this journey. Thank you so much to Mom, Dad, Pri, Dee, Brady, Aashna, Maddy, Emily, Mark, Fran, Sarah, Sue, Bernie, and all of the extended Patel family. Whether you've been there since day one or I gained you along the way, I truly appreciate your love and support. You mean the world to me. I must specifically thank (or blame?) my sisters for inspiring me to go down this path of pursuing a PhD. You're quite literally the best role models for all young, brown girls out there. I thank you for convincing me to apply to grad school, supporting me

throughout it, and for just being the wonderful humans you are. Brady – thanks for all of the bevs and the quiet, unwavering support. To my niece, Aashna, the biggest tiny goofball of them all – thanks for the endless Facetime calls, giggles, and smiles. I can't wait to teach you all about the galaxies!

To my love, Nick, thank you for being my rock. We had no idea what we were signing up for five years ago and I often questioned how we would make it work across 1,700 miles but one thing was always certain. You've always been there (thank you Skype!) to bring happiness to my low points, to celebrate any accomplishment big or small, and to enjoy life with me outside of work. Thank you for never having a doubt about whether I could do this. I love you and I am so looking forward to all of the new adventures we will have together. Berkeley, here we come!

Though she has only been in my life for a few months, I'd like to thank our dog, (Dr.) Pepper, for the comfort and cuddles she has showered me with in the short time I've known her. Thanks for bringing so much joy to my life, Peps!

I am thankful to the National Science Foundation's Graduate Research Fellowship program (Grant Award No. DGE-1143953, DGE-1746060) for funding me for three years of graduate school. I'd also like to acknowledge all of the Steward Observatory building and facilities staff for their hard work in maintaining our work spaces and making it possible for us to pursue science each and every day. Finally, a big thank you to Michelle Cournoyer for everything she does for the Steward grad students.

DEDICATION

For my sisters, Chandani and Priyam, the two fiercest, brightest, and most resilient women I know.

TABLE OF CONTENTS

TABLE OF CONTENTS – *Continued*

TABLE OF CONTENTS – *Continued*

TABLE OF CONTENTS – *Continued*

LIST OF FIGURES

LIST OF FIGURES – *Continued*

LIST OF TABLES

ABSTRACT

High-precision astrometric data from the *Hubble Space Telescope* (HST) and *Gaia* are revolutionizing our ability to study galaxies in the Local Group (LG) in unprecedented detail. Recent breakthroughs, such as high accuracy proper motion (PM) measurements for Andromeda (M31), Triangulum (M33), and many of the dwarf galaxies orbiting the Milky Way (MW) and M31 now make it possible to analyze the interaction histories between satellite galaxies and their hosts. In this dissertation, I explore how the combination of astrometric data with high-resolution cosmological simulations can be used to improve our classical understanding of the LG's dynamical history.

Using PMs from HST and the *Very Long Baseline Array* and independently measured PMs with *Gaia*, I show that the most plausible orbital history for M31's most massive satellite galaxy, M33, is a first infall scenario where M33 enters M31's halo in the last 2-4 Gyr, arriving at its closest position relative to M31 today. I also demonstrate that this orbital history is consistent with those of M33 analogs in M31-mass systems in *Illustris-1-Dark*. M33's new orbital history is contrary to its classical orbit (developed before M31's PM was measured) where M33 has a close (< 100 kpc), recent (< 3 Gyr) tidal interaction with M31, resulting in M33's curious morphology. If on first infall into M31's halo, M33 is expected to retain its infall mass and any associated satellite galaxies. Here, I quantify the predicted satellite galaxy population of M33 in a ΛCDM paradigm, which may provide an alternative explanation for M33's warped morphology and can be directly tested with existing observatories.

In the remaining chapters, I develop innovative methods to statistically constrain the precise masses of the MW and M31 by comparing the kinematic and dynamical properties of their satellite galaxies to the properties of simulated analogs in

Illustris-1-Dark. I show that the orbital angular momenta of satellite galaxies is the most reliable estimator of host halo mass over time. Using the angular momenta of multiple satellites simultaneously narrows the current uncertainty in the MWs mass by $\sim$25%, showing promise for improved constraints on the mass of M31 and ultimately the LG.

CHAPTER 1

Introduction

1.1 Overview

The Local Group (LG) is composed of our Milky Way (MW); its twin galaxy, Andromeda (M31); and the dozens of small satellite galaxies orbiting around each of them. Most of these satellite galaxies are dwarf galaxies with typical masses of $M_* \leq 10^9\,\mathrm{M}_\odot$ (mapping to $M_{\rm halo} \leq 10^{11}\,\mathrm{M}_\odot$). The exceptions are the Large and Small Magellanic Clouds (LMC, SMC), a pair of galaxies located 50 kpc from the MW, and Triangulum (M33), a flocculent spiral separated from M31 by about 200 kpc. M33 and the combined mass of the LMC and SMC amount to roughly one-tenth the mass of their host galaxies ($M_* \approx 3-5\times10^9\,\mathrm{M}_\odot$; $M_{\rm halo} \approx 2-3\times10^{11}\,\mathrm{M}_\odot$). Constraining the orbital histories of these *massive* satellite galaxies is especially important for gaining insight on the evolution of their host galaxies and the other low mass satellite companions in the halos of the MW and M31.

Orbital calculations require knowledge of the full 3-dimensional (3D) position and velocity vectors of satellites relative to their hosts. However, prior to the early 2000s much of our understanding of LG dynamics was based only on line-of-sight (LOS) velocity measurements. Measuring the transverse velocity (the motion perpendicular to the LOS, or *proper motion*) of stars in nearby galaxies became possible in the last decade with the *Hubble Space Telescope* (HST) and more recently *Gaia*. High precision astrometric measurements from these observatories now make it possible to trace the orbital histories of galaxies in the LG to their cosmic origins in the early Universe. Combined with large statistical data sets from cosmological simulations, these new data therefore define a new frontier for detailed studies of nearby galaxies and pave the way for a new and complete model of the LG's dynamical history and its current dark matter content.

1.2 Satellite Galaxies Around the Milky Way and Andromeda

Though named after Ferdinand Magellan who is said to have discovered them in the early 1500s, the Magellanic Clouds (MCs) have been known to humankind for many centuries prior to Magellan's expeditions to the Southern hemisphere. Mentions of the LMC and SMC in written literature date back to at least the first millennia (circa 964 CE) in a book by Persian astronomer Abd Al-Rahman Al-Sufi (known in the West as *Azophi*; al Sufi, 964). The MCs have held much significance for peoples across the globe, particularly in the Southern hemisphere where they are easy to pick out in the dark night sky. M31 was similarly discovered in the same era and also appears in Azophi's book.

The majority of the now known populations of satellite galaxies around the MW and M31 have been discovered in the last century. Fig. 1.1 shows the discovery timeline of satellite galaxies around the MW and M31 since the year 1700 with an inset indicating those satellites discovered between 1940 and the present day. Thus far, 52 satellite galaxies with sizes and magnitudes consist with confirmed MW satellites have been discovered (at distances < 300 kpc) and most have been spectroscopically confirmed as true satellites. An additional 37 satellite galaxies have been found around M31 (at distances < 400 kpc; McConnachie, 2012; McConnachie et al., 2018, and updated online table). A majority of these discoveries can be attributed to either wide-field surveys covering large swaths of the sky or dedicated surveys of the MW and M31 halos. Together these surveys have nearly doubled the known MW and M31 satellite populations since the early 2000s. A few of the most profitable surveys are highlighted below.

The first rapid rise in MW satellite discoveries in Fig. 1.1 around the early 2000s is attributed to the *Sloan Digital Sky Survey* (SDSS). Now known as the SDSS Legacy Survey, the first era of SDSS delivered deep, multi-color imaging (i.e. images taken in five filters) over 8,240 square degrees of the sky taken between 2000-2008. Using SDSS imaging, satellites as faint as the so-called "ultra-faint" dwarfs (defined in Tollerud et al. (2008) as $\sim 1000\,L_{\odot}$) were detected (e.g. Willman et al.,

2005; Zucker et al., 2006b,a; Grillmair, 2006; Irwin et al., 2007).

The second influx of MW satellite discoveries is a result of the first two years of data from the *Dark Energy Survey* (DES). Though its main scientific goal is to probe the origin of our accelerating universe and understand dark energy through a wide-area survey covering nearly 5,000 square degrees of the Southern sky, it also provides deep, five-filter imaging to several magnitudes deeper than SDSS. DES has resulted in nearly 20 new ultra-faint dwarfs (e.g. Bechtol et al., 2015; Drlica-Wagner et al., 2015; Kim et al., 2015; Kim and Jerjen, 2015; Koposov et al., 2015) and it has begun to pave the way for the discovery of faint galaxies as the *Large Synoptic Survey Telescope* (LSST) prepares for first light in 2020.

In the 2020s, LSST will create a huge influx of imaging data of faint stellar structures around the MW, which will be a major leap forward for understanding and testing predictions of small-scale ΛCold Dark Matter (ΛCDM) cosmology. Not only will LSST enable the faintest ever search for stellar systems around LG galaxies, but it may also resolve the discrepancy between the number of MW satellites detected to date and the number predicted from ΛCDM simulations. Also known as the "missing satellites problem" current predictions show that the MW may host ∼200 satellites with $M_* \geq 10^3\,\mathrm{M}_\odot$ within 300 kpc, meaning that nearly 75% of the total satellite population has yet to be detected (see Bullock and Boylan-Kolchin, 2017, for a thorough description and review of small-scale challenges to the ΛCDM paradigm).

Given its proximity and similar halo mass, searches for M31 satellite galaxies have also been very fruitful in the last few decades. Several of M31's satellites were also detected in the SDSS, as indicated by the sharp rise in the blue curve in Fig. 1.1 around the early 2000s. The other major survey that led to 16 additional satellite discoveries in the last decade is the Pan-Andromeda Archaeological Survey (PAndAS). PAndAS is a survey of the M31 and M33 region covering nearly 400 square degrees corresponding to a circular area of nearly 50 kpc in projection around M33 and 150 kpc in projection around M31. While PAndAS was only carried out in two filters compared the five filters used for SDSS and DES, this dedicated effort to image the faintest tidal structures in the M31 and M33 halos was extremely successful in

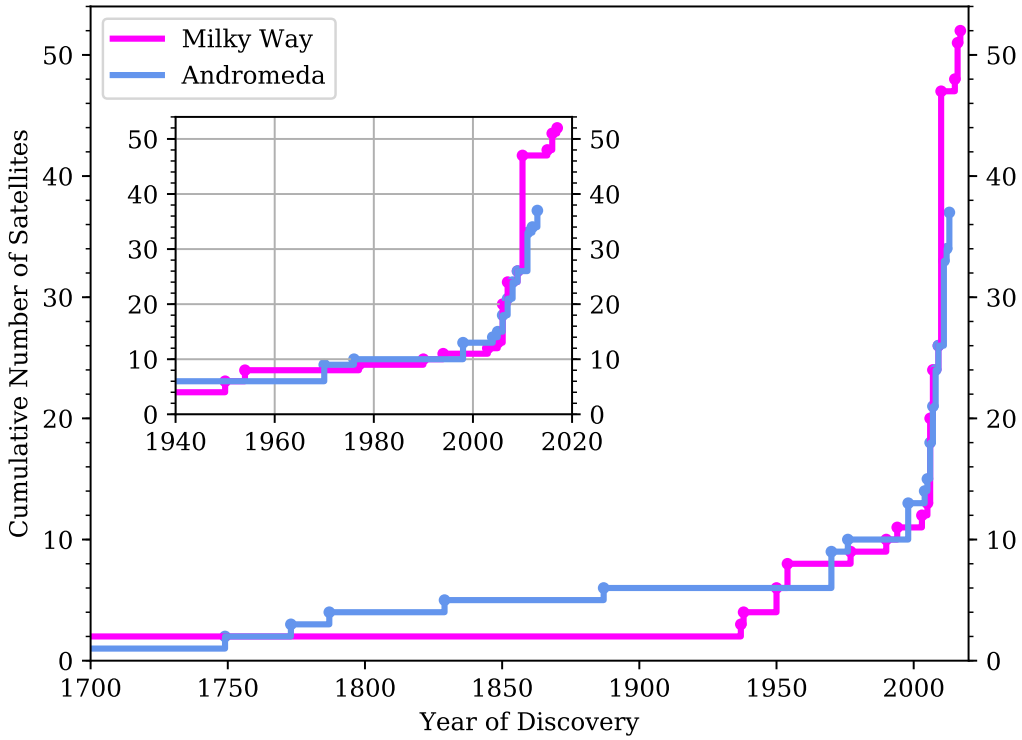

Figure 1.1: Discovery timeline for satellite galaxies discovered around the MW (magenta) and M31 (blue) since the year 1700. Prior to 1700, two (one) satellites were known to be associated satellites of the MW (M31).

finding and quantifying the properties of stellar streams, satellite galaxies, globular clusters, M31's stellar halo, and the stellar remnants of past accretion events.

Without wide-field surveys of this nature, many of these galaxies might never have been detected. It should also be noted that some satellite galaxies around the MW and M31 were not discovered using data from any of the surveys described thus far. For example, the Panoramic Survey and Rapid Response System (Pan-STARRS1, or PS1 for short), a survey of nearly 30,000 square degrees, has also been used to find a handful of dwarf satellites of M31 at distances beyond the PAndAS footprint (e.g. Martin et al., 2013a,b). Like the MW, much of M31's satellite population is likely yet to be detected in existing survey data. The faintest known satellite galaxies around M31 ($M_* \approx$ a few times $10^4\,\mathrm{M}_\odot$) are located in relatively isolated areas that do not suffer from high levels of contamination from M31's halo or the foreground. Based on current estimates for the mass of M31's halo, ΛCDM predictions suggest that only 25% of its total satellite population or less has been detected thus far. Given the location of LSST in the South, it will not reach the appropriate declination to observe the M31 region. A dedicated, wide-field survey in the North that reaches several magnitudes deeper than PAndAS (i.e. a northern counterpart to LSST) would therefore be the next best attempt at uncovering the remainder of M31's faint satellite galaxy population.

1.3 Satellite Galaxies as Tracers of Host Halo Mass

In ΛCDM cosmology, the mass in dark matter halos dominates the total mass in galaxies. For galaxies like the MW, about 6-10% of the mass is in stars, at least 2-6% is in the circumgalactic medium, 1-3% is made up of gas and dust in the interstellar medium, and the remaining $\geq$ 81% is in dark matter. Since this large reservoir of invisible mass cannot be observed directly, its properties must be inferred from the properties of the luminous baryons that orbit within and around it. As such, the dynamics of *tracers* in the halo are used to determine the underlying gravitational potential of the MW. Tracers include satellite galaxies, globular clusters, halo

and high velocity stars, as well as stellar streams. The properties of these tracer populations have been used across a variety of independent mass methods to infer the total mass of the MW's halo, yielding results between $0.5 - 2.5 \times 10^{12}\,\mathrm{M}_{\odot}$ (see Courteau et al., 2014; Bland-Hawthorn and Gerhard, 2016, for reviews on the MW's mass). Wang et al. (2015) and Callingham et al. (2019) provide nice comparisons for MW masses resulting from different approaches. Methods utilizing the dynamical information of multiple tracers simultaneously often require assumptions about the equilibrium of the tracer population (i.e. all satellites are bound in a steady state) and typically rely on 1D kinematics (radial velocities), ignoring velocity anisotropy, which can bias mass estimates (Watkins et al., 2010).

Satellite galaxies are particularly useful tracers of their host galaxy's halo mass because they are spatially distributed to nearly the virial radius of the galaxy ($\sim$ 300 kpc) and many of their 3D motions have been measured to high precision (see Section 1.5.1). While globular clusters (GCs) are more abundant than satellite galaxies, they are currently only good probes of the host halo potential to distances of 40-50 kpc from the center of the galaxy (e.g. Sohn et al., 2018; Watkins et al., 2019; Eadie et al., 2017). Similarly, halo stars currently only trace the inner halo like GCs and do not provide reliable mass estimates beyond $\sim$50 kpc (e.g. Cunningham et al., 2018), though this will improve as next generation radial velocity surveys and LSST reliably measure the positions of additional outer halo stars. Stellar streams provide a different avenue for estimating the total mass of a galaxy's halo, as these require iteratively modelling the disruption of the stream progenitor until a good match to the observational data is obtained (e.g. Gibbons et al., 2014; Dierickx and Loeb, 2017b). In doing so, many different masses can be tested for the MW, however, these too require some assumptions about the isotropy of the MW's halo and the shape of the halo itself. Furthermore, testing a broad range of values for many different halo and stream parameters is computationally expensive.

A specific benefit of using satellite galaxies as tracers of their host galaxy's halo potential is that recent advancements in computational techniques have made it possible to resolve satellite galaxies in cosmological N-body simulations (see Sec-

tion 1.5.2). These simulations provide large statistical samples of simulated satellite galaxies with diverse properties, eliminating the need to search a massive parameter space for idealized simulations of one galaxy halo. The combination of measurements of the 3D motions for true satellites of the MW and M31 with large samples of simulated satellite galaxies provides a powerful statistical technique to constrain halo properties of the MW and M31. In Chapter 4, the dynamics of the MW's classical satellite galaxies are compared to thousands of satellite analogs in a cosmological simulation to statistically constrain the mass of the MW. Unfortunately, these methods are not yet applicable to globular clusters or stellar streams, as the resolution of such large volume simulations is only reliable down to halo masses of $10^8 - 10^9\,\mathrm{M}_\odot$.

1.4 Satellite Galaxies as Probes of Halo Mass Assembly History

While the motions of satellite galaxies can be used to trace the dark matter halos of their hosts, satellite galaxies are also relics of their host halo's assembly history. In the ΛCDM paradigm, dark matter halos form through the continuous accretion of less massive halos and the galaxies that may[1] reside within them.

The positions of satellites galaxies of the MW and M31 as observed today are just a snapshot of the ongoing accretion process that occurs in hierarchical ΛCDM. By measuring the motions of these satellite galaxies (see Section 1.5.1), we can now trace their orbital histories backwards in time and constrain the moment they were first accreted into the dark matter halo of their host galaxies. For example, the motions of the MCs were used to determine that they entered the halo of the MW in the last 1-2 Gyr, making their most recent pericentric passage ∼50 Myr (Besla et al., 2007) ago. The combined mass of the MCs is approximately 10% the current mass of the MW (Garavito-Camargo et al., 2019), so by determining the infall time

[1]Below a certain halo mass threshold, halos are expected to be "dark". As this dissertation is concerned with satellite galaxies, it is important to note that satellite galaxies can only be used to trace assembly history down to halo masses of $\approx 10^9\,\mathrm{M}_\odot$ (see Bullock and Boylan-Kolchin, 2017, and references within).

of the MCs, we learn that the MW gained a significant fraction of its mass relatively recently in a single accretion event. The presence of the MCs has also been shown to correlate with the assembly history of their host halo. Since the existence of the MCs around MW-mass galaxies is rare (Boylan-Kolchin et al., 2011a), applying standard scaling relations based on halo mass will introduce bias. Disentangling what satellites are contributed by the MCs is therefore critical to understanding the true subhalo population of the MW (Lu et al., 2016, see also Section 7.4). The implications of massive satellites like the MCs on the subhalo mass function of the MW is discussed further in Chapter 4 and Appendix C.

The accretion history of M31's satellites is less well-known due to a lack of measurements for the motions of M31 satellite galaxies. However, current models show that the most recently accreted massive satellites (of order $10^{11}\,\mathrm{M}_{\odot}$) are M33 (see Chapter 2) and the progenitor of the Giant Southern Stream. Both are predicted to have fairly recent infall times between 2-3 Gyr ago (Fardal et al., 2006; Patel et al., 2017a). As the motions of additional M31 satellites are obtained, the assembly history of M31's system of satellite galaxies can be reconstructed. It will be especially interesting to quantify how common the accretion histories of the MW and M31 satellites are in a cosmological context given their close proximity to each other and the fact that they have both recently accreted substantially massive satellite galaxies. Comparisons between the MW and M31's assembly histories will be key to our understanding of $10^{12}\,\mathrm{M}_{\odot}$ halos as observational data for more distant L_* galaxies becomes available in the 2020s.

1.5 Modern Tools for Detailed Studies of the Dynamics of Local Group Galaxies

This section contains an overview of the two main tools that make the work in this dissertation possible. Further details on how they are used to address questions surrounding LG galaxies are provided within the chapters of this work.

1.5.1 Precision Astrometry for Local Group Galaxies

Understanding the motions of stars is critical for many aspects of galaxy formation and evolution. Specifically, the motions of stars encode some imprint of the initial conditions that formed them and secondly, the motions include information about their evolutionary history. Stellar dynamics are also important for mapping the 3D structures of galaxies, and ultimately, through gravity these motions help us learn about their underlying mass. For example, these dynamical measurements have been key to studying black holes lurking in the centers of galaxies like the MW and to understanding dark matter, the invisible matter that makes up 85% of all galaxies.

This dissertation is largely motivated by precision astrometry, spectroscopy, and deep photometry, which together enable accurate measurements of the 3D positions and 3D velocities of stars and galaxies (6D phase space). These methods have been particularly transformative for our knowledge of nearby galaxies where the highest accuracy and precision can be achieved down to levels equivalent to watching human hair grow at the distance of the Moon[2]. Prior to the advent of precision astrometry, much of our knowledge of stellar dynamics was based on LOS velocities measured with the Doppler shift from stellar spectra. This information is useful in understanding how stars are moving, however it only provides information along one dimension. Consequently, this requires many assumptions when it comes to accurately modeling the orbits of galaxies, especially when there are not good constraints on the underlying mass of the environment enclosed within the radius of such orbits.

Now we are able to measure the precise proper motion of stars in nearby galaxies relative to distant background objects. Proper motion (PM) refers to the observed change in angular position on the sky over time, which depends on the object's transverse velocity across the LOS. With observatories like HST and *Gaia*, these

[2]This rate is equivalent to accuracy of M31's proper motion ($\sim 30 - 50\,\mu\mathrm{as\,yr}^{-1}$) as measured by HST and reported in Sohn et al. (2012); van der Marel et al. (2012a). Credit to Roeland van der Marel for this analogy (van der Marel, 2015).

measurements are possible for many hundreds of stars within individual galaxies including the most prominent members of the LG: the MW, M31, M33, the LMC, the SMC. It is even possible to measure PMs for low mass satellite galaxies orbiting the MW and M31, though often only a few tens or fewer stars can be used to determine the absolute PM for these galaxies. When PMs for stars in an individual galaxy are averaged together, fit to a model, and corrected for both the internal motion of the galaxy and the relative motion of background reference objects, an absolute PM for the galaxy can be derived (see Chapter 6 for more details).

The work in this dissertation relies heavily on PM measurements for LG galaxies and the 6D phase space information (3D position plus 3D velocity) that can be derived from them. Below, I provide an overview of PM measurement techniques with specific emphasis on the observatories and corresponding PM analysis techniques that are used in this work.

Proper Motion Measurement Techniques

Proper motions can be measured from both the ground and space, though the resulting precision varies greatly depending on the technique and the distance[3] of the target object. From the ground, seeing-limited observations with long baselines (> 15 years) can be used to track the motions of stars in halo GCs or adaptive optics with shorter baselines can be used to measure the same motions (e.g. Dinescu et al., 1999; Fritz et al., 2017). These methods are sufficient for GCs, which are much more compact than satellite galaxies ($r_h = 1 - 10$ pc for GCs vs. $r_h = 10 - 1000$ pc for satellites), therefore they require a much smaller field of view and fewer background reference objects. Ground-based observations have also been used to determine the proper motion of the MW satellite galaxy, Fornax dSph, though the errors on the resulting measurements are a few tenths of a milliarcsecond per year

[3]Distance is not only relevant for how feasible it is to measure PMs, but the distance uncertainty (or distance modulus uncertainty) is also factored into the uncertainties on the 6D phase space information derived from the combination of PMs, distance, LOS velocity, and the uncertainties in each of those measurements.

(corresponding to transverse velocity errors of ~ 100 km s^{-1}), making it difficult to constrain the 3D orbital history of Fornax. Overall, optical ground-based methods for PM measurements for halo tracers require much longer baselines and/or do not provide high accuracy, high precision measurements, thereby motivating alternative ground-based or space-based measurements where the instruments are more stable, the field of view is wider, and the spatial resolution is much higher.

One ground-based approach that has proven to be very reliable for measuring high accuracy PMs is very long-baseline interferometry (VLBI). VLBI can be used to track the motion of water masers in galaxies, which are bright radio sources located in star-forming regions. Brunthaler et al. (2005) used this method to measure the PM of M33 using the *Very Long Baseline Array* (VLBA), an interferometer composed of ten stations located across the United States, each with a 25m radio antenna. Strong water masers in two HII regions in the Northeast and Southeast regions of M33 were observed in four epochs over the course of three years to obtain a measurement of the distance to M33 and its PM at the level of microarcseconds per year.

Astrometric data measured with the HST has also been pivotal to the work presented in this dissertation. The High-Resolution Space Telescope Proper Motion (HSTPROMO) collaboration[4] has used HST observations to deliver precise PMs for M31, the LMC, the SMC, and a majority of the classical MW dSph satellite galaxies. Through ongoing programs, it will also establish first-epoch imaging for all MW satellite galaxies out to 420 kpc that lack existing deep imaging (HST GO-14734, PI: N. Kallivayalil). Additionally, data for two dwarf elliptical galaxies in M31's halo – NGC 147 an NGC 185 – have already been measured and their analysis is currently underway. In total only four of the known 37 M31 satellites have measured PMs. Thus, HST is crucial for obtaining first-epoch imaging for the remaining M31 satellite galaxies while it is still in operation. Once JWST launches, it will provide second epoch data from which PMs can then be measured.

[4]Previously known as the Hubble Space Telescope Proper Motion Collaboration (see http://www.stsci.edu/∼marel/hstpromo.html).

Perhaps the most relevant HST PM measurement for this dissertation and the most ground-breaking result from the HSTPROMO collaboration is the first direct measurement of M31's PM (Sohn et al., 2012; van der Marel et al., 2012a,b). Prior to this, only indirect estimates and LOS velocity information were available for M31, leaving much uncertainty in the dynamical history of the LG, its future fate, and in the dynamics of the M31 satellite system. As discussed in Sohn et al. (2012), M31's PM was measured using three fields of data: one along the minor axis, one along the major axis, and one along the Giant Southern Stream. Imaging of these fields was taken five to seven years apart and collectively the fields contain thousands of M31 stars. The positions of M31 stars between multiple epochs of data were compared to the virtually static positions of hundreds of compact background galaxies within the same three fields of data. Six independent sets of images were taken for each field during the second-epoch of imaging, and the error-weighted mean PM for each field was calculated using all six exposures. The resulting PMs for all three fields are statistically consistent with one another. The final displacement of M31 stars is equivalent to a few thousandths of a pixel or 12 μas yr^{-1} ($\sim$ 45 km s^{-1}).

These M31 PM results do not account for any contributions from the internal kinematics of M31's disk, which are non-negligible compared to uncertainties in the PM measurements. Thus, van der Marel et al. (2012a) corrects for internal kinematics, the reflex solar motion in the MW, and viewing angles. The resulting M31 velocity vector with respect to the MW (and its uncertainties) is used in Chapter 2 to constrain the orbit of M33 around M31. In van der Marel et al. (2012b), the MW-M31 velocity is used to constrain the future collision between the two galaxies and the total mass of the LG. PM measurements and analysis techniques using HST observations for subsequent LG galaxies including the MCs and Leo I are described in Kallivayalil et al. (2006a,b, 2013); Sohn et al. (2013).

The *Gaia* mission is optimized for studying the MW, its satellite system, and other substructures in its halo including GCs and stellar streams as it charts the 3D motion of over one billion stars in the LG (Gaia Collaboration et al., 2018b,a). While the over-arching astrophysical goals of the mission are quite broad with topics

ranging from the Solar System to asteroids to Galactic structure, it will also yield the most precise 3D map of our Galaxy following in the footsteps of its predecessor, *Hipparcos*.

Key results from the first Gaia data release (DR1) include measurements of the internal rotation and PMs of the MCs (van der Marel and Sahlmann, 2016a), previously measured by van der Marel and Kallivayalil (2014) using HST. These measurements are crucial for deriving Galactocentric velocities from PM measurements, which must be corrected for internal motions as discussed above. *Gaia* offers a full view across the disks of the galaxies, a significant improvement on small, target fields of data from HST, which do not provide enough information to deduce the internal kinematics of stars in the disks.

The second data release (DR2) from *Gaia* allowed for a longer time baseline to measure PMs and additional stellar properties from repeated visits to the same regions of the sky over a 22 month period. However, given the complexity of the spacecraft scanning pattern, the cadence with which images are taken, and the systematics of how PMs are derived for individual stars, deriving PMs for galaxies is quite complicated. Nonetheless, *Gaia* DR2 led to a tremendous number of interesting results, including PMs for tens of MW satellite galaxies and GCs that had no prior PM measurements (Simon, 2018; Kallivayalil et al., 2018; Fritz et al., 2018; Watkins et al., 2019). DR2 was even used to measure the PMs and rotation of M33 and M31 using hundreds of the brightest supergiant stars that are observable with *Gaia* at the distance of the M31 system. The M33-M31 orbit and the future orbit of the MW-M31 are revisited in Chapter 6 of this dissertation (van der Marel et al., 2019, w. Patel) using the 3D velocities derived from these PMs. The accuracy and precision of *Gaia* DR2 PMs for MW substructures, M31, and M33 are not yet as high as those measured using HST and the VLBA. By the end of the planned mission, similar levels of accuracy and precision are predicted since uncertainties are expected to decrease as the 1.5th power of the time baseline.

1.5.2 High-Resolution Cosmological Simulations

Advanced high-performance computing (HPC) facilities and improved numerical methods have led to sizeable improvements in the creation of the highest resolution, large-scale simulations in astronomy. Cosmological simulations aim to reproduce a fraction of the observable Universe as it evolves for over 13 Gyr in volumes of typically (100-200 Mpc)^3. As these simulations include the physical imprint of the large scale structure in which thousands of simulated galaxies are embedded, they provide the most physically realistic testing ground for galaxy formation and evolution from early epochs to today. Furthermore, cosmological simulations generally reproduce the properties of galaxies in the observable Universe, including their diversity in mass, size, shape, and number densities across a large volume. Therefore, they provide a large statistical sample to provide context for observations and to draw connections between observations and predictions in ΛCDM cosmology.

Cosmological simulations also provide the added benefit that they track the evolution of dark matter. Dark matter is not directly observable, so its properties can only be inferred via the luminous baryons that it interacts with through gravity. These simulations provide a view of dark matter halos and their properties that cannot otherwise be seen in this level of detail, allowing for a better understanding of the galaxies residing within them. They also account for the live evolution of dark matter halos, which are important for calculating the orbital histories of satellites galaxies around their hosts. Analytic orbits typically consider static halo potentials for all host and satellite galaxies (see Garavito-Camargo et al., in prep. for analytic representations of time-evolving potentials), therefore using cosmological orbital properties in tandem with these calculations helps capture the complexities of halo formation and halo environment (i.e. groups vs. isolated halo environments) necessary for a more physically accurate picture of this dynamical evolution.

The Millennium and Millennium-II simulations (Springel et al., 2005a; Boylan-Kolchin et al., 2009) are well-known examples of large volume, cosmological simulations run with the `GADGET` code (Springel et al., 2001a; Springel, 2005b). The Millen-

nium runs are N-body simulations of dark matter in ΛCDM cosmology evolved over cosmic time. The second flavor of cosmological simulations are fully hydrodynamical simulations, which track the co-evolution of both dark matter and baryons. Hydrodynamical simulations therefore require more resolution elements and more complex numerical methods as they must calculate not only the gravitational forces between particles but also the equations of hydrodynamics for gaseous cells/particles. Additionally, hydrodynamical simulations include prescriptions for subgrid physics, which cover a range of hydrodynamical processes from star formation to feedback owing to supernovae and active galactic nuclei.

The EAGLE and Illustris projects are both suites of cosmological, hydrodynamical simulations (McAlpine et al., 2016; Vogelsberger et al., 2014b,a; Nelson et al., 2015) set in ΛCDM cosmology. Differences between each of these simulation suites include the cosmological parameters used to initialize the simulations, the numerical methods and codes used to calculate gravity (and hydrodynamics where included), the subgrid physics, the particle mass resolution, and the spatial resolution. Owing to computational advancements in the last 20 years, the number of resolution elements in simulations of this scale has increased by nearly five orders of magnitude from 10^5 to 10^{10}, allowing for more robust modeling of larger volumes with higher particle mass resolution[5].

High resolution is especially important for the work in this dissertation, as the studies presented here focus on some of the least massive galaxies in the Universe with dark matter halo masses of order $10^{11}\,\mathrm{M}_\odot$ or less. Studying these galaxies in detail requires an understanding of their frequency and properties in a statistical sense, which is only possible with simulations of this size and resolution. Current state-of-the-art cosmological volumes (i.e. the Illustris simulations and the EAGLE simulations) have dark matter particle mass resolutions $m_{\mathrm{DM}} = 7.6 - 9.7 \times 10^6\,\mathrm{M}_\odot$. Therefore, satellite galaxies identified in these simulations are composed of $10^2 - 10^4$ dark matter particles each. The main questions of interest in this dissertation only rely on the center of mass motion of satellite galaxies relative to their host

[5]http://www.illustris-project.org/about/#astronomers

galaxy's dark matter halo and the properties of the satellite's own dark matter halo. Therefore, just N-body cosmological simulations, such as the Illustris-1-Dark are necessary for this work rather than their fully hydrodynamical counterparts. As discussed in Chapter 2, nearly 500 LMC/M33 mass analogs are identified around a population of nearly 2,000 MW/M31 mass analogs, providing sufficient statistics to investigate the frequency and properties of massive satellite galaxies in the LG. In Chapters 3 and 4, mass analogs of the classical dSph MW/M31 satellites are identified to constrain the mass of the MW and M31's dark matter halo.

1.6 Thesis Outline

This dissertation is organized as follows. In Chapter 2, I quantify the preferred orbital histories for the LMC and M33 relative to the MW and M31, respectively, given PM measurements from HST and the VLBA and their uncertainties. I also compare the resulting orbital histories to the orbits of cosmological analogs of massive satellite galaxies in the *Illustris-1-Dark* simulation. In Chapter 3, I use the current kinematics and dynamics of the LMC and M33 to statistically constrain the total masses of MW and M31 in a Bayesian framework that combines 6D phase space information derived from high precision astrometry with the properties of simulated massive satellite galaxy analogs. In Chapter 4, I extend the methods outlined in Chapter 3 to include the properties of multiple satellite galaxies simultaneously, allowing for an improved mass estimate for the MW. In Chapter 5, I tabulate the expected satellite galaxy population of M33 using subhalo abundance methods calibrated on ΛCDM cosmological-zoom simulations and determine the consequences of various M33 orbital histories, including the new orbital history presented in Chapter 1. In Chapter 6, I discuss the orbital history of M33 and future fate of the LG using new M31 and M33 PMs from *Gaia*. Finally, in Chapter 7, I summarize the key conclusions in this dissertation and discuss future directions for studies of LG satellite galaxies.

CHAPTER 2

Orbits of Massive Satellite Galaxies - I. A Close Look at the Large Magellanic Cloud and a New Orbital History for M33

This chapter has been published previously as Patel, E., Besla, G., Sohn, S. T., 2017, MNRAS, 464, 3825

Abstract

The Milky Way (MW) and M31 both harbor massive satellite galaxies, the Large Magellanic Cloud (LMC) and M33, which may comprise up to 10 per cent of their host's total mass. Massive satellites can change the orbital barycenter of the host-satellite system by tens of kiloparsecs and are cosmologically expected to harbor dwarf satellite galaxies of their own. Assessing the impact of these effects depends crucially on the orbital histories of the LMC and M33. Here, we revisit the dynamics of the MW-LMC system and present the first detailed analysis of the M31-M33 system utilizing high precision proper motions and statistics from the dark matter-only Illustris cosmological simulation. With the latest *Hubble Space Telescope* proper motion measurements of M31, we reliably constrain M33's interaction history with its host. In particular, like the LMC, M33 is either on its first passage ($t_{inf} < 2$ Gyr ago) or if M31 is massive ($\geq 2 \times 10^{12}\,M_{\odot}$), it is on a long period orbit of about 6 Gyr. Cosmological analogs of the LMC and M33 identified in Illustris support this picture and provide further insight about their host masses. We conclude that, cosmologically, massive satellites like the LMC and M33 are likely completing their first orbits about their hosts. We also find that the orbital energies of such analogs prefer a MW halo mass $\sim 1.5 \times 10^{12}\,M_{\odot}$ and an M31 halo mass $\geq 1.5 \times 10^{12}\,M_{\odot}$. Despite conventional wisdom, we conclude it is highly improbable that M33 made a close (< 100 kpc) approach to M31 recently ($t_{peri} < 3$ Gyr ago). Such orbits are rare (< 1 per cent) within the 4σ error space allowed by observations. This conclusion

cannot be explained by perturbative effects through four body encounters between the MW, M31, M33, and the LMC. This surprising result implies that we must search for a new explanation for M33's strongly warped gas and stellar discs.

2.1 Introduction

Both the Milky Way (MW) and M31 host systems of satellite dwarf galaxies that are relics of their assembly history. These satellite galaxies are typically assumed to exert minimal gravitational forces on their hosts or on each other. As such, satellites are often considered point mass tracers of their host potentials. However, this assumption breaks down if the total mass of the satellite is a significant fraction of the host mass.

The MW and M31 both host such massive satellites, the Large Magellanic Cloud (LMC) and M33, respectively. With stellar masses of 3-5 $\times 10^9$ $M_\odot$, both galaxies are cosmologically expected to have dark matter masses of order 10^{11} $M_\odot$, roughly 10 per cent of the total mass of the MW or M31 (Moster et al., 2013).

While we generally think of satellites as being heavily affected by their hosts (via tides, ram pressure, etc.), massive satellites can in turn affect the dynamics and structure of their hosts as well. They can induce warps in the host galactic disc (e.g. Weinberg, 1998; Weinberg and Blitz, 2006), shift the orbital barycenter of the host-satellite system by tens of kiloparsecs (e.g. Gómez et al., 2015, hereafter G15), and are cosmologically expected to host dwarf satellite galaxies of their own (Sales et al., 2013; Deason et al., 2015).

The past orbital trajectory of these galaxies is critical to understanding the origin of and magnitude to which these effects play a role in the dynamical history of the Local Group. More specifically, the accretion time, number of pericentric approaches, and the host-satellite separation at those pericentric passages are key determinants for these phenomena. The survivability of satellites in the environment of their host halos is also directly connected to the time-scale over which satellites approach and potentially interact with their hosts.

Knowledge of warps in the gas discs of the MW and M31 date back to the mid-20$^{\text{th}}$ century (e.g. Oort et al., 1958; Roberts and Whitehurst, 1975; Newton and Emerson, 1977). Both warps reach heights up to several kiloparsecs above the disc plane. Several authors have argued that the LMC could be responsible for inducing the warp in the MW's disc (e.g. Weinberg, 1998; Weinberg and Blitz, 2006; Tsuchiya, 2002) or whether the influence of other satellites, such as the Sagittarius dSph, also play a role in this phenomena (Laporte et al., 2018; Gómez et al., 2013). Similarly, M31 satellites are suspects in the formation of the warp in M31's gas disc and other prominent substructures, such as its star forming ring (Block et al., 2006; Fardal et al., 2009). M33 being the most massive of those satellites may contribute to the current structure of M31's warped disc if it once reached a similar pericentric distance as the LMC ($\sim$50 kpc). On a lower mass scale, satellites of massive satellite galaxies could have similar impacts on their dwarf hosts if their orbits allow for close passages (e.g. the LMC's disc may be warped owing to interactions with the Small Magellanic Cloud; Besla et al., 2012, 2016).

In 2015, a slew of ultra-faint dwarf galaxy candidates were discovered in the Southern hemisphere, many of which are located in close proximity to the LMC (Bechtol et al., 2015; Koposov et al., 2015; Martin et al., 2015; Drlica-Wagner et al., 2015; Kim et al., 2015; Kim and Jerjen, 2015). Several studies have suggested that the new ultra-faint dwarfs are dynamical companions of the LMC (e.g. Deason et al., 2015; Jethwa et al., 2016; Martin et al., 2015). This association depends directly on the orbital history of the LMC and its purported system of satellites about the MW (Sales et al., 2011). For example, in a first infall scenario for the LMC, there has not been enough time for the MW's tides to disrupt the infalling system and consequently remove traces of common orbital trajectories and similar kinematics. Whether M33 may harbor faint satellite companions today will similarly depend sensitively on its orbital history about M31.

As massive satellites approach distances within tens of kpc from their hosts, the high mass ratio of the system becomes exacerbated. For example, at a separation of 50 kpc, the total mass of the LMC may be up to 25 per cent of the MW mass

enclosed within a similar radius. G15 illustrate that the MW experiences a strong gravitational influence due to the massive LMC residing nearby. As a result, the orbital barycenter of the MW-LMC sloshes back and forth over Gyr time-scales–this effect can also modify the orbital planes of other MW satellites like the Sagittarius dSph (G15). The M31-M33 system is similarly susceptible to this gravitational effect. Thus a constraint on the closest passage of M33 about M31 is crucial to understanding the current and future dynamics of M31 and its satellites.

Furthermore, the host-satellite separation determines the morphological impact that processes such as tidal stripping will have on the satellite. The time-scales over which satellite galaxies deplete their gas reservoirs and cease forming stars (quenching) is also sensitive to the orbital histories of the satellites about their hosts (e.g. Wetzel et al., 2014, 2015). It is curious that the MW and M31 both host a massive, gas-rich satellite at distances where other satellites are gas poor. These abundant gas reservoirs suggest that the LMC and M33 have only recently been accreted by their hosts. A recent accretion scenario is consistent with proper motion measurements of the LMC (Kallivayalil et al., 2013; Besla et al., 2007) and cosmological expectations (Boylan-Kolchin et al., 2011a; Busha et al., 2011; González et al., 2013). However, to date the orbital history of M33 about M31 has not been similarly examined.

A scenario under which M33 makes a close passage to M31 is presented by McConnachie et al. (2009) and Putman et al. (2009). The gas and stellar discs of M33 are substantially warped. These studies require that M33 made a close (50-100 kpc) encounter with M31 in the past 3 Gyr. We will use these models as a foundation to our assessment of M33's orbital history in analytic models and cosmological simulations.

To date, a rigorous, simultaneous study of the orbital history of M33, both numerically and cosmologically, has not been conducted. The major missing component for such an analysis has been a precise measurement of M31's proper motion. Recent *Hubble Space Telescope (HST)* observations have constrained the tangential velocity of M31 to $v_{tan} = 17 \pm 17$ km s^{-1} (Sohn et al., 2012; van der Marel et al., 2012a). Others have inferred the tangential velocity component of M31 by using the

kinematics of M31 satellites (van der Marel and Guhathakurta, 2008; Salomon et al., 2016), and the latter reports a value as high as $v_{tan} \sim 150$ km s^{-1}. The discrepancy between these values has severe implications for the history and current state of the Local Group. Depending on its orbital history, M33 may help minimize this discrepancy or it may simultaneously impact the motions of other M31 satellites, further complicating such analyses.

M33's proper motion was measured recently by Brunthaler et al. (2005) using the *Very Long Baseline Array (VLBA)*. Together, the proper motion measurements of M33 and M31 allow us to constrain the relative motion of the two galaxies, enabling us to quantify the plausibility of a recent, close M31-M33 encounter for the first time.

In this study we develop a self-consistent picture linking the observed morphological structure of M33 and the LMC with their numerically derived orbital histories and statistics from the *Illustris* cosmological simulation (Nelson et al., 2015; Vogelsberger et al., 2014b,a; Genel et al., 2014). We will constrain the orbit of M33 using the latest astrometric data and place it in a cosmological context for the first time. We also compare the similarities and differences in the orbital properties of the two most massive satellite galaxies in the Local Group. Using orbits extracted for massive satellite analogs in the dark matter-only Illustris simulation, we will not only place their present-day kinematics in a cosmological context, but also their full orbital histories. Finally, we assess the impact of massive satellites on the structure of their hosts, on other satellites, and discuss implications of this picture regarding their own morphological evolution.

This paper is structured as follows. Section 2.2 highlights the observed properties of the LMC and M33 including their morphology, proper motions, and mass estimates. In Sections 2.3 and 2.4, we develop and analyse orbital histories for each host-satellite system based on astrometric data. Section 2.5 describes the Illustris simulation and our sample selection methods for host-satellite analogs. Section 2.6 compares the average dynamical properties of the LMC and M33 to the cosmological sample of massive satellite analogs. Section 2.7 assesses the viability of a close M31-

M33 encounter in both a cosmological context and in light of the astrometric data. Finally, Section 2.8 contains our final remarks on the link between proper motions, analytic orbital models, and cosmological analogs for massive satellite galaxies and their hosts.

This is the first in a pair of affiliated papers. In Paper II (Patel et al., 2017b), the orbits of massive satellite analogs in cosmological simulations are used to constrain the halo mass of the MW and M31. While this has been previously done for the MW-LMC by Boylan-Kolchin et al. (2011a); Busha et al. (2011); González et al. (2013), we will constrain the mass of M31 for the first time in this fashion.

2.2 Observed Properties of the LMC and M33

2.2.1 HI Structure

The LMC and M33 are gas-rich satellites. They are both outliers with respect to the distance-morphology relation exhibited by Local Group satellites. Most satellite galaxies nearest their host galaxies typically contain the least amount of gas and little to no star formation while the farthest satellites tend to host larger gas reservoirs and have increased star formation activity (van den Bergh, 2006). Similar results are found for dwarf galaxies in the Local Volume (ANGST survey, Weisz et al., 2011).

At only 49.6 and 202.6 kpc, respectively, from their host galaxies, the LMC and M33 are amongst the satellite galaxies with the highest gas fractions given their separations. The high HI masses of these satellites suggest they may have followed similar orbital histories about their respective hosts. Both galaxies exhibit highly disturbed HI morphologies, which have been traditionally used to constrain their orbital interaction history in the absence of well-constrained 3D velocities.

Here, we discuss the detailed morphological structures of the LMC and M33, mainly focusing on the distribution of HI gas. We also provide an overview of the traditional orbital histories suggested due to these specific structural features.

LMC

The HI mass of the LMC is $\sim 5 \times 10^8$ $M_\odot$ (Brüns and Kerp, 2004; Brüns et al., 2005; Staveley-Smith, 2002). In addition to hosting a large gas reservoir (Staveley-Smith et al., 2003), the LMC and its companion, the Small Magellanic Cloud (SMC), are trailed by a larger gaseous system known as the Magellanic Stream (MS). The MS is a band of HI gas composed of filaments and clumps stretching more than 100° across the sky (Mathewson et al., 1977; Putman et al., 1998, 2003; Brüns et al., 2005; Nidever et al., 2008, 2010). Prior to the first set of proper motions for the Magellanic Clouds (MCs) reported by Kallivayalil et al. (2006a,b), the MS was the main feature used to constrain the orbits of the MCs (Murai and Fujimoto, 1980; Gardiner and Noguchi, 1996; Connors et al., 2006).

In this paradigm, the MCs and the MS have a shared orbital history such that the orbits of the Clouds are directly related to the formation of the stream (Fich and Tremaine, 1991). The most common theories for MS formation mechanisms invoke multiple passages of the MCs about the MW. Careful orbital analysis with numerical and cosmological simulations using the MCs' proper motions has shown they are actually more likely to be on their first orbital passage (e.g. Besla et al., 2007; Boylan-Kolchin et al., 2011a, hereafter B07, BK11). The presence of the SMC lends support to this picture, as binary LMC-SMC configurations are unlikely to survive multiple passages about a massive host (Gómez et al., 2013, BK11). Tidal interactions between such tenuous binaries can instead facilitate the formation of gaseous streams like the MS, without aid from their hosts, as several authors have shown (e.g. Diaz and Bekki, 2011, 2012; Besla et al., 2012; Guglielmo et al., 2014).

Galaxies like the MW are surrounded by gaseous halos referred to as the circumgalactic medium (CGM) (e.g. Werk et al., 2014). Recent simulations by Salem et al. (2015) illustrate that the gas disc of the LMC is affected by the MW's CGM. Its gas disc is truncated to a radius of 6 kpc in the direction of motion–this truncation depends sensitively on the density of the CGM and the pericentric approach of the LMC to the MW. If the LMC recently passed its first pericenter, the truncation

is naturally explained as the asymmetry washes out over time (Salem et al., 2015; Besla et al., 2016). Simulations show the CGM effects are also maximized at pericenter, where the CGM density the LMC faces and its relative speed are highest. Therefore, the distribution of gas in massive satellites needs to be taken into account to develop a self-consistent picture of their orbital histories.

M33

While M33 is not trailed by a gaseous stream, it has a very extended gas disc with a total HI mass of 1.4×10^9 $M_\odot$. The disc stretches nearly 22 kpc from its center of mass and it shows evidence of a strong warp (Putman et al., 2009, hereafter P09). The Pan-Andromeda Archaeological Survey (PAndAS) of M31 and its environment also show that M33 contains a previously unknown warped stellar disc that extends about 30 kpc in projected distance across the sky from its center in both the North and South (McConnachie et al., 2009, hereafter M09). These strongly disturbed features have been traditionally explained by a recent close approach of M33 about M31.

M09 reproduces the stellar distortions in M33 using N-body simulations where M33 reaches perigalacticon (relative to M31) at 53 kpc nearly 2.6 Gyr ago and an apogalacticon of 264 kpc just under a Gyr ago. This modeled apocenter and pericenter pair results in an eccentricity of about 0.67. It also implies M33 is currently receding from apocenter and is heading towards its second pericentric approach, consistent with the relative radial velocity of M33 with respect to M31. P09's models find that about 60 per cent of their orbits with a perigalacticon of $\lesssim 100$ kpc in the last 3 Gyr would recover a tidal interaction between M31 and M33, where the tidal radius is ≤ 15 kpc. They claim this interaction could cause the observed distortions in its gas disc. Taking today's position as apogalacticon, this model implies a minimum eccentricity of about 0.34. These studies suggest that, if M33 did have a recent, close encounter with M31, its orbital trajectory is unlikely circular. Both the stellar and gas disc warps require a recent, close encounter and its lack of gas depletion suggests M33 was not accreted at early times.

Aside from its warped morphology, the distribution of gas in M33's HI disc may hold clues to its interaction history with M31. Unlike the LMC, M33's immense gas disc does not show any significant signs of truncation. The marked lack of such truncation in the disc of M33 suggests either a much more diffuse CGM about M31 or a pericenter distance much larger than $\sim$50 kpc. The CGM of M31 is fairly similar to other L_* galaxies (e.g. Lehner et al., 2015). On the other hand, a larger pericenter distance would be in contention with the models of M09 and P09. These scenarios can be disentangled with an accurate picture of M33's orbital history, further motivating this work.

2.2.2 Proper Motions

The proper motion measurements of the MCs (Kallivayalil et al., 2013) and M33 (Brunthaler et al., 2005, hereafter B05) provide a foundation to analytic studies of their orbital histories. Recently, space based observatories, such as HST and the upcoming *Gaia* satellite, have enabled the measurement of proper motions to an accuracy of microarcseconds per year, providing a precise, instantaneous picture of the 3D motions of Local Group galaxies. With constrained dynamics, we can now readily identify kinematic analogs to these in cosmological simulations, where there exists a statistically significant population of massive satellites. In the following, we review the latest proper motion measurements of the most massive members of our Local Group: the LMC, M33 and M31.

	x (kpc)	y (kpc)	z (kpc)	r (kpc)	v_X (km s^{-1})	v_Y (km s^{-1})	v_Z (km s^{-1})	$v_{\rm tot}$ (km s^{-1})	$v_{\rm rad}$ (km s^{-1})	$v_{\rm tan}$ (km s^{-1})
LMC	-1.1 ± 0.3	-41.1 ± 1.9	-27.9 ± 1.3	49.6 ± 2.3	-57 ± 13	-226 ± 15	221 ± 19	321 ± 24	64 ± 7	314 ± 24
M33	-97.2 ± 23.8	-121.5 ± 35.1	-129.7 ± 19.1	202.6 ± 46.5	-24 ± 34	177 ± 30	94 ± 39	202 ± 38	-152 ± 48	133 ± 37

Table 2.1: The position and velocity components for the LMC and M33, each with respect to their host galaxy. Errors are computed in a Monte Carlo fashion (see K13) by sampling the proper motion error space of the LMC (K13), M33 (B05), and M31 (S12, vdM12), combined with uncertainties in their positions and the solar quantities. The Local Standard of Rest velocity at the solar circle $V_0 = 239 \pm 5$ km s^{-1} (McMillan, 2011) is used, rather than the IAU value of $V_0 = 220$ km s^{-1}. The solar peculiar velocity is adopted from Schönrich et al. (2010), who find $(\mathrm{U, V, W})_\odot = (11.1^{+0.69}_{-0.75}, 12.24^{+0.47}_{-0.47}, 7.25^{+0.37}_{-0.36})$ km s^{-1}.

LMC

The proper motion of the LMC was most recently measured by K13. They used observations taken with HST of 22 fields in the LMC over a $\sim$7 year baseline to measure the motion of LMC stars with respect to background quasars. In this study, the proper motion of the LMC is transformed to a Galactocentric position and velocity using the methods described in van der Marel et al. (2002). The uncertainties on the mean values are determined by a Monte Carlo scheme that propagates all uncertainties in the position and velocity of the LMC and the Sun. This Monte Carlo technique yields a sample of 10,000 position and velocity vectors from which the mean Galactocentric velocity and errors are computed (see K13 and references therein). We will make use of these 10,000 Monte Carlo drawings in later sections. The resulting total position and velocity of the LMC from these drawings are $R_{LMC} = 49.6 \pm 2.3$ kpc and $v_{LMC} = 321 \pm 24$ km s^{-1} . The LMC's current radial velocity is $v_{rad} = 64 \pm 7$ km s^{-1} with respect to the MW. 3D position and velocity vectors are reported in Table 2.1.

M31

Proper motions of M31 have been inferred indirectly from satellite kinematics where the line of sight velocities are used to fit for the transverse motion of M31 (van der Marel and Guhathakurta, 2008, hereafter vdMG08). The resulting tangential velocity component of M31 is $v_{tan} = 42 \pm 18$ km s^{-1} . Recently, Sohn et al. (2012, hereafter S12) directly measured the proper motion of M31 for the first time by tracking the motions of stars in three fields with respect to thousands of background galaxies. The observations were taken with HST over a 5-7 year baseline.

van der Marel et al. (2012a, hereafter vdM12) corrected the S12 measurements for M31's internal kinematics and viewing perspective. In the end, they quote a weighted average for M31's proper motion using both HST direct measurements (S12) and M31's satellite kinematics (vdMG08). In this analysis, we use this weighted average where the 68.3 per cent confidence level is $v_{tan} = 17 \pm 17$ km

s^{-1}. Again, the errors on the mean values for M31's position and velocity components are computed in a Monte Carlo fashion.

It should be noted that more recent estimates of M31's tangential velocity vector in Salomon et al. (2016, hereafter S16) find different values than those reported by vdM12. S16 reports a mean tangential velocity of ∼150 km s^{-1}. Their method utilizes Markov Chain Monte Carlo techniques to statistically maximize the likelihood of v_{tan} by using only satellite kinematics. They then weight the likelihoods by ΛCDM halo velocity dispersion profiles to estimate their best-fitting parameters. We will discuss the implications of these conflicting values further in Section 2.7.

M33

M33's proper motion was measured by B05 using the VLBA. The observations were taken over ∼3 years to measure the emission of water masers in two regions of M33 (IC133 and M33/19). By tracking emission features over 8 epochs, they compute a weighted average of their motions across the sky. They also propagate the errors in the velocity offset between specific maser features and the HI gas. These proper motions on the sky are transformed to Cartesian position and velocity coordinates in the MW reference frame through the same Monte Carlo methods as in K13.

This scheme is also used to obtain 10,000 Monte Carlo drawings from the 4σ proper motion error space of both M31 and M33. In addition to the proper motions and solar motion quantities, the Monte Carlo method incorporates distance errors into the analysis. Therefore, we adopt the M09 distance to M33 relative to the MW (∼800 kpc). It should be noted that other authors (e.g. U et al., 2009; Bonanos et al., 2006) have measured a significantly higher absolute distance to M33 (∼960 kpc). The maximum distance probed by the Monte Carlo scheme is ∼880 kpc. We will discuss the impact of a larger M33 distance in Section 2.7 where we explore if M33 could have reached within a close distance to M31.

The two sets of 10,000 unique position and velocity vectors are combined to form the relative position and velocity vectors of the M31-M33 system (see Table 2.1). The magnitude of the position and velocity of M33 are $R_{M33} = 202.6 \pm 46.5$ kpc and

$v_{M33} = 202 \pm 38$ km s^{-1}. At present, M33 has a radial velocity of -152 ± 48 km s^{-1} relative to M31. Hereafter, the subscript *M33* refers to the position or velocity relative to M31 just as *LMC* refers to kinematics relative to the MW.

2.2.3 Mass Estimates of the LMC and M33

Orbit determination and the identification of satellite analogs in cosmological simulations require knowledge of the satellite mass. In the following, we provide an overview of known mass constraints on the LMC and M33.

LMC

The LMC's rotation curve is well-defined, peaking at $v_{circ} = 91.7 \pm 18.8$ km s^{-1} and remains flat to about 8.7 kpc (van der Marel and Kallivayalil, 2014). Basic dynamical mass arguments ($V^2 = GM/r$) give an enclosed mass of M(8.7 kpc) $= 1.7 \times 10^{10}$ $M_\odot$.

The stellar mass of the LMC is $M_* \sim 2.7 \times 10^9$ $M_\odot$ with a neutral gas mass of $M_{gas} \sim 0.5 \times 10^9$ $M_\odot$ (Kim et al., 1998). This yields a total baryonic mass for the LMC of $M_{bary} = 3.2 \times 10^9$ $M_\odot$. Several lines of evidence point to the radius of the LMC extending to at least 15 kpc (Majewski et al., 2009; Saha et al., 2010; Mackey et al., 2016) at its outermost limits. At this radial extent, the total enclosed mass of the LMC is M(15 kpc) $\sim 3 \times 10^{10}$ $M_\odot$, assuming the rotation curve of the disc remains flat to this distance. While this is the total dynamical mass measured today, the LMC may have been significantly more massive at its time of infall. G15 and Besla (2015) propose its mass at infall is between $M_{vir,inf} = 6 - 20 \times 10^{10}$ $M_\odot$.

Abundance matching techniques find similar values for the infall mass of the LMC. For example, Guo et al. (2011) finds $M_{vir,LMC} = 1.6 \times 10^{11}$ $M_\odot$. In our cosmological study, we focus on satellites with a maximal mass in the range encompassing a factor of two about the LMC dark matter halo mass inferred from abundance matching, 8×10^{10} $M_\odot < M_{max} < 3.2 \times 10^{11}$ $M_\odot$ (see also BK11). Our analytic mod-

els probe a wider range of masses, extending down to the dynamical mass estimate: $3 - 25 \times 10^{10}$ $M_\odot$.

M33

The rotation curve of M33 is similarly well-defined using 21cm gas maps (Corbelli and Salucci, 2000). Unlike the LMC, M33's rotation curve continues to rise out to its most distant data point. Using the peak of the rotation curve, $v_{circ}(15kpc) = 130$ km s^{-1}, the dynamical mass of M33 is $M_{dyn}(15\ kpc) \sim 5 \times 10^{10}$ $M_\odot$. We adopt the combined stellar mass measured by Corbelli (2003) and inferred by Guo et al. (2010), averaging to $M_* = 3.2 \times 10^9$ $M_\odot$ (vdM12). Corbelli (2003) also measures a total gas mass of $M_{gas} \sim 3.2 \times 10^9$ $M_\odot$. Therefore, the average baryonic mass is $M_{bary} = 6.4 \times 10^9$ $M_\odot$.

Using the dynamical mass estimate of M33, the baryon fraction is $M_{bary}/M_{tot} =$ 12.8 per cent. This baryon fraction is a factor of a few more compared to average disc galaxies, suggesting that the total dark matter mass of M33 at infall was much larger than the dynamical mass inferred from the rotation curve. To get a more typical $M_{bary}/M_{tot} = 3 - 5$ per cent appropriate for disc galaxies, M33's mass at infall would have to be $M_{vir,inf} = 1.3 - 2.1 \times 10^{11}$ $M_\odot$. This range is well within the 1σ errors of abundance matching where $M_{vir,M33} = 1.7 \pm 0.55 \times 10^{11}$ $M_\odot$ (Guo et al., 2011). In our cosmological analysis, we examine satellites with maximal masses between 8×10^{10} $M_\odot < M_{max} < 3.2 \times 10^{11}$ $M_\odot$. These values encompass the full range of masses inferred from abundance matching for both the LMC and M33. In our analytic models, we adopt a similar mass range as for the LMC, except we account for M33's larger dynamical mass, giving $5 - 25 \times 10^{10}$ $M_\odot$.

2.3 Analytic Methods

Here, we describe methods to take the observed range of LMC and M33 positions, velocities and masses listed in the previous sections and extrapolate orbital histories. These analytic models represent the orbits preferred by the astrometric data,

independent of cosmological or morphological arguments. We follow the strategy outlined in G15 to track the orbital history of these satellites and the corresponding motions of their hosts. However, we implement a different scheme to account for dynamical friction (following Appendix A of van der Marel et al., 2012b). We consider the MW-LMC system to be independent of the M31-M33 system. This choice is justified in Section 2.4.3, where we show that M33 has not closely approached the MW within the past 6 Gyr, nor the LMC to M31.

To compute past orbital histories, the equations of motion are numerically integrated backwards in time. We adopt two mass models for both the MW and M31. For the MW, we use a total virial mass[1] of $1 \times 10^{12}\,\mathrm{M}_\odot$ and $1.5 \times 10^{12}\,\mathrm{M}_\odot$. For M31, we use slightly higher mass models, which are $1.5 \times 10^{12}\,\mathrm{M}_\odot$ and $2 \times 10^{12}\,\mathrm{M}_\odot$. The MW and M31 potentials are constructed to include three components: a Navarro-Frank-White (NFW) dark matter halo (Navarro et al., 1996)

$$\Phi_{\mathrm{halo}} = -\frac{\mathrm{GM_h}}{\mathrm{r}[\ln(1+\mathrm{c_{vir}}) - \mathrm{c_{vir}}/(1+\mathrm{c_{vir}})]} \ln\left(1 + \frac{\mathrm{r}}{\mathrm{r_s}}\right), \tag{2.1}$$

a Miyamoto-Nagai disc (Miyamoto and Nagai, 1975)

$$\Phi_{\mathrm{disc}} = -\frac{\mathrm{GM_d}}{\sqrt{\mathrm{r}^2 + \left(\mathrm{R_d} + \sqrt{\mathrm{z}^2 + \mathrm{z_d^2}}\right)^2}}, \tag{2.2}$$

and a Hernquist bulge (Hernquist, 1990)

$$\Phi_{\mathrm{bulge}} = -\frac{\mathrm{GM_b}}{\mathrm{r} + \mathrm{R_b}}. \tag{2.3}$$

For the NFW halo, $\mathrm{M_h} = \mathrm{M_{vir}} - \mathrm{M_d} - \mathrm{M_b}$.

The NFW dark matter halo of the host galaxy is adiabatically contracted due to the presence of the disc with the CONTRA code (Gnedin et al., 2004). The dark matter density profile is truncated at the virial radius of the host galaxy in each model.

[1]Virial mass is the mass enclosed within the virial radius ($\mathrm{R_{vir}}$). $\mathrm{R_{vir}}$ is the radius at which the average density within that radius reaches an overdensity of Δ_{vir} in a spherical 'top-hat' perturbation model. This Δ_{vir} factor depends directly on the cosmological parameters. The Illustris cosmology yields $\Delta_{\mathrm{vir}} = 357$ (or $\Delta_{\mathrm{vir}}/\Omega_{\mathrm{m}} = 97.4$). See Bryan and Norman (1998).

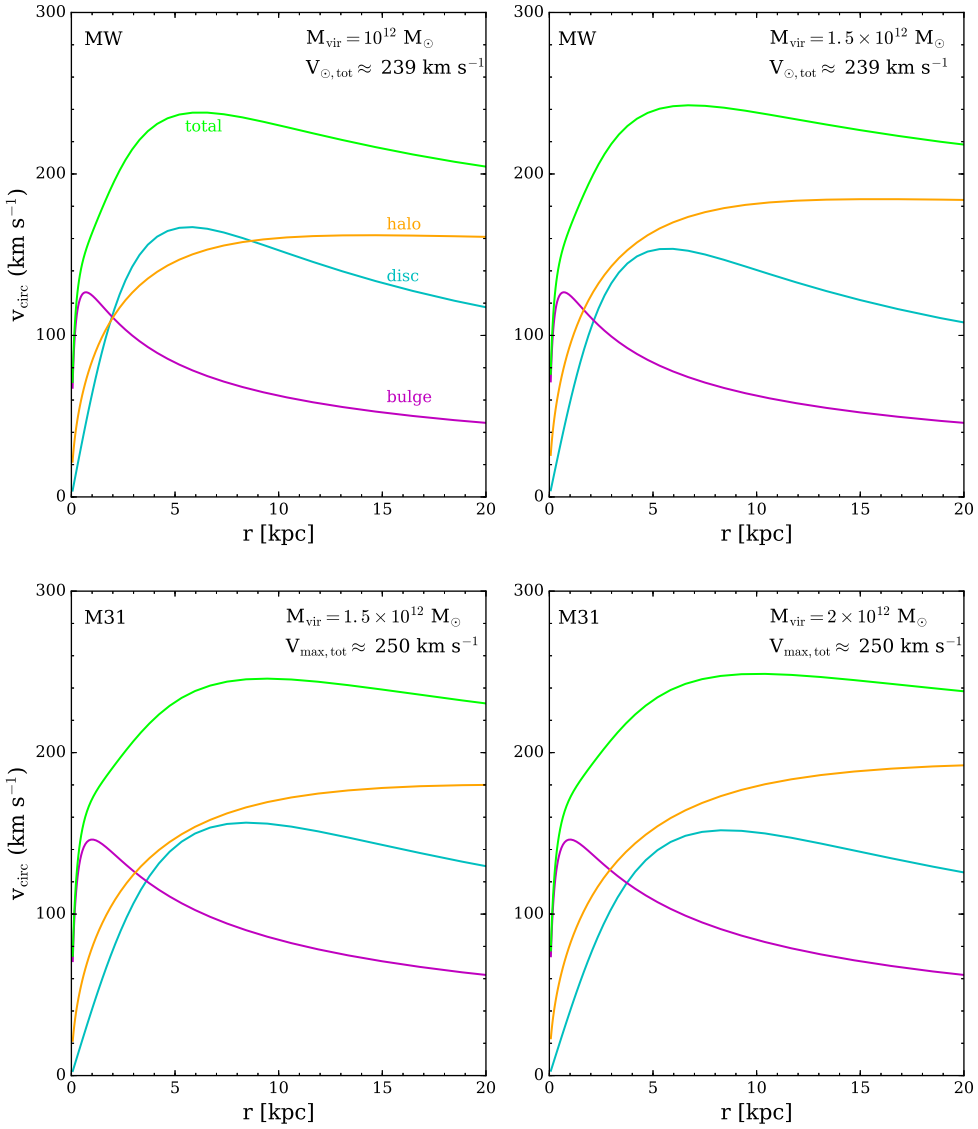

Figure 2.1: Model rotation curves of the MW and M31 used to calculate the orbital histories in Fig. 2.2. *Top:* Two different virial mass models for the MW have been constructed to match the observed rotation curve: M_{vir} =[1×10^{12}, 1.5×10^{12}] $M_\odot$. *Bottom:* Slightly higher virial mass models, M_{vir} =[1.5×10^{12}, 2×10^{12}] $M_\odot$, are used for M31. In each model, the individual contributions from the disc (cyan), halo (orange), and bulge (purple) are indicated. The disc mass was chosen to approximately reproduce the observed maximum circular velocity for each galaxy: $V_c \approx 239$ km s^{-1} at the solar radius for the MW (McMillan, 2011), $V_c \approx 250$ km s^{-1} for M31 (Corbelli et al., 2010). All halos have been adiabatically contracted due to the presence of the disc using the CONTRA code (Gnedin et al., 2004).

Table 2.2: Initial conditions for the mass distribution in host galaxies used in the orbit integrations. The disc masses have been chosen to match the observed maximum circular velocities (see also G15 and vdM12). See Fig. 2.1 for more details.

	MWa	MWb	M31a	M31b
M_{vir} [10^{10} $M_\odot$]	100	150	150	200
c_{vir}	9.86	9.56	9.56	9.36
R_{vir}[kpc]	261	299	299	329
M_d [10^{10} $M_\odot$]	6.5	5.5	8.5	8
R_d [kpc]	3.5	3.5	5.0	5.0
z_d [kpc]	0.53	0.53	1.0	1.0
M_b [10^{10} $M_\odot$]	1	1	1.9	1.9
R_b [kpc]	0.7	0.7	1.0	1.0

The disc mass in each model is chosen to approximately reproduce the observed maximum circular velocity for each galaxy: $V_c \approx 239$ km s^{-1} at the solar radius for the MW (McMillan, 2011), $V_c \approx 250$ km s^{-1} for M31 (Corbelli et al., 2010) at its peak. In all cases, the bulge scale length and mass remain fixed. The disc scale length and scale height are also held constant. All host galaxy parameters are listed in Table 2.2.

The rotation curves for each MW mass model are given in the top panels of Fig. 2.1. These show the circular velocity profile as a function of radius from the Galactic center for each of the halo (orange), bulge (purple), and disc (cyan) components as well as the total circular velocity curve (green). All MW models have been constructed to match the velocity of the Local Standard of Rest at the solar circle. Rotation curves for M31 are constructed in the same fashion as the MW's. The M31 models peak at its maximum circular velocity. They are given in the bottom panels of Fig. 2.1.

We consider three different mass models for the LMC and M33 respectively. For the LMC, we consider infall masses of $(3, 10, 25) \times 10^{10}\,M_\odot$. For M33, we use $(5, 10, 25) \times 10^{10}$ $M_\odot$ (see Section 2.2.3). There will thus be six orbital models for each host-satellite pair.

The satellites are represented as Plummer spheres such that their gravitational

potentials are:

$$\Phi_{\rm sat} = -\frac{\rm GM_{sat}}{\sqrt{\rm r^2 + k_{sat}^2}} \tag{2.4}$$

with masses and softening lengths ($\rm k_{sat}$) as listed in Table 2.3. The Plummer softening lengths have been calculated to match the measured dynamical masses of the LMC and M33. See Section 2.2.3.

Using a symplectic leapfrog integration method (Springel et al., 2001b), we follow the gravitational interactions between the host galaxy and satellite by integrating the equations of motion backwards in time for 13 Gyr. In all models, we use the mean 3D position and velocity vectors of each satellite as listed in Table 2.1 to describe the motions of the LMC with respect to the MW and M33 with respect to M31 at the present time. We will search the full error space when quoting statistical measures of the orbital properties for each system.

The orbit integrations also include the gravitational forces exerted on the host galaxies due to the massive satellites. G15 find that the acceleration of the MW due to the gravitational influence of the LMC is non-negligible. As a result, the orbital barycenter of the MW-LMC system is significantly displaced from the MW's center of mass. We allow M31's center of mass to move as a result of M33 and notice a comparable shift in the orbital barycenter of the M31-M33 system as well. The force exerted by the satellite on the host galaxy is therefore computed and updated at each time-step just like the force exerted on the satellite by the host.

Our models also include the damping effects resulting from dynamical friction. If the orbits are integrated forward in time, the damping causes the orbit to decay. Since we integrate the orbits backwards in time, dynamical friction actually acts as an accelerating force. We approximate this acceleration by the Chandrasekhar dynamical friction formula (Chandrasekhar, 1943):

$$\mathbf{F}_{df} = -\frac{4\pi \rm G^2 M_{sat}^2 ln\Lambda \rho(r)}{\rm v^2}\left[\rm erf(X) - \frac{2X}{\sqrt{\pi}}exp(-X^2)\right]\frac{\mathbf{v}}{\rm v}. \tag{2.5}$$

Here, $X = v/\sqrt{2\sigma}$ where σ is the one-dimensional galaxy velocity dispersion. We adopt the σ approximation for an NFW profile derived in Zentner and Bullock

(2003). $\rho(r)$ is the density of the contracted NFW dark matter halo at a distance $\mathbf{r}$ from the center of the host galaxy. For the Coulomb factor, lnΛ, we implement the parametrization described in van der Marel et al. (2012b, Appendix A):

$$\ln\Lambda = \max[\mathrm{L}, \ln(\mathrm{r}/\mathrm{Ca_s})^{\alpha}] \tag{2.6}$$

L, C, and α are constants. a_s is the softening length of the satellite, or $\mathrm{k_{sat}}$, the Plummer softening length for our models (see Table 2.3). Hashimoto et al. (2003) notes the importance of using lnΛ which varies with the distance of the secondary from the primary (r). van der Marel et al. (2012b) fits for lnΛ using N-body simulations where both the host and satellite are modeled as live, extended masses. They report the best-fitting parameters for a roughly equal mass orbit and a 10:1 host-satellite mass ratio tuned to match the future evolution of the M31-M33 system. We use the latter in our models for the MW-LMC and M31-M33 systems since both systems exhibit roughly this mass ratio at infall. The best-fitting results for unequal masses are L=0, C=1.22, α=1.0.

Note that this implementation of dynamical friction differs from that adopted in K13 and G15, as both studies implement the Hashimoto et al. (2003) lnΛ with a fixed softening length of 3 kpc for all satellite masses. If we keep the softening length fixed, we recover the same orbits for the LMC as K13 and G15. Finally, we ignore the dynamical friction effects on the MW (M31) due to the LMC (M33). With all of the relevant components, the total acceleration felt by the satellites is:

$$\ddot{\mathrm{r}}_{\mathrm{sat}} = \frac{\mathrm{d}\Phi_{\mathrm{bulge}}}{\mathrm{d}\mathbf{r}} + \frac{\mathrm{d}\Phi_{\mathrm{disc}}}{\mathrm{d}\mathbf{r}} + \frac{\mathrm{d}\Phi_{\mathrm{halo}}}{\mathrm{d}\mathbf{r}} + \frac{\mathbf{F}_{\mathrm{df}}}{\mathrm{M}_{\mathrm{sat}}} \tag{2.7}$$

and the total acceleration felt by the hosts is:

$$\ddot{\mathrm{r}}_{\mathrm{host}} = \frac{\mathrm{d}\Phi_{\mathrm{sat}}}{\mathrm{d}\mathbf{r}}. \tag{2.8}$$

$\mathbf{r}$ is always measured as the position vector between the host and the satellite, where both galaxies are free to move.

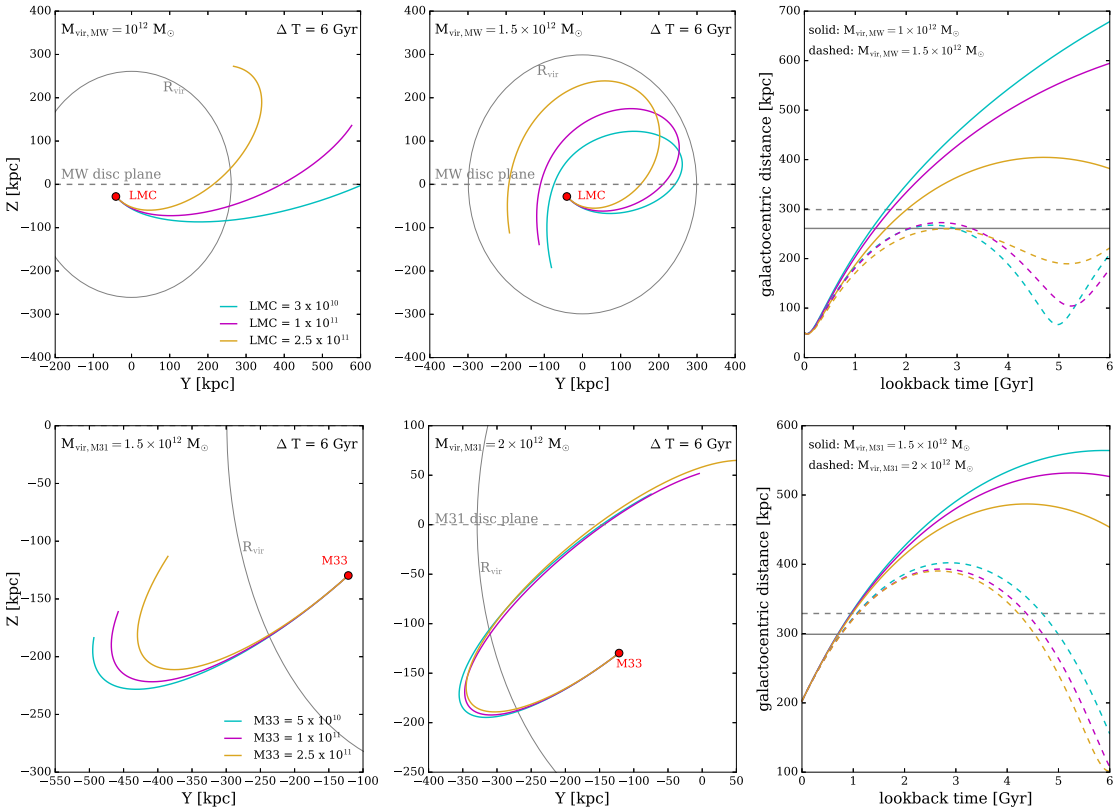

Figure 2.2: Numerical orbit integrations for the MW-LMC and M31-M33 models presented in Fig. 2.1 and Tables 2.2 and 2.3. The Y-Z orbital cross sections are shown for two different virial mass models for the MW (top) and M31 (bottom), respectively. The orbits have been integrated backwards in time for 6 Gyr using the mean position and velocity vectors as observed today for the initial conditions. Three different masses are considered for each of the LMC and M33 in all models (magenta, cyan, and gold solid lines). The disc planes of the host galaxies are indicated by the gray dashed line in the first and second column. The gray solid curves indicate the extents of the virial radius in each model. The third column shows the orbits for each of the two host galaxy models in time versus galactocentric distance. The coloured solid lines indicate the lower host galaxy mass for the MW and M31, while the dashed coloured lines show the resulting orbits in the higher host galaxy mass models. The dashed and solid gray lines represent the virial radius in the high and low virial mass models of the host galaxies.

Table 2.3: Initial satellite parameters for the analytic orbit integrations of the LMC and M33. The satellites are modeled as Plummer spheres with the given mass and the softening lengths are calculated to match the measured dynamical masses. These are $M_{LMC}(8.7\ kpc) = 1.7 \times 10^{10}\ M_\odot$ (van der Marel and Kallivayalil, 2014) and $M_{M33}(15\ kpc) \gtrsim 5 \times 10^{10}\ M_\odot$ (Corbelli and Salucci, 2000).

M_{LMC} [10^{10} $M_\odot$]	3	10	25
k_{LMC} [kpc]	5.9	13.1	19.5
M_{M33} [10^{10} $M_\odot$]	5	10	25
k_{M33} [kpc]	1	11.5	21

2.4 Analysis of Numerically Integrated Orbits

We consider the evolution of the LMC about the MW and M33 about M31 as two independent systems following the prescriptions outlined in the previous section. In the following, we analyse the resulting six orbital models for each host-satellite pair. For instance, in the case of the LMC, we determine if the analytic orbital models are in agreement with previous work. One main goal for M33 is to compare the resulting orbits to those presented by M09 and P09 to determine if a past interaction with M31 is a plausible cause of M33's warped structures.

2.4.1 LMC

In the top panel of Fig. 2.2, we present the orbital histories derived for the LMC about the MW over the past 6 Gyr, following the methods outlined in Section 2.3. We plot only the last 6 Gyr of the integration period because we do not include a live halo potential or satellite mass loss prescriptions. These processes may significantly affect the resulting orbits at earlier times.

For the lower MW virial mass model, where $M_{vir} = 1 \times 10^{12}\ M_\odot$, all LMC masses are consistent with a first infall scenario. The LMC's orbit indicates an infall time[2] of about 1.5-2 Gyr ago consistent with the results of B07, K13, and G15. One major difference between this work and G15 is that dynamical friction is reduced for the more massive satellites since we allow the Plummer softening length to vary with

[2]Infall time is defined as the first time the satellite crosses into the virial radius of its host.

Table 2.4: The first, second, and third quartiles for infall time, pericentric distance, and time of pericenter for the 10,000 orbits calculated from the LMC velocity error space. All orbits are integrated backwards for 13 Gyr. The listed times are lookback times. For both MW masses, the LMC's mass remains fixed at 1×10^{11} $M_{\odot}$.

MW M_{vir}	t_{inf} [Gyr]	r_{peri} [kpc]	t_{peri} [Gyr]
	q_1, q_2, q_3	q_1, q_2, q_3	q_1, q_2, q_3
1×10^{12} $M_{\odot}$	1.2, 1.4, 8.1	46.3, 48.0, 49.7	0.04, 0.05, 0.05
1.5×10^{12} $M_{\odot}$	5.9, 6.9, 8.7	46.1, 47.8, 49.6	0.05, 0.05, 0.06

satellite mass. In G15, the softening lengths were fixed, therefore the lowest satellite mass experienced the least dynamical friction. Here, we see the opposite trend.

The higher MW mass model, when $M_{vir} = 1.5 \times 10^{12}$ $M_{\odot}$, invokes at least one pericentric passage of the LMC about the MW with orbital periods of order 5 Gyr, regardless of LMC mass. For this MW mass model, the only difference between this analysis and previous work is the orbit of the highest LMC mass (gold dashed line). In G15, this mass combination does not result in a pericentric approach around 5 Gyr ago as seen here. Once again, this is a result of the modified dynamical friction term, and specifically the varying softening length. Note that a 5 Gyr orbital period is too long to explain the origin of the Magellanic Stream via MW tides, as the Stream is unlikely to have survived for greater than 2 Gyr (Bland-Hawthorn et al., 2007).

The models of the MW-LMC orbits presented in Fig. 2.2 only represent six specific orbital trajectories of the LMC as we have used the mean position and velocity vectors from Table 2.1. However, we also have 10,000 unique position and velocity vectors sampling the proper motion, position, and velocity error space of the LMC (see Section 2.2.2), which we use to compute statistical measures of the orbital properties allowed by the astrometric data. Holding the LMC's mass constant at 1×10^{11} $M_{\odot}$, we integrate the orbits backwards in time for 13 Gyr in both MW mass models. The first, second, and third quartile of important orbital properties are listed in Table 2.4.

For all orbits in the LMC velocity error space, at least one pericentric approach is

inevitable within a Hubble time (Růžička et al., 2009). Regardless of infall time, the orbits of the LMC are found to be consistent with recent studies–its first pericentric passage certainly occurs about $\sim$ 48 kpc from the MW in the last 50 Myr.

In agreement with G15, in the last 2 Gyr the MW's center of mass gains a velocity of $\sim$10-100 km s^{-1} (depending on the LMC mass) owing to the shift in the orbital barycenter of the MW-LMC system. This has been shown by G15 to cause noticeable shifts in the orbital planes of satellites like the Sagittarius dSph. We will explore similar effects for the M31-M33 system in the following section.

2.4.2 M33

Plausible orbital histories for M33 about M31 are presented in the bottom row of Fig. 2.2, using the mean relative velocity quoted in Table 2.1. In the low M31 mass model ($M_{vir} = 1.5 \times 10^{12}$ $M_{\odot}$), all of the M33 orbits are on first infall. These results are consistent with the orbital solutions found in Shaya and Tully (2013), who suggest that M33 is currently at its closest approach to M31.

M33's morphology may not naturally favor an orbital scenario other than a recent M31-M33 encounter. However, its extended stellar structures are still understandable without a close passage if M33 has interacted with other M31 satellites or if it has hosted satellites of its own in the past. We also note that Lewis et al. (2013) have pointed out that a spatial offset exists in the HI disc and stellar structures of M33. This offset could be attributed to accretion events or even mild ram pressure stripping in the halo outskirts ($\sim$100 kpc). Moreover, given that M33's total mass is $\sim 10^{11}$ $M_{\odot}$, it could have hosted several less massive satellite galaxies (see Sales et al., 2013), and the accretion of these satellites could have formed the stellar halo of M33 (McMonigal et al., 2016) through traditional hierarchical evolution. Furthermore, Berentzen et al. (2003) and Besla et al. (2012) have shown that off-center collisions with less massive satellites can perturb the stellar disc of host galaxies. One example of such phenomena is the multi-armed extended spiral structure detected in the outskirts of the LMC, a feature that Besla et al. (2016) suggests was induced by the SMC rather than MW tides.

For the high M31 mass model ($M_{vir} = 2 \times 10^{12}$ $M_\odot$), there is a chance of a pericentric passage at about 6 Gyr ago. However, this orbital period is almost twice that suggested by the P09 and M09 models, which were designed to match the observed morphological structure of M33. Both sets of orbits in Fig. 2.2 support the future M31-M33 orbits calculated in van der Marel et al. (2012b), which find M33's next pericentric passage about M31 will occur in the next 1-2 Gyr.

For the explored M33 mass range, we have also numerically integrated its orbit using the mean velocity of M31 resulting from the HST proper motion only (S12). By contrast, all previous orbits used the weighted average of the HST measurements and satellite kinematics (vdM12). We find that independent of M31 mass, all six orbits result in a first infall scenario and show no signs of a pericentric passage $<$ 12 Gyr ago.

The large M31 tangential velocity inferred by S16, however, has different implications for the orbit of M33. Using the S16 M31 velocity vector, in the low mass M31 model, we find that one pericentric passage between 2-3 Gyr ago is inevitable for all M33 masses explored here. However, the distance at pericenter is still large, reaching $\sim$175 kpc at best. In the high M31 mass model, all orbits evidence one or more pericentric passages. The most recent pericenter occurs between 2-3 Gyr ago and again, the separations are no less than $\sim$140 kpc.

Fig. 2.2 relied on the average M33 velocity but we can also explore the full velocity error space to quantify the most typical orbital histories. Calculating 10,000 orbits spanning the M33 and M31 velocity error space with a fixed M33 mass of 1×10^{11} $M_\odot$ results in the median orbital properties listed in Table 2.5. A first infall scenario is favored for the low M31 mass model, as proposed in Fig. 2.2. At this M31 mass, only about 48 per cent of all orbits contain a pericentric passage in an orbital period of 13 Gyr, but the distance of closest approach is more than twice that suggested by M09 and P09[3]. The median pericentric distances listed ($\sim$105

[3]We have also relaxed our assumption of halo truncation and turned off dynamical friction at the virial radius, but the resulting statistics only improve mildly for a recent, close passage scenario, independent of M31 mass.

kpc) are consistent with the findings of van der Marel et al. (2012b). The orbits with a pericentric passage unanimously have an infall time > 5 Gyr ago. In each case, the infall time occurs earlier than the time of pericenter.

If M31 is massive (2×10^{12} $M_{\odot}$), M33 follows a long period orbit of order 6 Gyr. In this scenario, it is unlikely that M33 made more than one pericentric passage about M31 in a Hubble time. Based on the values in Table 2.5, this host-satellite mass combination prefers early accretion, or $t_{inf} \gtrsim 5$ Gyr ago. At this M31 mass, 77 per cent of orbits reflect a pericentric passage also $\gtrsim 5$ Gyr ago. Similar to the low mass M31 model, the average pericentric distances are generally much higher than what is required to justify M33's warped structures by a close interaction with M31.

Therefore, the low mass M31 model typically favors a first infall scenario for M33, while a higher mass M31 suggests M33 made a distant pericentric approach about M31 about 5-6 Gyr ago. Consequently, a large fraction of the recent infall scenarios do not allow for a recent close encounter (within 100 kpc of M31) as suggested by M09 and P09. These results support the lack of a truncated gas disc in M33, which might be an artefact of a large distance at pericenter (> 100 kpc), consistent with our analysis.

The proper motions of the M31-M33 system are thus in direct conflict with the conventional orbital history of M33 adopted in the literature. We examine other host-satellite mass combinations in further detail in Section 2.7 to reconcile a recent pericentric passage of M33 about M31.

Following G15, we inspect the shift in M31's velocity due to the presence of M33. We find that M33 increases M31's velocity by $\sim$5-25 km s^{-1} for our explored mass range. Since M33's closest approach to M31 is much larger than that of the LMC to the MW, the magnitude of M31's velocity shift is lower. However, this shift is not negligible and may also result in observable signatures in the relative kinematics of M31 and its other satellites.

Table 2.5: Column 2 lists the first, second, and third quartiles in infall time for the 10,000 orbits spanning the M31-M33 velocity error space. Columns 3 and 4 give the quartiles in pericentric distance and time of pericenter for the fraction of orbits (48 per cent and 77 per cent, respectively, for low and high M31 mass) where M33 reaches distances closer than its current separation to M31. All orbits are integrated backwards for 13 Gyr. The listed times are lookback times. For both M31 masses, M33's mass remains fixed at 1×10^{11} $M_{\odot}$.

M31 M_{vir}	t_{inf} [Gyr]	r_{peri} [kpc]	t_{peri} [Gyr]
	q_1, q_2, q_3	q_1, q_2, q_3	q_1, q_2, q_3
1.5×10^{12} $M_{\odot}$	0.3, 0.4, 7.9	75.8, 104.9, 140.3	5.6, 7.4, 9.6
2×10^{12} $M_{\odot}$	4.3, 6.3, 8.4	74.3, 104.4, 137.0	4.6, 5.9, 8.0

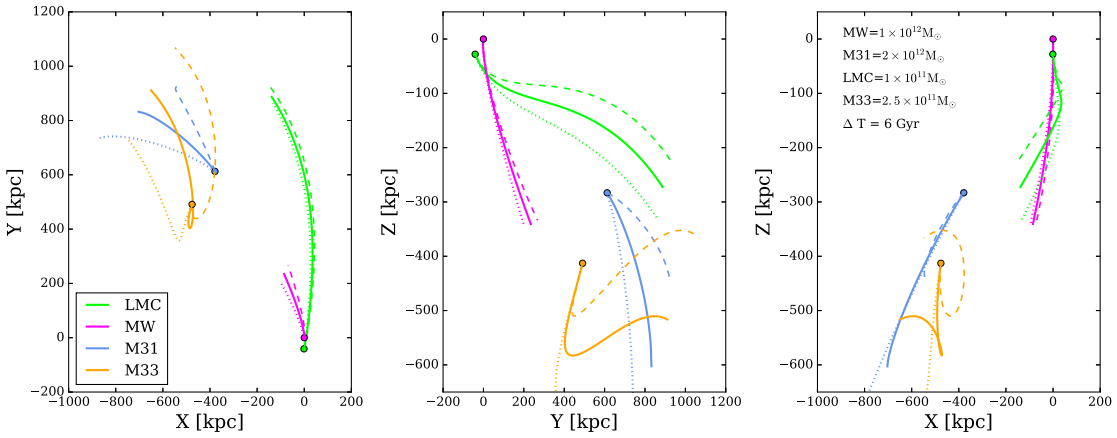

Figure 2.3: The numerically integrated orbital trajectories of the MW, LMC, M31, and M33 for the last 6 Gyr. All positions are plotted with respect to the MW's position as a function of time. Each galaxy exerts a gravitational force on all other galaxies. Dynamical friction is implemented in two regimes–for the host-satellite interactions and the host-host interactions. The solid lines are the resulting orbits computed at the mean velocity vectors of all galaxies. The dashed lines indicate the resulting orbital trajectory for a -1σ deviation in all four velocity vectors while the dotted lines are the +1σ deviation. The deviations represent the errors in the observed proper motion, position, and velocity error space for each galaxy.

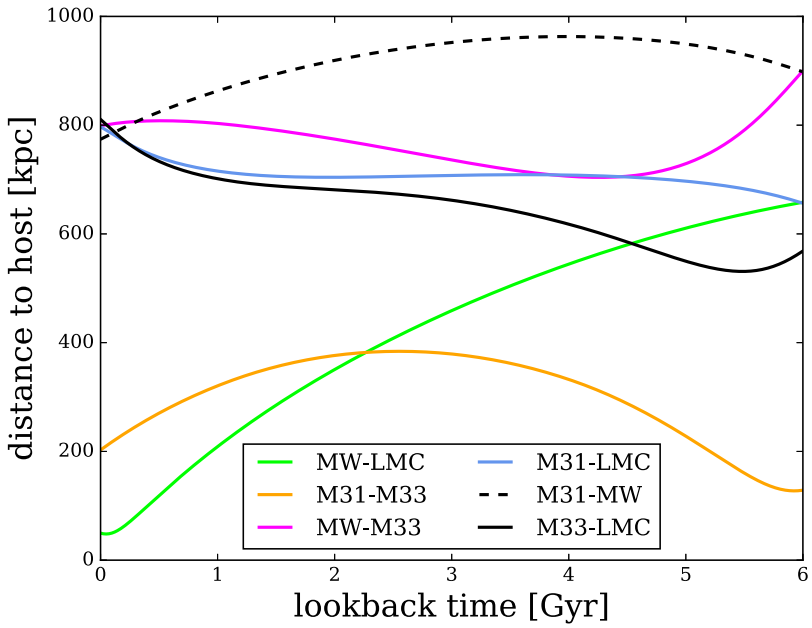

Figure 2.4: The orbital trajectories as a function of time for each pair of galaxies calculated at their mean velocities. The positions are plotted such that the first galaxy in the pair is the *host* and therefore the position of the corresponding *satellite* is plotted relative to that galaxy. Aside from the MW-LMC and M31-M33 pairs, no galaxies move closer than about 500 kpc from each other. The LMC is negligibly affected by M31 and M33 experiences little to no perturbations as a result of the MW.

2.4.3 The Four Body Orbit

Throughout this work, we treat the MW-LMC system and the M31-M33 as two, separate, isolated systems. Here, we validate this choice by numerically integrating the orbits of all four galaxies backwards in time simultaneously. Doing so ensures that the LMC has not been affected by the gravitational influence of M31, nor M33 by the MW during the past 6 Gyr. As van der Marel et al. (2012a,b) have shown, the MW and M31 are currently moving towards one another and will likely experience their first pericentric passage in about 4 Gyr. Therefore, in the past, the MW and M31 are moving away from one another.

Following the methodology of Section 2.3, we numerically integrate each galaxy's equations of motion backwards in time as they simultaneously experience the gravitational influence of each other. The satellites (LMC, M33) exert forces on both hosts (M31, MW) and dynamical friction is implemented for the satellites as described by Equations 2.5 and 2.6. The masses of the LMC and M33 are held constant at 1×10^{11} $M_{\odot}$ and 2.5×10^{11} $M_{\odot}$, respectively.

To approximate the gravitational interactions between the MW and M31, we use the dynamical friction tuning for a 1:1 mass ratio as given in Appendix A of van der Marel et al. (2012b). The softening lengths for the MW and M31 are chosen to match their observed masses within some radius compared to the total virial masses used in this model. The MW's virial mass is fixed at 1×10^{12} $M_{\odot}$ and M31's is 2×10^{12} $M_{\odot}$. For both galaxies, a Hernquist profile (Hernquist, 1990) is used to determine the softening length. The MW's mass enclosed within 50 kpc is about 3.8×10^{11} $M_{\odot}$ (B07 and references therein). M31's observationally constrained mass within 300 kpc is about 1.4×10^{12} $M_{\odot}$ (Watkins et al., 2010). Therefore, the resulting softening lengths are approximately $k_{MW} = 31.11$ kpc and $k_{M31} = 58.57$ kpc.

In Fig. 2.3, we present the orbital planes of the four-body interaction between the MW, LMC, M31, and M33 during the last 6 Gyr. All positions are plotted relative to the MW. The circular markers denote the position of each galaxy today. The dashed lines indicate the orbital trajectories resulting from a -1σ deviation in

the velocity vector of each galaxy and the dotted lines are due to a $+1\sigma$ deviation in each velocity vector.

Fig. 2.4 shows the orbital trajectory as a function of lookback time for each pair of galaxies amongst the four considered here. Notice that aside from the MW-LMC and M31-M33 pairs, the closest separation between any two galaxies is no more than $\sim$500 kpc. In particular, the LMC does not reach less than $\sim$650 kpc from M31 and M33 reaches no closer than $\sim$700 kpc from the MW. While the LMC's orbit may be perturbed slightly by M31 $>$ 6 Gyr ago, there is no strong evidence that this perturbation exists at more recent times. These results are consistent with Kallivayalil et al. (2009) who find that M31 does not significantly affect the LMC's orbit within the proper motion error space, unless M31 is sufficiently massive (i.e. $> 3.5 \times 10^{12}$). Thus, treating the MW-LMC and M31-M33 as isolated systems in the past is a reasonable simplification.

2.5 Analogs in the Illustris Simulation

Using the observed and inferred infall masses of the LMC and M33, we identify analogous host-satellite pairs in the *Illustris Project* (Nelson et al., 2015; Vogelsberger et al., 2014b,a; Genel et al., 2014), an N-body and hydrodynamic simulation spanning a cosmological volume of (106.5 Mpc)^3, carried out with the moving-mesh code `AREPO` (Springel, 2010). In this analysis, we use the highest resolution dark matter-only run, *Illustris-1-Dark* (hereafter Illustris-Dark), which follows the evolution of 1820^3 dark matter particles from $z = 127$ to $z = 0$, stored in a series of 136 snapshots. Illustris-Dark adopts the following cosmological parameters, which are consistent with *WMAP-9* measurements (Hinshaw et al., 2013): $\Omega_m = 0.2726$, $\Omega_\Lambda = 0.7274$, $\Omega_b = 0.0456$, $\sigma_8 = 0.809$, $n_s = 0.963$ and $h = 0.704$.

Dark matter halos and their bound substructures (i.e. subhalos) are identified in each of the 136 snapshots of the simulation using the `SUBFIND` halo-finding routine (Springel et al., 2001a; Dolag et al., 2009), which proceeds in the following way. First, dark matter halos are identified with the friends-of-friends (FoF) algorithm

(Davis et al., 1985), which links together any two particles separated by less than 0.2 times the mean interparticle separation. Then, for each of these halos (also known as FoF groups), subhalos are identified as overdense regions which are also determined to be gravitationally bound. Usually, each halo hosts a massive, central subhalo which contains most of the loosely bound material in the halo.

In order to follow such halos and subhalos across time, we use the merger trees[4] created with the recently developed SUBLINK code (Rodriguez-Gomez et al., 2015). The merger trees allow us to trace the histories of massive satellite analogs and therefore identify their properties at various epochs in cosmic history.

The large volume and high resolution in the Illustris-Dark simulation provide an ideal data set for studying the dynamics and properties of massive satellite galaxies in MW/M31-mass systems. The simulation achieves a dark matter particle mass resolution of $m_{DM} = 7.5 \times 10^6$ $M_\odot$. Therefore, a MW/M31-mass halo in Illustris-Dark is composed of up to a few times 10^5 dark matter particles and an LMC/M33-mass analog consists of up to $\sim 4 \times 10^4$ dark matter particles.

In the following, we identify a sample of MW/M31 mass analogs at $z = 0$. Within this set of halos, we search for those that host a massive subhalo analogous to the LMC or M33. With this population of massive satellite analogs and their hosts, we will examine the orbital dynamics of the analogs compared to the observed present-day dynamics of the real LMC and M33.

2.5.1 Sample Selection: Milky Way/M31 Analogs

Estimates for the virial mass of the MW's halo range from $\approx$ [0.7-2.5] $\times 10^{12}$ $M_\odot$ (e.g. Belokurov et al., 2014; Gibbons et al., 2014; Boylan-Kolchin et al., 2013; Sakamoto et al., 2003; Battaglia et al., 2005; Dehnen et al., 2006; Li and White, 2008; Gnedin et al., 2010; Watkins et al., 2010). M31's halo mass has been estimated via methods like abundance matching, satellite orbital dynamics, the timing argument, and cosmological simulations. Its halo mass is inferred to be as massive as the MW's

[4]The Illustris merger trees, halo catalogs, and group catalogs are all publicly available at www.illustris-project.org

or larger, especially by timing argument studies. A plausible virial mass range for M31 from the literature is $\approx$ [1-3] $\times 10^{12}$ $M_\odot$ (e.g. Evans et al., 2000; Watkins et al., 2010; Tollerud et al., 2012; Guo et al., 2010; Fardal et al., 2013). The M31 rotation curve peaks at a velocity greater than that of the MW and both its bulge and disc mass are also greater than the MW's (e.g. Guo et al., 2010; Wang et al., 2006; Loeb et al., 2005; Peebles, 1996; Kallivayalil et al., 2009; van der Marel et al., 2012a, and references therein). Therefore, we allow for a wide dark matter halo mass range to encompass a broad distribution from the literature.

MW/M31 analogs in Illustris-Dark are chosen as all central subhalos, as determined by `SUBFIND`, at $z = 0$ whose halo (or FoF group) virial masses are between 7×10^{11} $M_\odot$ $< M_{vir} <$ 3×10^{12} $M_\odot$. We have checked that the virial mass of each MW/M31 analog's halo is comparable to the central subhalo mass as given by `SUBFIND`. Since these quantities have nearly a one to one ratio, we take the virial mass of the halo (FoF group) as the halo mass of all hosts throughout this analysis. Our sample contains 1933 dark matter halos that satisfy these criteria. The distribution of virial mass for these MW/M31 analogs is indicated by the red histogram in Fig. 2.5. There are many more low mass halos, as one expects, due to the hierarchical evolution of cold dark matter halos.

2.5.2 Sample Selection: Hosts of Massive Satellites

The subset of MW/M31 analogs which host a massive satellite analog will be referred to as the host halo sample. About 24.4 per cent of the MW/M31 mass analogs host a massive subhalo. Throughout this analysis, *host halo* will exclusively refer to the dark matter halo of a MW/M31 mass analog which hosts a massive subhalo analogous to the LMC or M33. The blue histogram in Fig. 2.5 shows the probability of finding a host halo with a given mass from the full sample of MW/M31 analogs. The peak of the distribution lies at $\sim 10^{12}$ $M_\odot$ and only a few percent of host halos reach a mass close to the lower and upper limits: 0.7×10^{12} $M_\odot$, 3×10^{12} $M_\odot$. Thus, we allow for a broad range in the host halo mass. In practice, very few halos at the extrema of this range host massive satellite analogs.

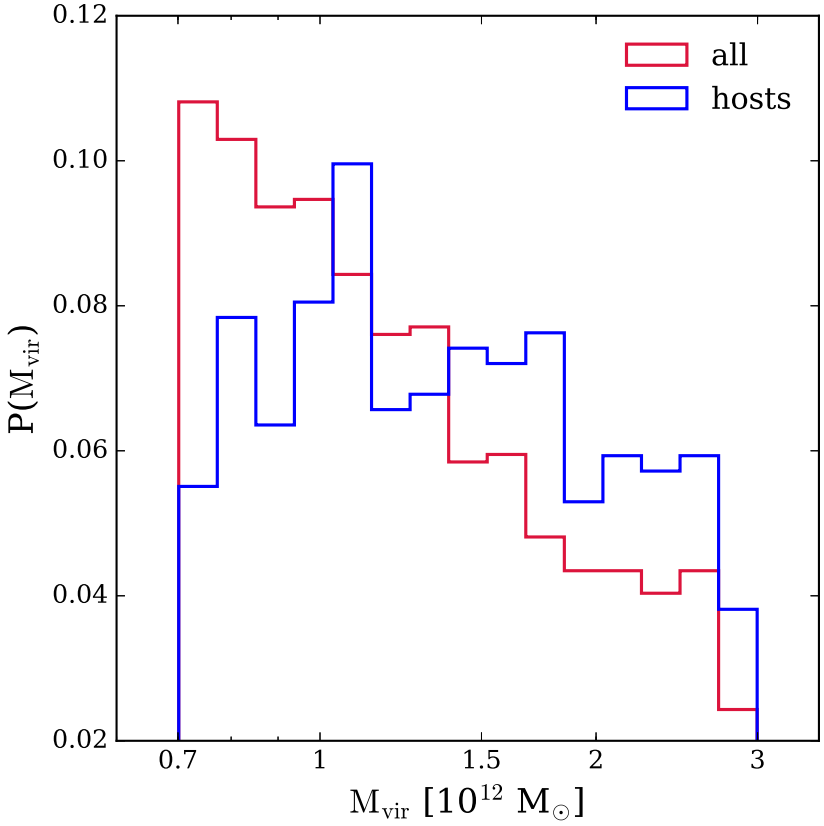

Figure 2.5: The distribution of virial mass ($\sim$ halo mass) for all MW/M31 mass analogs in the Illustris-Dark simulation at $z = 0$ (red). The distribution of virial mass for the MW/M31 mass analogs which also host a massive satellite analog at $z = 0$ (host halos, blue). This subset comprises 24.4 per cent of the full MW/M31 analogs sample. The bins are normalized to the size of each data set such that $\sum_{\mathrm{i=1}}^{\mathrm{N_{bins}}} \mathrm{M_{vir,i}} = 1$.

R_{vir} and V_{vir}, the virial circular velocity, can be computed from M_{vir} as follows

$$R_{vir} = 260 \left(\frac{M_{vir}}{10^{12}\ M_{\odot}} \right)^{1/3}\ \text{kpc}, \tag{2.9}$$

$$V_{vir} = 128.6 \left(\frac{M_{vir}}{10^{12}\ M_{\odot}} \right)^{1/3}\ \text{km s}^{-1}. \tag{2.10}$$

These virial quantities will be used to calculate satellite orbital dynamics (i.e. orbital energy and angular momentum) throughout this work.

2.5.3 Sample Selection: Massive Satellites

We follow the basic methods of BK11 to identify LMC/M33 analogs. BK11 used the Millennium-II (Boylan-Kolchin et al., 2009) ΛCDM cosmological simulation to study the dynamics of LMC and SMC analogs. However, in that study, the dynamics of the MCs were computed using the Kallivayalil et al. (2006a,b) proper motions, which have since been revised in K13. Here we extend their analysis to M33 and also update results for the LMC using the K13 proper motions.

For each MW/M31 analog identified in Section 2.5.1, we search through all subsequent satellite subhalos in the same FoF group to identify the subset of massive satellite analogs and their corresponding host halos. Below, we define the two samples used to accomplish this.

(i.) Preliminary Massive Satellite Analogs:
the most massive subhalo, identified by the maximal mass (M_{max}) ever attained, residing within R_{vir} of a MW/M31 analog's center at $z = 0$.

(ii.) Massive Satellite Analogs:
the subset of preliminary analogs with $8 \times 10^{10}\ M_{\odot} < M_{max} < 3.2 \times 10^{11}\ M_{\odot}$. The corresponding MW/M31 analog is then classified as a host halo (Section 2.5.2).

By this construction, each host halo is limited to one massive satellite analog. We use M_{max} to relate dark matter subhalos in simulations like Illustris-Dark to the observed galaxy properties because abundance matching techniques typically

correlate stellar mass to the maximal mass (in the form of $M_{200crit}$[5] or the FoF group mass) of halos. If we use the $z = 0$ satellite subhalo mass to identify analogs, the mass loss due to tidal stripping after accretion would have to be accounted for, requiring the implementation of mass loss prescriptions for interacting galaxies. Choosing satellite subhalos based on M_{max} does not necessarily mean that they are the most massive satellite subhalos in their FoF group at $z = 0$ but they have at least achieved the mass of a *massive satellite* (i.e. 10 per cent of the host halo mass) at some point in their history.

We impose a mass floor of 10^{10} $M_\odot$ ($\sim$1300 dark matter particles) at $z = 0$ for a satellite subhalo to be considered an analog of the LMC and M33. This value comes from the dynamical mass estimates of the LMC and M33 (see Section 2.2.3). While identifying preliminary LMC/M33 analogs, we also correct relative positions for the box edges to make sure that no subhalos are dismissed due to the finite box volume and simulation boundary conditions.

Requiring MW/M31 analogs to be the central subhalo in a FoF group and identifying LMC/M33 analogs in this fashion ensures that there are no massive companion galaxies in each group (i.e. no Local Group analogs). This choice is justified by the study of González et al. (2013) which concludes that the environment of Magellanic Cloud analogs, whether they are hosted by a MW mass analog or within an analog of the Local Group, does not strongly affect estimates of the MW's halo mass. However, the frequency of the latter is much lower cosmologically. This choice thus allows us to increase our orbital statistics.

Our host+massive satellite analogs sample consists of 472 systems. We therefore find that 24.4 per cent of MW/M31 mass halos harbor a massive satellite analog. BK11 finds about 35 per cent of their MW sample hosts an LMC analog in the Millennium-II simulation, however their host halo mass range has a lower limit of 10^{12} $M_\odot$. If we apply this lower halo mass limit to our MW/M31 host sample, about 33 per cent of them host an LMC/M33 analog, in good agreement with BK11.

[5]The mass contained within R_{200}, the radius at which the average overdensity of the universe is 200 times the critical density

Observational studies of the *Sloan Digital Sky Survey* also show that about 40 per cent of L_* galaxies host a bright satellite within 250 projected kpc (Tollerud et al., 2011a).

Fig. 2.6 indicates the distribution of host to satellite mass ratio at $z = 0$ (blue) and at the time where the satellites reach maximal mass (red). The peak of the distribution is about 10^{-1} at the time of maximal mass, indicating that analogs of the LMC or M33 are a significant fraction of their host's mass at that epoch. This is consistent with the work of Stewart et al. (2008) who suggest MW mass dark matter halos are built up by 1:10 mergers. Even at $z = 0$, the massive satellite analogs are no less than 10^{-2} of their host halo mass. The offset of the two distributions suggests that the sample of host+massive satellite analogs evolve quite noticeably from one epoch to the next, a property that cannot be captured in the analytic orbital models.

2.6 Orbital Analysis of LMC and M33 Analogs in Illustris

With a sample of several hundred massive satellite analogs and their respective hosts, we identify the average trends in their orbital histories. The mean positions and velocities of the LMC and M33 obtained from their proper motion measurements are used to infer the present-day dynamics of the satellites as a point of reference. By comparing these dynamical properties against the properties of the cosmological sample, we place the orbits of the LMC and M33 in a cosmological context.

2.6.1 Crossing Time

The first crossing time (t_{cross}) is synonymous with the time at which a subhalo infalls into its host halo. From our analytic orbit analysis in Section 2.4, we find the lower mass models for the MW and M31 both suggest recent, first infall scenarios for the LMC and M33, respectively. The higher host mass models show some evidence that longer-lived orbits, and therefore earlier crossing times are possible. Here, we identify the first crossing time for all massive satellite analogs in Illustris-Dark to

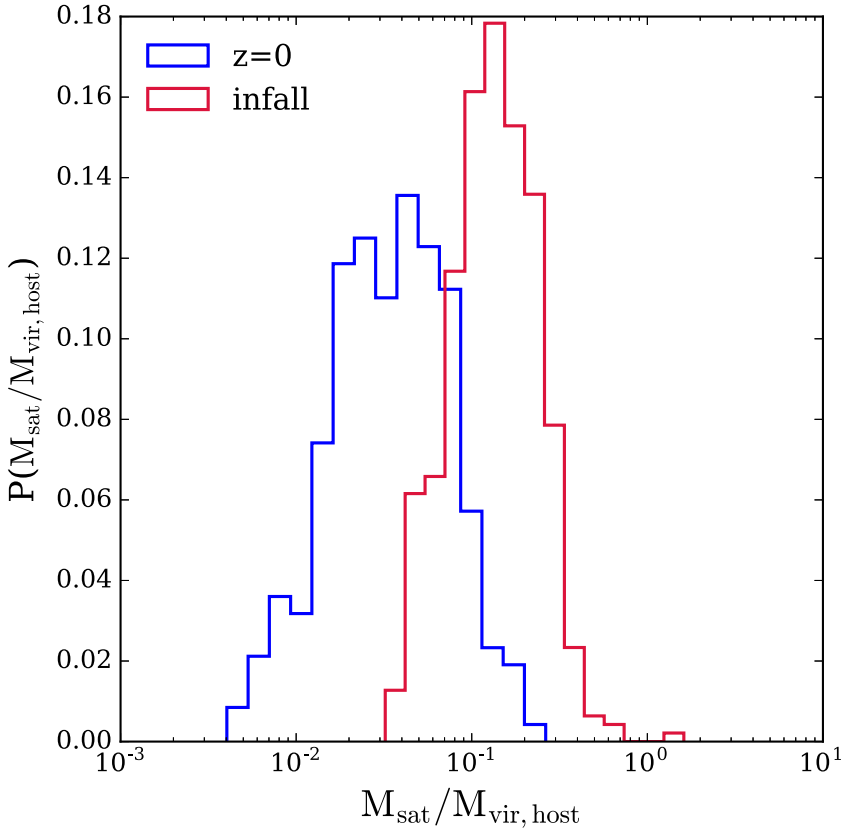

Figure 2.6: The distribution of satellite to host dark matter mass ratios at infall (red) and at $z = 0$ (blue) in the Illustris-Dark simulation. At infall, the mass ratio peaks at $\sim 10^{-1}$. At $z = 0$, the host-satellite mass ratios are no lower than $\sim 10^{-2}$.

statistically determine the most likely infall time for the LMC and M33, respectively, in a cosmological setting. To date, M33's infall time has not been constrained by a statistically significant cosmological sample.

BK11 defines the first crossing time (or BK t_{cross}) as 'the lookback time at which the LMC first crossed the physical $z = 0$ virial radius of the MW, moving inward'. It is important to note here, however, that as the host halo mass evolves over time, R_{vir} of that halo will also evolve. This halo evolution is especially important for subhalos that survive to $z = 0$ but were accreted early, or > 4 Gyr ago (by the BK11 definition). The virial radius of a host halo will have changed by a factor of a few from the crossing redshift to present-day such that the radius would typically increase with time. For these types of systems, some subhalos would falsely be identified as massive satellite analogs because these subhalos might only reside in the extended outskirts of a halo for a majority of their lives. Such subhalos would never achieve orbital dynamics that mimic those of the LMC or M33, and would therefore contaminate the massive satellite analogs sample.

To account for this discrepancy and avoid false identification of analogs, we use a modified definition for the first crossing time throughout this work. This definition, t_{cross}, uses the lookback time at which the subhalo crosses the time-evolving quantity $R_{vir}(z)$, instead of R_{vir} at $z = 0$. Thus, the physically evolving virial radius (and consequently M_{vir}) is accounted for and the misidentification of subhalos with early crossing times is diminished. $R_{vir}(z)$ is reported in the Illustris halo catalogs for each halo at every snapshot, therefore no approximation is necessary to implement our modified definition. Note that crossing time here refers to the first simulation snapshot when the subhalo's position relative to its host is within $R_{vir}(z)$.

Figure 2.7 illustrates the distribution of BK t_{cross} compared to t_{cross} used throughout this analysis. Notice that only $\lesssim 5$ per cent of our analog sample has $t_{cross} > 8$ Gyr. This motivates dividing our sample by infall times in increments of 2, 4, and 6 Gyr, whereas BK11 defines the lower bound of the earliest accreted population at $t_{cross} > 8$ Gyr. The divisions are indicated by the coloured lines in Fig. 2.7. The terms crossing time, infall time, and accretion time will all be used interchangeably

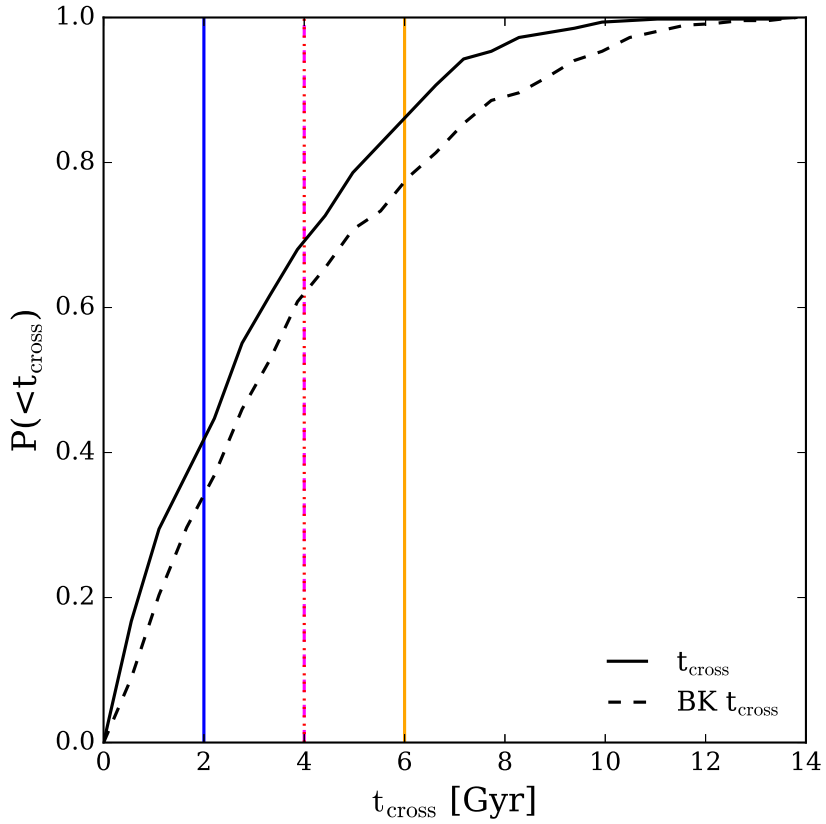

Figure 2.7: A cumulative distribution of the lookback time at which the satellites first crossed into their host halos. The solid black line illustrates results when the crossing time is defined using a time evolving virial radius. The dashed black line is the method used in BK11 where crossing time is defined as the lookback time at which a satellite first crosses the $z = 0$ physical radius of its host halo. t_{cross} yields a more recently accreted sample overall. 40 per cent of analogs have a crossing time < 2 Gyr ago, while about 70 per cent have a crossing time < 4 Gyr ago.

throughout this work, but all refer to the t_{cross} definition.

About 70 per cent of our massive satellite analogs have $t_{cross} \leq 4$ Gyr ago. This result is consistent with previous studies of the LMC (e.g. Busha et al., 2011, BK11). Here, we highlight that Fig. 2.7 similarly implies that cosmologically, M33 is also favored to be on its first approach towards M31.

While the choice of $R_{vir}(z)$ versus R_{vir} at $z = 0$ does affect the most likely infall time for the analog population, we recognize the choice of virial radius as the outer spatial boundary for a ΛCDM halo is arbitrary. There are other, more physically motivated criteria which could be used as a measure for infalling satellites instead. One example is the splashback radius (More et al., 2015), or the radius at which accreted mass reaches its first apocenter after the turnaround point in its orbit. Utilizing the splashback radius in the definition of crossing time as opposed to the virial radius would only shift the sample's average infall time to an earlier epoch. Since the splashback radius is considerably larger than the virial radius for a given halo at a specific redshift, the satellites would cross the splashback radius before crossing the virial radius. Therefore, the overall population would exhibit a tendency towards early infall times by definition, whereas our current method results in massive satellites crossing a smaller radius at more recent times.

Because the splashback radius is larger, it will lead to a higher percentage of early accretion scenarios. However, in this paper, we compare to recent orbital histories of massive satellite galaxies whose orbits are well constrained in the past 5 Gyr. We specifically focus on the interaction timescales that are relevant for the LMC–a few Gyr based on previous work–as this time-scale has shown that in its current orbital configuration, the LMC is dynamically affected by the MW and vice versa. Since the virial radius is the smaller of the two definitions for the host halos of interest in this work, its more restrictive nature within the Illustris-Dark parameter space is more suitable. A larger (i.e. splashback) radius would allow for too many orbital solutions that do not correspond to significant gravitational interactions between our host-satellite analogs and could therefore be physically misleading orbits in the context of our massive satellite analogs.

2.6.2 Specific Orbital Energy

Specific orbital energy encodes the relative position and velocity of the satellite as well its host halo mass, so it is a suitable property for determining the most favored crossing time and host halo mass of the LMC or M33. The specific orbital energy of the LMC and M33 today can be calculated from their mean position and velocity (as listed in Table 2.1) in a range of host halo masses. These quantities will be useful reference points to compare against the cosmological sample.

To calculate the orbital energy of massive satellites, we approximate the gravitational potential of the host halo in each host-satellite pair with an NFW profile. It is normalized by the energy of a circular orbit at $\mathrm{R_{vir}}$ of the host ($\tilde{E} = \mathrm{E_{sat}}/\mathrm{E_{circ}}(\mathrm{R_{vir}})$) to remove bias against the host halo mass.

$$\mathrm{E_{sat}} = \frac{1}{2}\mathrm{v}^2 + \Phi_{\mathrm{NFW}}(\mathrm{M_{vir}}, \mathrm{c_{vir}}, \mathrm{r}) \tag{2.11}$$

In Equation 2.11, the virial concentration, $\mathrm{c_{vir}}$, is approximated with the fitting formula of the Bolshoi simulation at $z = 0$ (Klypin et al., 2011):

$$c_{\mathrm{vir}}(M_{\mathrm{vir}}) = 9.60 \left(\frac{M_{\mathrm{vir}}}{10^{12} h^{-1} M_{\odot}} \right). \tag{2.12}$$

h will vary with the choice of cosmological parameters used in the simulation (i.e. *WMAP-9. Planck*, etc.) and $\mathrm{M_{vir}}$ varies for each host-satellite pair. Evidently, orbital energy is very sensitive to the combination of host halo mass, position, and velocity. The position and velocity ranges of the satellite analog sample are plotted in Fig. 2.8. The coloured markers with error bars indicate the observed properties of the LMC and M33 today. While the LMC is rare amongst the statistical sample, it is not surprising since it is approximately at pericenter today. Many more of the massive satellite analogs from Illustris-Dark populate the position-velocity space surrounding M33, which is reasonable since it might be somewhere between its apocenter and pericenter today.

Lowering the 10^{10} $\mathrm{M_{\odot}}$ mass floor at $z = 0$ to 3×10^9 $\mathrm{M_{\odot}}$ such that each satellite consists of $\geq$400 particles populates the phase space below 75 kpc more densely, as

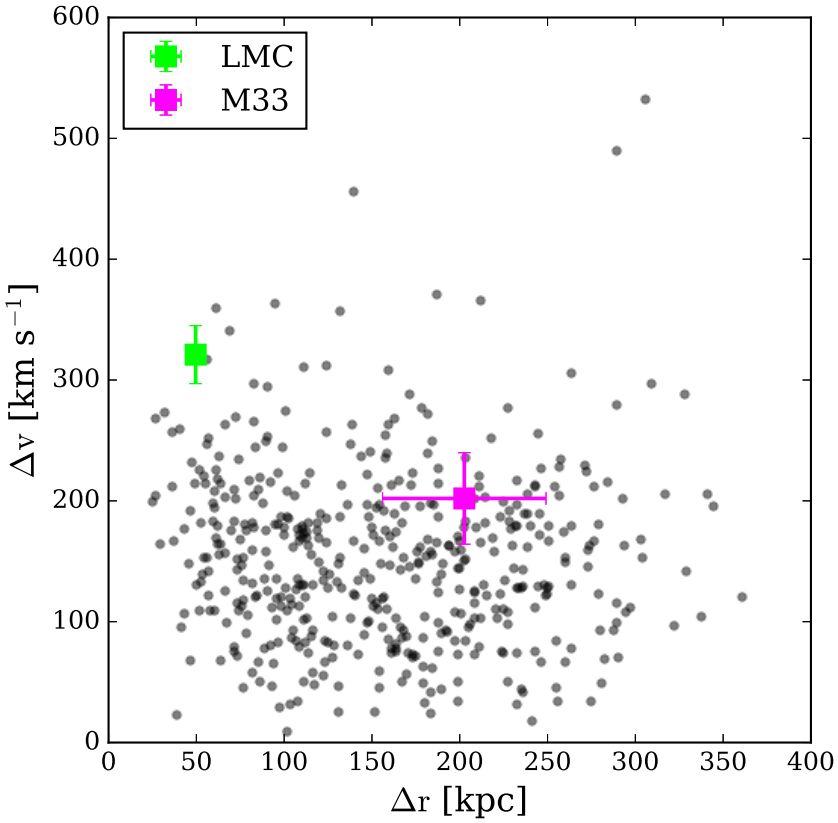

Figure 2.8: The relative positions and velocities for massive satellites in relation to their host halos. The observed properties of the LMC and M33 are shown in the coloured points with 1σ error bars in each direction. The LMC does have an error in its relative position with respect to the MW ($\sim$2 kpc) but it is significantly small compared to the other errors. The LMC's phase space properties are rare in the massive satellite population (as expected since it is approximately at pericentric approach), whereas M33 is common in this sample.

expected, since lower mass satellites are more likely to reside closer to their hosts. Halo-finding routines are often unable to identify subhalos when they come within close proximity of their host halos, so it is also possible that some massive satellite analogs which could be $\lesssim 50$ kpc from their host may be unaccounted for at $z = 0$. In these scenarios, `SUBFIND` would skip the snapshot at which a subhalo was unidentifiable and re-identify it at the next snapshot by matching particle membership. For our analysis, these effects are negligible since we aim to quantify the properties of massive satellites analogous to the LMC and M33 between their time of maximal mass and today, thus the 10^{10} $M_\odot$ mass floor is sufficient.

Figures 2.9 and 2.10 show the normalized, cumulative distribution of orbital energy for the massive satellite analogs, separated by crossing time. The hatched regions in Fig. 2.9 indicate the energetics of M33 in a variety of host halo masses. From left to right, the regions are the standard deviation about the mean energy for (0.7, 1.5, 3) $\times 10^{12}$ $M_\odot$ halos. The errors have been calculated using the 10,000 Monte Carlo samples from the allowed proper motion error space. The hatched regions in Fig. 2.10 represent the comparable quantities for the LMC. The solid cumulative distribution lines are identical in both figures.

Overall, the population of massive satellite analogs are bound to their host halos, i.e. $\tilde{E} > 0$. The early ($t_{cross} > 4$ Gyr) and late accreted ($t_{cross} < 4$ Gyr) populations exhibit distinctly different energetics. The early accreted subhalos are statistically more bound to their host halos as they have experienced more orbital decay, while the late-accreted subhalos are less bound. Only a small percentage of systems are energetically unbound, likely because these systems are in a short-lived configuration at $z = 0$ (i.e. a flyby satellite or a three-body encounter) or they have fallen into their host halos on highly eccentric orbits.

The mean values of orbital energy for M33 based on its position and velocity today residing within M31's halo with masses M_{vir} = (0.7, 1.5, 3) $\times 10^{12}$ $M_\odot$ are $\tilde{E} = (0.02, 0.88, 1.46)$. These are the mean energies in each of the hatched regions in Fig. 2.9. Comparing these values with the massive satellite analogs, only half of all analogs span the range of energies for M33 if M31's halo mass is 0.7-3$\times 10^{12}$ $M_\odot$

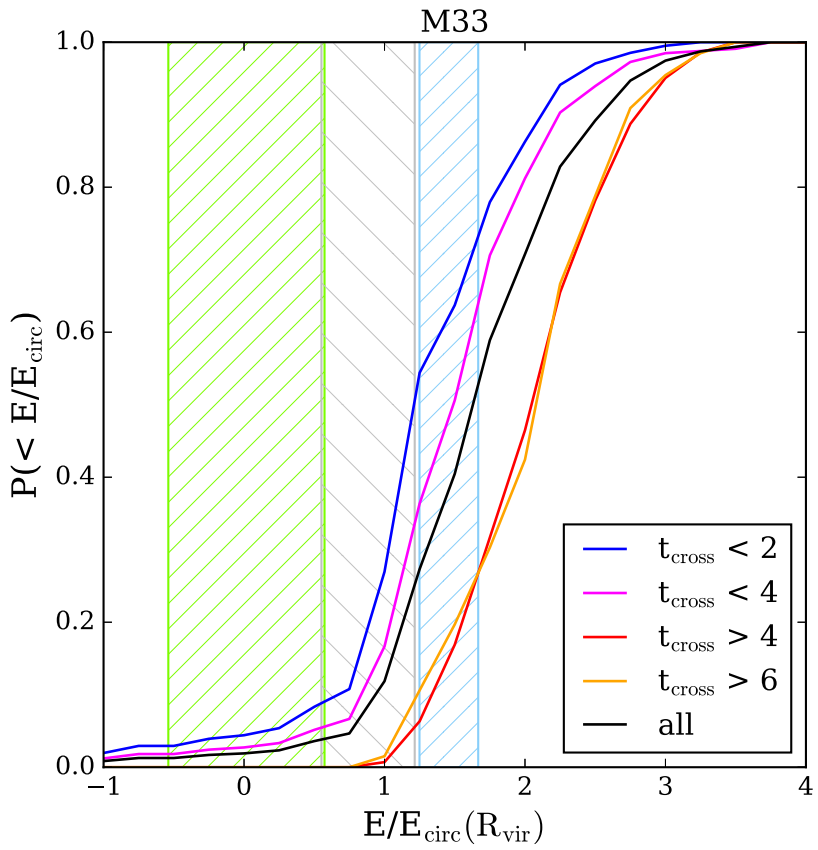

Figure 2.9: The cumulative distribution of orbital energy scaled to the energy of a circular orbit at the virial radius of each host for the massive satellite analogs. The satellite sample is split by t_{cross} (blue, magenta, red, orange solid lines). The black solid line represents the orbital energy for the entire analog sample. Overplotted in the green hatched region is the mean and 1σ errors of the M33 in a low mass host halo centerd at 0.7×10^{12} $M_{\odot}$. The gray hatched region indicates the energetics of M33 in an intermediate 1.5×10^{12} $M_{\odot}$ halo. The blue hatched region indicates the energetics in a high mass host halo of 3×10^{12} $M_{\odot}$. The width of the hatched regions is calculated using the Monte Carlo samples drawn to compute the mean position and velocity vectors of M33 relative to M31. M33's crossing time appears to be ≤ 4 Gyr ago, suggesting that it could not have arrived at its current position until recently.

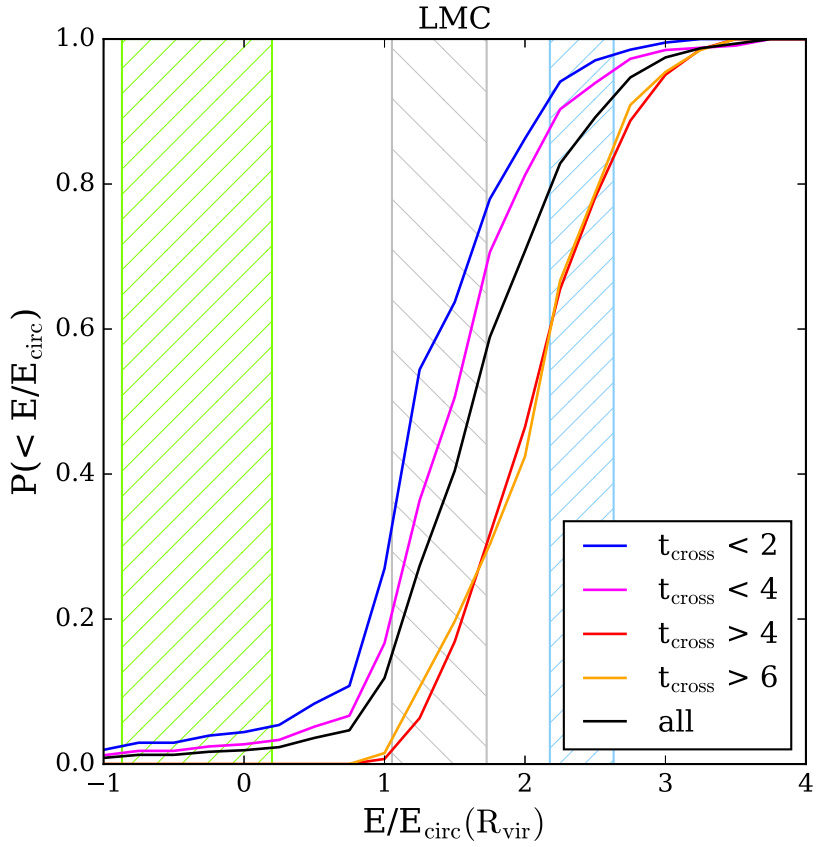

Figure 2.10: All solid lines are identical to those in Fig. 2.9. The hatched regions are the corresponding quantities for the MW-LMC systems and were calculated consistently. Comparing the simulation sample to the observed properties, the crossing time of the LMC is likely $\lesssim 4$ Gyr ago and a MW halo mass of $M_{vir} \sim 1.5 \times 10^{12}$ $M_\odot$ is statistically favored.

(black solid line). Those analogs which exhibit acceptable M33 energies today are dominantly satellites with crossing times $\leq$ 4 Gyr ago, suggesting that M33 could not have arrived at its current position until recently. These satellites prefer a high M31 halo mass $\geq 1.5 \times 10^{12}$ $M_{\odot}$. Early infall ($t_{cross} > 4$ Gyr ago) is allowed at the 20 per cent level, but if M31's halo mass is less than $\sim 3 \times 10^{12}$ $M_{\odot}$, first infall is certainly preferred.

These conclusions are somewhat at odds with the results of the numerical orbit analysis (Section 2.4) at the high mass end ($M_{vir,M31} = 2 \times 10^{12}$ $M_{\odot}$). The analytic models suggested a long period orbit for M33, whereas the cosmological analogs suggest a first infall scenario is more likely. This evidences that analytic models are not always suitable for inferring orbital histories over long ($\sim$ 6 Gyr) time-scales since they lack the appropriate physics to accurately capture the evolution of both massive satellites and their hosts (see also Lux et al., 2010).

For LMC-type satellites residing in a MW halo with masses M_{vir} = (0.7, 1.5, 3) $\times 10^{12}$ $M_{\odot}$, the mean values for orbital energy are $\tilde{E} = (-0.34, 1.39, 2.40)$. These are the mean energy values for the hatched regions in Fig. 2.10. Comparing to the sample of massive satellite analogs indicates the LMC's orbital energy is rather common. The black solid line representing the entire sample generally spans the full range of allowable LMC orbital energies as indicated by the hatched regions.

If the LMC is cosmologically typical based on its orbital energy, only about 15 per cent of the massive satellite analogs exhibit preference towards a MW halo mass $\lesssim 1.5 \times 10^{12}$ $M_{\odot}$. Similarly, about 85 per cent favor a MW halo mass $\gtrsim 1.5 \times 10^{12}$. Thus, independent of crossing time, a MW halo mass of $\sim 1.5 \times 10^{12}$ $M_{\odot}$ is most favored.

In this halo mass range, indicated by the gray hatched region, a first infall is preferred, which again differs from the orbital integration results in Section 2.4. The numerical orbit shows evidence for a pericentric passage around 5 Gyr ago. Early infall in this halo mass range is allowed at the 25 per cent level, which again likely indicates that backward integration schemes are not accurate tracers of cosmological orbits over such time-scales, especially for long period orbits.

Therefore, the distribution of orbital energy for the massive satellite analogs confirms M33 likely has an infall time within the last 4 Gyr and it prefers an M31 halo mass $\geq 1.5 \times 10^{12}$ $M_{\odot}$. It also suggests that the preferred MW halo mass is $\sim 1.5 \times 10^{12}$ $M_{\odot}$ based on the LMC's current position and velocity. If the LMC really is on its first infall with $t_{cross} \leq 4$ Gyr ago, the likelihood of this MW halo mass increases.

BK11 used the old proper motion values of the LMC (Kallivayalil et al., 2006a) and the Millenium-II simulations to conclude the most typical MW halo mass is $> 2 \times 10^{12}$ $M_{\odot}$ from orbital energy studies. However, the mean total velocity of the LMC has decreased by a significant 57 km s^{-1} . This illustrates that precise proper motion measurements are required to reliably compare the properties of Local Group satellites to statistics of cosmological analogs.

Examination of the specific orbital angular momentum of the massive satellite analogs sample results in the same conclusions as orbital energy. The angular momentum of the LMC and M33 today are common amongst the general sample of massive satellite analogs. Again, the cosmological sample prefers a recent infall time, within the last 4 Gyr, for M33 and the LMC based on their present-day angular momentum. In Paper II, we estimate the most typical halo mass for the MW and M31 in a Bayesian scheme based on the LMC and M33's angular momentum today.

2.6.3 Eccentricity

Orbital eccentricity is the final property we use to quantify the orbits of massive satellite analogs in Illustris-Dark. As discussed in Hashimoto et al. (2003), the orbits of satellite galaxies tend to circularize over time, or become less eccentric (e.g. Murai and Fujimoto, 1980; Ibata and Lewis, 1998). This circularization is closely tied to the pericentric approach and mass of the satellite galaxy. Since dynamical friction is directly proportional to M_{sat}^2 (see Equation 2.5), it is a determining factor in the orbital evolution of satellite galaxies, especially for massive satellites. The amount of circularization determines the ability of satellites to survive before merging with their hosts. As such, circularization of the LMC or M33 orbits may shed light on

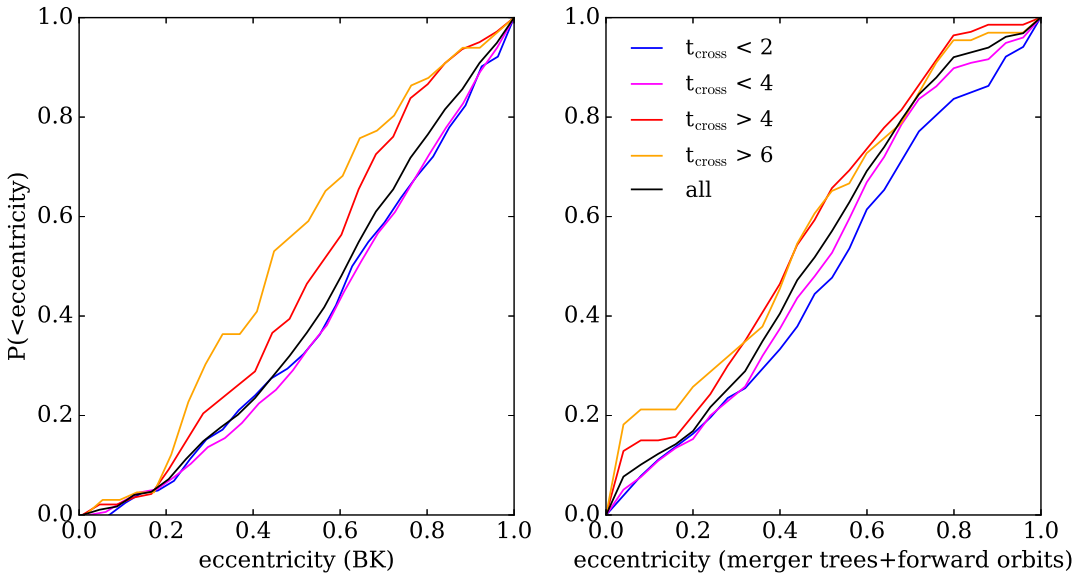

Figure 2.11: *Left:* The distribution of instantaneous orbital eccentricity at $z = 0$ for the massive satellite population in Illustris-Dark. Eccentricity is calculated using the position, velocity, and host halo mass at $z = 0$ by approximating the host halo as a spherical NFW halo potential and the subhalo as a point mass. *Right:* The distribution of orbital eccentricity from the combination of merger tree data and forward orbit integrations for the massive satellite analogs. See Appendix A.

their expected infall times.

We introduce two different methods for computing the eccentricity of the massive satellite analog orbits. The first is an instantaneous eccentricity method computed with the kinematics of massive satellite analogs at $z = 0$. The second uses the extracted orbital histories of the analogs to compute an eccentricity with real orbital data. In both methods, the following definition of eccentricity stemming from a combination of orbital apocenter (r_a) and pericenter (r_p) is implemented.

$$e \equiv \frac{r_a - r_p}{r_a + r_p} \tag{2.13}$$

Instantaneous Eccentricity from the Equation of Motion

The first eccentricity method is an instantaneous approximation given the $z = 0$ properties of each massive satellite analog, identical to BK11. In this approximation, apocenter and pericenter are defined as the roots of the following equation of motion from Binney and Tremaine (2008), Chapter 3.

$$u^2 + \frac{2[\Phi(1/u) - E]}{L^2} = 0 \tag{2.14}$$

Φ is the gravitational potential of the fixed massive object and E is the Hamiltonian for the system. $u = 1/r$, where r is the distance of the satellite from its host. L is the magnitude of the angular momentum vector per unit mass for the orbiting body.

This method is similar to the reduced mass approach of Wetzel (2011), except we approximate the host as an extended potential. We assume the satellites are orbiting within a spherical dark matter halo that is well approximated by an NFW profile and calculate the apocenter and pericenter instantaneously with their $z = 0$ properties. Unlike our numerical orbital models, the satellites are modeled as point masses. All unbound orbits (E < 0) are assigned a default eccentricity of 1, so $e = 0$ describes a perfectly circular orbit.

Table 2.6 lists the eccentricity values for the LMC and M33 using their current positions and velocities from Table 2.1 in host halos with M_{vir} = (0.7, 1, 1.5, 3)

Table 2.6: The instantaneous eccentricity for the observed position and velocity of the LMC and M33 in host halos of varying virial mass. The eccentricity is computed using Equations 2.13 and 2.14. The LMC is on an unbound orbit in a host halo with $M_{vir} = 0.7 \times 10^{12}$ $M_{\odot}$, corresponding to an eccentricity > 1 (i.e. parabolic or hyperbolic orbit).

Host halo mass [$M_{\odot}$]	0.7×10^{12}	1×10^{12}	1.5×10^{12}	3×10^{12}
LMC	unbound	0.904	0.714	0.431
M33	0.952	0.808	0.694	0.623

$\times 10^{12}$ $M_{\odot}$. The left panel of Fig. 2.11 shows the cumulative probability distribution of orbital eccentricity for the massive satellite analogs split by crossing time. The black solid line indicates the distribution of orbital eccentricity for the entire analog sample. The mean value is $\sim$0.6, or fairly eccentric. Early accreted satellites ($t_{cross} > 4$ Gyr) tend to be on more circularized orbits, which suggests they have experienced the most mass loss and have become circularized by dynamical friction in the presence of their host halos for many billions of years.

BK11 implemented this eccentricity method and found a similar distribution of eccentricity for the population of LMC analogs in their study. Using the old LMC proper motion values, they conclude the LMC is on an unbound orbit in a 10^{12} $M_{\odot}$ MW halo when it is represented as an NFW halo that extends to infinity. However, the significant change in the updated proper motion values of the LMC allows us to re-evaluate this claim. With the new proper motion values, the LMC is indeed bound in a 10^{12} $M_{\odot}$ NFW halo with $e = 0.904$. Therefore, it is possible for the MW's halo mass to be as low as 1×10^{12} $M_{\odot}$ with the LMC's current orbital conditions even though it would be an outlier since only $\sim$10 per cent of our overall sample has $e \geq 0.9$, independent of infall time.

Eccentricity from Merger Trees and Forward Orbits

While the previous method utilizes the $z = 0$ properties to compute instantaneous eccentricities, the Illustris-Dark cosmological simulation and associated merger trees (Rodriguez-Gomez et al., 2015) allow us to trace the orbital histories of each mas-

sive satellite analog throughout cosmic time and directly identify their most recent apocenter and pericenter distance to their host, if they exist. Apocenter and pericenter are defined here as true critical points in the satellite's distance relative to its host as a function of time. If a satellite has both an apocenter and pericenter as defined here, the eccentricity is calculated by Equation 2.13. Only 46 per cent of the massive satellite analogs sample contains an apocenter and pericenter in their past orbital trajectories since a majority of the sample is on first infall. The average value of eccentricity for that subset of analogs is about 0.4. There is no clear correlation between merger tree eccentricity and infall time for this sample.

For those satellites where only a pericenter or neither critical points are recovered in the past orbital trajectories (i.e very recent t_{cross} scenarios), the orbits are numerically integrated forward in time for 6 Gyr using the $z = 0$ position and velocity vectors relative to their host halos, following the methodology of Section 2.3. The trajectories are then analysed to find the first pericenter and/or apocenter. In the case where the merger tree data contains a pericenter and no apocenter, only the apocenter is taken from the forward orbit. More details of this forward orbit integration are discussed in Appendix A.

Using both the merger tree data and the forward orbit integrations, eccentricities for 96 per cent of the massive satellite analogs sample are recovered. The right panel of Fig. 2.11 shows the cumulative distribution of eccentricity separated by crossing time for this method. The remaining 4 per cent of analogs are likely fly-by satellites, so they are omitted in Fig. 2.11. Note that for the recently accreted satellites, it is not necessarily true that the pericenter and apocenter have occurred in the time between infall and today, but rather between infall and 6 Gyr in the future. The average eccentricity for the sample increases to about 0.45.

Similar to the instantaneous eccentricity method, the real eccentricities extracted from orbital trajectories indicate some correlation with infall time. The early accreted massive satellite analogs ($t_{cross} > 4$ Gyr) are on more circular orbits than those accreted more recently. However, the correlation between eccentricity and infall time is much weaker and therefore cannot be used to discriminate between

satellites with early versus recent infall times.

We attribute this weak correlation to the rapid circularization of massive satellite analogs after infall owing to their high masses. As a result, their eccentricities are inherently more circular overall. The early accreted satellites enter their host halos at larger separations ($>$ 150 kpc) and with higher relative velocities ($>$ 200 km s^{-1}) as compared to the recently accreted analogs. Consequently they are able to survive until $z = 0$ because dynamical friction is less efficient at decaying their orbits quickly.

Figure 2.12 illustrates that recently accreted ($t_{cross} < 4$ Gyr ago) massive satellites do not lose a significant fraction of their infall masses. Plotted is the ratio between total dark matter mass when the satellite first crosses the virial radius of its host relative to its bound mass at $z = 0$, split by early and late crossing times. The most recently accreted satellites (blue) manage to sustain their masses since infall, while the early accreted satellites (red) experience more mass loss, decreasing in mass by a factor of 10 at most. Neither infall time nor mass loss correlate strongly with eccentricity, so massive satellite galaxies should be treated with care (i.e. treated as extended bodies with significant mass) when quantifying their survivability time-scales.

2.7 Discussion

We have numerically constrained the orbital histories of the LMC about the MW and M33 about M31 using the allowed proper motion error space of each system and a wide range of mass models. We found that both satellites favor a recent infall scenario unless the total mass of the MW or M31 is in excess of 1.5×10^{12} $M_{\odot}$ or 2×10^{12} $M_{\odot}$, respectively, in which case the orbital periods of these satellites are of order 5-6 Gyr.

We have also characterized the preferred infall times for a population of massive satellite analogs in the Illustris-Dark simulation and found that massive satellites exhibiting orbital properties similar to the LMC and M33 also prefer a recent infall

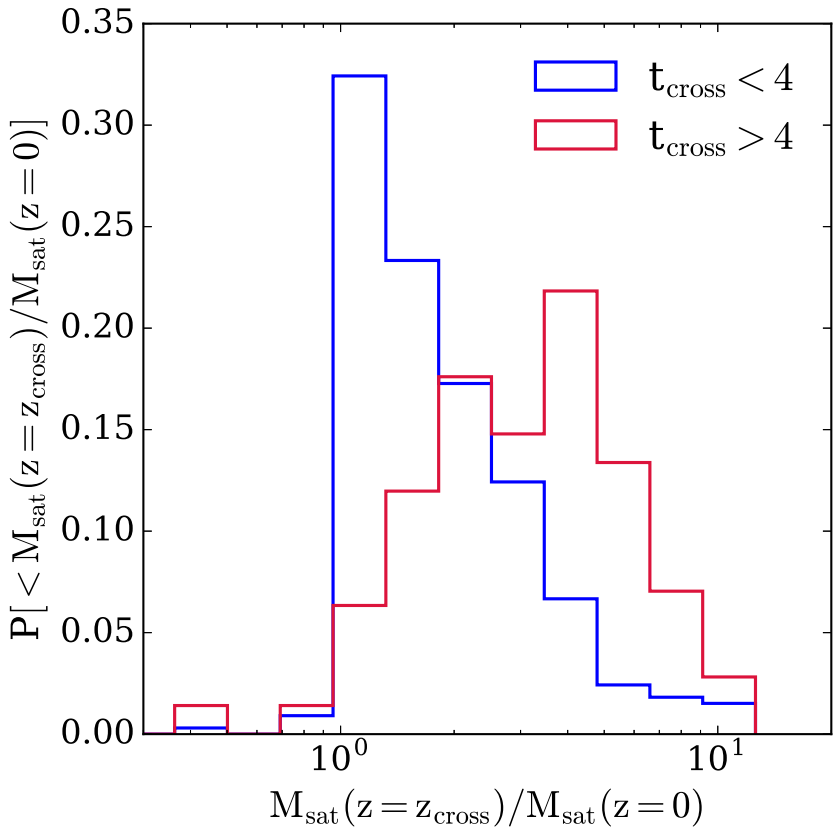

Figure 2.12: The distribution of the ratio of mass at crossing and at $z = 0$ for Illustris-Dark massive satellite analogs with recent crossing times (blue, $t_{cross} < 4$ Gyr ago) and early crossing times (red, $t_{cross} > 4$ Gyr ago). The distributions are normalized individually such that the y-axis shows the probability of a given mass ratio.

scenario. While the numerical models and the simulation results are consistent with one another with respect to infall time, Illustris-Dark favors recent infall unless the host halo masses are even more massive than those used in the numerical orbit integrations: MW $\gtrsim 2 \times 10^{12}$ $M_\odot$, M31 $\gtrsim 3 \times 10^{12}$ $M_\odot$.

While our cosmological studies revealed tension with orbital histories over long time-scales, the analysis appears robust over time-scales < 5 Gyr. In Section 2.4, we illustrated that orbits allowed by M33's velocity error space do not exhibit a recent, close passage about M31, in tension with conventional models based on the morphology of M33. A recent, close passage scenario is also relevant for the LMC, since it is just past its pericenter about the MW. In the following we examine this controversial result in detail.

2.7.1 Did M33 Have a Close Encounter with M31?

The scenarios put forth by M09 and P09 to recover the warped structure of the HI gas disc and the stellar disc of M33 require the satellite to have made a pericentric passage within 50-100 kpc of M31 in the last 3 Gyr. The minimum eccentricities from P09 and M09 described in Section 2.2.1 are about 0.34 and 0.67, respectively. The former is computed using the current position of M33 as the apogalacticon, therefore it yields only a minimum value for eccentricity.

From Fig. 2.11, about 70 per cent of the massive satellite analogs sample has an eccentricity $\gtrsim 0.34$, while approximately 20 per cent has an eccentricity $\gtrsim 0.67$. To first order, it is not rare to find orbits of massive satellite analogs in Illustris-Dark that resemble those theorized by M09 and P09. In the following, we examine the question of M33's pericentric approach to M31 first by exploring the allowed proper motion error space and then by using cosmological simulations.

Table 2.7: The fraction of M33 orbits for three different M31-M33 mass combinations which satisfy specific orbital criteria determined by numerical integration. In all models, 10,000 orbits are calculated in the M31-M33 error space and the mass of M31 is fixed at 2×10^{12} $M_{\odot}$. The final three columns indicate the three M33 masses tested.

Identifier	N_{peri}	t_{peri}	t_{inf}	r_{peri}	5×10^{10} $M_{\odot}$	1×10^{11} $M_{\odot}$	2.5×10^{11} $M_{\odot}$
ARP	≥ 1	≤ 6 Gyr ago	–	–	35.90%	38.43%	34.44%
TI6	≥ 1	≤ 6 Gyr ago	≤ 6 Gyr ago	–	18.16%	19.25%	21.03%
RP100	≥ 1	≤ 6 Gyr ago	≤ 6 Gyr ago	$r_{peri} < 100$ kpc	6.25%	6.32%	3.59%
RP100T	≥ 1	≤ 3 Gyr ago	≤ 6 Gyr ago	$r_{peri} < 100$ kpc	0.27%	0.04%	0.14%
RP55	≥ 1	≤ 6 Gyr ago	≤ 6 Gyr ago	$r_{peri} < 55$ kpc	1.00%	1.06%	0.84%
RP55T	≥ 1	≤ 3 Gyr ago	≤ 6 Gyr ago	$r_{peri} < 55$ kpc	0%	0%	0%

Two data samples are defined to carry out this analysis. The first is the analytic recent pericenter (ARP) sample, which describes the orbital histories recovered by searching 10,000 Monte Carlo drawings from the 4σ proper motion error space as described in Section 2.2.2. Second, we define the Illustris-Dark recent pericenter (IRP) sample. This set includes all massive satellite analogs identified in Section 2.5 containing a recent pericentric passage in their orbital history.

The Analytic Recent Pericenter Sample

M33 and M31 have been modeled as a system where M33 has a recent, close (50-100 kpc) encounter with M31 (P09, M09). This close encounter may be strong enough to induce the formation of warps in the gas and stellar discs of M33. Given its gas content and cosmological expectations, it is most likely to have been accreted within the past 4 Gyr or so. Here, we seek to reconcile these two requirements given the observationally constrained parameter space.

We follow the methodology outlined in Section 2.3, assuming M33's mass is fixed at 2.5×10^{11} $M_{\odot}$ and M31's virial mass is 2×10^{12} $M_{\odot}$. A lower M31 mass would only weaken the statistics for a recent, close passage scenario since it would be less effective at decaying the orbit of M33 via dynamical friction. We use the highest M33 mass from Fig. 2.2 because its orbital trajectory exhibits the lowest eccentricity. Lower M33 mass models are tested later in this section.

10,000 backwards orbits are computed for 6 Gyr, spanning the M31-M33 velocity error space. We first identify the orbits that allow M33 to have made a pericentric passage about M31 in the last 6 Gyr, regardless of infall time. Pericenter is defined such that it is a true critical point in the orbital trajectory and the relative position of M33 at pericenter has a magnitude less than its separation today. This sample will be referred to as the analytic recent pericenter sample (ARP). 34.44 per cent of the allowed orbits belong to the ARP sample. The average orbital properties of the ARP sample are: $t_{inf} = 5.5 \pm 0.9$ Gyr ago, $r_{peri} = 130.7 \pm 45.6$ kpc, and $t_{peri} = 4.5 \pm 1.1$ Gyr ago.

Fig. 2.13 shows the distribution of M33's velocity vector components with respect

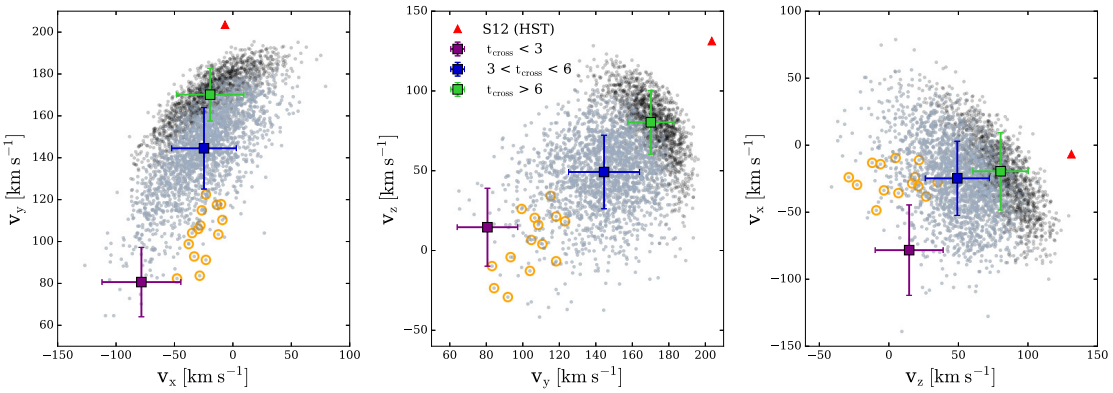

Figure 2.13: For the ARP sample, the x, y, and z velocity components are plotted for M33's current velocity vector with respect to M31 in the highest M31 and M33 mass model (black points). Lower host mass models would only weaken the statistics. Overplotted in blue-gray points are those vectors within the ARP sample where the orbits evidence an infall time ≤ 6 Gyr ago (TI6 sample). The orange circles highlight only those vectors that belong to the RP100T subset. This subset represents the orbits that are most reflective of the criteria outlined in P09 and M09, which are designed to reproduce the warps in M33's gaseous and stellar discs. See Table 2.7 for more details. The square markers with error bars indicate the average velocity components for all samples, binned by satellite infall time. The error bars are the standard deviation within each infall time bin for each velocity component. The red triangles denote the velocity components from the HST only proper motion of M31 (S12). The S16 velocity vector is $\mathbf{v}$=(135.30, 0.33, 117.60) km s^{-1}, but these velocity components do not lie in the same direction as the locus of RP100T orange circles.

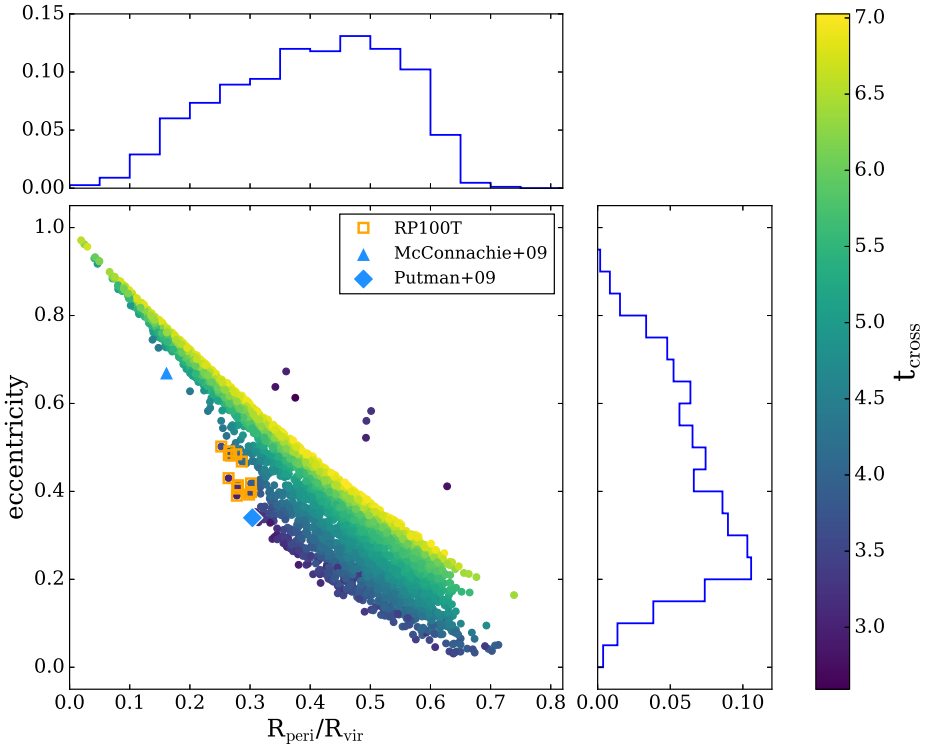

Figure 2.14: The distribution of eccentricities and pericenters for the same ARP sample plotted in Fig. 2.13. The x-axis gives the pericentric distance with respect to the virial radius of M31. M31 is 2×10^{12} $M_{\odot}$ and its R_{vir} = 329 kpc for this model. The points are coloured by their crossing time, the time at which the satellite infalls into the host's virial radius. The orange squares highlight those which have a crossing time in the last 6 Gyr and a pericentric approach within 100 kpc of M31 in the last 3 Gyr (RP100T, 0.14 per cent). No orbits reach within 55 kpc during the last 3 Gyr as suggested by M09 (RP55T). The blue triangle shows the eccentricity and pericenter distance they conclude would result in M33's stellar warp. The blue diamond represents the eccentricity and most probable pericenter put forth by P09. The five outliers above the swath of points are position and velocity vectors that result in a positive radial velocity, suggesting M33 is moving away from M31 instead of towards it. These vectors are likely artefacts of the edges of the allowed proper motion error space.

to M31 for the ARP sample (all points). Overplotted in blue-gray points are the components of M33's velocity vectors whose orbits also indicate an infall time during the last 6 Gyr. The coloured squares with error bars denote the average velocity components for the orbits within the given infall time range.

The orange circles in Fig. 2.13 indicate the velocity components of the allowed proper motions where the orbits have recent infall times ($t_{cross} \leq 6$ Gyr) and reach a pericentric distance within 100 kpc of M31 in the last 3 Gyr. *Only 0.14 per cent of the full orbital sample exhibit these criteria* (denoted by RP100T in Table 2.7). These criteria most closely resemble those estimated by P09 to reproduce M33's gaseous warps. The velocity components of the RP100T sample are clearly outliers in the y and z directions. The mean v_Y and v_Z components of this sample both lie about 2.5σ from M33's mean velocity components listed in Table 2.1.

Further restricting the allowed orbits such that the pericentric distance must be within 55 kpc of M31 in the last 6 Gyr whittles the fraction down to about 1 per cent (RP55), but there are no orbits that recover $r_{peri} < 55$ kpc in the last 3 Gyr (RP55T). Therefore, M09's proposed M33 orbit cannot be recovered within the proper motion error space of M31-M33. The final column of Table 2.7 indicates the percentage of orbits that achieve each of the aforementioned criteria for this M31-M33 mass combination.

To ensure that these statistics for the highest M33 and M31 masses are not sensitive to our dynamical friction prescription, we recomputed all allowed orbits without any dynamical friction term. This model would be most likely to reproduce the M09 and P09 orbits. We find that the RP100T sample increases to 7.57 per cent and the RP55T sample contains 2.09 per cent of all allowed orbits as opposed to zero. Regardless, these results do not change our conclusion that a close passage between M33 and M31 is unlikely within the error space.

We also test two other M33 mass models to constrain whether a lower mass satellite is more statistically effective at recovering a recent, close encounter with M31 in the allowed error space. However, the statistics only improve minimally. Table 2.7 provides a summary of the same constraints placed on these orbital sam-

ples. We have also considered the gravitational influence of the MW on M33, but our computations show that the MW never reached $\leq$ 770 kpc relative to M33 in the last 6 Gyr for all three M31-M33 mass combinations.

Fig. 2.14 further demonstrates the properties of the ARP sample. The distribution of pericenter to virial radius and eccentricity are shown relative to their crossing times, assuming a host mass of 2×10^{12} $M_{\odot}$ and a virial radius of 329 kpc. The orange squares highlight the RP100T orbits, corresponding to the orange circles in Fig. 2.13. They most closely resemble the orbit suggested by P09, denoted by the light blue diamond. No orbits in the M31-M33 proper motion error space resemble the orbit in M09's work. This is likely because the orbits which do recover recent pericenters generally have a r_{peri} that is too high ($\gtrsim$ 100 kpc), and therefore they are inconsistent with a recent, *close* interaction with M31.

In Section 2.2.2, we note that several recent works have quoted larger M33 distances than that of M09. U et al. (2009) and Bonanos et al. (2006) both quote values of approximately 960 kpc between M33 and the MW, as opposed to ∼800 kpc which has typically been used in previous works and which we use in this analysis. Our set of 10,000 Monte Carlo drawings considers M33 distances in the range ∼715-880 kpc. If M33's true distance is 880 kpc, we find that the resulting orbit only ratifies our results from the ARP sample–a recent, close pericentric passage of M33 about M31 is rare. A larger M33 distance further indicates that a first infall scenario is more favorable. Even larger distances to M33 ($>$ 880 kpc) are expected to continue this orbital trend.

From the ARP sample, we conclude it is not rare to find M33 in a recent infall scenario within the observationally constrained phase space of the M31-M33 system. A recent ($\sim$ 4-6 Gyr ago) pericentric passage of M33 about M31 is also allowed. Both scenarios are plausible at the 20-30 per cent level (see Table 2.7). However, it is very rare to find close pericentric passages, within 50-100 kpc from M31. M09 and P09 require M33 to achieve a separation of 53 kpc and 100 kpc, respectively. At most, we find only $\leq$ 0.27 per cent of orbits reach within 100 kpc of M31 in the last 3 Gyr and no orbits get as close as 55 kpc to M31 during that time. Therefore, the

long period orbit mentioned in Section 2.4 is still preferred by the proper motions of M31 and M33 when M31 is massive (2×10^{12} $M_\odot$). At higher M31 halo masses, the statistics improve somewhat as M33's orbit will turn over at more recent times, but at a virial mass of 3×10^{12} $M_\odot$, the total mass of the Local Group would also have to increase.

While the desired trajectory is infrequent in our numerically integrated orbits, we use the Illustris-Dark massive satellite sample to infer its likelihood in a cosmological setting.

The Illustris Recent Pericenter Sample

We have shown that the allowed proper motion error space of M31-M33 does not favor a recent, close pericentric passage of M33 about M31. Here, we will examine the orbital trajectories of the massive satellite analogs from Section 2.5.3 to quantify the frequency of this scenario in a cosmological setting.

In Section 2.6.3, we used the Illustris-Dark merger trees to extract the orbital histories of all massive satellite analogs. Given that a majority of the analogs were accreted recently, 71.8 per cent of orbits contain a pericentric passage but only 46 per cent of all orbits contain both an apocenter and pericenter. The average orbital properties for all that contain at least a pericentric passage are: $t_{inf} = 3.9 \pm 2.1$ Gyr ago, $r_{peri} = 89.8 \pm 60.2$ kpc, $t_{peri} = 1.6 \pm 1.2$ Gyr ago.

The average infall time for all analogs without a pericenter in their merger tree data is $t_{inf} = 0.6 \pm 1.2$ Gyr ago. Unsurprisingly, these massive satellite analogs were accreted recently. For these analogs, we integrate their orbits forward in time from $z = 0$ for only 3 Gyr (instead of 6 Gyr as in Section 2.6.3) since we are looking for recent accretion scenarios. Typically, the time between infall and 3 Gyr in the future totals to $\sim$4-6 Gyr, approximately equivalent to an average orbital period. The average orbital properties for all forward integrations that contain a pericentric passage in the future are: $r_{peri} = 53.3 \pm 61.0$ kpc and $t_{peri} = 1.4 \pm 0.8$ Gyr beyond today.

The combined merger tree data and forward orbits increase the fraction of mas-

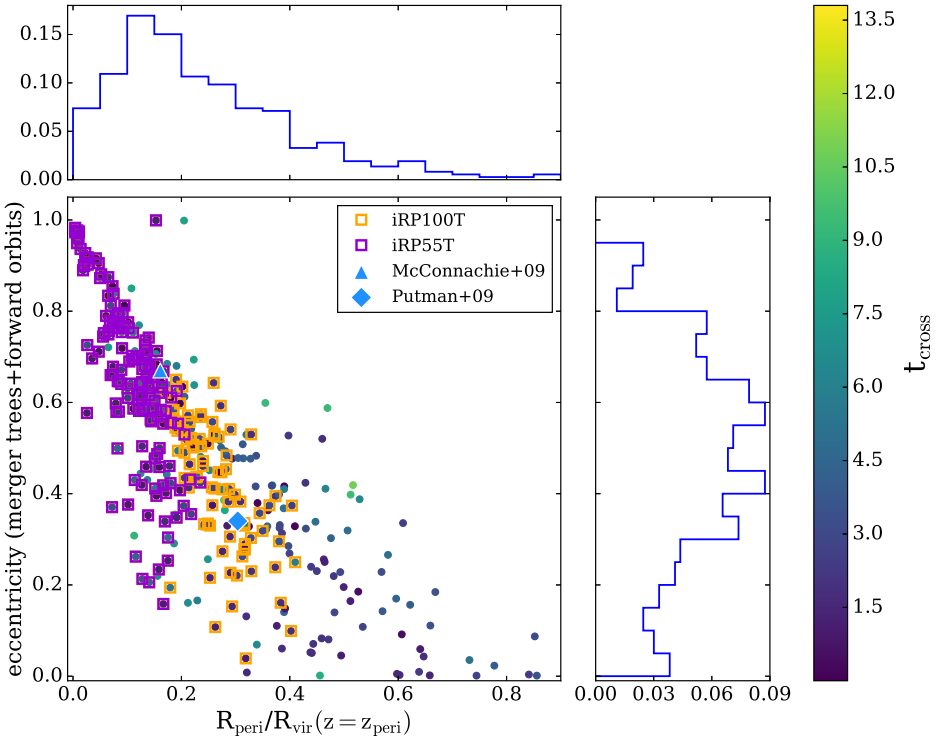

Figure 2.15: Like Fig. 2.14, the distribution of pericenter and eccentricity is shown for the sample of massive satellite analogs in Illustris-Dark belonging to the IRP sample. The orbital data are taken from the merger trees directly or they are combined with a forward orbit integration using the $z = 0$ host-satellite properties. The points are coloured by their crossing times. The x-axis indicates pericenter relative to the virial radius at the time of pericenter. For those where the pericenter was found in the forward orbit, the $z = 0$ R_{vir} was used. The orange squares highlight those massive satellite analogs where the pericenter reaches < 100 kpc of the host halo (49.36 per cent) within 3 Gyr of today (iRP100T). The purple squares are those where the pericenter is within 55 kpc of the host halo (32.42 per cent) in ± 3 Gyr of $z = 0$ (iRP55T). The blue triangle references the M09 orbit and the blue diamond shows the P09 results.

sive satellite analogs with both an apocenter and pericenter to 87.92 per cent. For every analog that shows evidence for a true pericentric passage in the past trajectory, we use this value and corresponding time. The remaining 12.08 per cent of satellites are either on long-period orbits or they are short-lived fly by encounters at $z = 0$.

Using this combined set of orbital histories, we define the Illustris-Dark recent pericenter (IRP) sample as the subset of 472 massive satellite analogs which have made one pericentric passage between their time of infall and $z = 0$ in the merger tree data or infall and 3 Gyr in the future determined by forward orbits. The IRP sample encompasses 77.54 per cent of the massive satellite analogs population. The pericenters have been confirmed as true minima and occur at a separation less than their $z = 0$ positions to be consistent with the ARP sample. The average infall time of the IRP sample is $t_{inf} = 3.0 \pm 2.5$ Gyr ago.

Fig. 2.15 shows the distribution of eccentricities and pericenter as a fraction of the host halo virial radius for the IRP sample. The points are once again coloured by crossing time. The virial radius of the host halo at the time of pericenter is adopted for all massive satellite analogs with a pericenter in their merger tree data. For all pericenters taken from the forward orbit integrations, the virial radius of the host halo at $z = 0$ is used as an approximation.

The orange squares highlight the fraction of the IRP sample where the satellites have an infall time ≤ 6 Gyr and a pericentric passage within 100 kpc of their host halo in the last 3 Gyr, or the iRP100T sample. This sample represents 49.36 per cent of the total population of massive satellite analogs. Further restricting the IRP sample to those where the pericentric distance is < 55 kpc from the host halo in the last 3 Gyr, we find 32.42 per cent of analogs satisfy these criteria (denoted by iRP55T). The iRP55T sample is overplotted in purple squares. Table 2.8 summarizes the fraction of all orbits that satisfy each criteria.

The IRP sample demonstrates that cosmologically, the orbits required by both P09 and M09 to reproduce M33's warped structures are not rare. A recent pericentric passage reaching within 100 kpc of the host is true for about half of all massive

Table 2.8: The fraction of 472 massive satellite analogs in Illustris-Dark satisfying the following orbital criteria from the combination of their merger tree data and forward orbits. For the analogs whose orbits have been integrated forward in time, we search for those where the pericenter occurs between the satellite's time of infall (so long as it is < 6 Gyr ago) and 3 Gyr in the future. For the iRP100T and iRP55T samples, the time of pericenter must occur within ± 3 Gyr of $z = 0$.

Identifier	N_{peri}	t_{peri}*	t_{inf}	r_{peri}	
IRP	≥ 1	≤ 6 Gyr ago	–	–	77.54%
iTI6	≥ 1	≤ 6 Gyr ago	≤ 6 Gyr ago	–	67.58%
iRP100	≥ 1	≤ 6 Gyr ago	≤ 6 Gyr ago	$r_{peri} < 100$ kpc	51.90%
iRP100T	≥ 1	≤ 3 Gyr ago	≤ 6 Gyr ago	$r_{peri} < 100$ kpc	49.36%
iRP55	≥ 1	≤ 6 Gyr ago	≤ 6 Gyr ago	$r_{peri} < 55$ kpc	32.42%
iRP55T	≥ 1	≤ 3 Gyr ago	≤ 6 Gyr ago	$r_{peri} < 55$ kpc	32.42%

satellite analogs but only about one-third of analogs reach a distance < 55 kpc from their hosts in that time. The existence of a reasonable cosmological population of subhalo orbits satisfying this strict orbital criteria supports the possibility that, in general, massive satellite galaxies can be responsible for warps in the baryonic discs of their hosts. However, larger pericentric approaches are more common.

The results of the IRP sample are also generally applicable to the B07 orbital model for the LMC–its close approach of 50 kpc is not typical, but also not cosmologically rare.

Upon further inspecting the orbits identified as the iRP100T orbits, we find that it is uncommon for those massive satellite analogs to have a virial host halo mass $\geq 1.5 \times 10^{12}$ $M_\odot$. Only 15.46 per cent of all analogs belong to the iRP100T sample and have a host halo that massive, while only 1.5 per cent of all analogs belong to the iRP100T sample and have a host halo mass $\geq 2.5 \times 10^{12}$ $M_\odot$. This may provide an upper limit on the halo mass of the MW and also for M31 if M33 truly had a recent, close encounter.

Ramifications for the Lack of a Close Encounter

From our discussion of the morphologically motivated orbit for M33, we conclude that a recent, close encounter between M33 and M31 is rare within our analytic

models and only as likely as a large pericentric approach cosmologically. In this case we must search for alternative scenarios to explain the origin of M33's warped morphology.

For instance, M33 could host its own system of less massive satellites as predicted by galaxy formation models. Recent work has suggested the same could be true for the LMC (see Section 2.1). If these satellites of satellites exist and have had close interactions with M33, one or more could have contributed to some degree of the warped structures observed in its disc. Of the known satellites within the M31 system, And XXII has been suggested as a potential companion of M33 since it has a similar systemic velocity. While it may or may not be bound to M33 at present, several authors suggest that mutual interactions between M33 and And XXII could have distorted M33's discs if they were once associated in the past (Tollerud et al., 2012; Chapman et al., 2013; Shaya and Tully, 2013; Martin et al., 2009).

Ram pressure stripping could also play a role in warping M33's gas disc. However, the magnitude of ram pressure stripping depends on orbital eccentricity and the inclination of its disc relative to its orbital plane. Each of the above scenarios requires careful modeling and should be studied in further detail in attempt to fully understand the morphological and dynamical history of M33. These goals are beyond the scope of this paper.

The orbital history of M33, whether it really is on first infall or if it made a passage about M31 $\sim$5-6 Gyr ago, is also relevant for the proposed plane of satellites surrounding M31 (e.g. Ibata et al., 2013) wherein, 13 satellites are suggested to be co-rotating about M31 in a plane about 13 kpc in width. While this plane does not include all of the known M31 satellites or M33, it could be affected by the massive nature of M33. For example, if M33 has been on a long-period orbit or if it is moving radially towards M31 for the first time, the presence of M33 would likely have some gravitational influence on the plane of satellites, especially for the Southern half of the plane. Therefore, M33's history is not only crucial to understanding the evolution of its own galactic features, but it may also influence the larger M31 system of satellites and their dynamical history.

2.7.2 Implications for the Proper Motion Measurements of M31

In recent years, the tangential velocity component of M31 has been measured in various ways. Several results, measured directly and inferred indirectly, are plotted in Fig. 2.16 and summarized here. S16 used the kinematics of 40 M31 satellites to estimate the motion of M31 via ΛCDM simulations and statistical fitting methods (green square). vdMG08 performs three statistical techniques and reports a weighted average using line of sight velocities for 17 satellites, the proper motions of two satellites, and line of sight velocities for five Local Group galaxies (blue triangle). S12 recently used HST to take direct measurements of M31's proper motion (red triangle). The black circle indicates the weighted average of S12 and vdMG08, which are the values used in this analysis (vdM12). Finally, the diamond indicates the resulting velocity components for zero tangential velocity. These values are shifted away from the origin due to the Sun's motion.

The large disparity between the S16 and S12 values is immediately evident. Consequently, the tangential velocity components reported by each team has serious implications for our understanding of the Local Group. The results of S16 imply the Local Group is not a bound system, complicating our understanding of its history. On the other hand, the S12 values imply M31's baryonic center of mass is offset in velocity from its outer dark matter halo. The latter has been proposed by Gao and White (2007) in their analysis of central galaxies in ΛCDM simulations. Their conclusion is further supported by G15, who claim the massive nature of the LMC causes a dynamical impact on the MW and therefore a velocity shift. From our numerical orbit analysis, we know that the presence of M33 does indeed cause a shift in M31's velocity up to tens of km s^{-1} as well.

Aiming to reconstruct M33's morphology, Loeb et al. (2005) estimated the tangental velocity for M31 by designing a numerical model where M33's stellar disc remains unperturbed by tidal disruptions over the last 10 Gyr and they recover a value of $v_{tan} = 100 \pm 20$ km s^{-1}. Similarly, we constrain M31's tangential velocity using only the theorized dynamical history of M33 which supports the formation of

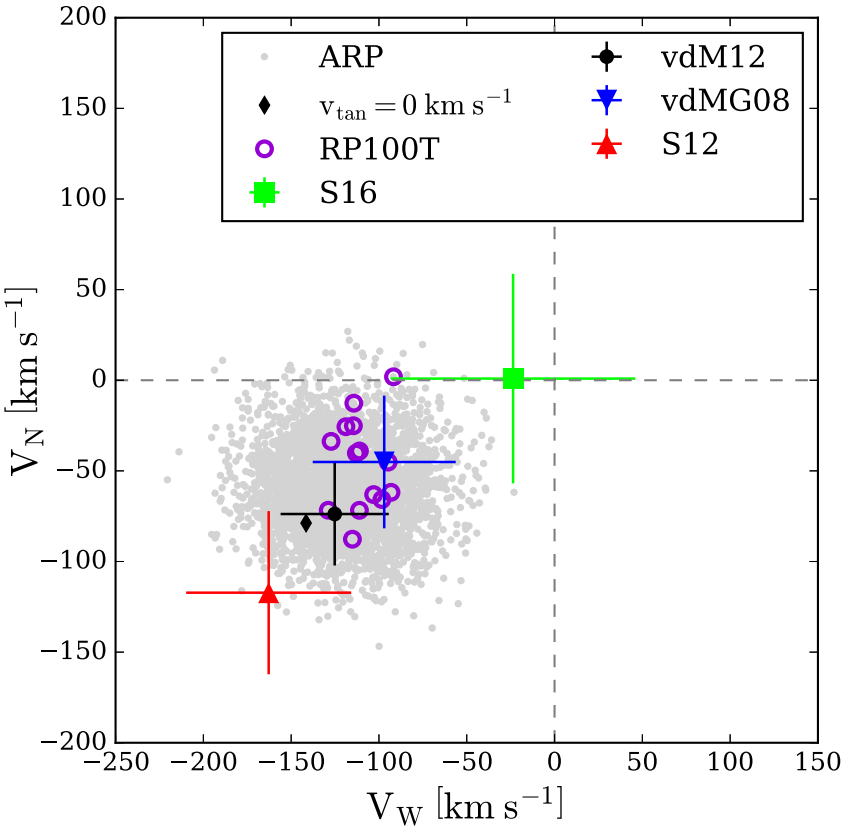

Figure 2.16: Proper motion measurements of M31 in units of North and West tangential velocity components. The gray points are the ARP sample for the high mass M31 and 2.5×10^{11} $M_\odot$ M33. The red triangle is the HST proper motion result from S12. The blue triangle is measured by satellite kinematics in vdMG08. The black circle is from vdM12 and is the weighted average of vdMG08 and S12. The green marker indicates the proper motion results of S16 using the satellite kinematics of the M31 system estimated from ΛCDM simulations. Finally, the black diamond is the proper motion resulting from a zero tangential velocity of M31. It is offset from the origin due to the Sun's motion. The analytic orbits that have a pericenter within 100 kpc of M31 in the last 3 Gyr are indicated by purple circles (RP100T sample).

its warp through a past interaction with M31 (P09, M09).

In Fig. 2.16, we show the North and West tangential velocity components corresponding to the 3D velocity vectors of M31 for the entire ARP sample (gray points)[6]. The points cluster in between the S12 and S16 values, with no particular preference towards either. The purple circles highlight just the RP100T orbits where a close ($\leq$ 100 kpc), recent ($t_{peri} < 3$ Gyr ago) pericenter exists. These orbits trace a specific region of the West velocity component, between about -150 and -100 km s^{-1} . About half of these orbits fall within the vdM12 1σ error space, which is the average of the S12 and vdMG08 results.

We find that the close passage for M33 is inconsistent with the HST PM measurement of M31 by S12. However, a more precise PM for M31 will (i) better constrain the tangential motion of M31 with direct measurements and (ii) rule out whether a recent, close passage scenario for M33 has occurred given its current motion. Doing so would suggest that a past interaction between M31 and M33 is not the one and only source of significant warps in the discs of M33, motivating a re-evaluation of the dynamical history of the M31 system.

2.8 Conclusions

The orbital evolution of massive satellite galaxies, and specifically those of the LMC and M33, have been explored in three contexts in this work: by numerically integrating their orbits backwards in time using astrometric data, by studying a large sample of massive satellite analogs in the Illustris-Dark simulation (Nelson et al., 2015; Vogelsberger et al., 2014a,b; Genel et al., 2014), and by determining their consistency with orbital expectations informed by morphology.

We have explored plausible orbital histories for the LMC and M33 about the MW and M31, respectively, using their observationally constrained velocity error space and backward integration schemes (e.g. B07, G15). The recently determined proper motion of M31 (S12) has enabled the study of M33's orbital history for

[6]Proper motion is converted to tangential velocity components by $\mu_i = v_i/(4.74 * d_{M31})$.

the first time in this fashion. We find consistency with previous studies of LMC's orbital history. If the MW's total mass is $< 1.5 \times 10^{12}$ $M_\odot$, the LMC is on its first approach to the MW and only recently completed its first pericentric passage. Surprisingly, we find that M33 is either also completing its first orbit about M31, or if M31 is massive ($> 2 \times 10^{12}$ $M_\odot$) then it is on a long period orbit. Note that in this study we have adopted a new dynamical friction approximation (van der Marel et al., 2012b), which reduces the orbital decay of satellite trajectories as their gravitational softening lengths and masses increase.

From our sample of massive satellite analogs in Illustris-Dark, we find that the orbital energetics and eccentricities of the LMC and M33 are generally consistent with a recent infall scenario ($t_{cross} < 4$ Gyr). Comparing the kinematics from recently updated LMC proper motion measurements to the orbital energies of the massive satellite analogs in Illustris-Dark, we find that a MW halo mass of $\sim 1.5 \times 10^{12}$ $M_\odot$ is preferred for recently accreted satellites. Early accretion for an LMC analog is cosmologically likely only if the MW's halo mass is $> 3 \times 10^{12}$ $M_\odot$. Applying the same analysis using M33's kinematics favors an M31 halo mass $\geq 1.5 \times 10^{12}$ $M_\odot$ if M33 is accreted recently. Early accretion of M33 is only plausible at the 20 per cent level if M31's halo mass is $\sim 3 \times 10^{12}$ $M_\odot$. Therefore, first infall is certainly favored from energetics alone. These results are generally consistent with the results of the numerical orbit integrations.

We conclude that both the LMC and M33 are most likely completing their first orbits about their hosts. The MW's halo mass is likely $\sim 1.5 \times 10^{12}$ $M_\odot$. M31's halo mass is likely $\geq 1.5 \times 10^{12}$ $M_\odot$. Paper II will focus on estimating the most typical halo masses for the MW and M31 based on the LMC and M33's present-day orbital angular momentum. We will apply Bayesian inference methods to analogs in the Illustris-Dark simulation to compute the posterior distribution of halo mass from satellite properties via importance sampling and kernel density estimation.

The orbital eccentricities of LMC and M33 cosmological analogs were extracted directly from the merger trees and also computed using the instantaneous position and velocity of the satellite, treating the satellite as a point mass. We find markedly

different results in the correlation between eccentricity and infall time. In particular, the weak correlation between infall time and eccentricity computed from orbital trajectories implies that eccentricity should not be used to characterize satellites by early and late infall times.

Our orbital analysis further reveals that M33 is unlikely to have reached closer than 100 kpc to M31, regardless of its orbital history. This is at odds with conventional models, where M33 is expected to have approached within 50-100 kpc of M31 in order to reproduce its observed warped morphology (P09, M09). We find that orbits recovering this scenario are $\sim$2.5σ outliers from the mean v_Y and v_Z components of M33's velocity vector relative to M31 (representing only 0.14 per cent of orbits recovered by sampling the full error space 10,000 times in a Monte Carlo fashion). Upon testing these conclusions when M31 is modeled with a total mass near its predicted upper limit of 3×10^{12} $M_\odot$, we still find that the orbits suggested by M09 and P09 are rare within the proper motion error space explored in this paper. Furthermore, high mass host halos ($> 2.5 \times 10^{12}$ $M_\odot$) are cosmologically rare in this orbital configuration.

Cosmologically, recently accreted massive satellite are about equally likely to have made recent (< 3 Gyr), close (< 100 kpc) encounters as recent wide encounters (> 100 kpc). There is no cosmological preference for either case. 32.42 per cent of such recently accreted massive satellite analogs have encounters < 55 kpc–i.e. the LMC's orbit, which brings it within 50 kpc of the MW, is not cosmologically rare. From the combined numerical integration and cosmological analysis of M33's orbit, we propose that other sources of its warped disc should be investigated (i.e. other M31 satellites, ram pressure stripping, etc.).

While the proper motions generally do not support a recent, close interaction between M33 and M31, the few numerically integrated orbits that do support this scenario are not consistent with the M31 tangential velocity components measured directly with HST (S12) or inferred by satellite kinematics (S16). More precise M31 proper motion measurements are necessary to disentangle M33's true orbital history.

The orbital histories of the four most massive members of the Local Group are

computed simultaneously to demonstrate that the LMC's trajectory has not been significantly perturbed by M31, nor M33 by the MW during the last 6 Gyr. Allowing the MW and M31 to move freely in these integrations also demonstrates that the LMC and M33 change the velocity of their hosts by tens and sometimes up to a hundred kilometers per second in just the last 2 Gyr, which may have important implications for the inferred orbital histories of their other satellites (e.g. G15), such as those used in S16 to infer properties of M31.

We conclude that the third and fourth most massive members of the Local Group, M33 and the LMC, respectively, are recent interlopers in the environment of their hosts. Such recent infall scenarios suggest they should both still contain a majority of their cosmological infall masses ($\sim$10 per cent of their host's mass) today. Therefore, we must account for their dynamical influence on all other MW and M31 satellites.

This article has been accepted for publication in *Monthly Notices of the Royal Astronomical Society* ©: 2017 Ekta Patel. Published by Oxford University Press on behalf of the Royal Astronomical Society.

CHAPTER 3

Orbits of Massive Satellite Galaxies - II. Bayesian Estimates of the Milky Way and Andromeda Masses Using High-Precision Astrometry and Cosmological Simulations

This chapter has been published previously as Patel, E., Besla, G., Mandel, K., 2017, MNRAS, 468, 3428

Abstract

In the era of high precision astrometry, space observatories like the *Hubble Space Telescope* (HST) and *Gaia* are providing unprecedented 6D phase space information of satellite galaxies. Such measurements can shed light on the structure and assembly history of the Local Group, but improved statistical methods are needed to use them efficiently. Here we illustrate such a method using analogs of the Local Group's two most massive satellite galaxies, the Large Magellanic Cloud (LMC) and Triangulum (M33), from the Illustris dark-matter-only cosmological simulation. We use a Bayesian inference scheme combining measurements of positions, velocities, and specific orbital angular momenta (j) of the LMC/M33 with importance sampling of their simulated analogs to compute posterior estimates of the Milky Way (MW) and Andromeda's (M31) halo masses. We conclude the resulting host halo mass is more susceptible to bias when using measurements of the current position and velocity of satellites, especially when satellites are at short-lived phases of their orbits (i.e. at pericenter). Instead, the j value of a satellite is well-conserved over time and provides a more reliable constraint on host mass. The inferred virial mass of the MW (M31) using j of the LMC (M33) is $\mathrm{M_{vir,MW}} = 1.02^{+0.77}_{-0.55} \times 10^{12}\,\mathrm{M_\odot}$ ($\mathrm{M_{vir,M31}} = 1.37^{+1.39}_{-0.75} \times 10^{12}\,\mathrm{M_\odot}$). Choosing simulated analogs whose j values are consistent with the conventional picture of a previous (< 3 Gyr ago), close encounter ($<$ 100 kpc) of M33 about M31 results in a very low virial mass for M31 ($\sim 10^{12}\,\mathrm{M_\odot}$).

This supports the new scenario put forth in Patel et al. (2017a), wherein M33 is on its first passage about M31 or on a long period orbit. We conclude that this Bayesian inference scheme, utilising satellite j, is a promising method to reduce the current factor of two spread in the mass range of the MW and M31. This method is easily adaptable to include additional satellites as new 6D phase space information becomes available from HST, *Gaia* and JWST.

3.1 Introduction

The Milky Way (MW) and Andromeda (M31) both host a plethora of known substructures within their respective dark matter halos. These substructures include dwarf satellite galaxies, globular clusters, and also several stellar streams. Most of these systems are dynamically bound to their given host halo at present, making them unique tracers of their host's gravitational potential.

With instruments like the *Hubble Space Telescope* (HST), proper motions of dwarf satellite galaxies, globular clusters, and stellar streams have been measured with microarcsecond per year precision. High precision astrometry promises to be an especially fruitful field with the recent launch of the *Gaia* satellite. Results from *Gaia* data release 1 (DR1, Gaia Collaboration et al., 2016) have already confirmed the proper motions of the Magellanic Clouds (van der Marel and Sahlmann, 2016b) previously measured by Kallivayalil et al. (2013, hereafter K13) and others (e.g., Kallivayalil et al., 2006a,b; Piatek et al., 2008; Vieira et al., 2010). We aim to leverage the full 6D phase space information for nearby, massive satellite galaxies ($\sim 10^{11}\,\mathrm{M}_{\odot}$) to inform us about the assembly and structure of our Local Group of galaxies using high resolution dark matter simulations of large cosmological volumes.

The precise motion of satellite galaxies and remnant streams have already acted as a stepping stone for dynamical mass estimates of the MW. Their 3D positions and velocities derived from the proper motions are used as instantaneous tracers of the halo potential and can therefore estimate the total mass enclosed within a given radius. For example, numerical models designed to reproduce properties of the

stellar debris in the Sagittarius stellar stream have yielded conflicting estimates on the mass of the MW. Estimates derived from the tidal disruption of the Sagittarius dSph imply a rather light MW mass of M(200 kpc)=$5.6 \pm 1.2 \times 10^{11}\,M_{\odot}$ (68 per cent credible interval; Gibbons et al., 2014), but more recent simulations of the Sagittarius stellar stream are able to reproduce its kinematics in a MW mass of order $10^{12}\,M_{\odot}$ within 206 kpc (Dierickx and Loeb, 2017a). Such orbital models have not yet converged to a consistent result for the mass of the MW and demonstrate just one instance of ambiguity in its measurement.

Many other independent methods have also been used to measure the mass of the MW. Zaritsky et al. (1989); Kochanek (1996); Wilkinson and Evans (1999); Sakamoto et al. (2003); Eadie et al. (2017) have all considered the motion of multiple satellite galaxies, globular clusters, or both to determine the MW's mass. Other methods include abundance matching between cosmological simulations and observational surveys (e.g. Moster et al., 2013), applying the cosmological baryonic fraction of the MW to estimate the lower bound on its mass without invoking dynamics (Zaritsky and Courtois, 2017), computing mass via the MW-M31 timing argument (e.g. van der Marel et al., 2012a,b), and more (see Dehnen and Binney, 1998; Dehnen et al., 2006; Moore and Davis, 1994; Murali, 2000; Binney and Evans, 2001; Rasmussen and Pedersen, 2001; Klypin et al., 2002; Smith et al., 2007; Brown et al., 2006).

Cosmological simulations provide an independent statistical method for constraining the MW's halo mass under the assumption that they accurately capture the physics and underlying cosmology of our Universe. Together, with high precision astrometry, these simulations have opened a new door for near–field cosmology. Dynamical properties, such as orbital energy and angular momentum, computed from 6D phase space measurements can be used to statistically infer the total mass of a host galaxy's halo. Boylan-Kolchin et al. (2011a, hereafter BK11) used the dynamics of the Magellanic Clouds (MCs) from the Kallivayalil et al. (2006a,b) proper motions and the frequency of their analogs in the Millennium-II Simulation (Boylan-Kolchin et al., 2009) to conclude that the MW's virial mass is $\geq 2 \times 10^{12}\,M_{\odot}$. In Patel et al.

(2017a, hereafter Paper I), we followed a similar methodology using revised proper motions of the LMC from K13 and the Illustris dark matter-only cosmological simulation (Nelson et al., 2015; Vogelsberger et al., 2014b,a) to illustrate that the hosts of LMC-like systems (of similar mass and orbital energy) have typical halo masses of order $1.5 \times 10^{12}\,\mathrm{M}_{\odot}$.

A similar analysis can now be applied to M31 for the first time, as its proper motion was only recently measured with HST (Sohn et al., 2012; van der Marel et al., 2012a, hereafter S12 and vdM12). The proper motion for M33, the most massive satellite galaxy of M31, was measured by observing water masers with the *Very Long Baseline Array* (Brunthaler et al., 2005, hereafter B05). These combined measurements enable us to study both the MW-LMC and M31-M33 systems as isolated host-satellite systems in tandem. In Paper I, we demonstrated that satellites identified in Illustris with masses and specific orbital energy comparable to that of M33 are most likely on their first approach about their hosts. The M31 analogs that host such satellites have typical halo masses $\geq 1.5 \times 10^{12}\,\mathrm{M}_{\odot}$. Many independent efforts have also been made to estimate the mass of M31 (e.g. Klypin et al., 2002; Watkins et al., 2010; Tollerud et al., 2012).

While the above numerical and cosmological methods are promising, the MW's plausible mass range is $\approx 0.7-1.5\times10^{12}\,\mathrm{M}_{\odot}$ and that of M31 is $\approx 1.5-2.5\times10^{12}\,\mathrm{M}_{\odot}$. Observational evidence shows that the total mass of M31 should be higher than that of the MW's as M31's stellar disk is more massive and it hosts dwarf elliptical galaxies. We will demonstrate that inferred masses of the MW and M31 using only positions and velocities of satellites contradict this general belief.

The advent of high mass resolution cosmological simulations with large volumes ($\gtrsim$100 Mpc per side; e.g. Illustris, EAGLE, Millennium-II, Bolshoi) has provided a statistically significant data set to explore a novel inference method that may help us to further constrain this mass range for the MW (Busha et al., 2011, hereafter B11) and for the Local Group (González et al., 2013, hereafter G13). B11 developed and applied a Bayesian inference scheme to a set of Magellanic Cloud (MC) analogs in the Bolshoi (Klypin et al., 2011) cosmological simulation using the observed positions,

velocities, and circular velocities derived from their proper motions (Kallivayalil et al., 2006a,b, 2013). Assuming that the errors on these measured properties are Gaussian, they invoked an importance sampling technique to infer the posterior distribution of the MW's halo mass.

One major assumption in all of these studies that utilised inference techniques is that the position and velocity of the LMC today are typical, however, it is well known that the LMC is likely just past pericenter, and such orbital configurations are short-lived (Besla et al., 2007, 2012; Kallivayalil et al., 2013; Gómez et al., 2015). Furthermore, the position and velocity of the LMC today are rare amongst the phase space of known Local Group dwarf satellites. In contrast, M33 is between apo- and pericenter, and therefore exhibits a less transient configuration (Patel et al., 2017a; Putman et al., 2009; McConnachie et al., 2009).

G13 examined the effects of the larger environment of the MW (i.e. including an M31 companion galaxy) in determining its mass and found MW mass estimates in agreement with B11, concluding that the requirement of a Local Group environment does not affect the inferred mass of the MW. More recent work (Williamson et al., in prep.) uses the combined constraints from the MW–LMC–M31–M33 to identify analogs of the Local Group and place further constraints on these mass estimates with a Bayesian approach. Carlesi et al. (2017) have also obtained the mass of the Local Group in a statistical fashion, finding a MW mass estimate of 0.6-0.8$\times10^{12}$ $M_{\odot}$, somewhat lower than that typically determined with the timing argument.

In this work, we will focus on the specific orbital angular momentum of the LMC (and M33), as it is generally well conserved with time, and use it to infer the most typical MW (M31) mass. By doing so, we aim to avoid any bias that may be introduced due to the transient nature of the LMC's current orbital configuration. Using these two massive satellites galaxies in tandem to constrain their respective host halo masses will test the robustness of the adopted Bayesian inference technique while also providing insight on how the orbital histories of massive satellites can uncover important properties of their host environment.

For this paper, we allow the halo mass of the host galaxy (the MW or M31) to be a

free parameter and estimate its most probable value using the present-day dynamics of the LMC or M33 in combination with the Illustris cosmological simulation via Bayesian methods adopted from B11. Recent proper motion measurements and the higher mass resolution of Illustris motivate us to re-examine the MW-LMC system. While Fardal et al. (2013) have inferred the mass of M31 in a Bayesian fashion using constraints from the Giant Southern Stream, we extend B11's Bayesian method to compute the mass of M31 using observed properties of M33 for the first time. In the era of high astrometric precision, these types of statistical analyses will be key to refining our understanding of the Local Group. In future work, we will further explore how this technique may be expanded to include more (less massive) satellite galaxies as their proper motions are obtained with HST and *Gaia* in the upcoming years.

This paper is organized as follows. In Section 3.2, we describe the dark matter-only Illustris cosmological simulation and the sample criteria for identifying a control set of host-satellite pairs analogous to the MW-LMC or M31-M33. Section 3.3 details the Bayesian inference method implemented to determine the posterior mass distributions for the MW and M31. In Section 3.4, we present results for the masses of the MW and M31 using two different likelihoods in combination with the properties of the LMC and M33, respectively. Section 3.5 further discusses the implications of different satellite orbital histories on the mass estimates of their host galaxies, the impact of measurement and cosmic variance errors on this analysis, and the results of this method as compared to previous work. Finally, Section 3.6 contains a summary of our findings and addresses future prospects.

3.2 The Illustris Simulation and Sample Selection

In Paper I of this series, we identified several hundred massive satellite analogs of the LMC and M33 in the *Illustris-1-Dark* (hereafter Illustris-Dark) cosmological simulation (Nelson et al., 2015; Vogelsberger et al., 2014b,a). We found that orbital energy shows a tight correlation with host halo mass (see also Boylan-Kolchin et al.,

2011a). As the absolute value of the specific orbital energy increases, the host mass also increases. However, satellites may spend a significant amount of time in orbit about their hosts and suffer orbital decay owing to dynamical friction. As such, here we utilise this control sample of massive satellite analogs to gauge the stability of dynamical properties of satellite orbits, such as orbital angular momentum and orbital energy over time.

Since we use analogs of the LMC and M33, which are currently at different positions within their orbits, we must first identify properties of these satellites that remain stable with time so that our analysis is consistent for both host-satellite systems.

In the following, we describe the specifications of the Illustris-Dark dark matter-only cosmological simulation and the criteria for selecting a control sample of host-satellite pairs that mimic the mass ratio of the MW-LMC and M31-M33 systems. The host-satellite control sample is used to determine which satellite dynamical properties are most suitable for the statistical analysis described in Section 3.3.

3.2.1 Simulation

The *Illustris Project*[1] is a suite of N-body+hydrodynamic simulations run with the `AREPO` code, spanning a cosmological volume of $(106.5\ \mathrm{Mpc})^3$ (Nelson et al., 2015; Vogelsberger et al., 2014b,a; Genel et al., 2014). As in Paper I, we use only the Illustris-Dark simulation, which follows the evolution of 1820^3 dark matter particles from $z = 127$ to $z = 0$. Illustris-Dark uses the *WMAP-9* cosmological parameters (Hinshaw et al., 2013):

$$\Omega_m = 0.2726, \Omega_\Lambda = 0.7274, \Omega_b = 0.0456, \sigma_8 = 0.809, n_s = 0.963, h = 0.704. \quad (3.1)$$

These cosmological parameters differ slightly from the parameters used in the Bolshoi (Klypin et al., 2011) and Millennium-II (Boylan-Kolchin et al., 2009) cosmological simulations. However, we have reproduced the methodology of previous studies,

[1]The Illustris catalogs are all publicly available at www.illustris-project.org

as described later, and recover consistent results. We will make further comparisons to previous work in Section 3.5.4.

Halos and halo substructure in Illustris-Dark are identified with the SUBFIND routine (Springel et al., 2001a; Dolag et al., 2009). We use the Illustris-Dark merger trees created with the SUBLINK code (Rodriguez-Gomez et al., 2015) to trace the orbital histories of massive satellite analogs in this analysis. In addition to the full orbital histories, merger trees also provide information about the mass and size evolution of both hosts and satellites throughout cosmic time.

The Bolshoi simulation has a much larger simulation volume compared to Illustris-Dark (250 h^{-1} Mpc per side vs. 75 h^{-1} Mpc per side), however the dark matter particle mass is only of order $10^8\,\mathrm{M}_\odot$. Upon identifying LMC/M33 mass analogs by our definition (see Paper I) in the Bolshoi simulation, each analog would only consist of $10^2 - 10^3$ dark matter particles, whereas Illustris provides at least $10^3 - 10^4$ dark matter particles per massive satellite analog with a dark matter mass resolution of $\mathrm{m_{DM}} = 7.5 \times 10^6\,\mathrm{M}_\odot$. Thus, while Bolshoi will provide a larger statistical sample of massive satellite analogs, the Illustris-Dark analogs are individually better resolved.

3.2.2 Control Sample Selection

MW/M31 analogs are all central subhalos (i.e. the primary subhalo containing the majority of the bound material in a given halo as determined by SUBFIND) whose halo virial mass (see Paper I for definition) at $z = 0$ is $\mathrm{M_{vir}} = 0.7 - 3 \times 10^{12}\,\mathrm{M}_\odot$. We use this generous mass range to reflect all reported values for masses of the MW and M31 in recent literature. In total, 1933 halos satisfy these criteria. Therefore, MW/M31 mass analogs are composed of order 10^5 dark matter particles each. Virial mass and virial radius for all MW/M31 analogs are taken directly from the Illustris-Dark halo catalogs and are based on the spherical tophat approximation.

Host halos are then defined as the subset of MW/M31 analogs which also host a massive subhalo like the LMC or M33. Section 5 of Paper I outlines more details regarding the sample selection criteria of host halos and their subsequent massive

satellite analogs (also see BK11). In Illustris-Dark, we find about 24.4 per cent of MW/M31 mass halo analogs host a massive satellite analog like the LMC or M33 within their virial radius. This frequency is consistent with observational surveys of L_* galaxies and previous theoretical studies of the MCs using cosmological simulations (e.g. Tollerud et al., 2011a; Boylan-Kolchin et al., 2011a; Liu et al., 2011). The full control sample of host-satellite analogs consists of 472 systems. See Figs. 3 and 4 in Paper I for the distribution of host halo virial mass and the host to satellite mass ratios. This sample of host-satellite pairs will only be used as a control sample in this paper, specifically to test the stability of satellite orbital dynamics over time in the following section.

The Evolution of Satellite Orbital Dynamics in Illustris

Previous studies have estimated the dark matter halo mass of the MW based on the observed properties of the MCs, such as relative position, velocity, and maximum circular velocity (BK11, B11, G13). For example, the properties of the LMC used in B11 are: $r^{obs} = 50 \pm 2$ kpc, $v_{tot}^{obs} = 378 \pm 36$ km s^{-1}, and $v_{max}^{obs} = 65 \pm 15$ km s^{-1} based on the LMC proper motions given by Kallivayalil et al. (2006a,b).

Folding these properties into a Bayesian scheme automatically assumes that these observed properties are typical amongst the population of massive satellite galaxies in a given redshift range. It is well known that while the orbits of satellite galaxies can be fairly eccentric upon infall into their host's halo (e.g. Wetzel, 2011; Benson, 2005), these orbits decay significantly as they experience dynamical friction and mass loss. Consequently, the positions and velocities of satellites relative to their hosts' motion will evolve accordingly with time. Choosing a satellite based on its instantaneous position and velocity therefore implies a unique location within the orbit, rather than the most *typical* location. This can dramatically limit the number of plausible analogs, particularly if the satellite is in an unusual location in its orbit.

Instead, we examine the total specific orbital angular momentum and the specific orbital energy of massive satellite analogs. By quantifying the time evolution of these orbital 'constants', we can assess whether they are accurate tracers of the satellite

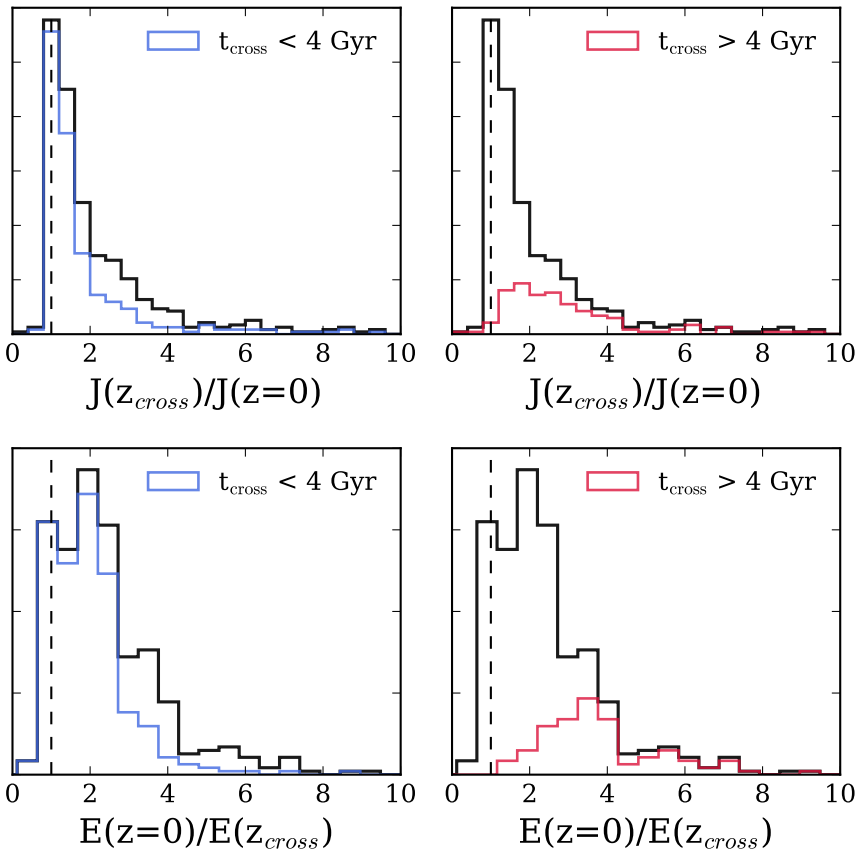

Figure 3.1: *Top:* The ratio of specific orbital angular momentum for the Illustris-Dark massive satellite control sample with $t_{cross} < 4$ Gyr (left panel, blue) and the $t_{cross} > 4$ Gyr satellite sample (right panel, red). The orbital angular momentum ratios peak around one (vertical dashed line) for both samples indicating very little angular momentum loss between infall and $z = 0$. *Bottom:* The ratio of specific orbital energy for the the $t_{cross} < 4$ Gyr sample (left panel, blue) and the $t_{cross} > 4$ Gyr sample (right panel, red). Orbital energy varies more significantly and changes by up to a factor of four for most systems. For reference, the distribution of angular momentum ratios and energy ratios for the entire sample are given in black solid histograms. All histograms are normalised to the size of the full sample (black) such that each pair of blue and red histograms sums to the black histogram when stacked.

orbital properties since their time of infall. The infall time is defined as the point in time at which the satellite first crossed their host's time-evolving virial radius (see Paper I, Section 6.1).

This technique ensures that the massive satellite analogs with orbits most similar to those of the LMC or M33, respectively, are chosen from the Illustris-Dark simulation to estimate the halo mass of the MW or M31. It also eliminates any contamination from satellite analogs that may only instantaneously satisfy a specific position and velocity criteria at $z \approx 0$, but which ultimately fail to identify in the same family of orbits as those of interest in this work (i.e. the LMC and M33).

In the following, we compare the stability of specific orbital energy and specific angular momentum for the control sample of host-satellite analogs described above. By doing so, we decipher which quantity is more stable over time, justifying its usage in a Bayesian inference scheme. Specific orbital energy and specific orbital angular momentum for the control sample of massive satellite analogs are calculated using Eqs. 3.2-3.4.

$$\mathrm{E_{sat}} = \frac{1}{2}\mathrm{v}^2 + \Phi_{\mathrm{NFW}}(\mathrm{M_{vir}}, \mathrm{c_{vir}}, \mathrm{r}) \tag{3.2}$$

In Equation 3.2, the gravitational potential of each host halo is approximated by a Navarro-Frenk-White (Navarro et al., 1996, NFW) profile. The virial concentration, $\mathrm{c_{vir}}$, is calculated with the fitting formula of the Bolshoi simulation at $z = 0$ (Klypin et al., 2011):

$$c_{\mathrm{vir}}(M_{\mathrm{vir}}) = 9.60 \left(\frac{M_{\mathrm{vir}}}{10^{12} h^{-1} M_{\odot}} \right). \tag{3.3}$$

The total specific orbital angular momentum is computed by:

$$\mathrm{j} = |\mathbf{r} \times \mathbf{v}|. \tag{3.4}$$

Here $\mathbf{r}$ is the relative position vector connecting the host and satellite, whereas $\mathbf{v}$ is the velocity vector of the satellite relative to its host. The total specific orbital angular momentum (j) is therefore the magnitude of their cross product.

For each host-satellite member of our control sample we compute the satellite's specific orbital angular momentum and the specific orbital energy at the redshift of satellite crossing time ($z = z_{cross}$) and at $z = 0$. The distribution of the ratio of these values ($E(z = 0)/E(z_{cross})$ and $J(z_{cross})/J(z = 0)$) is plotted in Fig. 3.1 for all control satellites (black), separated by those accreted at early ($t_{cross} < 4$ Gyr ago; left) and late ($t_{cross} > 4$ Gyr ago; right) crossing times[2]. The ratios are computed in this order so the distributions share the same horizontal axis.

The top panels in Fig. 3.1 show the distribution of the ratio of specific orbital angular momentum at $z = z_{cross}$ to $z = 0$. Recently accreted satellites in the control sample (top left panel) experience an angular momentum change less than a factor of two on average. For the early accreted satellites (top right panel), the angular momentum loss is only slightly more significant, reaching factors of four or six for small fractions of the sample. The latter results are naturally expected because these orbits have decayed more substantially since their time of infall.

The bottom panels of Fig. 3.1 highlight that changes in position, velocity, and host halo virial mass result in a loss of orbital energy since the time of infall because satellite orbits decay via dynamical friction (see Paper I, Section 6.3). Dynamical friction is proportional to the satellite mass squared, therefore the more massive the satellite, the faster its orbit decays. Fig. 3.1 shows that recently accreted satellites can lose up to four times the orbital energy exhibited at infall while early accreted satellites can lose up to eight times their original orbital energy. Generally, the distribution of orbital energy evolution is broader than that of orbital angular momentum, independent of satellite crossing time. This is especially crucial for the most recently accreted satellites since about 70 per cent of the massive satellite analogs in Illustris-Dark were accreted in the last 4 Gyr (see Paper I, Section 6.1).

We conclude that orbital angular momentum is more stable than orbital energy for the population of massive satellite analogs over time. By examining Eqs. 3.2-3.4, it is also clear that orbital angular momentum is not directly correlated with host

[2]Infall time is used interchangeably with crossing time–the first time a satellite crosses into the time-evolving virial radius of its host halo.

halo mass as M_{vir} does not appear in Eq. 3.4, unlike in Eqs. 3.2 and 3.3. Thus, orbital angular momentum introduces less intrinsic host mass bias. In the following section, total specific orbital angular momentum is treated like an observable to determine the most likely host halo mass for the LMC and M33. This methodology falls in line with action–angle dynamics where actions (angular momentum coordinates) and angles replace position–velocity coordinates in numerically integrated (periodic) orbital models to simplify orbit calculations. For example, Bovy (2014); Sanders and Binney (2014); Helmi and Koppelman (2016); Helmi and White (1999) track the orbits of various MW substructures using this technique.

This method is of particular interest with regards to the LMC because many previous studies (Patel et al., 2017a; Besla et al., 2007, B11, K13, and references therein) have concluded it is just past pericenter – a unique epoch in a satellite galaxy's lifetime as it is a short-lived configuration. To constrain the host halo mass with the most physically motivated and informative sample of massive satellites, we must consider the family of orbits to which the LMC belongs rather than just its position and velocity today.

Note that, in Paper I, we found that M33 could be just past apocenter and therefore more common amongst the phase space of massive satellite analogs. Given this orbital history, it may still be reasonable to consider M33's position and velocity today as an indicator of host halo mass. We will explore both the B11 (position and velocity) likelihood function and a newly developed angular momentum likelihood function in our importance sampling technique moving forwards.

3.3 Bayesian Inference Method

Now we reverse our analysis from Paper I and constrain host halo mass by using satellite dynamics in a Bayesian inference scheme. The host halo mass is left as a free parameter and is informed only by the observed properties of the LMC/M33 in combination with host-satellite analogs in the Illustris-Dark simulation. The recent HST proper motion analysis of M31 (Sohn et al., 2012; van der Marel et al., 2012a)

allows us to apply this method to the M31-M33 system for the first time.

We follow the Bayesian inference method described by B11, who used the halo catalogs from the Bolshoi simulation to estimate the mass of the MW. Note that we focus on the presence of just one massive subhalo analogous to the LMC or M33, while B11 requires each halo to host an analog of both the LMC and SMC.

The statistical method relies on applying a set of observables as priors to the full Illustris-Dark halo catalog. In the first case, we will examine the resulting masses of the MW and M31 upon considering the position and velocity of the LMC and M33 as independent observables. The second case treats the angular momentum of the satellites as an observable, thereby considering a larger fraction of satellite phase space. The code developed for this work is publicly available on GitHub.

3.3.1 Observed Properties

As discussed in Paper I, the proper motions of the LMC, M33 and M31 make it possible to study the orbital histories of the MW-LMC and M31-M33 systems in detail. K13 measured the LMC's proper motions directly using HST, updating previous results from Kallivayalil et al. (2006a). The LMC's proper motions are transformed to Galactocentric positions and velocities using the methods of van der Marel et al. (2002). Uncertainties on these values are determined by a Monte Carlo scheme that samples the 4σ error space of proper motions, radial velocity, position, and the solar motion quantities. This scheme yields 10,000 unique position and velocity vectors from which their standard errors are calculated. These vectors can also be used to compute average dynamical quantities such as orbital angular momentum and its standard error.

The proper motion of M33 was measured using the *Very Long Baseline Array* by B05. M31's proper motion was measured directly, also using HST, by S12. These measurements were corrected for viewing perspective and internal motions by vdM12. Both sets of measurements are transformed to Galactocentric quantities in the same fashion as the LMC. They are combined to yield 10,000 unique position and velocity vectors in the combined error space of the M31-M33 system. Again, these

vectors can be used to compute mean position, velocity, and angular momentum of M33 with respect to M31 (see Table 1 of Paper I).

The final observable required for this statistical analysis is the maximum circular velocity of the LMC and M33. Maximum circular velocity is used as a proxy for satellite mass enclosed at a given radius since $v_c^2 = GM_{sat}(r)/r$. See Appendix B.1 for a short discussion on the stability of circular velocity compared to subhalo mass in simulations.

The LMC's rotation curve was most recently measured by van der Marel and Kallivayalil (2014), who conclude that its circular velocity peaks at $v_{circ,max} = 91.7 \pm 18.8$ km s^{-1}. M33's rotation curve was measured by Corbelli and Salucci (2000); its circular velocity at 15 kpc from its center (the farthest radial data point measured) is $v_{circ} \sim 130$ km s^{-1}, thus we adopt this value for M33's $v_{circ,max}$, although it is expected that the rotation curve continues to rise at larger radial distances. Since we use the dark matter-only version of Illustris throughout this study, we need only to account for the peak circular velocity (v_{max}^{obs}) of the dark matter halo. The halo's circular velocity typically peaks in the outer halo where there is minimal contribution from the baryonic disk, which instead peaks within the innermost few kpc of a galaxy.

We adopt the LMC's peak halo velocity modeled by Besla et al. (2012) and the peak halo velocity of M33 modeled by vdM12. The models estimate the individual contributions of the halo, disc, and bulge for the LMC and M33 such that the total rotation curve reproduces the observed data. We use the peak values of the halo rotation curves in these models and assign a halo peak circular velocity error[3] of 10 km s^{-1} to both satellite velocities (see van der Marel and Kallivayalil, 2014; Corbelli and Salucci, 2000). The observed properties of the LMC and M33 used in this analysis are summarized in Table 3.1. Note that we have adopted these satellite properties to remain consistent with those used in Paper I. We stress that new measurements of any of these properties can be easily implemented using this

[3]We have also tested an error of 15 km s^{-1} (as in B11) and find no significant differences in the results presented in Section 3.4.

Table 3.1: Observational data (**d**) for the LMC and M33 used to build likelihoods in the Bayesian inference scheme includes the maximum circular velocity, current separation from the host galaxy, and total velocity relative to the host galaxy. a: The maximal circular velocity of the LMC's halo rotation curve is adopted from Besla et al. (2012).; b: M33's halo rotation curve maximum is duplicated from van der Marel et al. (2012b). M33's position, velocity, and their errors are adopted from Paper I (Table 1) and references within.

	LMC μ	LMC σ	M33 μ	M33 σ
v_{max}^{obs} [km s^{-1}]	85[a]	10	90[b]	10
r^{obs} [kpc]	50	5	203	47
v_{tot}^{obs} [km s^{-1}]	321	24	202	38
j^{obs} [kpc km s^{-1}]	15,688	1,788	27,656	8,219

methodology (e.g. a more refined measurement of M33's distance[4]).

3.3.2 Statistical Methods

In this section, we describe how we compute the posterior distribution, $P(M_{vir}|\,\mathbf{d})$, of the host halo mass M_{vir}, given the observational data **d**. In principle, this is obtained from the marginalisation

$$P(M_{vir}|\,\mathbf{d}) = \int P(\mathbf{x}, M_{vir}|\,\mathbf{d})\,d\mathbf{x} \tag{3.5}$$

where $P(\mathbf{x}, M_{vir}|\,\mathbf{d}) = P(\boldsymbol{\theta}|\,\mathbf{d})$ is the joint posterior distribution of the physical parameters $\boldsymbol{\theta} = \{\mathbf{x},\ M_{vir}\}$ of a host-satellite system. The parameters **x** are the true, latent values of the observable satellite subhalo properties, and consist of:

- v_{max}, the observed maximum circular velocity of a satellite (either the LMC or M33),
- r, its position relative to its host,
- j, the total specific orbital angular momentum, and

[4]The 10,000 Monte Carlo samples drawn from the M31-M33 proper motion error space do contain position vectors which reflect the suggested high distance measurement to M33 of ∼968 kpc (U et al., 2009).

- v_{tot}, the satellite's total velocity relative to its host galaxy (the MW or M31).

The observable parameter vector $\mathbf{x}$ is a subset of these properties that depends on the type of analysis we perform (as described in Section 3.3.2). The observational data $\mathbf{d}$ consist of the measurements of the parameters in $\mathbf{x}$. (If measurement errors were zero, then $\mathbf{d} = \mathbf{x}$). The superscript ^{obs} will indicate the observed values that remain constant in this analysis. For example, r^{obs} is the observed measurement of the true distance r. See Table 3.1.

The joint posterior distribution is computed from the likelihood and prior via Bayes' theorem:

$$P(\boldsymbol{\theta}|\,\mathbf{d}) \propto P(\mathbf{d}|\,\boldsymbol{\theta})\,P(\boldsymbol{\theta}). \tag{3.6}$$

The prior $P(\boldsymbol{\theta})$ encodes the correlations between the observable parameters $\mathbf{x}$ and M_{vir}, as determined by the physics of galaxy formation and evolution in the Illustris-Dark simulation. The likelihood $P(\mathbf{d}|\,\boldsymbol{\theta})$ constrains the values of the physical parameters consistent with the measurements $\mathbf{d}$ of a particular subhalo (LMC or M33). The posterior combines the prior and likelihood to obtain constraints on the M_{vir} of the halo (MW or M31).

In practice, we compute the posterior distribution (Eq. 3.6) using a technique called importance sampling. We treat halo analogs from the Illustris-Dark simulation, with physical parameters $\boldsymbol{\theta}$, as draws from the prior, which are then weighted by a likelihood function, $P(\mathbf{d}|\,\boldsymbol{\theta})$, in proportion to their similarity to the observed measurements $\mathbf{d}$. The resulting importance weights are used to compute posterior inferences on the virial mass, M_{vir}.

In the following sections, we describe the selection criteria (denoted by $\mathbf{C}$) for the prior, how we calculate the appropriate likelihoods and importance weights for host halos in Illustris-Dark, and how we compute the resulting posterior inferences for host halo mass from the observational data.

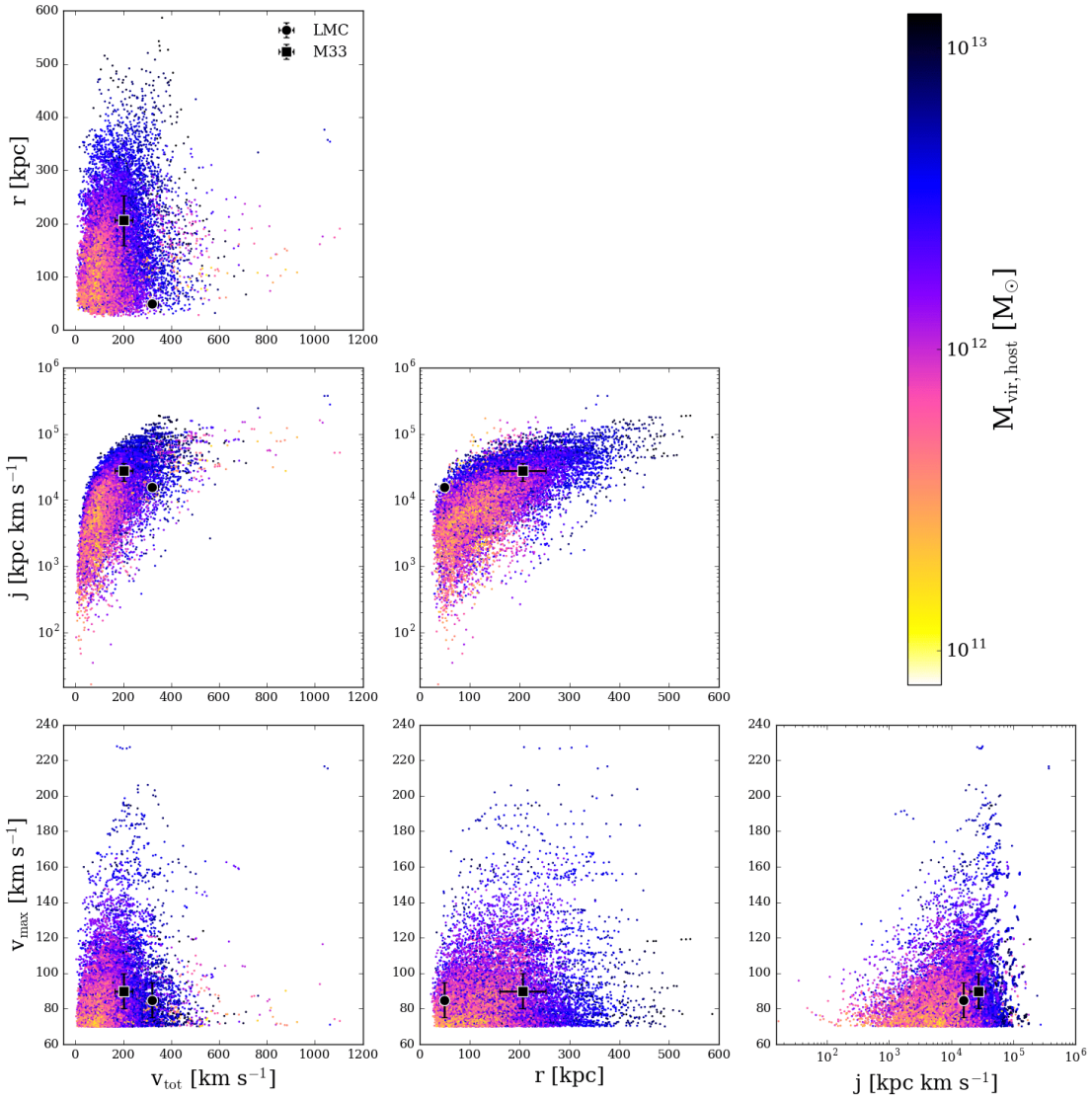

Figure 3.2: For all host-satellite systems selected from Illustris-Dark ($P(\theta)$), the distribution of the satellite subhalo properties ($\mathbf{x}$) are shown for each pair of satellite parameters. All points are colored by the corresponding host halo virial mass (M_{vir}) to which they belong. The LMC's properties are indicated by a black circle, while M33 is represented with a black square. These reference points indicate that host halos in Illustris-Dark do host massive satellite analogs with properties similar to that of the LMC and M33. Total orbital angular momentum (j^{obs}) suggests that M33 should reside in a higher host halo mass than the LMC, however, similar conclusions cannot be drawn for v_{max}^{obs}, r^{obs}, and v_{tot}^{obs}.

Prior

The prior P($\boldsymbol{\theta}$) is a collection of halos from the full Illustris-Dark halo catalog. Several selection criteria (**C**) are applied to the halo catalog to choose halos that host appropriate analogs of the LMC and M33. Those halos that satisfy them are treated as draws from the underlying prior distribution. Therefore, the prior is truly P($\theta|\,\mathbf{C}$). Note that the prior is different from the control sample used in Section 3.2.

To infer the most typical host halo mass for the MW and M31 given that they both host at least one massive satellite galaxy, we must first apply some selection criteria, **C**, to the Illustris-Dark halo catalog. **C** restricts the Illustris halo catalog by requiring the following criteria.

> C_1: A subhalo is considered a massive satellite analog only if $v_{\rm max} > 70$ km s^{-1}.
>
> C_2: The massive satellite analog must reside within its host's virial radius ($R_{\rm vir}$) at $z \approx 0$.
>
> C_3: The massive satellite analog must have a minimal subhalo mass of $10^{10}\,M_\odot$ at $z \approx 0$.

Only host-satellite systems where exactly $N_{\rm sub}$=1 massive satellite analog satisfies these qualifications are considered. All other systems (i.e $N_{\rm sub}$=0 or $N_{\rm sub} > 1$[5]) are dismissed from the prior.

We build the prior by searching for all systems that fit these criteria over a redshift window of $z = 0 - 0.26$. This redshift window corresponds to 20 Illustris -Dark simulation outputs, or equivalently 60 snapshots of the Bolshoi simulation output, as B11 and G13 have used. Note that we only search for additions to the prior sample across this redshift range to increase the number of systems that could

[5]Note that G13 does weigh the consequences of including any number of subhalos in their selection criteria for their prior sample. They found insignificant changes to the resulting MW and Local Group mass when considering exactly two MC subhalo analogs versus any number of subhalos in their analysis.

be analogs of the MW/M31 at present day. We find 19,653 systems over this redshift range that satisfy the selection criteria (**C**). Throughout the rest of this work, we use only this sample of host-satellite analogs (the prior PDF, $P(\theta)$ in Eq. 3.6) to find the probability distribution of host halo mass.

There are several differences in the selection criteria for specific satellite properties in G13, B11, and in this work that should be noted. First, we alter the value of v_{max} used for the lower bound on the prior sample. We have increased this value from 50 km s^{-1} to 70 km s^{-1} because $\sim$ 70 km s^{-1} corresponds to the maximal circular velocity for an $8 \times 10^{10}\,M_\odot$ halo approximated with an NFW density profile. Since $8 \times 10^{10}\,M_\odot$ is the lower mass bound on our massive satellite analogs sample in Paper I from abundance matching, we also use it here for consistency.

An extra mass floor, which requires each subhalo to be at least $10^{10}\,M_\odot$ at $z = 0$, is also imposed since observations show that the dynamical masses of both the LMC and M33 are greater than this value (e.g., Corbelli, 2003; Majewski et al., 2009; Saha et al., 2010; Corbelli and Salucci, 2000; van der Marel and Kallivayalil, 2014).

Finally, we require each massive satellite to be within the virial radius of its host instead of within 300 kpc (G13/B11 method). Since the virial radius evolves with time, we choose this criteria instead of an arbitrarily fixed position. In all, the method described here includes as much known information about the true properties of the LMC and M33 to infer host halo mass with the simulation data while leaving the host halo mass itself (M_{vir}) as a free parameter.

The distribution of properties for all host-satellite systems in the prior can be seen in Fig. 3.2. All pairs of observable parameters are plotted for the satellite subhalos and each point is colored by the corresponding host halo mass from Illustris-Dark. Notice that the colorbar encompasses more than two orders of magnitude for host halo mass. The LMC and M33 are indicated by a black circle and square, respectively, on each panel. The value of j^{obs} for M33 seems to indicate that it should reside in a higher host halo mass than the LMC, while r^{obs} and v_{tot}^{obs} do not illustrate the same trend. Therefore, we generally expect satellites with higher total angular momenta to reside in higher mass host halos. Our subsequent analysis

allows for the combination of satellite properties to statistically infer the most likely host halo masses.

Likelihood

In Eq. 3.6, $P(\mathbf{d}|\,\boldsymbol{\theta})$ is the sampling distribution of the measured data $\mathbf{d}$ given the physical parameters $\boldsymbol{\theta} = \{\mathbf{x},\ M_{vir}\}$. However, this only depends on the true values of the observables $\mathbf{x}$, and the measurement error distribution. Equivalently, given $\mathbf{x}$, the data $\mathbf{d}$ is conditionally independent from M_{vir}. The individual satellite properties for the LMC and M33 are treated as independent measurements as the covariance between the observed position and velocity of a given satellite was shown to be significantly smaller than the variances on the measurements in B11. Therefore, $P(\mathbf{d}|\,\boldsymbol{\theta}) = P(\mathbf{d}|\,\mathbf{x})$. When viewed as a function of the parameters with the observed data fixed, this factor is the joint likelihood function, $\mathcal{L}(\boldsymbol{\theta}|\,\mathbf{d}) = \mathcal{L}(\mathbf{x}|\,\mathbf{d})$. $\mathcal{L}(\mathbf{x}|\,\mathbf{d})$ is simply a product over the individual data, d_i:

$$\mathcal{L}(\mathbf{x}|\,\mathbf{d}) = P(\mathbf{d}|\,\mathbf{x}) = \prod_{i}^{m} P(d_i|\,x_i), \tag{3.7}$$

We construct two different likelihoods that each utilise a different set of satellite properties. One main difference between the likelihood function in G13/B11 and this paper is that they build a joint likelihood based on the existence of two massive satellites (analogs of the MCs) and their subsequent observed properties (such that $m = 6$ properties), whereas we only require host halos to have one massive satellite (and thus $m = 3$ properties for the instantaneous method and $m = 2$ for the momentum method). We do not include more than one massive satellite in this analysis because we generalize this method for application to both the MW and M31.

Furthermore, for the MW's mass estimate, if we require all prior halos to contain both an LMC and SMC analog, the sample size effectively reduces to approximately zero. As we discuss in Section 3.5.2, the rarity of the LMC's (and SMC's) current orbital configuration alone reduces the number of halos in the prior that contribute to the inference scheme. Additionally, simply requiring host halos to contain MC

analogs based on the three observed properties discussed above does not account for the binarity and shared orbital trajectories of the MCs, so we omit these criteria and the SMC from this analysis.

I. Instantaneous Likelihood

The Instantaneous Likelihood uses as the observable parameters $\mathbf{x}$: the satellite's maximum circular velocity $\mathrm{v_{max}}$, its separation r from the host, and the total velocity today relative to the host galaxy $\mathrm{v_{tot}}$. The data $\mathbf{d}$ are the observed measurements of these quantities (Table 3.1).

$$\mathcal{L}(\mathbf{x}|\,\mathbf{d}) = \mathrm{N}(\mathrm{v_{max}^{obs}}|\,\mathrm{v_{max}}, \sigma_{\mathrm{v}}^2) \times \mathrm{N}(\mathrm{r^{obs}}|\,\mathrm{r}, \sigma_{\mathrm{r}}^2) \times \mathrm{N}(\mathrm{v^{obs}}|\,\mathrm{v_{tot}}, \sigma_{\mathrm{v}}^2), \tag{3.8}$$

where

$$\mathrm{N}(\mathrm{y}|\,\mu, \sigma) = \frac{1}{\sqrt{2\pi\sigma^2}} \exp\left[\frac{-(\mathrm{y}-\mu)^2}{2\sigma^2}\right]. \tag{3.9}$$

is a Gaussian probability density for random variable y with mean μ and variance σ^2. The σ quantities are the standard deviations of the measurement errors of the corresponding observations. We use this likelihood to compare with the results of G13 and B11.

II. Momentum Likelihood

Our second method for computing the joint likelihood uses a different subset of the satellite parameters $\mathbf{x}$ and data $\mathbf{d}$, focusing more on orbital dynamics. Our Momentum Likelihood is based on only two parameters: the satellite's $\mathrm{v_{max}}$ and the magnitude of its orbital angular momentum, j. Fig. 3.2 demonstrates that these properties are also only very weakly covariant, so they can be approximated as independent measurements. The angular momentum likelihood is therefore,

$$\mathcal{L}(\mathbf{x}|\,\mathbf{d}) = \mathrm{N}(\mathrm{v_{max}^{obs}}|\,\mathrm{v_{max}}, \sigma_{\mathrm{v}}^2) \times \mathrm{N}(\,\mathrm{j^{obs}}|\,\mathrm{j}, \sigma_{\mathrm{j}}^2), \tag{3.10}$$

where j is the magnitude of the orbital angular momentum vector. The mean and the standard deviation on j (i.e. $\mathrm{j^{obs}}$ and σ_{j}) for the LMC and M33 are computed

from the 10,000 Monte Carlo samples described in Section 3.3.1.

Since orbital angular momentum is generally stable over time compared to other orbital parameters, we investigate how closely this likelihood construction agrees with the B11 method. We still use the same draws from the Illustris-Dark halo catalog as described in Section 3.3.2 as the prior, but we change how the importance sampling weights are computed from the likelihood, as described below.

Importance Sampling

Now that the prior and likelihood have been defined, we return to Bayes' theorem

$$\mathrm{P}(\mathbf{x}, \mathrm{M_{vir}}|\,\mathbf{d}, \mathbf{C}) \propto \mathrm{P}(\mathbf{d}|\,\mathbf{x}) \times \mathrm{P}(\mathbf{x}, \mathrm{M_{vir}}|\,\mathbf{C}), \tag{3.11}$$

where we explicitly denote the dependence on the prior selection criteria $\mathbf{C}$.

With the prior and likelihoods defined, the marginal distribution of $\mathrm{M_{vir}}$ and therefore the posterior distribution for the halo mass of the MW and M31 can now be computed using this form of Bayes' theorem.

The posterior PDF is computed using a technique called importance sampling. In importance sampling, a set of samples is drawn from an importance sampling function and weighted accordingly while calculating integrals over the posterior PDF (see B11 and references therein). The importance sampling function is chosen to be the prior PDF, as in B11, so that our weights are proportional to the likelihoods. Using these importance weights, we can calculate integrals summarising the posterior PDF for our target parameter – the host galaxy's halo mass. These integrals describe the mean halo mass, credible intervals surrounding the mean, and a representation of the marginal posterior PDF for host halo mass, Eq. 3.5 (in the form of counts per $\mathrm{dM_{vir}}$).

Expectations of functions of the physical parameters under the posterior PDF are approximated as sums over the n samples as follows:

$$\begin{aligned}\int \mathrm{f}(\boldsymbol{\theta})\mathrm{P}(\mathbf{x}, \mathrm{M_{vir}}|\,\mathbf{d}, \mathbf{C})\,\mathrm{d}\boldsymbol{\theta} &= \frac{\int \mathrm{f}(\boldsymbol{\theta})\mathrm{P}(\mathbf{d}|\,\mathbf{x})\mathrm{P}(\mathbf{x}, \mathrm{M_{vir}}|\mathbf{C})\,\mathrm{d}\boldsymbol{\theta}}{\int \mathrm{P}(\mathbf{d}|\,\mathbf{x})\mathrm{P}(\mathbf{x}, \mathrm{M_{vir}}|\,\mathbf{C})\,\mathrm{d}\boldsymbol{\theta}} \\ &\approx \frac{\sum_j^n \mathrm{f}(\boldsymbol{\theta}_\mathrm{j})\mathrm{P}(\mathbf{d}|\,\mathbf{x}_\mathrm{j})}{\sum_j^n \mathrm{P}(\mathbf{d}|\,\mathbf{x}_\mathrm{j})}.\end{aligned} \tag{3.12}$$

The denominator of this equation is the normalization constant. If the chosen $f(\theta)$ depends only on $\mathrm{M_{vir}}$, then the final sum implicitly computes an expectation with respect to the marginal posterior of $\mathrm{M_{vir}}$:

$$\begin{aligned}\int \mathrm{f(M_{vir})P(M_{vir}|\,\mathbf{d},\mathbf{C})\,dM_{vir}} & \\ &= \int \mathrm{f(M_{vir})\,P(\mathbf{x},M_{vir}|\,\mathbf{d},\mathbf{C})\,d\mathbf{x}\,dM_{vir}} \\ &\approx \frac{\sum_j^n \mathrm{f(M_{vir}^j)\,P(\mathbf{d}|\,\mathbf{x}_j)}}{\sum_j^n \mathrm{P(\mathbf{d}|\,\mathbf{x}_j)}} \\ &= \sum_j^n \mathrm{f(M_{vir}^j)\,w_j}\end{aligned} \tag{3.13}$$

where $\mathrm{w_i = P(\mathbf{d}|\,\mathbf{x}_i)/\sum_j^n P(\mathbf{d}|\,\mathbf{x}_j)}$ are importance weights. The weights derived from the likelihood function represent the degree to which subhalo properties in Illustris-Dark resemble the observed properties of the LMC and M33 and consequently how much each halo contributes to the posterior probability density function (PDF) for the halo mass of the MW or M31.

Setting $f(\boldsymbol{\theta}) = \mathrm{M_{vir}}$ gives the posterior mean value for host halo mass of the MW or M31. To create a representation over the full posterior PDF, Eq. 3.13 is computed for contiguous intervals in host halo mass. For example, to calculate the posterior probability that the host halo mass is between $1 - 1.5 \times 10^{12}\,\mathrm{M_\odot}$, set $f(\mathbf{x}) = 1$ for all Illustris-Dark halos in the prior that satisfy this fiducial range or let $f(\mathbf{x}) = 0$ otherwise. Repeating this method for many fiducial halo mass ranges results in a coarsely sampled representation of the posterior PDF in a histogram-like fashion. For more details on how we create a smooth representation of the posterior PDFs, see Appendix B.2, which describes the kernel density estimation technique used here.

In practice, it is more convenient to compute and report summaries on a log scale, i.e. $\mathrm{P(\log_{10} M_{vir}|\mathbf{x},\mathbf{C})}$[6] rather than $\mathrm{P(M_{vir}|\mathbf{x},\mathbf{C})}$. This is because the former is more roughly Gaussian, and thus more easily summarised by a central value and width, whereas the latter is non-Gaussian with a skewed right tail. Hence, we

[6] $\mathrm{\log_{10} M_{vir}}$ should be interpreted as $\mathrm{\log_{10}(M_{vir}/M_\odot)}$.

summarise the posterior PDF of $\log_{10} M_{vir}$ with its posterior mean and 68 per cent highest posterior density credible intervals. When we report the mass estimates on a physical scale as $M_{vir} = X^{+U}_{-L} M_{\odot}$, these should be interpreted on a log scale, such that $\log_{10}X$ is the posterior mean of $\log_{10} M_{vir}$, and $[\log_{10}(X - L), \log_{10}(X + U)]$ is the 68 per cent credible interval in $\log_{10}M_{vir}$ with the highest posterior density[7].

3.4 MW and M31 Mass Results From Massive Satellite Properties

Following the statistical method described in Section 3.3, we present the posterior distributions for the halo mass of the MW and M31 based on the dynamics of their most massive satellites. The posterior distributions have been computed for two different likelihood functions (instantaneous vs. momentum; Section 3.3.2). We also examine the robustness of the two methods as a function of time and satellite orbital history.

3.4.1 Bayesian Inference with Instantaneous Satellite Kinematics

From the observed data in Table 3.1 ($v_{max}^{obs}, r^{obs}, v_{tot}^{obs}, j^{obs}$) and the statistical method described above, we find posterior mean values for the most likely halo mass of the MW and M31. Fig. 3.3 shows the posterior distribution of the resulting MW and M31 halo masses using the observed properties of the LMC and M33, respectively, as inputs to the instantaneous likelihood function (Eq. 3.8). The individual curves represent the posterior PDFs based on specific satellite parameters. For example, posteriors are calculated based on the full prior sample (blue), v_{max} (red), r (orange), v_{tot} (green), and all satellite properties combined (black).

For the host halos weighted for subhalo properties most like the LMC, we find that the preferred halo mass for the MW is $M_{vir} = 1.70^{+1.33}_{-0.52} \times 10^{12} M_{\odot}$ (top panel of Fig. 3.3). Applying the same rationale using the properties of M33, we find the

[7]We caution that these summaries on the log scale should not be naively translated to constraints on the linear scale. For example, the posterior mean of $\log_{10} M_{vir}$ is generally not equivalent to the $\log_{10}$ of the posterior mean of M_{vir}, as probability densities do not trivially transform under a nonlinear change of variables.

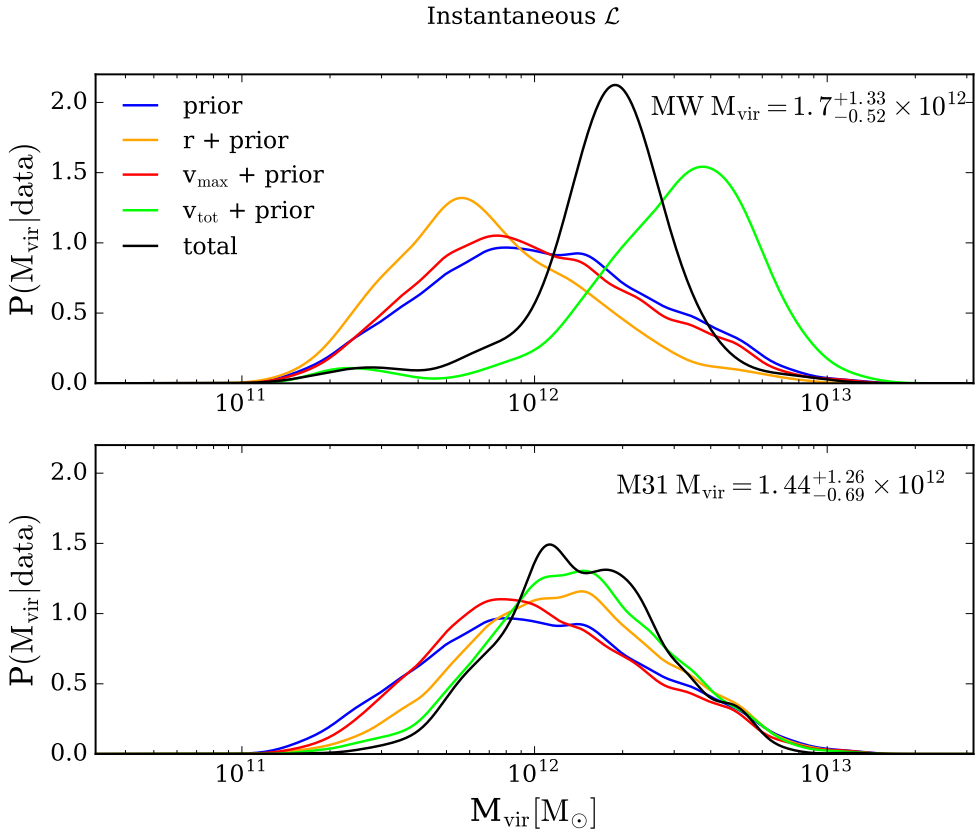

Figure 3.3: The posterior distribution of the MW (top) and M31's (bottom) halo mass inferred from the properties of their brightest and most massive satellites, the LMC and M33. The solid lines show the posterior PDFs calculated with the Illustris-Dark halo catalog based on the following properties: (a) the existence of exactly one satellite with $v_{max} > 70$ km s^{-1}, a $z = 0$ dark matter mass $\geq 10^{10}\,M_\odot$, and residing within the virial radius of its host (blue), (b) the maximum circular velocities v_{max} of the LMC or M33 (red), (c) the distance of the satellite from the center of its host (orange), (d) the velocity of the satellite relative to the host (green), and (e) all of these properties. The set of host-satellite halos drawn from the Illustris-Dark halo catalog passing the selection criteria (**C**) give a combined (black solid line) MW halo mass $M_{vir} = 1.70^{+1.33}_{-0.52} \times 10^{12}\,M_\odot$, or $\log_{10} M_{vir} = 12.23^{+0.25}_{-0.16}$ (68 per cent credible interval). Using the instantaneous position and velocity of M33, the halo mass of M31 is $M_{vir} = 1.44^{+1.26}_{-0.69} \times 10^{12}\,M_\odot$, or $\log_{10} M_{vir} = 12.16^{+0.27}_{-0.28}$ (68 per cent credible interval).

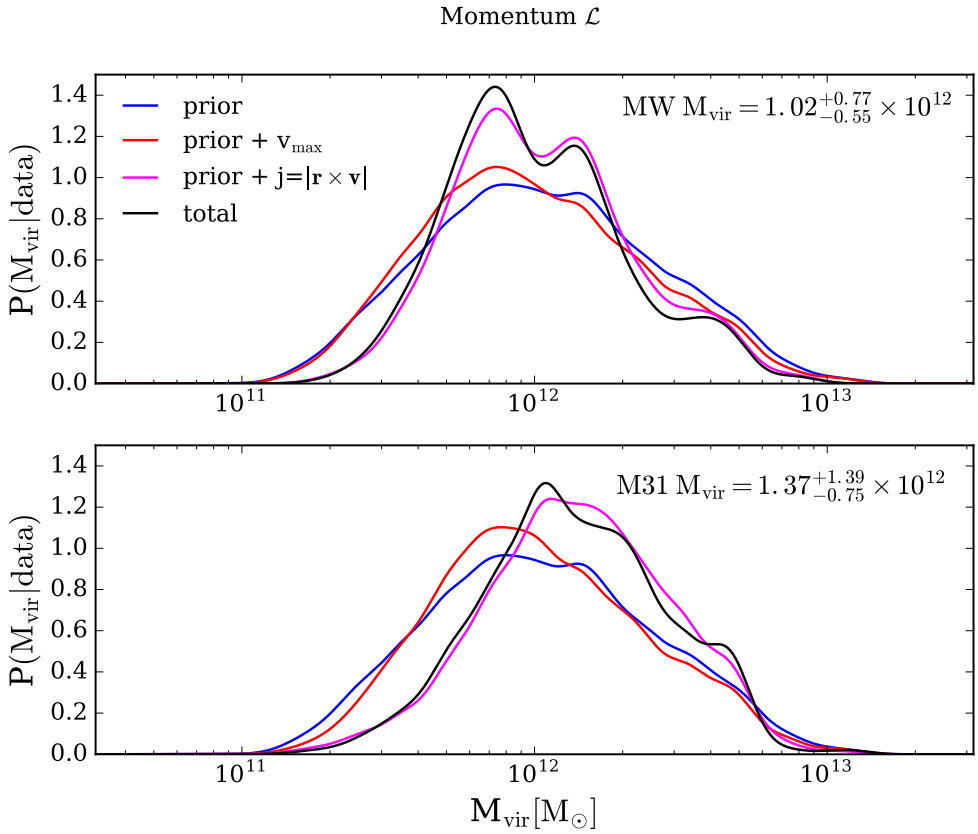

Figure 3.4: The posterior PDFs for the inferred halo mass of the MW (top) and M31(bottom) based on (a) the existence of exactly one satellite with $v_{max} > 70$ km s^{-1}, a $z = 0$ dark matter mass of $\geq 10^{10}\,M_\odot$, and residing within the virial radius of its host (blue), (b) the maximum circular velocities v_{max} of the LMC or M33 (red), (c) the magnitude of orbital angular momentum (magenta) for the satellite, and (d) all of these properties combined (black). The total posterior PDF infers a MW halo mass $M_{vir} = 1.02^{+0.77}_{-0.55} \times 10^{12}\,M_\odot$, or $\log_{10} M_{vir} = 12.01^{+0.25}_{-0.34}\,M_\odot$ (68 per cent credible interval). Using the orbital angular momentum of M33, the halo mass of M31 is $M_{vir} = 1.37^{+1.39}_{-0.75} \times 10^{12}\,M_\odot$ (bottom), or $\log_{10} M_{vir} = 12.12^{+0.32}_{-0.35}$ (68 per cent credible interval). In contrast to the results of Fig. 3.3, here hosts of M33 satellites are found to be more massive than those that host satellites with properties similar to the LMC. In general, the momentum method also results in broader constraints on the mass of the MW and M31, respectively.

most typical host halo mass for M31 is $M_{vir} = 1.44^{+1.26}_{-0.69} \times 10^{12}\, M_{\odot}$ (bottom panel of Fig. 3.3). Interestingly, the inferred mean value for the MW is higher than that of M31. This is likely due to the high relative velocity of the LMC today compared to that of M33, thereby suggesting that the instantaneous method is not reliable. The link between satellite orbital phase and the resulting host halo mass estimates will be discussed in further detail in Section 3.5.1.

Comparing the two host-satellite systems, we find that the inferred halo mass is highly correlated to the uniqueness of the combined observed satellite parameters (Table 3.1). Since the LMC has a small relative separation and a high velocity relative to the MW at present day, the total posterior (black solid line) for the MW's halo mass is approximately centered between the contributions from the position (orange solid line) and velocity (green solid line) posteriors. M33's present-day position and velocity are much more typical in a population of massive satellites (see top left panel of Fig. 3.2), so we find that the individual and total posteriors are all in good agreement with each other.

While our prior is composed of ∼20,000 halos, it is important to know how many of these halos actually contribute to this statistical inference. Table 3.2 indicates how many halos in the prior host subhalos with properties within an average of 1σ and 2σ on the observed properties of the LMC and M33, respectively. The final column shows the effective sample size (ESS) of each likelihood method for each of the satellites. The ESS is the number of halos that actually statistically contribute to the importance sampling and therefore most heavily influence the posterior PDF of host halo mass. See Appendix B.2 for more details.

As the instantaneous properties of the LMC today (v_{max}, r, v_{tot}) are rare, very few halos in the Illustris-Dark prior host LMC analogs that exhibit this specific combination of observed satellite properties. Consequently, the ESS is low and few halos statistically determine the posterior halo mass of the MW for the instantaneous likelihood method. To determine the sampling noise on the inferred MW mass with the instantaneous likelihood method, we create 25 bootstrap resampled mock catalogs from the original prior described in Section 3.3.2 and recompute the MW's

Table 3.2: The number of halos in the prior that contribute to the statistical inference. A total of 19,563 halos are considered for the analysis. The second column lists the number of halos with massive satellites within an average of 1σ on the subset of observed properties for the LMC and M33 used in the instantaneous (v_{max}, r, v_{tot}) and momentum (v_{max}, j) likelihood methods. The third column provides the number of halos with satellites exhibiting properties within the 2σ range of the observed values used for both likelihoods. The final column provides the effective sample size (ESS, see Eq. B.2), which is the number of statistically relevant halos for importance sampling.

	1σ	2σ	ESS
MW/LMC Instantaneous	10	56	42
M31/M33 Instantaneous	503	5,902	3,033
MW/LMC Momentum	971	3,459	3,465
M31/M33 Momentum	1,347	8,017	8,143

mass using the instantaneous likelihood method. By doing so, we can separate how much additional uncertainty on the posterior mean mass of the MW comes from the Monte Carlo error caused by a small ESS. The standard deviation of the posterior mean MW mass from the 25 mock catalogs is $0.13 \times 10^{12}\,M_{\odot}$. For the instantaneous likelihood method using M33's observed properties, we find that there is minimal ($0.01 \times 10^{12}\,M_{\odot}$) additional uncertainty associated with the posterior mean mass of M31 due to a small ESS. The ESS is significantly high as M33's observed instantaneous properties are not rare like the LMC's.

Implications for Different M31 Proper Motion Measurements and the Instantaneous Method

In Paper I, we explored the implications for different values of M31's proper motion component on the orbital history of M33. We use the M31 proper motion reported by vdM12 throughout Paper I and this work. The vdM12 results are an extension of the direct measurement of M31's proper motion with HST by S12 such that vdM12's measurement is a weighted average of the proper motion inferred from the kinematics of M31 satellites and the S12 direct measurements (see also van der Marel and Guhathakurta, 2008). They find a combined proper motion of $v_{tan} = 17 \pm 17$

km s^{-1} .

Other teams have also measured the proper motion of M31 using different techniques. Salomon et al. (2016, hereafter S16) recently inferred the tangential proper motion of M31 using the motions of its satellites and find a value of $v_{tan} \sim 150$ km s^{-1} . Here, we compute the posterior distributions for M31's halo mass where v_{tot}^{obs} and σ_v from Table 3.1 are changed to reflect the total velocity of M33 relative to M31 using the M31 proper motion measured by each of S12 and S16 independently.

Using only the S12 M31 proper motion, rather than the average vdM12 reported value, M33's velocity relative to M31 becomes $v_{tot}^{obs} = 242$ km s^{-1} and $\sigma_v = 76$ km s^{-1} . The mean M31 halo mass inferred using these velocity values is $M_{vir} = 1.48^{+1.70}_{-0.77} \times 10^{12}\,M_\odot$. As expected, the mean value and 68 per cent credible interval of M31's halo mass increases compared to the top panel of Fig. 3.3 since v_{tot}^{obs} and σ_v both increase.

For the S16 tangential velocity, $v_{tot}^{obs} = 139$ km s^{-1} and $\sigma_v = 52$ km s^{-1} , which is substantially lower than both the value listed in Table 1 and the S12 results. Using these values as inputs to the instantaneous likelihood function (Eq. 3.8), we find that M31 $M_{vir} = 1.03^{+0.82}_{-0.55} \times 10^{12}\,M_\odot$. The decrease in total velocity reduces the posterior mean mass for M31 significantly and the 68 per cent credible interval also shifts towards lower values. Overall, both of the mean values resulting from the two different tangential velocity measurements are encompassed within the 68 per cent credible interval of the original posterior mean mass of M31 determined with the properties listed in Table 3.1 and the instantaneous likelihood method. However, these results seem to favor the S12 HST proper motions over the S16 results.

3.4.2 Bayesian Inference with Angular Momentum

We have now replaced the posterior distributions in instantaneous position and velocity by a single posterior describing the orbital angular momentum (Section 3.3.2). The posterior distributions resulting from the orbital angular momentum likelihood function are shown in Fig. 3.4. The posterior distributions are shown based on the prior (blue), v_{max} (red), j (magenta), and all of those properties combined (black).

By weighting the host halos based on the LMC's properties, we find that the most typical halo mass for the MW is $M_{vir} = 1.02^{+0.77}_{-0.55} \times 10^{12}\,M_{\odot}$ (top panel). Weighting the host halos by M33's properties, we find the most typical halo mass for M31 is $M_{vir} = 1.37^{+1.39}_{-0.75} \times 10^{12}\,M_{\odot}$ (bottom panel).

In this likelihood construction, the halo masses for the MW and M31 are as expected, with M31 being more massive (see Section 3.1). Overall, the two methods agree in that the inferred host halo masses and errors still encompass the same broad range of mass from the literature. For the MW's mass, the combination of position and velocity versus angular momentum causes more drastic differences in the posterior *mean* values for halo mass compared to the results for M31. This disparity is likely due to the short-lived current position and velocity of the LMC versus its orbital angular momentum, which is fairly common amongst massive satellite analogs. We will further explore the change in inferred MW mass as a function of the LMC's orbital history in Section 3.4.3.

Unlike the instantaneous method, we find that there is insignificant additional uncertainty on the posterior mean mass of the MW and M31 with the momentum likelihood method due to Monte Carlo error ($\sim 0.01 \times 10^{12}\,M_{\odot}$). For both host-satellite systems, the ESS is significantly high (see Table 3.2) and the 25 bootstrap resampled mock catalogs provide results that are in very good agreement with those from the original prior.

Implications for Different M31 Proper Motion Measurements and the Momentum Method

We now repeat our momentum method calculations for the mass of M31 using the tangential velocities reported by S12 and S16, respectively. Using the S12 v_{tan} value, we have repropagated the errors in distance, radial velocity, and proper motion to calculate a total orbital angular momentum value of $j^{obs} = 28,940$ kpc km s^{-1} with $\sigma = 10,062$ kpc km s^{-1}. With this j^{obs} value and its associated error, the inferred mass of M31 is $M_{vir} = 1.33^{+1.44}_{-0.74} \times 10^{12}\,M_{\odot}$. This result is in very good agreement with the vdM12 results listed above, as expected, since the vdM12 value is derived

from S12.

For the S16 v_{tan} value, the average of the total observed angular momentum is $j^{obs} = 28,278$ kpc km s^{-1} with $\sigma = 3,739$ kpc km s^{-1}. These properties yield an M31 mass of $M_{vir} = 1.65^{+1.58}_{-0.84} \times 10^{12}\, M_{\odot}$. This is the highest M31 mass inferred thus far in this work, and it does not strictly conform to the trend we observed with M33 and the LMC earlier in Section 3.3.2, where the satellite with higher orbital angular momentum suggests a higher host halo mass. The S12 v_{tan} value provides the highest total orbital angular momentum for M33 (though only by a few percent) but it does not result in the highest corresponding M31 mass. A more precise direct measurement of M31's proper motion will better constrain v_{tan} and therefore j^{obs}, thereby providing more precise measurements of M31's mass in a statistical fashion.

A summary of all posterior mean halo masses included in the 68 and 90 per cent credible intervals for the MW and M31 are presented in Table 3.3.

Table 3.3: The values for posterior halo mass of the MW and M31 included at the 68 and 90 per cent credible intervals for all likelihood functions explored in this analysis.

	MW M_{vir} $[10^{12}\ M_\odot]$		**M31** M_{vir} $[10^{12}\ M_\odot]$	
	68 per cent	90 per cent	68 per cent	90 per cent
Instantaneous $\mathcal{L}$	$1.70^{+1.33}_{-0.52}$	$1.70^{+2.89}_{-1.07}$	$1.44^{+1.26}_{-0.69}$	$1.44^{+2.74}_{-0.95}$
Sohn et al. (2012) M31 v_{tot}	–	–	$1.48^{+1.70}_{-0.77}$	$1.48^{+3.55}_{-1.0}$
Salomon et al. (2016) M31 v_{tot}	–	–	$1.03^{+0.82}_{-0.55}$	$1.03^{+2.03}_{-0.71}$
Momentum $\mathcal{L}$	$1.02^{+0.77}_{-0.55}$	$1.02^{+2.4}_{-0.70}$	$1.37^{+1.39}_{-0.75}$	$1.37^{+3.67}_{-0.91}$
Sohn et al. (2012) M31 v_{tot}	–	–	$1.33^{+1.44}_{-0.74}$	$1.33^{+3.74}_{-0.9}$
Salomon et al. (2016) M31 v_{tot}	–	–	$1.65^{+1.58}_{-0.84}$	$1.65^{+3.83}_{-1.04}$

3.4.3 The Bayesian Inference Technique as a Function of Time

Thus far, the posterior distributions for the halo mass of the MW and M31 resulting from both likelihood functions have been calculated using only the observed properties of the LMC and M33 today. Orbital timescales of massive satellites are typically about 5-6 Gyr (see Paper I for orbits of the LMC and M33) and satellites will exhibit a range of positions and velocities during a single orbital period. Some satellites experience more variation than others depending on their host environment, eccentricity, and impact parameter at infall. We have already shown that satellite orbital angular momentum remains fairly well-conserved during that time in Section 3.2.2, aside from some angular momentum loss between infall and today due to dynamical friction. In this section, we test the robustness of the instantaneous and momentum likelihood methods as a function of time using the numerically integrated orbital histories of the LMC from Paper I.

We consider two orbital histories for the LMC – one in a low mass MW halo ($10^{12}\,M_\odot$) and one in a high mass MW halo ($1.5 \times 10^{12}\,M_\odot$). Both orbital histories represent an average of orbits computed using an LMC mass range of $3-25\times10^{10}\,M_\odot$ and the mean position and velocity of the LMC. In the low mass MW halo, the LMC is on first infall into the MW's halo. In the higher mass halo, it has achieved a pericenter about 5 Gyr ago and remains within the virial radius of the low mass MW model (261 kpc) for the entirety of the last 6 Gyr. Full details for these orbital models can be found in Paper I.

In intervals of 0.25 lookback Gyr, we recompute the posterior distribution for the MW's halo mass using both the instantaneous and momentum methods with the properties of the LMC at each time interval along its integrated orbital trajectory. The calculations for $t = 0$ lookback Gyr were computed with the LMC's properties listed in Table 3.1 and were already summarized in Section 3.4. This process is repeated until 3.25 Gyr ago using the position and velocity (instantaneous likelihood) or orbital angular momentum (momentum likelihood) of the LMC. We terminate the analysis at $\sim$3 Gyr ago because the host-satellite systems that constitute the

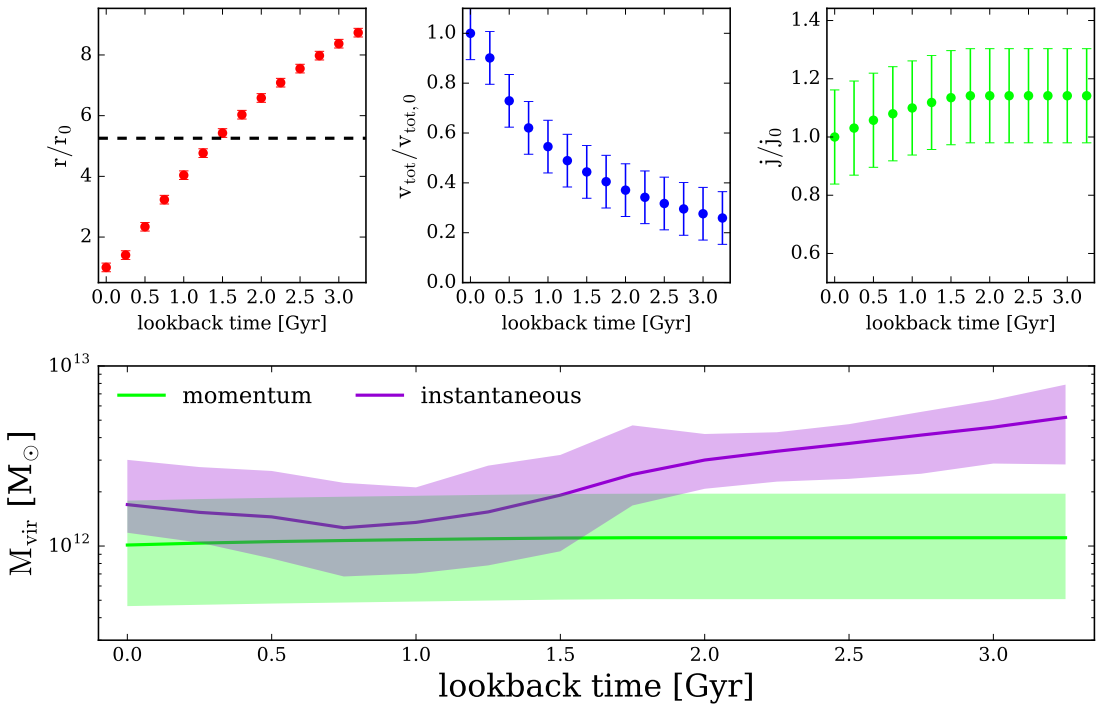

Figure 3.5: Posterior mean mass estimates for the MW based on the orbital history of the LMC using the two likelihood functions. The top left panel shows the average past orbital history for the LMC (as calculated in Paper I) when the MW's mass is held fixed at $10^{12}\,M_\odot$ with a virial radius of 261 kpc. This average orbital history encompasses an LMC mass range of $3-25\times10^{10}\,M_\odot$. The relative distance between the LMC and the MW is shown as a ratio with its current distance. The virial radius of the MW in the LMC orbital model is shown by the black dashed line. The top middle panel shows the velocity of the LMC along its orbit relative to its $z = 0$ velocity, while the top right-most panel shows the total orbital angular momentum of the LMC along its trajectory relative to its $z = 0$ value. The error bars for the panels in the top row are propagated to reflect HST's precision on the position and velocity of the LMC today. The bottom panel shows the resulting predictions for the mass of the MW using the instantaneous (purple) likelihood and the momentum (green) likelihood as a function of orbital configuration. When the LMC's orbit is outside of the virial radius ($>$ 1.5 lookback Gyr), the mass of the MW is naturally biased towards higher values. However, there is still a factor of two deviation in the results from the instantaneous method in just the last $\sim$ 1 Gyr, which is of order the current uncertainty in the MW's mass.

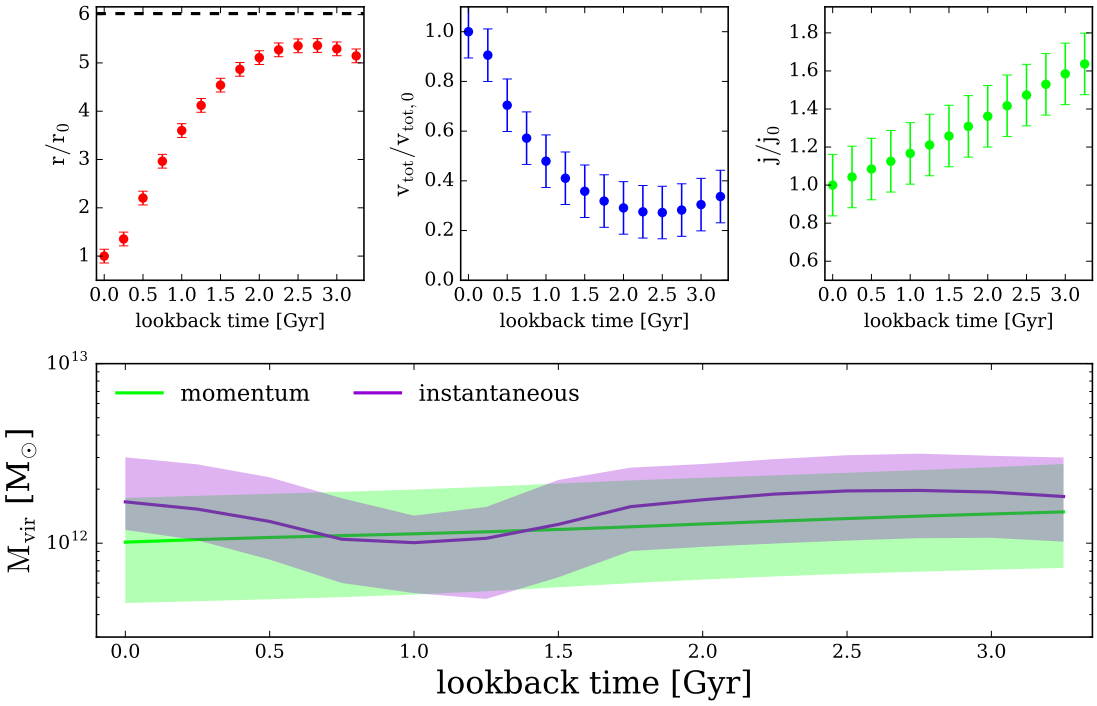

Figure 3.6: The posterior mean mass estimates for the MW are shown using the LMC's orbital history calculated with a fixed MW mass of $1.5 \times 10^{12}\,\mathrm{M}_{\odot}$ and a virial radius of 299 kpc. See Fig. 3.5 for more details. When the LMC is not on a first infall orbital trajectory, the instantaneous and momentum methods are in better agreement over time. However, there is still a factor of two deviation in the inferred mass of the MW with the instantaneous method, proving that it is highly sensitive to satellite orbital configuration.

prior have been chosen from a redshift range of $z = 0 - 0.26$ ($\sim$3 Gyr).

The evolution of the statistically inferred MW halo mass for the two different LMC orbital histories are shown in Figs. 3.5 and 3.6. The top left panel shows the evolution of the LMC's position relative to the MW as function of time, scaled to the LMC's position today ($r_0^{obs} = 50$ kpc). The top middle panel shows the velocity of the LMC along its orbit relative to its $z = 0$ velocity ($v_0^{obs} = 321$ km s^{-1}), while the top right panel shows the evolution of its total orbital angular momentum scaled to its value today ($j_0^{obs} = 27,656$ kpc km s^{-1}). Given these *observed* LMC properties at each interval in lookback time, the posterior mean MW halo mass included in the 68 per cent credible intervals are plotted in the bottom panels of Figs. 3.5 and 3.6 for the instantaneous (purple) and momentum likelihoods (green). The measurement errors for all quantities in the top panel are assigned to match the precision of the observed LMC properties today.

Fig. 3.5 shows that the posterior mean MW halo mass inferred by the instantaneous likelihood construction and a first infall scenario changes drastically as a function of time. In just 3 Gyr, the mean inferred MW mass varies from about 10^{12} at minimum to $\sim 4 \times 10^{12}$ M$_\odot$ at maximum. On the other hand, the posterior mean mass of the MW remains mostly constant at 1-1.1$\times 10^{12}$ M$_\odot$ when computed using the orbital angular momentum of the LMC as a function of time. The contrast between these two results clearly demonstrates how strongly the inferred mass of the MW can be biased by the satellite parameters, especially when those parameters change significantly with time. Therefore, while the LMC's position and velocity today yield a reasonable mass estimate for the MW that is in agreement with the MW mass inferred by the LMC's orbital angular momentum, this result largely hinges on the LMC's orbital phase at any given time and therefore its past orbital history.

Note that for the first infall scenario (Fig. 3.5), the LMC does not remain within the virial radius of the adopted MW mass model for all 3 lookback Gyr. However, the satellites in the prior from which the MW mass results are calculated are all chosen such that they reside within the virial radius of their host. Therefore, in the first infall scenario, MW mass estimates determined at times when the LMC is

outside of the virial radius ($>$ 1.5 lookback Gyr) are necessarily biased to high MW mass and thus deviate the most strongly. However, the inferred mass of the MW with the instantaneous method still varies by a factor of almost two in just the last $\sim$ 1 Gyr, which is of order the current uncertainty on the mass of the MW.

We have also checked that the ESS values for each time interval are sufficiently large (a few factors greater than the ESS at $t = 0$ lookback Gyr). As the position and velocity of the LMC become more common amongst the phase space of the subhalos in the prior, the ESS increases beyond $t = 0$ lookback Gyr. Therefore, the reported MW mass values included in the 68 per cent credible interval are statistically representative of the prior and not just an artifact of a low ESS value.

When the posterior mean masses of the MW are computed using a less energetic orbital history where the LMC has made a pericentric passage 5 Gyr ago, we find that the results are less dependent on any specific likelihood construction. Fig 3.6 demonstrates that the inferred posterior mean mass of the MW calculated with the instantaneous and momentum likelihoods are in much better agreement over time. However, the posterior mean mass of the MW inferred with the instantaneous method still varies by approximately a factor of two, whereas the momentum method provides consistent results with time. The 68 per cent curves for both constructions agree for a majority of the last 3 Gyr, demonstrating that the satellite's orbital trajectory is key to the robustness of these Bayesian techniques. We conclude that the instantaneous method is therefore less reliable for inferring host halo mass, regardless of the satellite's orbital energy, as was demonstrated by the two different LMC scenarios. Orbital 'constants' like orbital angular momentum prove to be more reliable with time, and thus the momentum method is preferred.

Satellites on high speed orbits will be most affected by this issue, though this may also hold true for satellites in lower energy orbits that are fairly eccentric. For example, Leo I, a MW dSph satellite that resides at a distance of about 260 kpc today, also appears to be on its first infall into the halo of the MW (Sohn et al., 2013). On such a high energy orbit, Leo I has proven to be an outlier as a tracer of the MW's mass thus far as it may or may not be gravitationally bound to the MW

at present. In a follow up paper (Patel et al. 2017c, in prep.), we apply the Bayesian inference scheme to Leo I and show that there is a disparity in the inferred mass estimates of the MW that is similar to that of the LMC's such that the instantaneous method results in a much higher MW mass estimate compared to the momentum method. Therefore, implementing two different likelihood functions is not only a test of how reliable satellite properties are to make such inference measurements for the MW's mass, but it also separates the satellites that are on high energy first infall orbits from those which are much more circular and less energetic.

Ultimately, we conclude that the Bayesian technique utilising the observed angular momentum of satellites could be a powerful method for determining host mass by using a *population* of satellites belonging to the same halo, rather than focusing on individual cases. The momentum method differentiates between low and high orbital angular momenta and therefore could provide insight into the host mass based on the fraction of low and high angular momenta satellites it hosts. We will apply the momentum method to several low mass MW satellites in future work to determine whether more accurate and precise constraints for the MW's mass can be determined from the phase space information of nine MW satellites.

3.5 Discussion

By computing the posterior probability distribution of the MW and M31's mass in several ways, we have explored how different orbital properties of massive satellites (LMC, M33) can provide insight on the most statistically significant halo mass of their hosts (MW, M31). Our first method takes the maximum circular velocity of the satellite, relative position, and relative velocity to determine the most probable halo mass of the MW and M31, respectively. By doing so, we find that the resulting halo mass distributions are fairly broad and in agreement with the current literature for both host-satellite systems, though they are biased by satellite orbital phase. By using satellite angular momentum as an input to the statistical scheme, we tend to find lower posterior mean values for the mass of the MW and M31 with slightly

broader credible intervals (in log space). However, this method is more consistent as a function of time.

In what follows, we discuss several caveats that are necessary to consider when combining high precision proper motions and cosmological simulations in a Bayesian statistical scheme. In particular, we focus on the bias introduced by the different orbital histories of the LMC and M33 individually. We also examine the specific case of M31's mass when we impose a close passage of M33 about M31 during the last few Gyr. Measurement error, cosmic variance error, and how they may affect the mass estimates of their hosts are also discussed. Finally, we compare our results to previous analyses.

3.5.1 Orbital Histories of the LMC and M33

The LMC is on a significantly different orbital trajectory than M33–it is just past pericenter in its orbit, whereas M33 appears to be just past apocenter of a long period orbit or on first infall (see Paper I). Given its current orbital configuration, the LMC is about four times closer to the MW than M33 is to M31 and the LMC has a total relative velocity that is more than two times the velocity of M33 with respect to M31. Thus, the LMC is on a high energy orbit at present where its position and velocity exhibit extreme values.

M33, however, is at a much more common place in its orbital trajectory in the context of massive satellite analogs. We found in Paper I that it appears to be approaching pericenter in the next few Gyr, so its current position and velocity are not rare compared to the positions and velocities of the satellites in the control sample, for example (see Fig. 3.1). As a result, the posterior distribution of M31's halo mass is more broad compared to that of the MW.

By using the orbital angular momentum of Illustris-Dark halos instead of their positions and velocities, we find similarly broad posterior halo mass distributions for both the MW and M31. Orbital angular momentum is not exclusive to a unique combination of one position and velocity vector, but rather a set of positions and a set of velocities. Thus, it is not surprising that the resulting posterior distributions

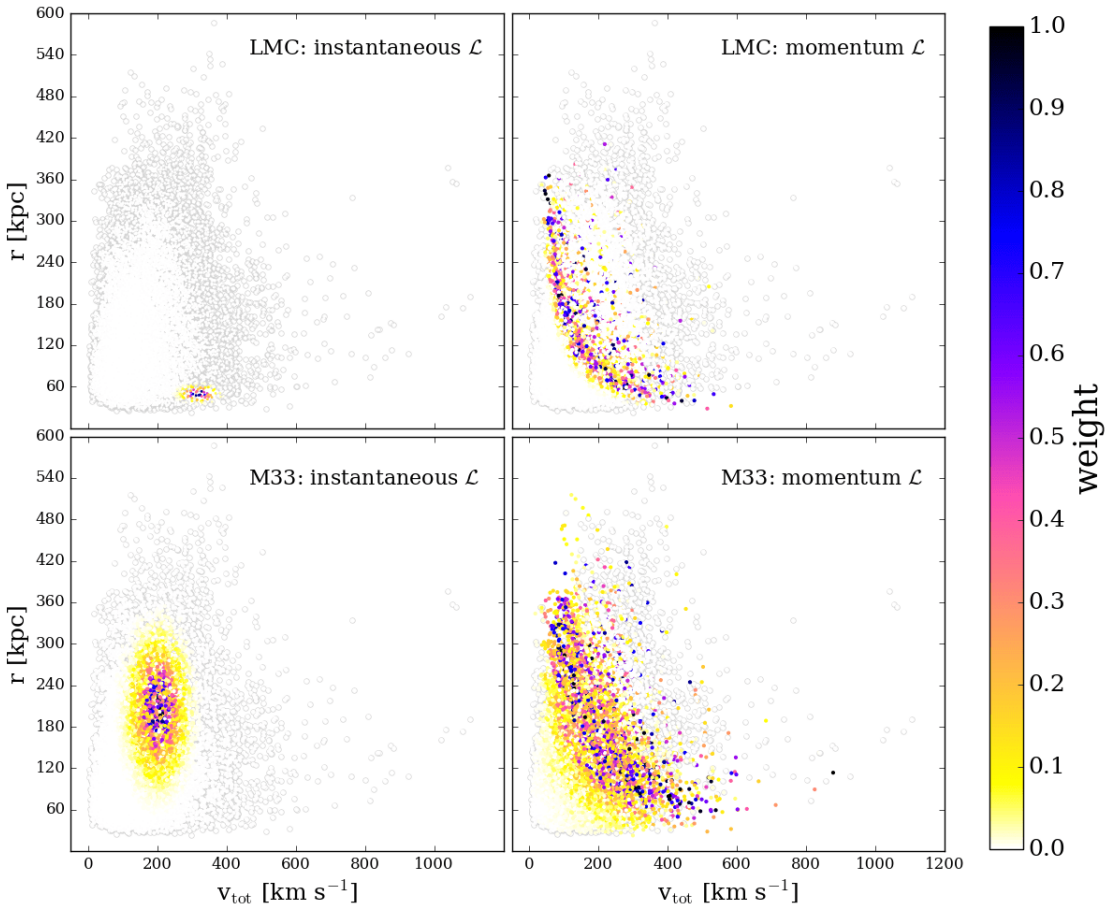

Figure 3.7: *Top:* The distribution of relative position and velocity for all Illustris-Dark host-satellite systems in the prior. The points are colored by the weight (w_i) assigned to each host halo, which represents how closely its associated subhalo resembles the current properties of the LMC. The weights are proportional to the respective likelihood functions and normalised here for easy comparison. The left panel shows the points colored by weights that are proportional to the instantaneous likelihood given by Eq. 3.8. The right panel shows the same points now colored by the weights proportional to the momentum likelihood given by Eq. 3.10. *Bottom:* The left and right panel are computed in the same fashion as the top row but now the points are weighted according to their similarity with M33's properties today. All points with a normalised weight < 0.025 have been colored white and are outlined in gray to easily distinguish between those host-satellite systems that are statistically significant to the inference scheme. The small fractions of colored points in the left column compared to the right demonstrates how significantly orbital phase can bias inferred host halo masses using the instantaneous method, as unique combinations of satellite position and velocity are less common in simulated analogs.

are more broad (and account for a larger fraction of phase space) than a posterior computed based on satellite position and velocity individually. In the case of the LMC, the two likelihood methods result in a noticeable difference in the shapes of the posterior PDFs, but for M33, both results are in good agreement with each other. We expect this is closely related to the rarity of the LMC's current orbital configuration.

To demonstrate how significantly the orbital phase of a satellite galaxy affects the inferred mass of its host, Fig. 3.7 shows the distribution of satellite position to satellite velocity for all host-satellite systems contained in the prior as a function of their likelihood weights for both the instantaneous and momentum likelihood functions. The weights (or color of the data point) in the top left panel are computed using the LMC's observed properties today (see Table 3.1) and the instantaneous likelihood function, while the bottom left panel shows the same distribution calculated with the properties of M33 today. In all panels, the weights are normalised so that the results of both (left and right panels) methods can be easily compared.

Notice that the uniqueness of the LMC's position and velocity at present yields far fewer points with a non-zero weight in the instantaneous likelihood construction. As M33's position and velocity are somewhat more common amongst the phase space of massive satellite analogs, a larger fraction of points have non-zero weights from the instantaneous likelihood. The number of colored points in each panel of Fig. 3.7 approximately corresponds to the ESS values listed in Table 3.2, which are representative of how many simulated halos actually host subhalos within the $\sim 2\sigma$ average of the LMC/M33's observed properties.

The right column of Fig. 3.7 is computed in a similar fashion, but uses the momentum likelihood construction given by Eq. 3.10. Far more satellites in the prior exhibit orbital angular momenta similar to the LMC or M33, however, a more significant fraction of the prior aligns with M33's current orbital angular momentum instead of the LMC's. Again, this is a result of the LMC and M33 residing at different orbital phases in their trajectories about their respective host galaxies. Therefore, it appears that the disparity between the results of the two likelihood methods is

Table 3.4: The orbital sample descriptions for the criteria used in Paper I to quantify the plausibility of a recent, close passage of M33 about M31. The ARP sample is the subset of all orbits where M33 has made a pericentric passage about M31 during the last 6 Gyr. TI6 refers to the further subset of orbits where M33 also fell into the modeled halo of M31 during the last 6 Gyr. Finally, the strictest sample (RP100T) is designed to match the M33 orbital models suggested by Putman et al. (2009) (see also McConnachie et al., 2009). The final column shows the average magnitude of specific orbital angular momentum for each sample. Here, the magnitude of the orbital angular momentum is computed using the initial M31-M33 position and velocity vectors for the orbital integrations. This table is adapted from Table 7 in Paper I.

Identifier	N_{peri}	t_{peri} [Gyr ago]	t_{inf} [Gyr ago]	r_{peri} [kpc]	avg. j^{obs} [kpc km s^{-1}]
ALL	–	–	–	–	27,656 ± 8,219
ARP	$\geq$1	≤ 6	–	–	23,094 ± 4,747
TI6	$\geq$1	≤ 6	≤ 6	–	22,113 ± 4,272
RP100T	$\geq$1	≤ 3	≤ 6	$r_{peri} < 100$	16,134 ± 1,118

much more drastic for satellites with a unique orbital configurations like the LMC.

Bayesian Inference with a Close Pericentric Passage

In Paper I, we discussed the plausibility that M33 made a pericentric approach about M31 of < 100 kpc during the last 3 Gyr. This type of orbit is typically used to explain the formation of the stellar and gas disk warps observed in the structure of M33 today (McConnachie et al., 2009; Putman et al., 2009). We calculated 10,000 orbits for M33 in the allowed proper motion and velocity error space of the M31-M33 system to find that fewer than 1 per cent (RP100T sample) of all allowed orbits satisfy these criteria. When we further restrict our analysis to those orbits that achieved a pericenter < 55 kpc, we found that zero orbits satisfied this criteria. Table 7 of Paper I describes the exact orbital criteria applied to narrow down these statistics.

Here we revisit our M31-M33 analysis from Paper I to identify what M31 halo mass is preferred using the orbital angular momentum associated with the conventional and newly ascribed M33 orbital histories. By using the mean and standard

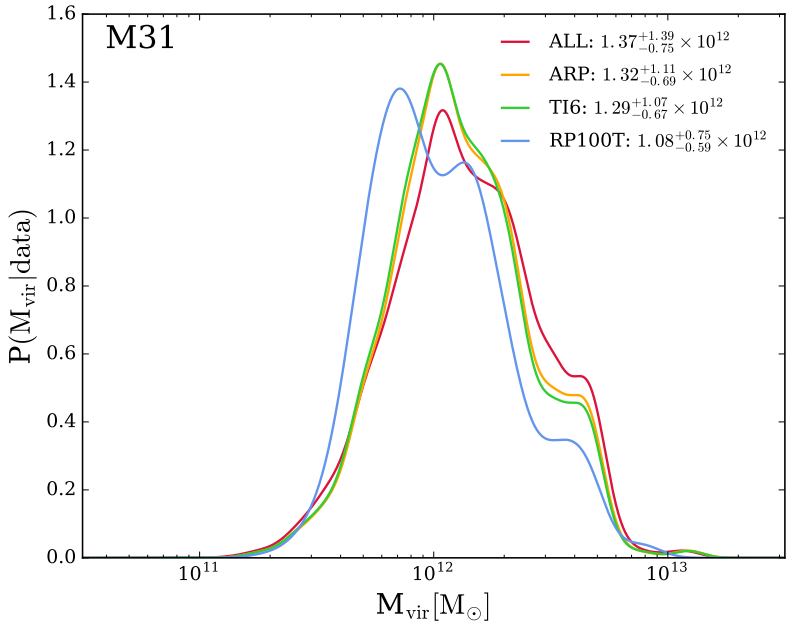

Figure 3.8: The posterior distribution for M31's halo mass based on the properties of M33. Using the orbital angular momentum of M33 about M31 and its approximate v_{max}^{obs} value from Table 3.1, we calculate the posterior distribution for M31's halo mass for each of the orbital samples described in Table 3.4. The likelihood function (Eq. 3.10) used to calculate importance weights from the prior takes the average orbital angular momentum and standard error for each sample as inputs. The RP100T criteria are designed to match the conventional M33 orbit involving a close (< 100 kpc), recent (< 3 Gyr) encounter between M31 and M33 (Putman et al., 2009; McConnachie et al., 2009), however, it yields the most discrepant M31 mass ($\sim 10^{12}\,M_\odot$). This value contradicts estimates from the timing argument and abundance matching, further supporting the new M33 orbital models presented in Paper I.

error on the angular momentum of each individual orbital sample described in Table 3.4 (adapted from Paper I), we can estimate the mass of M31, applying the Bayesian methodology described in Section 3.4.2. Therefore, momentum likelihoods are calculated for the prior such that the values of j^{obs} and σ_j are adjusted to reflect each orbital criteria sample.

In Fig. 3.8, the posterior distribution in red, which refers to the full orbital sample (ALL), is the least restrictive and is identical to the black posterior distribution in the bottom panel of Fig. 3.4. It encompasses all possible orbits of M33 in the allowed proper motion error space of the M31-M33 system. Each of the subsequent samples (orange, green, blue) requires one or more additional orbital parameters that further limits the value of the average angular momentum that goes into the momentum likelihood function. The ARP sample represents all orbits which show evidence of a pericentric passage in the last 6 Gyr. The TI6 sample is the subset of the ARP sample where M33 also fell into the halo of M31 in the last 6 Gyr. The most restrictive orbital criteria (RP100T) is constructed to match the orbits described in Putman et al. (2009) and McConnachie et al. (2009), which both suggest that M33 made a close passage (< 100 kpc) about M31 in the last 3 Gyr.

In general, the posterior mean value for M31's mass shifts to lower values and the width of the credible intervals narrows as more criteria are added. Notice that the strictest criteria, the RP100T sample (blue), favors a posterior mean M31 halo mass $\sim 10^{12}\,M_\odot$. This implies that if M33 really did achieve a distance of 100 kpc or less from M31 in the last $\sim$3 Gyr, then its corresponding orbital angular momentum suggests M31's mass would have to be quite low. We expect that the orbital angular momentum for an orbital sample that achieves a pericenter of 55 kpc or less would result in M31's mass being $< 10^{12}\,M_\odot$. However, we cannot directly test this hypothesis since none of our 10,000 numerical orbits achieved these criteria in Paper I, so the corresponding orbital angular momenta for such an orbit is unknown.

Our results are also supported by the cosmological analogs defined in Paper I. By extracting simulated orbital histories of massive satellite analogs that are capable of reaching such close pericentric distances recently, we found that they are likely to

have host halos with virial masses $\leq 1.5 \times 10^{12}\,M_{\odot}$. Generally, these cosmological and statistical results are also applicable to the MW-LMC system as the LMC is currently just past pericenter ($\sim$ 50 kpc) in its orbital history, thereby suggesting that the MW's mass should also be $\sim$1-1.5$\times 10^{12}\,M_{\odot}$.

We conclude that the inferred M31 virial mass of $\sim 10^{12}\,M_{\odot}$ is well below the current expectation for the M31 mass based on abundance matching (Moster et al., 2013), the timing argument (vdM12), and satellite kinematics (Watkins et al., 2010). These low M31 mass results reinforce the assertion in Paper I that M33 is unlikely to be on an orbit that yields a recent, close encounter with M31, contrary to conventional wisdom. These results also further illustrate that the statistical methods applied here could be used to assess the plausibility of a given orbital history for a satellite. As we have shown for the M31-M33 system, the resulting halo mass of M31 is at odds with observational evidence, suggesting a revision of M33's conventional orbital model.

3.5.2 Measurement Errors on the Observed Properties of the LMC and M33

A major source of error to consider for Bayesian inference schemes such as the one outlined in this paper is the error due to the measurement error, or the precision with which observational data were measured. The measurement errors on the observed properties of satellites can significantly impact the resulting host halo masses such that the posterior means shift and/or the credible intervals narrow and shift as measurement precision increases. Some aspects of this were already demonstrated in Section 3.4 when several velocity and orbital angular momenta values of M33 were used to estimate the mass of M31.

Here, we recompute the results from Sections 3.4.1 and 3.4.2 with measurement errors that are only half as large as those listed in Table 3.1 to quantify how much precision affects our results. By doing so, we aim to illustrate that this technique may be a powerful method moving forwards as future measurements are made with smaller uncertainties. The measurement errors on M33's kinematics and dynamics

are naturally larger given the distance of M33 from the MW compared to the LMC.

Using the instantaneous likelihood, we find that the resulting posterior mean masses for the MW and M31 are: $1.70^{+1.59}_{-0.49} \times 10^{12}\,\mathrm{M}_{\odot}$, $1.68^{+1.03}_{-0.75} \times 10^{12}\,\mathrm{M}_{\odot}$ (68 per cent credible interval). The mean mass of the MW changes insignificantly since the LMC's position and velocity are known to within 10 per cent, but the 68 per cent credible interval increases slightly. M31's posterior mean halo mass increases by 16 per cent when the measurement errors on M33's position and velocity are halved. The 68 per cent credible interval's upper limit shifts up as the measurement error on total velocity decreases from 38 km s^{-1} to 19 km s^{-1}. Reducing the measurement error on M33's position by half still amounts to about 24 kpc, therefore, the posterior distribution is still quite broad.

Using the momentum likelihood method, we find that the posterior mean virial masses within the 68 per cent credible intervals are $1.06^{+0.76}_{-0.60} \times 10^{12}\,\mathrm{M}_{\odot}$ (MW) and $1.60^{+1.49}_{-0.82} \times 10^{12}\,\mathrm{M}_{\odot}$ (M31). Again, the MW's mass estimate changes minimally and M31's inferred mass goes up by about 16 per cent as the measurement errors are halved. Therefore, measurement error does contribute to the overall uncertainty of this method. However, its contributions are minor and even ≤ 10 per cent precision on M31 and M33's distance and proper motions may not provide an extremely precise range for M31's halo mass.

3.5.3 Cosmic Variance and its Effect on the Mass Estimates of the MW and M31

The posterior means and credible intervals, which summarize the posterior PDFs calculated in this work, simultaneously factor in both the measurement error on the observed satellite properties and the irreducible uncertainty associated to the imperfect correlation between host halo masses and satellite dynamics. The latter is often referred to as 'cosmic variance'. In other words, even if the 6D phase space information for all satellites of the MW (or M31) was known and if that information was incorporated into our importance sampling technique, there would still be an intrinsic scatter due to the cosmology of the Illustris-Dark simulation, as it is only

one realization of the universe.

The magnitude of measurement error and how it affects the posterior PDF was already discussed in Section 3.5.2. Here, we wish to quantify the remaining uncertainty, if any, due to cosmic variance. This irreducible uncertainty is essentially the variance on the conditional probability distribution $P(M_{vir}|\,\mathbf{x})$. Even if we knew the observational data $\mathbf{d}$ perfectly with zero measurement error, there would still be some intrinsic scatter associated with $P(M_{vir}|\,\mathbf{x})$ due to the correlation between host halo mass and satellite dynamics (i.e. $\mathbf{x}$ does not perfectly predict M_{vir}). We do not have an analytic function to describe $P(M_{vir}|\,\mathbf{x})$, but we do have samples from $P(M_{vir}, \mathbf{x})$, which we can use to quantify the magnitude of cosmic variance error.

Our method for computing posterior PDFs requires us to assume a finite measurement error so that our ESS is reasonably large. In practice, we can treat a random set of host-satellite systems from the prior as the *data* (assuming some fixed measurement error) and apply our two likelihood methods. By doing so, we measure how well our statistical method can predict the true host halo mass and if the contribution from this irreducible uncertainty is properly accounted for by the reported credible intervals.

For this purpose, we randomly select 25 host-satellite systems from the prior where the satellite's position relative to its host is < 150 kpc. We have chosen this distance so that we can apply reasonable measurement errors that are informed by the true properties and measurement errors for satellites in the MW's halo. Therefore, the measurement errors assigned to $v_{max}, r, v, \text{and}\, j$ are 10, 10, 15, and 18 per cent, respectively.

For all 25 systems, we calculate the host halo mass using both the instantaneous and momentum methods, ensuring that the ESS remains reasonably large compared to our bootstrapping results in Section 3.4. We then compute the root mean square (RMS) error of the posterior log halo mass estimate relative to the true log halo mass across our 25 host-satellite test cases, once for each likelihood method. The posterior log mass estimate is determined from the total posterior PDF using either the instantaneous or momentum method.

For the instantaneous method, the ratio of the RMS error across all 25 systems to the average of the posterior standard deviations of $\log_{10} \mathrm{M_{vir}}$ (σ_{post}) is approximately 0.78[8]. For the momentum method, we find this ratio is about 0.87. Therefore, both the instantaneous and momentum methods accurately encompass and even overestimate the uncertainty due to cosmic variance since the average of the standard deviations is always greater than the RMS error. The RMS errors, averages of the posterior standard deviations (in $\log_{10} \mathrm{M_{vir}}$), and the ratio of these quantities are listed in Table 3.5. These quantities are reported on a log scale to avoid any bias from transforming posterior quantities calculated in log space to linear space.

If we reduce the assigned measurement errors listed above by half (i.e. 5, 5, 7.5, 9 per cent) and redo our analysis for all 25 systems, we find that the RMS errors and the average posterior standard deviations for each respective method change insignificantly or remain the same. Little to no change in these quantities demonstrates that the measurement error is not the main source of uncertainty. Instead, the intrinsic scatter related to cosmic variance and therefore the imperfect correlation between host halo mass and satellite dynamics is the key source of uncertainty. Thus, more accurate halo mass estimates are not necessarily guaranteed with these methods if higher precision proper motion and distance measurements are obtained for a single satellite, but including measurements of more than one satellite galaxy may result in better halo mass constraints. This will be the focus of future work.

3.5.4 Comparison to Previous Work

The Mass of the MW

Using the kinematics of the LMC and SMC derived from (Kallivayalil et al., 2006a,b), B11 finds the virial mass of the MW is $1.2^{+0.7}_{-0.4} \times 10^{12}\,\mathrm{M_\odot}$ within the 68 per cent credible interval. G13 estimated the mass of the MW based on the properties

[8]Note that posterior standard deviation refers the standard deviation of the total posterior PDF computed for each given system (i.e.for the MW-LMC, this would be the standard deviation of the black curves shown in the top panels of Figs. 3.3 or 3.4.)

Table 3.5: The first two columns give the RMS error and the average posterior standard deviations ($\sigma_{\rm post}$) in $\log_{10} {\rm M_{vir}}$ across 25 host-satellite test cases randomly chosen from the prior. The final column shows the ratio of these quantities. The first two rows indicate the values using the instantaneous likelihood function where the assigned measurement errors (ME) on ${\rm v_{max}, r, v, and\, j}$ are respectively 10, 10, 15, and 18 per cent and then reduced by half to 5, 5, 7.5, and 9 per cent. The last two rows show the same quantities for the momentum likelihood functions across the same 25 test cases.

	RMS [dex]	avg. $\sigma_{\rm post}$ [dex]	$\frac{\rm RMS}{\rm avg.\, \sigma_{post}}$
Instantaneous (10, 10, 15,18 per cent ME)	0.20	0.26	0.78
Instantaneous (5, 5, 7.5, 9 per cent ME)	0.20	0.24	0.84
Momentum (10, 10, 15,18 per cent ME)	0.27	0.30	0.87
Momentum (5, 5, 7.5, 9 per cent ME)	0.27	0.30	0.91

of the MCs (from K13) and the larger Local Group environment to find a MW mass of $\log {\rm M_{200}} = 12.06^{+0.31}_{-0.19}$ encompasses the 90 per cent credible interval.

These results were computed by applying a statistical inference scheme to the combination of the Bolshoi cosmological simulation and the observed properties of the MCs, with respect to the year in which these studies were conducted. The Bolshoi simulation has a much larger volume (nearly 37 times larger) than the simulation used in this analysis, Illustris-Dark. Secondly, the simulations use slightly different cosmological parameters. Finally, we choose our priors using different selection criteria. Together these differences account for the variation between our MW mass results.

Due to the significantly smaller volume of Illustris-Dark, we find that it is actually statistically impossible to apply the exact G13 (or B11) methodology to infer the MW's virial mass. When we choose our priors identically to theirs, which requires that each host halo has an analog of the LMC and the SMC, we find that zero systems lie within the average 2σ range of the observed properties of the MCs from

a redshift of $z = 0.26$ to $z = 0$. With no matches to the observed properties of the MCs, the ESS is effectively zero and therefore the importance sampling technique cannot be applied with two massive satellites akin to the MCs in Illustris-Dark. However, as we demonstrated in Section 3.4, requiring only one massive satellite analog when selecting the prior provides a reasonable statistical sample in Illustris-Dark for which importance sampling can be accomplished.

Therefore, by modifying the analysis of B11 to use only the kinematics of one massive satellite (the K13 properties for the LMC), we find that the virial mass of the MW is $\log_{10} \mathrm{M_{vir}} = 12.23^{+0.25}_{-0.16}\,\mathrm{M_\odot}$ within the 68 per cent credible interval and $\log_{10} \mathrm{M_{vir}} = 12.23^{+0.43}_{-0.43}$ within the 90 per cent credible interval. Our posterior mean is consistent with G13's result when their value of $\mathrm{M_{200}}$ is extrapolated to approximately $\mathrm{M_{vir}}$. The small discrepancy between posterior means and the width of the credible intervals can likely be attributed to using just one satellite in our analysis. The G13 posterior mean is slightly lower than our findings, and we suspect this might be driven by the inclusion of the SMC and its low velocity relative to the MW. The difference between our results and B11's is mainly driven by the prior selection criteria, and the subsequent inclusion of both MCs. B11 adopts the properties of the MCs that were derived from the Kallivayalil et al. (2006a,b) proper motions, which not only changed significantly in K13, but also have much higher measurement errors than the revised values of K13.

Finally, we have compared the halo mass functions for the Bolshoi simulation and Illustris-Dark, and we conclude that the choice of cosmology does not contribute significantly to the difference in inferred MW masses from our analysis and G13's (or B11's). If we adopt a fiducial mass for the LMC that is 100 times less than the MW's, then by comparison of the abundance ratio of halos with a mass of $\sim 1.7 \times 10^{12}\,\mathrm{M_\odot}$ (our instantaneous MW result) and $\sim 1.7 \times 10^{10}\,\mathrm{M_\odot}$ we can assess the magnitude of error introduced by different values for σ_8 and h. In the Bolshoi simulation, we find an abundance ratio of 66.1 and in Illustris-Dark, the ratio is 66.6. Thus, the simulations agree to within 1 per cent of each other for halo abundances and using one over the other would not affect our MW mass estimate.

The Mass of M31

Recent mass estimates for M31 are directly affected by the assumed value of its transverse motion and corresponding measurement error. Until the proper motion of M31 was directly measured by S12, the assumed values spanned a generous range of velocities. While no previous authors have applied a Bayesian scheme using satellite dynamics to infer the mass of M31, as we have done in this work, our results are still in good agreement with estimates resulting from several independent techniques. We highlight several selected results below.

Fardal et al. (2013) used N-body models that reproduce the Giant Southern Stream in the halo of M31 to estimate its enclosed mass as $\log_{10}\mathrm{M}_{200} = 12.32 \pm 0.1$. Watkins et al. (2010) used the line of sight velocities and distances to 23 satellite galaxies in the halo of M31 to find a mass of $\mathrm{M}_{300} = 1.4 \pm 0.4 \times 10^{12}\,\mathrm{M}_{\odot}$. This is approximately equivalent to the virial mass and is in very good agreement with our mass estimates even though these results were derived using multiple satellites and we only use the properties of one satellite galaxy in the halo of M31 (i.e. M33).

Many authors have used the well known timing argument to estimate the masses of the MW, M31, and the Local Group simultaneously. Some recent works include that of vdM12, who estimate M31's virial mass to be $\sim$1.5-1.7$\times10^{12}\,\mathrm{M}_{\odot}$ for a low tangential velocity and nearly radial orbit relative to the MW. More recently, Carlesi et al. (2017) estimated the mass of M31 using the timing argument in a Bayesian fashion using ΛCDM cosmological simulations and find values of 1-2$\times10^{12}\,\mathrm{M}_{\odot}$. These studies incorporate the measured tangential velocity of M31 in their models and are therefore most similar to our analysis. Note, however, that these mass estimates contradict the rather low M31 mass ($\sim 10^{12}\,\mathrm{M}_{\odot}$) inferred by imposing a close M31-M33 encounter (Section 3.5.1).

While our mass estimates for M31 using the observed properties of M33 are no more profound than previous estimates, they do help test the viability of different likelihood functions. As the full 6D phase space information from future proper motion measurements of other M31 satellites become available, this hypothesis can

be tested.

3.6 Conclusions

We have modified and expanded the Bayesian inference scheme developed by B11 to infer the masses of the MW and M31 using the observed properties of their satellites. This method combines high precision astrometric measurements of satellites with high mass resolution cosmological simulations in a statistical fashion to constrain host galaxy mass. We find this to be a promising statistical scheme to learn about the hosts of satellites in the era of high precision astrometry.

By analyzing a set of massive satellite galaxy analogs (i.e. analogs of the LMC and M33) defined in Paper I, we confirmed that orbital angular momentum is well conserved over time and is therefore an ideal orbital property for constraining the larger host environment of a satellite galaxy. We therefore expand the B11 inference scheme by creating a new likelihood function that uses orbital angular momentum instead of the individual position and velocity of a satellite relative to its host to infer the mass of the MW and M31, respectively. Therefore, the masses of the MW and M31 are each determined using halos from the Illustris-Dark cosmological simulation as the prior in the following ways: (1) apply a likelihood function that uses the current position and velocity (instantaneous method) of the LMC or M33 to determine host halo mass and (2) apply a likelihood function that uses current orbital angular momentum (momentum method) of the LMC or M33 to infer host halo mass.

Since the instantaneous method uses satellite position and velocity, which are both susceptible to large variations at different orbital phases (i.e. pericenter vs. in between apo- and pericenter), overall, it is a less reliable method for determining host halo mass with cosmological analogs from Illustris-Dark. Instead, we find that the momentum method produces more accurate though less precise results compared to the instantaneous method.

The results of the instantaneous method are $\log_{10} \mathrm{M_{vir}} =$

$12.23^{+0.25}_{-0.16}$ (MW), $12.16^{+0.27}_{-0.28}$ (M31), suggesting that the MW is more massive than M31, contradicting conventional wisdom. The new likelihood function developed in this paper, the momentum likelihood, yields the following mass estimates: $\log_{10} \mathrm{M_{vir}} = 12.01^{+0.25}_{-0.34}$(MW), $12.12^{+0.32}_{-0.35}$ (M31), where M31 is now more massive than the MW.

Furthermore, when we require M33 analogs to have a made a recent (< 3 Gyr ago), close encounter (< 100 kpc) relative to its host halo, our statistical analysis yields an estimated M31 mass of only $\sim 10^{12}\,\mathrm{M_\odot}$. Such a low mass is inconsistent with several independent M31 mass estimates, and therefore further supports the new orbital histories for the M31-M33 system presented in Paper I. These results also imply that such statistical methods may be useful in constraining satellite orbital histories such that the imposition of incorrect orbital trajectories might result in unlikely host halo masses, and therefore could help constrain the plausibility of a given orbital scenario (e.g. the case of M33). Our cosmological analogs in Paper I preferred an M31 mass $\geq 1.5 \times 10^{12}\,\mathrm{M_\odot}$ based on the orbital energy of M33 and a majority of these analogs are also on a first infall orbit. Furthermore, our numerical orbit integrations independently showed that a first infall scenario was very plausible in the proper motion error space of M31-M33, demonstrating the links between satellite dynamics, host mass, and orbital histories.

We have also shown that the instantaneous method is more susceptible to bias as a function of time and orbital history by applying it along the LMC's past orbital trajectory, which was calculated in Paper I. When the LMC's time-dependent position and velocity are used as inputs for the instantaneous method, the inferred MW masses over time show deviations of approximately a factor of two. In contrast, the momentum method infers consistent MW masses over time, regardless of the LMC's orbital phase. Therefore, the combined analysis of the MW-LMC and M31-M33 system at present and the application of the statistical scheme as a function of time together demonstrate that the momentum method is the most reliable method for estimating host halo mass for a variety of host-satellite systems.

A close inspection of sources of error that may contribute to our statistical

method has demonstrated that the precision and accuracy of mass estimates for the MW and M31 are primarily dominated by the irreducible uncertainty caused by cosmic variance. While our methods correctly capture the magnitude of this uncertainty, higher precision measurements of proper motions and distances to a single massive satellite galaxy may not guarantee better measurements of its host's mass. However, *simultaneously* incorporating precise measurements of more than one satellite (i.e. a population of satellites) in a given host halo may improve our overall mass estimates.

While this work has only used the dynamical information of one satellite galaxy in each of the MW and M31's halos, proper motions are currently available for nine other dwarf satellite galaxies of the MW besides the MCs, and many more will become available in the near future. Now that we have established that estimating the mass of the MW should be approached from the perspective of orbital constants, we must continue to improve our statistical methods such that the maximal amount of phase space information for satellites (and eventually other substructures in the MW and M31's halos) can be used to achieve high precision mass measurements of the MW and M31.

In our next paper (Patel et al. 2017c, in prep), we will calculate the MW's mass using the properties of each low mass dwarf satellite (derived from their 6D phase space information), and finally, we will compute the MW's mass using the combined information from the ensemble of dwarf satellites. By doing so, we aim to illustrate the full power of this technique in the era of high precision astrometry.

Interestingly, this technique can be modified to address several broader topics in near-field cosmology. We have already established that it is trivial to add more satellites into consideration for the MW's halo and plan to demonstrate this in upcoming work. When proper motion data becomes available for M31 satellites (e.g. HST-GO proposal #14769 for NGC 185/147), this technique will be easily applicable to the M31 system. Furthermore, one could extend the statistical method that we have outlined here to include not only the magnitude but also the direction of satellite specific orbital angular momentum vectors (e.g. to address the alignment

of satellite orbits). Finally, a prior sample chosen from a suite of cosmological zoom simulations could be used so that both globular clusters and dwarf satellite galaxies can be included in this type of analysis.

CHAPTER 4

Estimating the Mass of the Milky Way Using the Ensemble of Classical Satellite Galaxies

This chapter has been published previously as Patel, E., Besla, G., Mandel, K., Sohn, S. T., 2018, ApJ, 857, 78

Abstract

High precision proper motion (PM) measurements are available for approximately 20% of all known dwarf satellite galaxies of the Milky Way (MW). Here we extend the Bayesian framework of Patel et al. (2017b) to include all MW satellites with measured 6D phase space information and apply it with the Illustris-Dark simulation to constrain the MW's mass. Using the properties of each MW satellite individually, we find that the scatter among mass estimates is reduced when the magnitude of specific orbital angular momentum (j) is adopted rather than their combined instantaneous positions and velocities. We also find that high j satellites (i.e. Leo II) constrain the upper limits for the MW's mass and low j satellites rather than the highest speed satellites (i.e. Leo I and LMC), set the lower mass limits. When j of all classical satellites is used to simultaneously estimate the MW's mass, we conclude the halo mass is $0.85^{+0.23}_{-0.26} \times 10^{12}\,\mathrm{M}_{\odot}$ (including Sagittarius dSph) and $0.96^{+0.29}_{-0.28} \times 10^{12}\,\mathrm{M}_{\odot}$ (excluding Sagittarius dSph), cautioning that low j satellites on decaying orbits like Sagittarius dSph may bias the distribution. These estimates markedly reduce the current factor of two spread in the mass range of the MW. We also find a well-defined relationship between host halo mass and satellite j distribution, which yields the prediction that upcoming PMs for ultra-faint dwarfs should reveal j within $5 \times 10^3 - 10^4$ kpc km s^{-1} . This is a promising method to significantly constrain the cosmologically expected mass range for the MW and eventually M31 as more satellite PMs become available.

4.1 Introduction

Satellite galaxies around the Milky Way (MW) are often used to study the structure and assembly history of the Galaxy's dark matter and stellar halo. In particular, the kinematics of halo tracers (satellites, globular clusters and stellar streams) have been used to constrain the Galaxy's gravitational potential and total mass. Many efforts have been made to constrain the current factor of two spread in the total mass range of the MW, but a high precision estimate has yet to be made.

Leo I, as one of the highest speed MW satellites, is often used to place lower limits on the mass of the MW. However, because its relative velocity hovers around the MW's escape speed at its current separation of $\sim$260 kpc, any MW mass constraint requires the assumption that Leo I is bound. Boylan-Kolchin et al. (2013, hereafter BK13) illustrate that unbound satellites within the virial radius are rare. By assuming that Leo I is bound at its current position and velocity, BK13 used the Aquarius cosmological zoom simulations (Springel et al., 2008) to infer that the virial mass of the MW must be $> 10^{12}\,\mathrm{M}_{\odot}$, with a median mass of $1.6 \times 10^{12}\,\mathrm{M}_{\odot}$. Other studies relying on the boundedness of Leo I, such as Li and White (2008), used a radial timing argument analysis similar to that of Zaritsky et al. (1989) to determine that the MW's mass is $2.43 \times 10^{12}\,\mathrm{M}_{\odot}$ with a lower limit of $0.8 \times 10^{12}\,\mathrm{M}_{\odot}$. Non-radial timing argument studies predict a MW mass as high as $> 3 \times 10^{12}\,\mathrm{M}_{\odot}$ if Leo I is bound (Sohn et al., 2013).

If Leo I is unbound, however, these methods would likely overestimate the true mass of the MW. The case of Leo I strongly motivates a study to calibrate the impact of using a single satellite to constrain the mass of its host. We argue in this study that a single satellite can result in a significantly biased mass estimate, especially when satellites are on extreme orbits (see also Sales et al., 2007; Patel et al., 2017b). Instead, we have developed a novel method of estimating the mass of the MW using an ensemble of observed satellites and analogs in cosmological simulations.

The HST Proper Motion (HSTPROMO) collaboration (Sohn et al., 2017; Kalli-

vayalil et al., 2013; Sohn et al., 2013; Massari et al., 2013; Kallivayalil et al., 2006a,b, e.g.) and other authors (Piatek et al., 2016, 2008, 2007, 2006, 2005, 2003, 2002; Walker et al., 2008; Scholz and Irwin, 1994) have now measured the proper motions of several low mass dwarf galaxies in the MW's halo. With the combined 6D phase space information derived from the proper motions for the classical MW satellites (LMC, SMC, Carina, Draco, Fornax, Sculptor, Leo I, Leo II, Ursa Minor, Sextans, and the Sagittarius dSph), we can now use the 3D dynamics of a population of halo tracers to further our understanding of the MW's dark matter halo and its global properties. In this work, we utilize the magnitude of specific orbital angular momentum of each satellite, rather than their instantaneous position and velocity, as motivated in Patel et al. (2017b, hereafter P17B). An important benefit is that we make no assumption of whether a satellite is bound, simply whether it currently resides within the virial radius of the MW.

As the two most massive MW satellites, the Magellanic Clouds (MCs) are also often used to characterize properties of the MW, specifically via analogs selected from cosmological simulations. Both Boylan-Kolchin et al. (2011a) and Busha et al. (2011) have used the instantaneous characteristics of the MCs, such as their current position and velocity, to make predictions for the MW's mass in a frequentist and Bayesian fashion, respectively (see also González et al., 2013). Using the Kallivayalil et al. (2013) proper motions, the Bayesian posterior mean mass estimate for the MW using the Large Magellanic Cloud (LMC) alone is $1.70 \times 10^{12}\,\mathrm{M}_{\odot}$ (P17B) and approximately $1.15 \times 10^{12}\,\mathrm{M}_{\odot}$ using both MCs (González et al., 2013).

While the MCs are well-studied members of the MW's halo, their current properties including the spatial proximity of the MCs to the MW ($\sim$50 kpc), to each other ($\sim$23 kpc), and their unique orbital configuration (just past pericenter), make them rare in a cosmological context (Besla et al., 2007, 2012; Boylan-Kolchin et al., 2011a). Less than 5% of simulated MW mass halos host two massive satellites that have made a recent first pericentric approach as close as 50 kpc. We showed in P17B that MW mass estimates are highly susceptible to the orbital phase of the LMC and thus conclusions based on the current properties of only the MCs should be taken

with caution. As a result, we must turn to other satellite properties to estimate the mass of the MW in an unbiased fashion.

The *momentum method* developed in P17B relies on orbital angular momentum and thus affords a larger simulated data set from which MW mass estimates can be formed since it does not limit satellite analogs to a narrow range of position and velocity combinations as in the *instantaneous method*. For the MW-LMC system, a nearly ten-fold increase in the number of statistically significant satellite analogs from the dark-matter-only Illustris simulation (or Illustris-1-Dark) enables us to combine inferences for the MW's mass even for rare systems (i.e. unique orbital configurations), thus providing a powerful method moving forward as more high precision data becomes available for halo tracers.

The impact of only one satellite on the mass estimate of the MW is clearly evident with regards to Leo I. This motivates the need to use several satellites simultaneously to form a MW mass estimate. Here, we extend the P17B method to all classical low mass MW satellites (satellites less massive than the MCs) to constrain the mass of the MW. This will test whether satellites like Leo I are still outliers in these MW mass estimation techniques or if other satellites will become more critical players. For example, recent studies by Gibbons et al. (2014); Belokurov et al. (2014) have suggested a lower mass bound for the MW based on the properties of the Sagittarius dSph stellar stream, indicating a lower limit of about $7 \times 10^{11}\,\mathrm{M}_{\odot}$. With this statistical framework, such assertions can be tested in a cosmological context for the first time.

In Section 4.2, we compile properties of the nine low mass satellites used in this study and describe the details of the Illustris dark-matter-only cosmological simulation. Section 4.3 provides the details of the Bayesian framework that has been extended from P17B to accommodate a population of lower mass satellites. The results of these methods are presented in Section 4.4. Section 4.5 contains a discussion of the global trend between the distribution of satellite specific orbital angular momenta and host halo mass. Finally, Section 4.6 summarizes our results.

4.2 Simulation and Observed Satellite Properties

In P17B, we combined the properties of the most massive satellite galaxies in the halos of the MW and M31(the LMC and M33) with a state-of-the-art cosmological simulation in a Bayesian statistical framework to infer the masses of their host halos. In this work, we extend our previous analysis to lower mass satellites and additionally implement a method that uses multiple satellites simultaneously to refine MW mass estimates. This section describes the observational data that is currently available for the low mass MW satellites considered and the specifications of the Illustris-1-Dark simulation, which we will use to select low mass satellite analogs.

4.2.1 Observed Properties of Nine Low Mass MW Satellites

To date, the proper motions of the nine brightest MW dwarf satellite galaxies (after the MCs) have been measured with high astrometric precision in the last decade. In principle, any halo tracer (e.g., satellite galaxies, globular clusters) with proper motion information can be used in this type of statistical analysis to estimate the mass of its host if a sufficiently large set of simulated analogs are also available.

The classical[1] low mass satellites considered in this work include: Carina, Draco, Fornax, Sculptor, Leo I, Leo II, Ursa Minor, Sextans, and the Sagittarius dSph. The stellar masses of these dwarf spheroidal (dSph) galaxies are between $10^5 - 10^7\,\mathrm{M}_\odot$ (see McConnachie, 2012) and their masses at infall are predicted to be $10^8 - 10^{10}\,\mathrm{M}_\odot$ from cosmological expectations (Boylan-Kolchin et al., 2012; Moster et al., 2013). For reference, the LMC's stellar mass is about $3 \times 10^9\,\mathrm{M}_\odot$ at present and its total mass at infall could be as high as a few times $10^{11}\,\mathrm{M}_\odot$ (Kim et al., 1998; Besla et al., 2010; Wang et al., 2006).

[1]Classical in this case refers to those satellites that were known prior to the Sloan Digital Sky Survey. These satellites are also the brightest (and most massive) MW satellites aside from the Magellanic Clouds (MCs).

	r^{obs} [kpc]	1σ [kpc]	v_{tot}^{obs} [km s^{-1}]	1σ [km s^{-1}]	j^{obs} [kpc km s^{-1}]	1σ [kpc km s^{-1}]	References Dist. + v_{rad}	PM
Leo II	236	14	138	42	32,105	9,998	1	4
Fornax	149	12	193	45	28,471	8,712	1	5
Leo I	258	15	202	19	27,918	9,146	1	3
Sculptor	86	6	213	10	17,232	1,267	1	2
Sextans	89	4	206	22	17,097	2319	1	8
LMC	50	5	321	24	15,688	1,788	1,10	10
Ursa Minor	78	3	173	49	12,545	4,375	1	7
Draco	76	6	183	4	12,241	1,229	1	2
Carina	107	6	97	41	10,322	4,532	1	6
Sagittarius dSph	18	2	320	23	5,249	1,000	1	9

Table 4.1: Observational MW Satellite Data

Note. — Observational data ($\boldsymbol{d}$) for the LMC and the nine MW dSph galaxies with proper motions (PMs). The satellites are listed in order of descending j^{obs}. Data for the distance, radial velocity, and PMs of each satellite were taken from the following references.

References. — (1) McConnachie (2012, and references therein), (2) Sohn et al. (2017), (3) Sohn et al. (2013), (4) Piatek et al. (2016), (5) Piatek et al. (2007), (6) Piatek et al. (2003), (7) Piatek et al. (2005), (8) Casetti-Dinescu et al. (2018), (9) Sohn et al. (2015), (10) Kallivayalil et al. (2013).

The observed data ($\boldsymbol{d}$) for each low mass satellite and the LMC are provided in Table 4.1. These data consist of: i.) the observed position relative to the MW ($r^{\rm obs}$), ii.) the total velocity relative to the MW ($v_{\rm tot}^{\rm obs}$), and iii.) the magnitude of the specific orbital angular momenta about the MW ($j^{\rm obs}$), where $j = |\mathbf{r} \times \mathbf{v}|$. The mean values of these quantities and the uncertainties associated with them have been calculated from a set of 10,000 Monte Carlo samples drawn from the 4σ error space of distance, radial velocity, and proper motion of each satellite. For the low mass satellites, all adopted distances and radial velocities are taken from the compilation presented in McConnachie (2012) and the references therein. The proper motions of the galaxies come from a variety of groups and programs (most measurements come from the *Hubble Space Telescope*), as indicated in the final column of Table 4.1. In this analysis we do not use the properties of the SMC explicitly due to the low frequency of LMC and SMC analogs in cosmological simulations (see Boylan-Kolchin et al., 2011a), but SMC analogs may exist about the halos included in the prior sample (see Section 4.3.1).

4.2.2 The Illustris-Dark Simulation

To choose a broad set of MW halo analogs, we use the halo catalogs from the publicly available Illustris Project, a suite of N-body+hydrodynamic simulations run with the `AREPO` code (Vogelsberger et al., 2014a,b; Genel et al., 2014; Nelson et al., 2015). For this analysis, we use only the Illustris-1-Dark (hereafter Illustris-Dark) simulation, which spans a cosmological volume of $(106.5\ {\rm Mpc})^3$ and follows the evolution of 1820^3 dark matter particles from redshift $z = 127$ to $z = 0$. Each dark matter particle has a mass of $m_{\rm DM} = 7.5 \times 10^6\,{\rm M}_\odot$. Hydrodynamical processes are not included in the main body of this analysis because Illustris-Dark affords a larger set of cosmological analogs. However, we have included a comparison to the Illustris-1 hydrodynamics simulation in Appendix C.1. All Illustris simulations use the *WMAP-9* cosmological parameters (see Hinshaw et al., 2013).

Substructures in each of the 136 snapshots of the Illustris-Dark simulation are identified using the `SUBFIND` algorithm (Springel et al., 2001a; Dolag et al., 2009).

SUBFIND is a halo-finding routine that first identifies halos using a friends-of-friends (FoF) method and then finds substructures within each identified halo that are overdense, gravitationally bound regions. Typically, each FoF group contains a massive, central subhalo that contains most of the loosely bound material in the halo. A selection of these centrals will act as MW analogs in this work. The Illustris-Dark merger trees were created using the SUBLINK code (Rodriguez-Gomez et al., 2015). All relative positions for halos and subhalos are corrected for the box edges.

In this work, we will refer to the virial mass and radius of FoF groups in our sample. While the virial mass is the mass of all substructures in a FoF group, it is approximately equivalent to the mass of the primary, central subhalo in each halo. Virial mass is defined as the mass enclosed within the virial radius – the radius at which the average density within that radius reaches an overdensity of $\Delta_{\rm vir}$ in a spherical'top-hat' perturbation model. For a $10^{12}\,{\rm M}_{\odot}$ halo, this corresponds to a virial radius of about 260 kpc. The $\Delta_{\rm vir}$ factor depends directly on the cosmological parameters (see Bryan and Norman, 1998). The Illustris-Dark cosmology yields $\Delta_{\rm vir}$ = 357 (or $\Delta_{\rm vir} \times \Omega_{\rm m} = 97.3$). The virial mass and radius are taken directly from the Illustris-Dark group catalogs. A variety of other mass definitions, such as those based on the splashback radius or R_{200}, could also be used in this analysis.

4.3 Statistical Methods

In this section, we identify the subset of host halos from P17B's prior that have exactly one massive satellite analog and at least one satisfactory low mass subhalo analogous to the classical satellites. Note that while the MW actually hosts several low mass satellites, we only require a minimum of one low mass satellite analog per prior sample host halo due to the simulation's resolution limits. We also outline the modified selection criteria ($\mathbf{C}'$) for the prior sample, likelihood functions tailored for low mass satellites, and the statistical approximation used to infer the mass of the MW using the ensemble of low mass satellites simultaneously.

4.3.1 Prior Samples

Massive Satellite Analogs

While this work focuses on the low mass MW satellites, it is important to include the presence of a massive satellite analog (weighing approximately 10% of their host's total mass) since they could alter the gravitational potential of their host halos and subsequently affect the kinematics of other nearby satellites (see Section 4.5). The existence of a massive satellite analog also ensures that MW analogs that have similar mass assembly histories are chosen. We also note that the subhalo abundances around host halos with and without a massive satellite analog differ, which we discuss in detail in Appendix C.2.

To build a prior sample, we first require that exactly one massive satellite analog satisfying the following selection criteria (**C**) from P17B exists in all halos from the final 20 snapshots ($z \approx 0.26$ to $z = 0$) of the Illustris-Dark simulation. We consider only the final 20 snapshots to be consistent with P17B and previous work (e.g., Busha et al., 2011; González et al., 2013).

> C_1: A subhalo is considered a massive satellite analog only if $v_{\rm max} > 70$ km s^{-1}.
>
> C_2: The massive satellite analog must reside within its host's virial radius ($R_{\rm vir}$) at $z \approx 0$.
>
> C_3: The massive satellite analog must have a minimal subhalo mass of $10^{10}\,M_\odot$ at $z \approx 0$.

Note that subhalo mass is provided in units of $M_\odot\ h^{-1}$, where $h = 0.704$, in the Illustris-Dark halo catalogs and is used as given. $v_{\rm max}$ is the maximum circular velocity of a subhalo. These selection criteria return a total of 19,653 host halos, each with a companion massive satellite analog. This data constitutes the prior sample used in P17B.

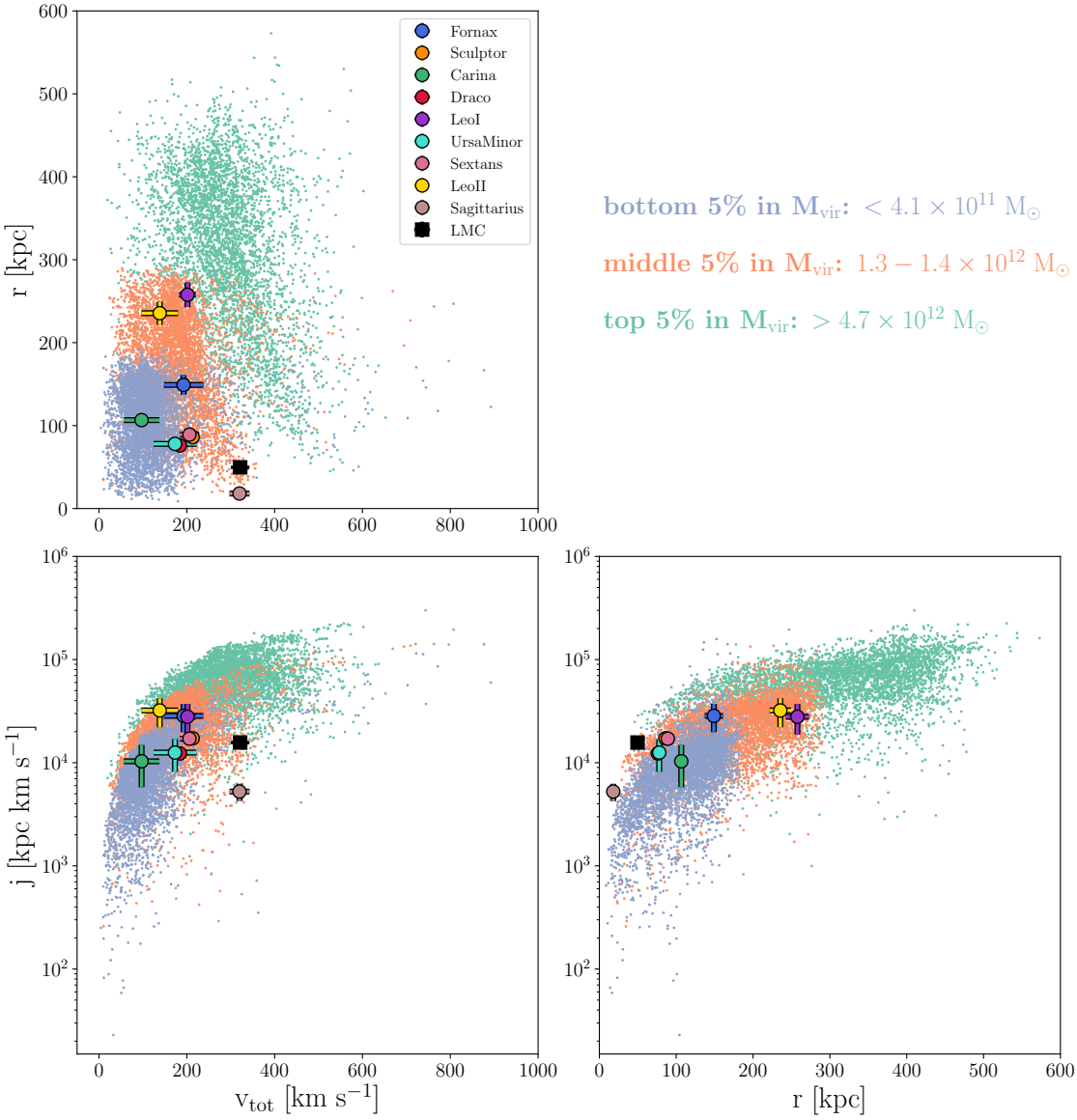

Figure 4.1: For the low mass satellite analogs selected to be in Prior 2, the distribution of satellite subhalo properties ($\boldsymbol{x}$) are shown for each pair of satellite parameters. Only those properties for low mass satellite analogs residing in the bottom 5% ($< 1.4 \times 10^{11}\,M_\odot$), middle 5% ($1.3 - 1.4 \times 10^{12}\,M_\odot$) and top 5% ($> 4.7 \times 10^{12}\,M_\odot$) of the host halo mass (M_{vir}) distribution are shown to illustrate the spread in satellite subhalo properties as a function of host halo mass. The colored points with error bars denote the observed properties ($\boldsymbol{d}$) for all satellites listed in Table 4.1. The overlap between the observed satellite properties and the properties of the prior sample indicate that our prior selection criteria are chosen appropriately.

Low Mass Satellite Analogs

Analogs of the low mass classical MW satellites must belong to the first 15 subhalos in each FoF group, which are ranked by decreasing subhalo mass. This ensures that systems with multiple *massive* satellite analogs (see previous section) are omitted. Ideally, the prior sample would contain only those halos that host a massive satellite analog in addition to about 10 low mass satellite analogs. However, simulations with large volumes and sufficient resolution are currently unable to resolve a statistically significant number of halos that represent true analogs of the MW in this way, so these constraints are relaxed. Small scale cosmological volumes with higher mass resolution and perhaps finer redshift spacing are likely the most ideal simulations to build such a prior sample in the future.

We require that all low mass satellite analogs have $v_{\rm max} < 45$ km s^{-1} to ensure that we are truly selecting just the low mass subhalos (i.e. the MCs have $v_{\rm max} > 50$ km s^{-1}). To avoid the 'Too Big to Fail' (TBTF) problem (Boylan-Kolchin et al., 2011b), only an upper $v_{\rm max}$ bound is used in these criteria. TBTF is a discrepancy that arises in dissipation-less ΛCDM simulations where subhalos with masses analogous to the classical MW dwarfs fail to host bright satellites. This discrepancy leads to a mismatch between simulated $v_{\rm max}$ values and their observed counterparts such that the observed values are much lower than that of their simulated analogs.

Our goal in this work is to choose dynamical analogs, not analogs based purely on mass or energetics. Since dynamical friction plays an insignificant role in the orbital evolution of these low mass satellites, the kinematics (positions, velocities, specific angular momenta) are not expected to decrease drastically between infall and today. The selection criteria for low mass satellite analogs (denoted by $\mathbf{C}'$) are summarized below.

C'_1: A subhalo is considered a low mass satellite analog only if $v_{\rm max} < 45$ km s^{-1} .

C'_2: The satellite analog must reside within its host's virial radius ($\mathrm{R_{vir}}$) at $z = 0$.

C'_3: The satellite analog must have a subhalo mass $\geq 10^9\,M_\odot$ at $z = 0$.

A minimum subhalo mass of $10^9\,M_\odot$ corresponds to ∼133 dark matter particles in Illustris-Dark.

Prior 1

Prior 1 is the sample of host halos that host exactly one massive satellite analog (criteria **C**, Section 4.3.1) and one or more low mass satellite analogs (criteria **C′**, Section 4.3.1). Approximately 92.8% of host halos from the prior sample used in P17B satisfy these combined criteria. *This subset of 18,236 host halos and the properties of their associated massive satellite analogs will be referred to as* **Prior 1** *from here on.* Note that this prior is only trivially different from that selected in P17B. The LMC's properties will be used with Prior 1 to compute the mass of the MW.

Prior 2

We find 87,598 subhalos that satisfy the low mass satellite analog criteria in a total of 18,236 unique host halos. Thus, many *host halos* harbor more than one low mass satellite analog, as expected. *This set of host halos and the properties of their associated low mass satellite analogs will be referred to as* **Prior 2**. Prior 2 will be used to compute the mass of the MW using the properties of all classical MW satellites less massive than the MCs.

Fig. 4.1 shows the distribution of latent properties $\boldsymbol{x}$ for a select set of subhalos in Prior 2. We have plotted the properties of subhalos residing in the bottom, middle, and top 5% of the host halo mass distribution. Each panel indicates a pair of two parameters in $\boldsymbol{x} = [r, v_{\rm tot}, j]$ colored by the corresponding host halo mass. Overplotted are the observed properties $\boldsymbol{d} = [r^{\rm obs}, v_{\rm tot}^{\rm obs}, j^{\rm obs}]$ for all MW satellites listed in Table 4.1. The overlap between the observed properties and prior sample properties shows that the low mass satellite analogs accurately represent the true MW satellite properties. Without implementing any statistical techniques, the

current properties of the classical MW satellites are most similar to those subhalos residing in host halos with masses $< 1.4 \times 10^{12}\,\mathrm{M}_{\odot}$.

The greatest number of low mass satellite analogs (by definition) hosted by any individual host halo in Prior 2 is 14 subhalos. Only 0.05% of all halos considered in the prior sample host exactly 14 low mass satellite analogs. About 6% of all host halos have 10 or more satisfactory subhalos within their virial radii. Typically, halos host between 2-5 low mass satellite analogs. See Appendix C.2 for more information on the abundance of subhalos within the virial radii of host halos in Prior 2.

The covariance between measurement errors of r^{obs} and $v_{\mathrm{tot}}^{\mathrm{obs}}$ is small, as shown in Busha et al. (2011), so we treat these two measurements independently in the *instantaneous method*, which uses these two satellite properties to compute likelihoods for all halos in the prior sample. We consider the magnitude of specific orbital angular momenta separately in a parallel analysis, which we refer to as the *momentum method*. The most ideal candidates for our analysis are those residing at 100-300 kpc from the center of mass of their host halos since they are least affected by strong tides from the host (see Appendix C.1 for more details).

Multiplicity of Host Halos

In Prior 2, all host halos with more than one low mass satellite analog are counted towards the prior distribution of host halo masses multiple times. For example, if a host halo has a virial mass of $\mathrm{M}_{\mathrm{vir}} = 1.23 \times 10^{12}\,\mathrm{M}_{\odot}$ and hosts four low mass satellite analogs, its virial mass will appear four times in the list of halo masses that correspond to low mass satellite analogs. In P17B (and subsequently Prior 1), there is a one to one relation between host halos and massive satellite analogs since that prior was limited to hosts with just one massive satellite analog.

4.3.2 Likelihood Functions for Low Mass Satellites

For those host halos and low mass satellite analogs included in Prior 2, the physical parameters of interest are $\boldsymbol{\theta} = \{\boldsymbol{x}, M_{\mathrm{vir}}\}$, where $\mathrm{M}_{\mathrm{vir}}$ is the virial mass of the

corresponding host halo for any given subhalo. The parameters $\boldsymbol{x}$ are the latent, observable properties for satellite subhalos in Illustris-Dark. Fig. 4.1 illustrates these for a fraction of the subhalos in the prior. The observational data ($\boldsymbol{d}$) listed in Table 4.1 are measurements of the parameters $\boldsymbol{x}$, so if the measurement errors are zero, then $\boldsymbol{d} = \boldsymbol{x}$. Subsets of the physical parameters $\boldsymbol{x}$ are used in the different likelihood functions to estimate the mass of the MW.

The likelihood functions from P17B are altered such that they no longer rely on $v_{\rm max}^{\rm obs}$ due to the TBTF problem. We implement two methods to compute the likelihood of a given MW mass, as given below.

Instantaneous

$$\mathcal{L}(\boldsymbol{x}|\,\boldsymbol{d}) = N(r^{obs}|\,r, \sigma_r^2) \times N(v_{tot}^{obs}|\,v_{tot}, \sigma_v^2), \tag{4.1}$$

Momentum

$$\mathcal{L}(\boldsymbol{x}|\,\boldsymbol{d}) = N(\ j^{obs}|\ j, \sigma_j^2) \tag{4.2}$$

All measured satellite properties are assumed to have Gaussian error. The posterior distribution for the virial halo mass of the MW using the properties of each low mass satellite is computed using Prior 2 and these likelihood functions via importance sampling.

Importance Sampling

Bayes' theorem is written as

$$P(\boldsymbol{x}, M_{\rm vir}|\,\boldsymbol{d}, C') \propto P(\boldsymbol{d}|\,\boldsymbol{x}) \times P(\boldsymbol{x}, M_{\rm vir}|\,\boldsymbol{C'}), \tag{4.3}$$

where we denote the dependence on the prior selection criteria $\boldsymbol{C'}$. The left hand side is the posterior probability distribution. $P(\boldsymbol{x}, M_{\rm vir}|\,\boldsymbol{C'})$ represents the prior probability distribution and $P(\boldsymbol{d}|\,\boldsymbol{x})$ is the likelihood (equivalent to $\mathcal{L}(\boldsymbol{x}|\,\boldsymbol{d})$).

A posterior probability density function (PDF) is then calculated by drawing a set of samples (n) from an importance sampling function. Here, we have chosen the importance sampling function to be the prior PDF (as in P17B). For each sample in n, an importance sampling weight proportional to the likelihood (using either

Eq. 4.1 or 4.2) is assigned. Using these weights, integrals that summarize the posterior PDF for halo mass are calculated as follows where the denominator is a normalization constant.

$$\begin{aligned}\int f(\boldsymbol{\theta}) P(\boldsymbol{x}, M_{\rm vir}|\, \boldsymbol{d}, C')\, d\boldsymbol{\theta} = \\ &\frac{\int f(\boldsymbol{\theta}) P(\boldsymbol{d}|\, \boldsymbol{x}) P(\boldsymbol{x}, M_{\rm vir}|\boldsymbol{C}')\, d\boldsymbol{\theta}}{\int P(\boldsymbol{d}|\, \boldsymbol{x}) P(\boldsymbol{x}, M_{\rm vir}|\, \boldsymbol{C}')\, d\boldsymbol{\theta}} \\ &\approx \frac{\sum_j^n f(\boldsymbol{\theta}_j) P(\boldsymbol{d}|\, \boldsymbol{x}_j)}{\sum_j^n P(\boldsymbol{d}|\, \boldsymbol{x}_j)}.\end{aligned} \tag{4.4}$$

If $f(\theta)$ only depends on $\mathrm{M_{vir}}$, a representation of the marginal posterior PDF for $\mathrm{M_{vir}}$ can be derived by computing Eq. 4.5 over a grid of potential halo mass values (i.e. using kernel density estimation).

$$\begin{aligned}\int f(M_{\rm vir}) P(M_{\rm vir}|\, \boldsymbol{d}, C')\, dM_{\rm vir} \\ &= \int\int f(M_{\rm vir})\, P(\boldsymbol{x}, M_{\rm vir}|\, \boldsymbol{d}, C')\, d\boldsymbol{x}\, dM_{\rm vir} \\ &\approx \frac{\sum_j^n f(M_{\rm vir}^j)\, P(\boldsymbol{d}|\, \boldsymbol{x}_j)}{\sum_j^n P(\boldsymbol{d}|\, \boldsymbol{x}_j)} \\ &= \sum_j^n f(M_{\rm vir}^j)\, w_j\end{aligned} \tag{4.5}$$

where $w_i = P(\boldsymbol{d}|\, \boldsymbol{x}_i)/\sum_j^n P(\boldsymbol{d}|\, \boldsymbol{x}_j)$ are importance weights. Setting $f(\boldsymbol{\theta}) = \mathrm{M_{vir}}$ gives the posterior mean value for virial halo mass of the MW. For more details on the importance sampling technique, see Section 3.2 of P17B.

Note that in practice all calculations are carried out in $\log_{10} \mathrm{M_{vir}}$ (by directly replacing $\mathrm{M_{vir}}$ with $\log_{10} \mathrm{M_{vir}}$ in all equations) because the posterior distribution of $\log_{10} \mathrm{M_{vir}}$ is more roughly Gaussian than the posterior distribution of $\mathrm{M_{vir}}$, and therefore more easily summarized by a central value. Consequently, all results reported on a physical scale as $\mathrm{M_{vir}} = X^{+U}_{-L}\, \mathrm{M}_\odot$ should be interpreted on a log scale. For example, $\log_{10}$X is the posterior mean of $\log_{10} \mathrm{M_{vir}}$ and [$\log_{10}$(X-L), $\log_{10}$(X+U)] is the 68% credible interval in $\log_{10} \mathrm{M_{vir}}$. These summaries should not be naively translated to constraints on a linear scale as probability densities do not trivially

transform under a nonlinear change of variables (see Jensen's inequality). The MW mass inferred by each satellite is discussed in Section 4.4.1.

4.3.3 A Statistical Approximation to Include Several Low Mass Satellites Simultaneously

Thus far, we have only outlined how to infer the virial mass of the MW using the properties of any individual satellite galaxy for which the proper motion has been measured. While these individual estimates are interesting on their own, such an analysis leads to the question: what if the phase space information of all satellites is used simultaneously to infer the mass of the MW? One might expect that additional information from multiple satellites will yield a more precise MW mass.

Below we outline a statistical approximation to simultaneously infer the MW's mass using the properties of all nine low mass satellites. An approximation is necessary to make a combined MW mass estimate since Prior 2 does not exclusively include only halos with approximately 10 low mass satellites each (see Section 4.3.1). To consider an arbitrary number of satellites with measurements $\{\boldsymbol{d}_s\}$, Bayes' Theorem yields the joint posterior of host halo virial mass $\boldsymbol{M}_{\rm vir}$:

$$P(\{\boldsymbol{x}_s\}, M_{\rm vir}|\,\{\boldsymbol{d}_s\}, \boldsymbol{C}') = \frac{P(\{\boldsymbol{d}_s\}|\,\{\boldsymbol{x}_s\}) \times P(\{\boldsymbol{x}_s\}, M_{\rm vir}|\,\boldsymbol{C}')}{P(\{\boldsymbol{d}_s\}|\,\boldsymbol{C}')} \tag{4.6}$$

where $s = 1 \ldots N_{\rm sat}$ and $N_{\rm sat}$ is the total number of satellites considered. Because the measurements of each satellite are independent from the others, the likelihood can be written

$$P(\{\boldsymbol{d}_s\}|\,\{\boldsymbol{x}_s\}) = \prod_{s=1}^{N_{\rm sat}} P(\boldsymbol{d}_s|\,\boldsymbol{x}_s). \tag{4.7}$$

Next, we note that the prior factor can be written, using the definition of conditional probability,

$$P(\{\boldsymbol{x}_s\}, M_{\rm vir}|\,\boldsymbol{C}') = P(M_{\rm vir}|\,\boldsymbol{C}') \times P(\{\boldsymbol{x}_s\}|\,M_{\rm vir}, \boldsymbol{C}'). \tag{4.8}$$

If we make the *naive Bayes* assumption that, given the mass $M_{\rm vir}$, the satellites

properties $\{\boldsymbol{x}_s\}$ are conditionally independent, we have

$$P(\{\boldsymbol{x}_s\}|\, M_{\rm vir}, \boldsymbol{C}') = \prod_{s=1}^{N_{\rm sat}} P(\boldsymbol{x}_s|\, M_{\rm vir}, \boldsymbol{C}'), \tag{4.9}$$

and therefore,

$$P(\{\boldsymbol{x}_s\}, M_{\rm vir}|\, \boldsymbol{C}') = P(M_{\rm vir}|\, \boldsymbol{C}') \times \prod_{s=1}^{N_{\rm sat}} P(\boldsymbol{x}_s|\, M_{\rm vir}, \boldsymbol{C}'). \tag{4.10}$$

Putting this all together, we have

$$\begin{aligned} &P(\{\boldsymbol{x}_s\}, M_{\rm vir}|\, \{\boldsymbol{d}_s\}, \boldsymbol{C}') = \\ &\frac{\left[\prod_{s=1}^{N_{\rm sat}} P(\boldsymbol{d}_s|\, \boldsymbol{x}_s) P(\boldsymbol{x}_s|\, M_{\rm vir}, \boldsymbol{C}')\right] \times P(M_{\rm vir}|\, \boldsymbol{C}')}{P(\{\boldsymbol{d}_s\}|\, \boldsymbol{C}')}. \end{aligned} \tag{4.11}$$

The individual prior factors can be written

$$P(\boldsymbol{x}_s|\, M_{\rm vir}, \boldsymbol{C}') = \frac{P(\boldsymbol{x}_s, M_{\rm vir}|\boldsymbol{C}')}{P(M_{\rm vir}|\boldsymbol{C}')}, \tag{4.12}$$

so the joint posterior becomes:

$$\begin{aligned} &P(\{\boldsymbol{x}_s\}, M_{\rm vir}|\, \{\boldsymbol{d}_s\}, \boldsymbol{C}') = \\ &\frac{\left[\prod_{s=1}^{N_{\rm sat}} P(\boldsymbol{d}_s|\, \boldsymbol{x}_s) P(\boldsymbol{x}_s, M_{\rm vir}|\, \boldsymbol{C}')\right] \times P(M_{\rm vir}|\, \boldsymbol{C}')^{1-N_{\rm sat}}}{P(\{\boldsymbol{d}_s\}|\, \boldsymbol{C}')}. \end{aligned} \tag{4.13}$$

Next we notice that the posterior given the data for a single satellite s, is

$$P(\boldsymbol{x}_s, M_{\rm vir}|\, \boldsymbol{d}_s, \boldsymbol{C}') = \frac{P(\boldsymbol{d}_s|\, \boldsymbol{x}_s) P(\boldsymbol{x}_s, M_{\rm vir}|\, \boldsymbol{C}')}{P(\boldsymbol{d}_s|\, \boldsymbol{C}')}, \tag{4.14}$$

so the joint posterior is

$$\begin{aligned} P(\{\boldsymbol{x}_s\}, M_{\rm vir}|\, \{\boldsymbol{d}_s\}, \boldsymbol{C}') = &\left[\prod_{s=1}^{N_{\rm sat}} P(\boldsymbol{x}_s, M_{\rm vir}|\, \boldsymbol{d}_s, \boldsymbol{C}')\right] \times \\ &P(M_{\rm vir}|\, \boldsymbol{C}')^{1-N_{\rm sat}} \times \frac{\prod_{s=1}^{N_{\rm sat}} P(\boldsymbol{d}_s|\, \boldsymbol{C}')}{P(\{\boldsymbol{d}_s\}|\, \boldsymbol{C}')}. \end{aligned} \tag{4.15}$$

Integrating out $\{\boldsymbol{x}_s\}$, we find the marginal posterior for the mass given all of the satellites' data.

$$\begin{aligned} P(M_{\rm vir}|\, \{\boldsymbol{d}_s\}, \boldsymbol{C}') = &\left[\prod_{s=1}^{N_{\rm sat}} P(M_{\rm vir}|\, \boldsymbol{d}_s, \boldsymbol{C}')\right] \times \\ &P(M_{\rm vir}|\, \boldsymbol{C}')^{1-N_{\rm sat}} \times \frac{\prod_{s=1}^{N_{\rm sat}} P(\boldsymbol{d}_s|\, \boldsymbol{C}')}{P(\{\boldsymbol{d}_s\}|\, \boldsymbol{C}')} \end{aligned} \tag{4.16}$$

The last factor is a normalization constant that does not depend on the parameters. Since we already know how to calculate $P(M_{\rm vir}|\,\boldsymbol{d}_s, \boldsymbol{C'})$ for one satellite at a time using Eq. 4.5, a useful expression for the marginal posterior is:

$$P(M_{\rm vir}|\,\{\boldsymbol{d}_s\}, \boldsymbol{C'}) \propto \Big[\prod_{s=1}^{N_{\rm sat}} P(M_{\rm vir}|\,\boldsymbol{d}_s, \boldsymbol{C'})\Big] \times P(M_{\rm vir}|\,\boldsymbol{C'})^{1-N_{\rm sat}}. \tag{4.17}$$

By writing the marginal posterior distribution in this form, the multiplicity from including Prior 2 $N_{\rm sat}$ times is eliminated. Again, all calculations are computed in $\log_{10} \mathrm{M_{vir}}$ as noted in Section 4.3.2. Results for the combined MW mass estimates using this statistical approximation are discussed in Section 4.4.2.

4.3.4 The Conditional Independence Assumption and Computing the Joint Posterior Distribution

The conditional independence assumption states that the properties of a subhalo in a given host halo are independent from those of another subhalo in the same host halo for each given value of host halo mass. Here, we demonstrate the validity of this assumption for our statistical framework.

The conditional independence assumption requires that the correlation based on $P(j_{\rm sat,1}, j_{\rm sat,2}|M_{\rm vir})$, for example, is zero for all $\mathrm{M_{vir}}$ where $j_{\rm sat,1}$ and $j_{\rm sat,2}$ are the values of total specific orbital angular momentum for the first two low mass satellite analogs in each host halo (where at least two analogs exist). In Fig. 4.2, we plot $j_{\rm sat,1}$ versus $j_{\rm sat,2}$ for the fraction of Prior 2 as four subsamples split by host halo mass. The assumption should hold for all values of host halo mass. The Pearson correlation coefficient (r) between $j_{\rm sat,1}$ and $j_{\rm sat,2}$ for each subsample yields values between 0.12-0.27 with uncertainties < 0.07.

Physically, this weak correlation shows that there is reasonable scatter amongst satellite specific orbital angular momenta for the same host halo. This suggests that satellites' angular momenta vectors are not set by the strength of the large scale tidal field but rather by more complex processes such as varying accretion and orbital histories even for satellites orbiting the same host. Such values suggest there

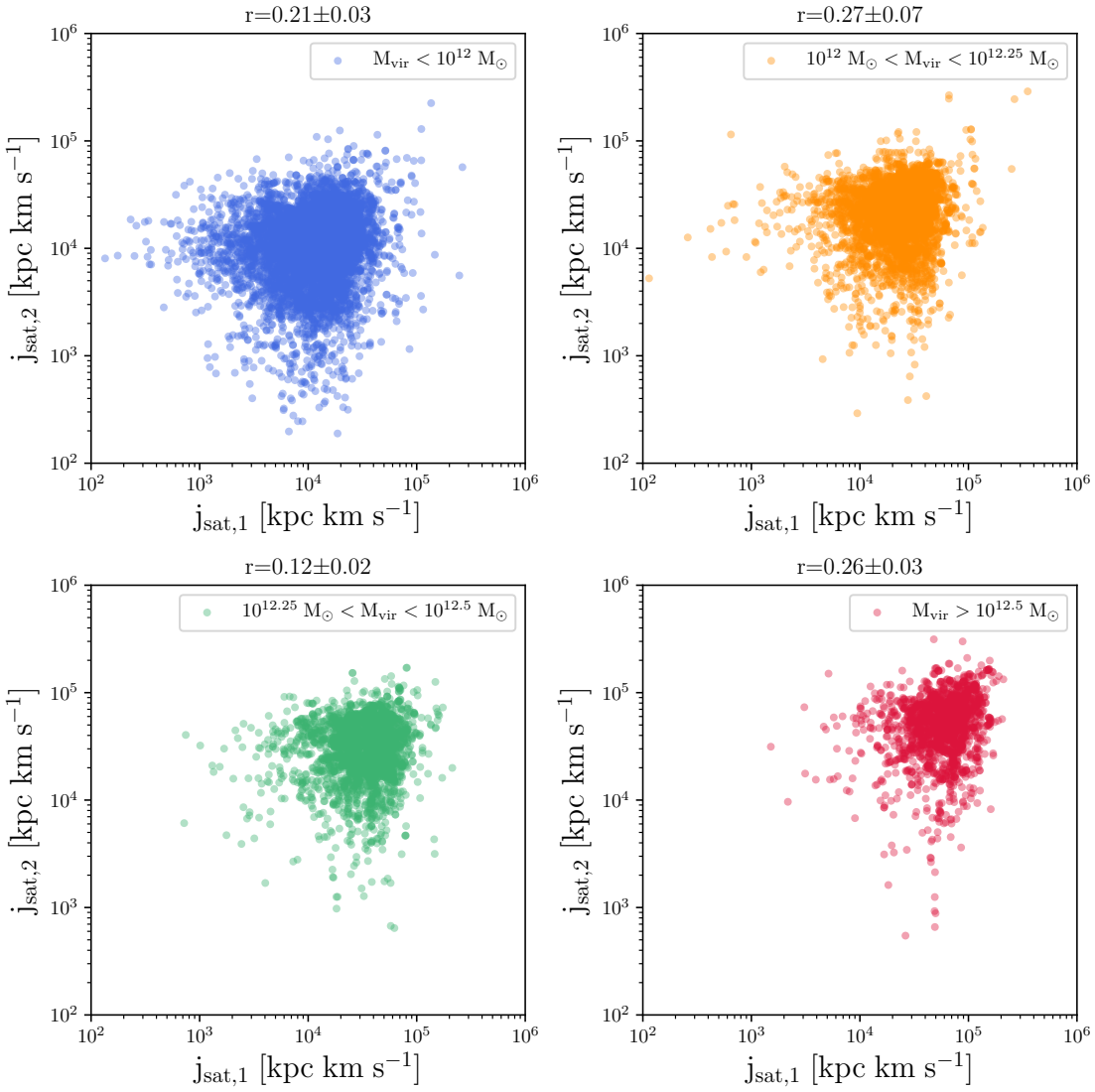

Figure 4.2: For all hosts in Prior 2 that host at least two low mass satellite analogs, the magnitude of the specific orbital angular momentum of the first (more massive) satellite is plotted against that of the second satellite. The sample is split into four bins based on host halo mass. Pearson's correlation coefficient (PCC) for each subsample is denoted by the r value above each panel. The PCC for the whole sample population is $r_{all} = 0.56 \pm 0.01$. Errors are computed using bootstrap resampling. There is only a weak correlation between $j_{\rm sat,1}$ and $j_{\rm sat,2}$, indicating that the conditional independence assumption is reasonable.

is only a weak 2-point correlation and therefore that the conditional independence is a useful and reasonable approximation. The conditional independence assumption actually requires that the N dimensional joint distribution factors as:

$$\begin{aligned} &P(j_{\rm sat,1}, j_{\rm sat,2}..., j_{\rm sat,N}|M_{\rm vir}) = \\ &P(j_{\rm sat,1}|M_{\rm vir}) \times P(j_{\rm sat,2}|M_{\rm vir}) \times ... \times P(j_{\rm sat,N}|M_{\rm vir}.) \end{aligned} \tag{4.18}$$

However, we have only demonstrated this for N=2 in Fig. 4.2, as it is difficult to rigorously show this for N $>$ 2.

Calculating Eq. 4.17 directly can sometimes lead to numerical underflow or overflow errors. To prevent this, we compute the logarithm of Eq. 4.17, apply it to our data, and exponentiate to retrieve the final results. This strategy is successful in a majority of cases unless the product of all satellite kernel density estimate (KDE) posteriors and the KDE estimate of the prior in Eq. 4.17 both approach zero in a numerically unstable way. In such cases, the limiting edge effects must be carefully considered to produce a stable result. Such numerical caveats will be unnecessary when more advanced high resolution simulations are available.

4.4 MW Mass Results Using the Classical Dwarf Satellites

We now infer the mass of the MW using both the instantaneous and momentum likelihood methods with the properties of each individual dwarf satellite and the Illustris-Dark cosmological simulation. While we already demonstrated in P17B that the momentum method is more reliable as a function of time and satellite orbital phase, we will report results from both likelihood functions for comparison. We also include the results for the ensemble MW mass estimates using all classical satellites.

In what follows, we provide mass estimates of the MW using the LMC's orbital properties and Prior 1. However, this mass estimate cannot be combined with those resulting from the lower mass satellite galaxies as the two sets of results are computed from two different prior samples (Prior 1 vs. Prior 2).

Table 4.2: Summary Statistics for MW Mass Estimates

	Instantaneous M_{vir} [10^{12} $M_\odot$]	Momentum M_{vir} [10^{12} $M_\odot$]
LMC	$1.45^{+1.75}_{-0.41}$	$1.0^{+0.79}_{-0.56}$
Leo II	$1.52^{+0.58}_{-0.59}$	$1.54^{+1.14}_{-0.7}$
Fornax	$1.11^{+0.84}_{-0.45}$	$1.44^{+1.11}_{-0.63}$
Leo I	$2.02^{+0.60}_{-0.69}$	$1.41^{+1.13}_{-0.62}$
Sculptor	$1.12^{+0.55}_{-0.39}$	$1.14^{+0.94}_{-0.51}$
Sextans	$1.03^{+0.64}_{-0.35}$	$1.12^{+0.93}_{-0.50}$
Ursa Minor	$0.80^{+0.65}_{-0.33}$	$0.96^{+0.76}_{-0.48}$
Draco	$0.91^{+0.57}_{-0.34}$	$0.92^{+0.70}_{-0.45}$
Carina	$0.66^{+0.46}_{-0.33}$	$0.91^{+0.76}_{-0.45}$
Ensemble (8 sats)	$1.19^{+0.19}_{-0.21}$	$0.96^{+0.29}_{-0.28}$
Sagittarius dSph	–	$0.78^{+0.76}_{-0.39}$
Ensemble (9 sats)	–	$0.85^{+0.23}_{-0.26}$

Note. — The posterior mean and 68% credible interval in halo mass for the MW using the properties of each of the nine low mass satellites and the LMC. The MW halo mass computed using host halos in Prior 2 and the properties of eight (nine) low mass satellites simultaneously is given in the third to last row. The MW mass derived using the LMC was calculated with Prior 1 (first row). The LMC is excluded from the ensemble mass estimates since these calculations use fundamentally different prior samples (Prior 1 vs. Prior 2). The SMC's properties are not considered due to the low frequency of LMC-SMC analog pairs in Illustris-Dark.

4.4.1 MW Mass Estimates from Individual Low Mass Dwarf Satellites

Instantaneous Likelihood

The top left panel of Fig. 4.3 shows the MW mass estimates and associated uncertainties for each low mass satellite using the instantaneous likelihood method. The inferred MW masses are plotted against the total velocity of each satellite relative to the MW today (Table 4.1, Column 4). Error bars indicate the MW's posterior mean mass included in the 68% credible interval of the posterior distribution for host halo mass. The colored lines in the bottom left panel of Fig. 4.3 show the corresponding posterior distributions. All results are also listed in Table 4.2. The

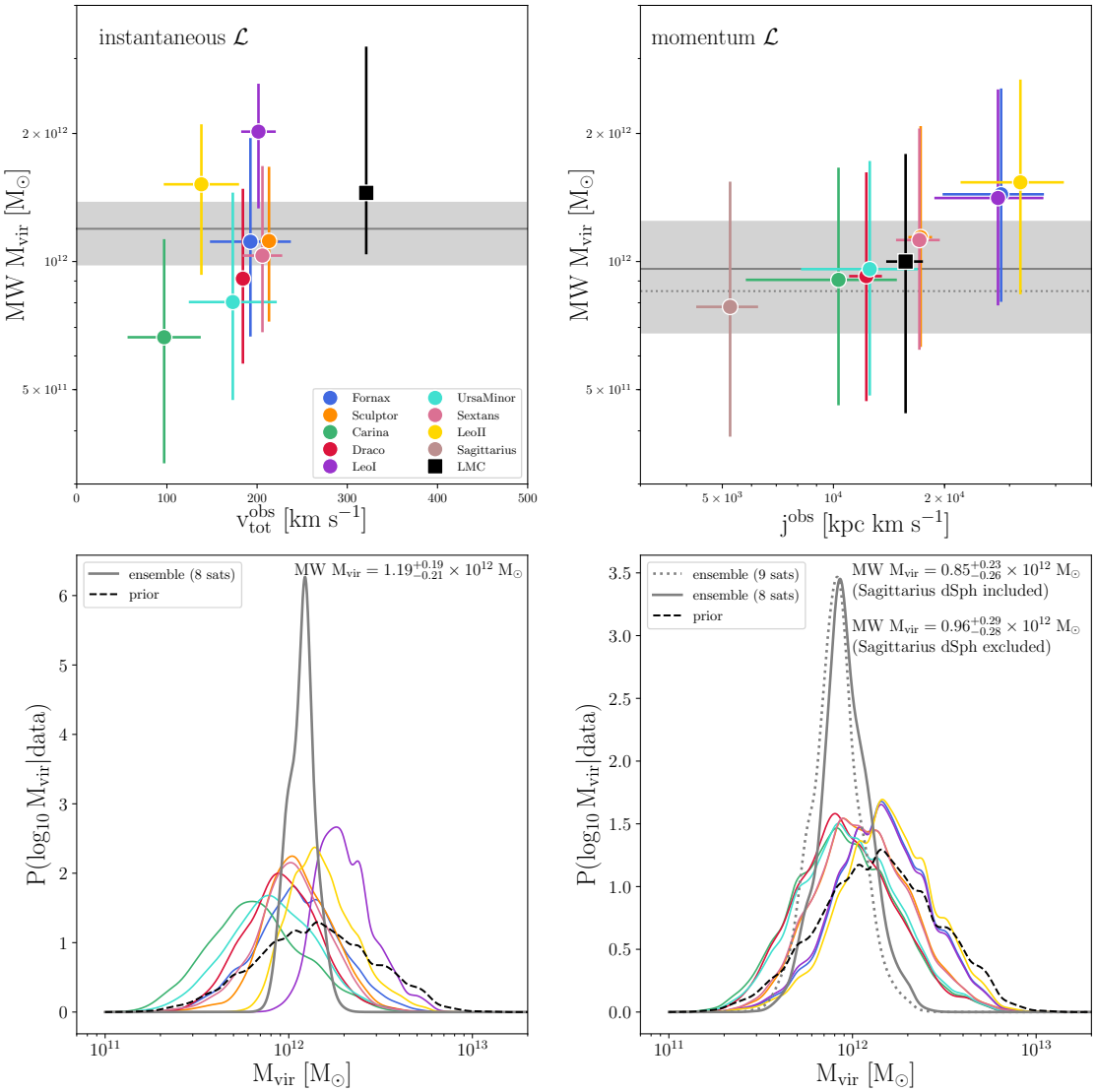

Figure 4.3: *Top panels:* Summaries of the posterior distributions for MW halo mass using Prior 2 and the observed properties of the classical low mass MW satellites with proper motions. Markers with error bars indicate the posterior mean halo mass and the halo mass included in the 68% credible interval. The left panel shows the results from the instantaneous likelihood method versus the total velocity of each satellite today relative to the MW. The right panel shows the results from the momentum likelihood method versus the magnitude of the current specific orbital angular momenta. The gray shaded regions indicate the 68% credible interval for MW halo mass using the ensemble of low mass satellites (i.e. excluding the MCs and Sgr dSph). *Bottom panels:* The posterior distributions in MW halo mass for each individual low mass satellite are shown as colored curves. The black dashed lines indicate the probably distribution of the prior sample given equal likelihood weights. The solid gray curves represent the ensemble posterior distributions (excluding Sgr dSph) and the dotted gray curve in the right panel is the ensemble posterior including Sgr dSph. The resulting posterior mean masses are listed in the top right of each panel. All calculations are computed in $\log_{10}(M_{vir})$. See Section 4.4.2 for details on the alignment of the ensemble posterior distributions with the individual posterior distributions.

LMC is indicated by a black square in Fig. 4.3.

The results of the instantaneous method display a fairly large scatter (standard deviation of ~ 0.14 dex) among the posterior mean mass estimates for the MW using each individual satellite. The lowest value for the MW's mass comes from Carina, which suggests a posterior mean MW mass of only $0.66 \times 10^{12}\,\mathrm{M}_{\odot}$. As expected, the highest MW mass estimate ($2.02 \times 10^{12}\,\mathrm{M}_{\odot}$) with the instantaneous method comes from Leo I. This mass is consistent with the bound mass arguments given by BK13 and the mass inferred by the radial timing-argument, but lower than that given by the non-radial timing argument (Li and White, 2008; Sohn et al., 2013). Carina is on a low energy, fairly circular orbit about the MW (Pasetto et al., 2011), whereas Leo I is on a high energy orbit and has recently completed its first pericentric approach (Sohn et al., 2013). The difference in orbital energies suggests a strong correlation between energy and halo mass.

As any one individual satellite can produce a MW mass estimate that could be misleading given its orbital energy, this warrants combining as many satellites as possible to infer the mass of the MW in tandem. The instantaneous method essentially reproduces expectations for the MW's mass from traditional methods such that Leo I pushes the MW's mass to higher values and satellites on more circular orbits that experience little to no dynamical friction prefer lower MW halo masses.

The Sagittarius dSph has been omitted from the results for the instantaneous method as the effective sample size reduces to just a few during the importance sampling step given its unique combination of position and velocity. Upon examining the cumulative number density of subhalos in Prior 2 at any given distance relative to their respective host, we find that the minimum host-satellite separation is $\sim$ 30 kpc. Therefore, very few subhalos are found at the separation of Sagittarius (20 kpc) in Illustris-Dark. This problem may be two-fold as the gravitational smoothing length of Illustris-Dark may not be able to sufficiently resolve distinct halos at these small separations and there may also be a depletion of subhalos in the inner regions of halos due to tidal disruption, especially for subhalos on radial orbits (Garrison-

Kimmel et al., 2017c).

While only ∼20% of the known MW satellites (e.g. Drlica-Wagner et al., 2015) are considered in this analysis, the individual estimates using the instantaneous method already demonstrate a factor of three scatter in MW halo mass, even larger than that in the literature to date. The instantaneous method is not recommended if unbiased MW mass estimates are desired.

Momentum Likelihood

MW mass estimates for the momentum method are plotted in the top right panel of Fig. 4.3 against the current magnitude of specific orbital angular momentum for each satellite. The bottom right panel shows the corresponding posterior distributions. In general, we see a similar trend amongst the low mass satellites as we did for the LMC and M33 analysis in P17B – satellites that have a higher total specific orbital angular momentum value (see Table 4.1) infer higher MW masses. The same trend is not strictly true for v_{tot}^{obs} (Fig. 4.3, top left panel) or r^{obs}. Overall, the scatter among individual MW mass estimates using the momentum method is far better constrained to a range of $0.78 \times 10^{12}\,M_{\odot}$ (Sagittarius dSph) – $1.54 \times 10^{12}\,M_{\odot}$ (Leo II), in agreement with the current factor of two spread in MW mass. Excluding Sagittarius dSph, the scatter of our results is narrowed even further to $0.91 - 1.54 \times 10^{12}\,M_{\odot}$. Comparing the standard deviation across individual estimates from the instantaneous method and the momentum method gives ~ 0.14 dex versus ~ 0.09 dex, clearly demonstrating the improvement that the momentum method provides if satellites are used individually.

In P17B, we demonstrated that using instantaneous properties like position and velocity skew the resulting MW mass estimates because they change significantly with time. The specific orbital angular momentum vector of Sagittarius dSph has likely undergone significant changes since its infall into the halo of the MW due to the tidal stripping of its stars and subsequent formation of the Sagittarius stellar stream (see Belokurov et al., 2014). It is therefore unsurprising that Gibbons et al. (2014) and our analysis yield such low MW masses using the Sagittarius dSph (or its

associated stream). The MW mass inferred by the Sagittarius dSph should therefore be taken with caution.

Contrary to previous studies, Leo II, rather than Leo I, puts limits on the MW's mass. Leo II has the highest specific orbital angular momentum of the satellites considered in this analysis, so it brackets the upper end of the MW's plausible mass range.

Satellites on the most extreme orbits, where they have only made one pericentric passage about the MW (Leo I or the LMC), also show the biggest deviations between the posterior mean masses estimates using the instantaneous versus the momentum method. The fact that the MW mass estimates vary so drastically for these satellites provides further evidence that the combination of position and velocity is not reliable for recovering the mass of the MW accurately, and cautions against using one satellite alone to infer the MW's mass.

We conclude that the momentum method is not only a more consistent estimator of host halo mass as a function of time and orbital evolution but it is also a more consistent method for determining the mass of a host halo given the 6D phase space information for a *population* of satellite galaxies. The momentum method directly correlates inferred host halo mass and satellite specific orbital angular momentum, thereby distinguishing between halos that can host a population of satellites exhibiting a given observationally constrained distribution of specific orbital angular momenta and those that cannot. The correlation between the distribution of specific orbital angular momentum for a population of satellites and host halo mass will be discussed further in Section 4.5.

While the momentum method for low mass satellites only considers one physical property associated with each satellite – the magnitude of the specific orbital angular momentum – it encompasses some 6D phase space information of each satellite too as $j = |\boldsymbol{r} \times \boldsymbol{v}|$, where $\boldsymbol{r}$ and $\boldsymbol{v}$ are 3D vectors. The direction of the specific orbital angular momentum method is not utilized in this method, as given. In principle, such information could be incorporated into the momentum likelihood function, but this is beyond the scope of this work.

Caveats for the Individual MW Mass Estimates

In P17B, we carried out an additional bootstrap analysis to address the sampling noise associated with our technique. This is especially important for satellites in unique orbital configurations, like the LMC and the Sagittarius dSph. Since Prior 2 is significantly larger than that considered in P17B, the effective sample size does not rapidly decrease to zero for most of the classical MW satellites (except Sagittarius dSph) considered. We also showed in Section 5.2 of P17B that smaller measurement errors can improve host halo mass estimates, but when the precision is already as low as a few percent (as is the case for the LMC, Sculptor, Draco), the change in results is insignificant. The Gaia mission will be able to reduce the measurement errors on proper motions and derived quantities for the nearest classical satellite galaxies (van der Marel and Sahlmann, 2016a), further narrowing MW mass estimates using those satellites.

The barrier to achieving very high precision MW mass estimates for the individual satellites is the irreducible uncertainty owing to cosmic variance (Section 5.3, P17B), or the intrinsic correlation between host halo mass and satellite dynamics. We expect that the most significant improvements to the precision of MW mass estimates will therefore arise from using the properties of several satellites simultaneously.

4.4.2 MW Mass Estimates from the Ensemble of Low Mass Dwarf Satellites

Using the statistical approximation outlined in Section 4.3.3, the most probable MW mass resulting from the ensemble of low mass classical satellites and each of the likelihood methods are represented by the gray shaded regions in the top panels of Fig. 4.3 and by the gray lines in the bottom panels of Fig. 4.3.

For the instantaneous method, the combination of eight low mass satellites (Sagittarius dSph excluded) yields an ensemble MW mass estimate of $M_{vir,MW} = 1.19^{+0.19}_{-0.21} \times 10^{12}\,M_\odot$ ($\log_{10}(M_{vir}/M_\odot) = 12.08^{+0.06}_{-0.09}$). The ensemble MW halo mass

resulting from the momentum likelihood using the same eight satellites is $M_{vir,MW} = 0.96^{+0.29}_{-0.28} \times 10^{12}$ ($\log_{10}(M_{vir}/M_\odot) = 11.98^{+0.11}_{-0.15}$). When Sagittarius dSph is included in the combined mass estimate using the momentum method, the mass of the MW decreases to $M_{vir,MW} = 0.85^{+0.22}_{-0.26} \times 10^{12}\,M_\odot$ ($\log_{10}(M_{vir}/M_\odot) = 11.93^{+0.11}_{-0.16}$) with a larger uncertainty. The larger measurement errors for the observed j values results in a wider 68% credible interval for the momentum method compared to the instantaneous method, but all results are narrower than the current factor of two spread in mass and far more precise than those predicted by any one satellite.

Note that the posterior distributions for the ensemble mass estimates in Fig. 4.3 are slightly shifted relative to the posterior distributions for each individual satellite. This is because the ensemble posterior mass distributions are calculated by dividing out the multiplicity of the prior, whereas the individual posteriors still include one instance of the prior. If instead all of the individual posterior distributions were multiplied together to form the joint posteriors, they would align with the individual posterior distributions.

Recall that the SMC was excluded from the prior selection criteria (see Section 4.3.1) and therefore its specific orbital angular momentum ($j_{SMC} = 13,209 \pm 2,067$ kpc km s^{-1}) is not included in the ensemble mass estimates. While the SMC is not explicitly accounted for in this analysis, we expect that it is unlikely to significantly change the results since its specific orbital angular momentum lies approximately between that of Ursa Minor and the LMC.

Our ensemble mass estimates suggest that Leo I could be bound to the MW within the associated credible intervals. According to the upper 68% credible interval when the Sagittarius dSph is excluded from our momentum method results, MW masses between $0.96 - 1.25 \times 10^{12}\,M_\odot$ ($R_{vir} > 260$ kpc) suggest that Leo I is bound to the MW. However, these results are preliminary since we only use the phase space information for 20% of all known MW satellite galaxies. These conclusions should be revisited as the observational data set increases.

We conclude that sampling the full range of specific orbital angular momentum for the observed MW satellite population provides the most reliable mass estimate

as it includes much of the available 6D phase space information in an unbiased fashion. Our results are in good agreement with the complementary work of Li et al. (2017). They have used nine cosmological zoom simulations and a scaling method with the angular momentum and energy distribution of the classical MW satellites to conclude a MW mass of $1.3 \times 10^{12}\,\mathrm{M}_{\odot}$ with a $\sim$40% error. They are also consistent with independent mass estimation methods such as those presented in Kafle et al. (2012, 2014), which use observations of the stellar halo and blue horizontal branch stars to estimate the MW's mass.

Tests and Caveats for Ensemble MW Mass Estimates

To test whether the statistical approximation outlined in Section 4.3.3 yields accurate results when the individual posteriors of the classical MW satellites are combined via a statistical approximation, we estimated the mass of 100 random halos from Illustris-Dark. By comparing the estimated masses to the true host halo mass for these 100 halos, we can assess whether our method accurately recovers host halo mass. For this calculation, all subhalos in the 100 randomly chosen host halos were assigned a 20% measurement error on the magnitude of their specific orbital angular momenta. For the true MW satellites, measurement errors range from about 7% up to about 40%. We find that in approximately 90% of these halos, the true mass is contained within two posterior standard deviations of the posterior mean (in dex). Ideally, this would be true for 95% of the halos but we expect that this 5% deficit will disappear when more suitable simulations are available. Similar results are recovered when a 10% measurement error is applied to the properties of all subhalos in these 100 test halos.

Note that the MW mass estimates resulting from the ensemble of classical satellites in this work are preliminary. Currently, Fig. 4.3 only shows the results for about 20% of all known MW satellites. Recent work suggests that this satellite population is less than 10% of the total number of satellites predicted around the MW (see Tollerud et al., 2011a; Newton et al., 2018). When the proper motions of additional low mass satellites, such as ultra-faint dwarfs, and a large volume sim-

ulation that can resolve analogs of ultra-faints become available, we can rigorously test the limits of this method. However, we expect that the combined MW mass estimate calculating using N satellites will eventually plateau due to cosmic variance. See Li et al. (2017) for predictions in the context of satellite galaxies and Wang et al. (2017) on how the number of independent phase-space structures contributes to mass uncertainties.

4.5 Discussion

In Section 4.4.1, we note the strong correlation between the specific orbital angular momenta distribution of the observed satellite population and the MW mass inferred by those satellites. Naturally, this leads to the question: is there a correlation between host halo mass and the distribution of specific orbital angular momentum for a population of subhalos? We use simulated analogs from Illustris-Dark to explore if this intrinsic relationship exists and how it might inform our knowledge of the MW's true mass.

4.5.1 The Halo Mass-Specific Angular Momenta Distribution Relation in the Presence of a Massive Satellite

Fig. 4.4 shows the distribution of total specific orbital angular momenta for subhalos in Prior 2 (Section 4.3.1) binned by their corresponding host halo mass. The specific orbital angular momenta shown are the median values for each host halo mass bin and the error bars indicate the extents of the 25th and 75th quartiles. The gray shaded area shows the median and quartiles of the specific orbital angular momentum distribution for the population of classical MW satellites considered in this work.

The high concentration of subhalos residing in halos with masses between $\log_{10}(M_{vir}/M_{\odot}) \approx 11.8 - 12.3$ suggests that this is the most typical MW halo mass independent of our results from Section 4.4. This mass range is in agreement with the frequentist MW mass predictions from Patel et al. (2017a) using the energetics

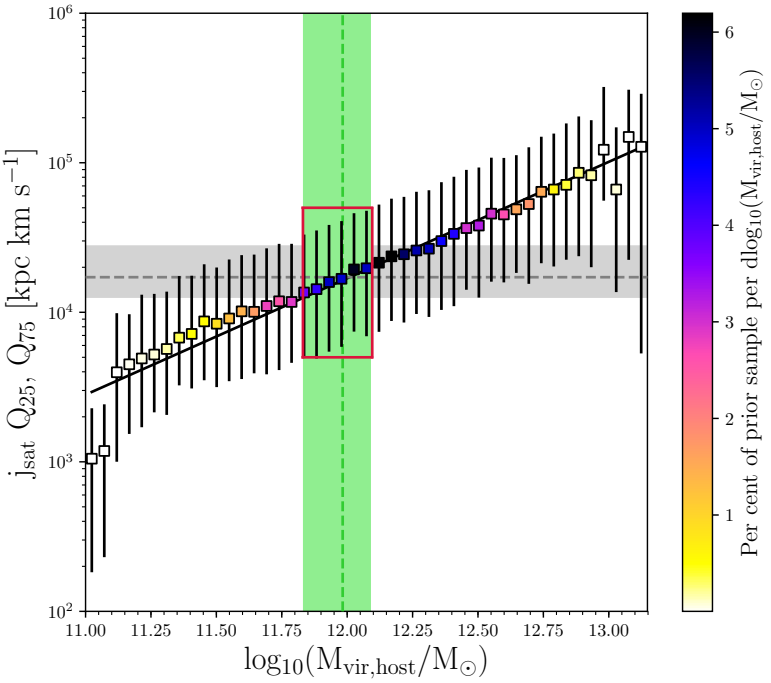

Figure 4.4: The median value of specific orbital angular momentum for the low mass satellite analogs in Prior 2 binned by host halo virial mass. The error bars show the extents of the 25th and 75th percentiles for specific orbital angular momentum in each mass bin. The gray dashed line and shaded region show the median specific angular momentum value of eight low mass MW satellites (Sagittarius dSph excluded) and the extents of corresponding quartiles. The green dashed lines and shaded region represent the posterior mean mass of the ensemble estimate using the momentum likelihood and the corresponding 68% credible interval ($\log_{10}(M_{vir}/M_\odot) = 11.98^{+0.11}_{-0.15}$). The color map indicates the percent of low mass subhalos in Prior 2 that fall in each host mass bin. The highest percentages of subhalos reside in host halos with masses $\log_{10}(M_{vir}/M_\odot) \approx 11.8$-$12.3$, consistent with the properties of the classical dSphs and the results reported in this work. The black solid line is the line of best fit. When the specific orbital angular momentum values of the LMC analogs are added to the data sample shown here, the overall relation between the specific orbital angular momentum distribution and halo mass still holds. The red box indicates the expected j values for ultra-faint dwarf galaxies.

of LMC analogs in Illustris-Dark. Note that this region is also coincident with the gray shaded area, which represents the true distribution of orbital angular momentum for eight of the classical MW satellites. The green dashed line and shaded region represent the posterior mean and 68% credible interval included in the ensemble MW mass estimate from the momentum method (see Table 4.2, last row). The black solid line is the line of best fit with a slope of $m = 0.779 \pm 0.0280$ and an intercept of $b = -5.116 \pm 0.339$ in units of dex (i.e. the fits are calculated using $\log_{10}(\mathrm{j_{sat}})$ and $\log_{10}(\mathrm{M_{vir}/M_{\odot}})$).

When we further explore if the specific orbital angular momenta-host halo mass trend is correlated with the orbital history of the massive satellite analogs, we find that the linear relationship shown in Fig. 4.4 is generally unaffected. The subhalos residing in halos whose massive satellite analogs have crossing times[2] less than 4 Gyr ago (first infall scenarios) and those hosting massive satellite analogs with crossing times more than 4 Gyr ago (multiple passages about their hosts) exhibit slopes in agreement with the best fit line in Fig. 4.4 (black solid line).

Using Fig. 4.4, we can also make predictions for the specific orbital angular momenta of ultra-faint dwarf galaxies. The red box, which encompasses the region of highest subhalo abundance (darkest blue squares), our MW mass estimate (green shaded region), and the observed distribution in specific orbital angular momentum of satellites (gray shaded region) warrants the prediction that ultra-faint dwarfs should generally exhibit 5×10^3 kpc km s$^{-1} < j^{obs} < 5 \times 10^4$ kpc km s^{-1} if the MW's true mass is $\sim 10^{12}\,\mathrm{M_{\odot}}$. Upcoming observations of ultra-faint dwarf galaxies will be some of the most interesting in this regard given their expected abundance.

4.5.2 The Halo Mass-Specific Angular Momenta Distribution Relation in the Absence of a Massive Satellite

We now explore whether the absence of a massive satellite analog changes the satellite specific angular momentum distribution as a function of host halo mass. To do

[2]Crossing time is defined as the first time a subhalo crosses the time-evolving virial radius of its host halo, moving inwards. See Patel et al. (2017a) for more details.

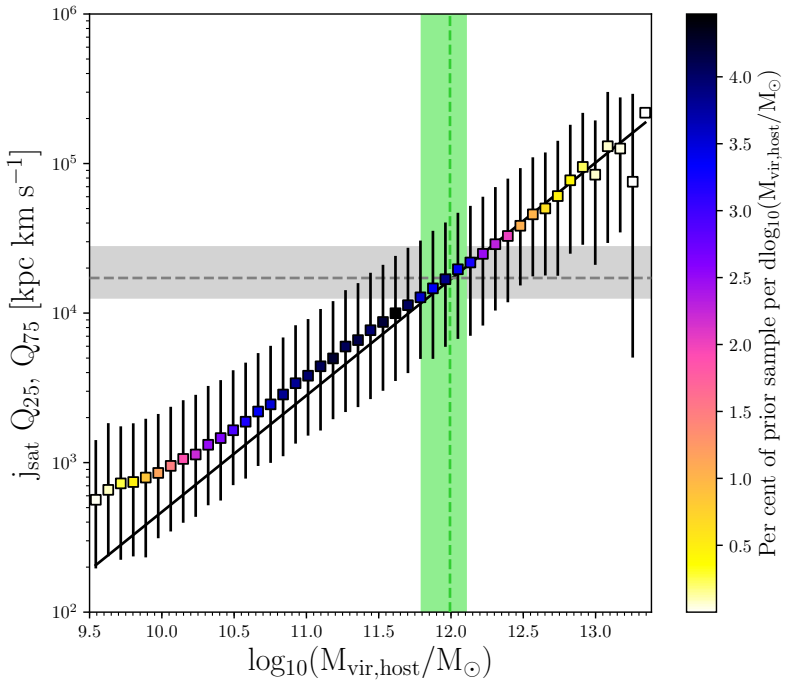

Figure 4.5: Similar to Fig. 4.4 except these subhalos reside in systems where a massive satellite analog (Section 4.3.1) is not required. This sample is chosen from the final five snapshots of the Illustris-Dark halo catalogs and consists of 179,381 subhalos. The green dashed lines and shaded region now represent the ensemble posterior mean mass of the MW using eight satellites and the corresponding 68% credible interval using the momentum likelihood and this new data sample ($\log_{10}(M_{vir}/M_\odot) = 11.99^{+0.12}_{-0.20}$). The black solid line is the line of best fit from Fig. 4.4. The general relationship between host halo mass and specific orbital angular momenta holds, except at the low mass end. In low mass host halos, the angular momentum distribution is on average higher if massive satellite analogs are not included. Without a massive satellite analog, subhalos are most likely to be found in halos with masses ranging from $\log_{10}(M_{vir}/M_\odot) \approx 10.6$-12.1. The agreement in MW mass estimates (green shaded region) between these results and Fig. 4.4 shows that the method is not strongly biased by the selection of the prior sample.

so, we choose a new sample including all host halos in the final five snapshots of Illustris-Dark that pass the low mass satellite analog selection criteria ($\mathbf{C}'$) given in Section 4.3.1 without requiring that a massive satellite analog (Section 4.3.1) also resides in the halo. Thus, the host halos included in Prior 1 are strictly excluded from this sample. The new sample contains 179,381 low mass satellite analogs residing in 104,362 unique host halos.

Fig. 4.5 shows the distribution of subhalo specific orbital angular momenta binned by halo mass for this alternate set of Illustris-Dark subhalos. These subhalos reside in halos with masses extending down to $\log_{10}(M_{vir}/M_{\odot}) \approx 9.3$ due to the absence of a massive satellite analog, roughly two orders of magnitude lower than in Fig. 4.4. The gray shaded region is identical to that shown in Fig. 4.4 and represents the range of specific orbital angular momenta for eight low mass classical MW satellites. The green shaded region represents the posterior mean and 68% credible interval included in the ensemble MW mass estimate from the momentum method calculated using this new sample (i.e. no massive satellite analogs).

The black solid line is the line of best fit from Fig. 4.4 and it indicates that the overall relationship between halo mass and specific orbital angular momentum distribution (i.e. the slope of the distribution) still exists. However, at very low host halo masses, the corresponding orbital angular momentum distribution begins to deviate from this trend such that the median specific orbital angular momentum is higher than if a massive satellite analog is included. This is important because it means that massive satellites (i.e. $\sim 10\%$ of their host's mass) may affect the orbital histories and kinematics of lower mass satellites, but it is harder to see explicitly in the higher host halo masses because a wide range of massive satellite analogs were included in the analysis. We conclude that there is a relationship between these two quantities only in host halos with masses $\log_{10}(M_{vir}/M_{\odot}) > 11.5$ whether or not a massive satellite analog (i.e. LMC-mass companion) is present.

A few additional points of interest are also worth noting upon comparing Figs. 4.4 and 4.5. The abundance of low mass satellite analogs as a function of host halo mass (depicted by the color bars) is highest in halos with $\log_{10}(M_{vir}/M_{\odot}) \approx$

$11.8 - 12.3$ in Fig. 4.4 when massive satellite analogs are present compared to a range of $\log_{10}(M_{vir}/M_{\odot}) \approx 10.6$-12.1 in Fig. 4.5 when they are not present. Such differences are expected from the hierarchical assembly of galaxy halos and are probably closely linked to the subhalo abundance functions for halos with and without a massive satellite companion (see Appendix C.2). Despite these differences, the analysis still yields narrow MW mass ranges that are in agreement with each other (green shaded regions). This suggests there is no bias associated with the presence or absence of a massive satellite analog and that our prior selection criteria are justified.

The existence of a strong correlation between halo mass and the distribution of orbital angular momenta for subhalos provides a generalized trend that can be applied to halos and their subsequent satellite populations. While the MW system is often considered common in a cosmological context, recent work by Geha et al. (2017) cautions against thinking about the MW as a *typical* halo in their study of observational MW analogs and their satellite populations' abundance and properties. Our notes on this trend are therefore widely applicable.

4.6 Conclusions

Building on the Bayesian framework used to estimate the MW's virial mass from P17B, we provide a new methodology to combine the 6D phase space information of multiple low mass dwarf satellites. By doing so, we are able to estimate the mass of the MW using each of the following satellites individually and as an ensemble: Fornax, Sculptor, Carina, Draco, Leo I, Ursa Minor, Sextans, Leo II, Sagittarius dSph. This method is straightforwardly generalizable to include more dwarf satellites as new data is obtained. The main conclusions of this work are summarized below.

- When the mass of the MW is inferred using each low mass satellite individually, we find a much larger scatter in the mass of the MW using the instantaneous method. This method yields a MW mass range of $0.6 - 2 \times 10^{12}\,M_{\odot}$ across eight low mass satellites (Sagittarius dSph excluded), while the momentum method

spans a much narrower range from $0.9 - 1.5 \times 10^{12}\,\mathrm{M}_{\odot}$ for eight satellites. The latter results are more constrained than the current values in the literature.

- By combining the posterior distributions associated with each satellite, we also report ensemble MW mass estimates. The combination of eight low mass satellites with the instantaneous method results in a MW mass of $\mathrm{M}_{\mathrm{vir,MW}} = 1.19^{+0.19}_{-0.21} \times 10^{12}\,\mathrm{M}_{\odot}$ ($\log_{10}(\mathrm{M}_{\mathrm{vir}}/\mathrm{M}_{\odot}) = 12.08^{+0.06}_{-0.09}$). Using the momentum method, the ensemble mass estimate is $\mathrm{M}_{\mathrm{vir,MW}} = 0.96^{+0.29}_{-0.28} \times 10^{12}$ ($\log_{10}(\mathrm{M}_{\mathrm{vir}}/\mathrm{M}_{\odot}) = 11.98^{+0.11}_{-0.15}$). If Sagittarius dSph is included from the latter estimate, it decreases to $\mathrm{M}_{\mathrm{vir,MW}} = 0.85^{+0.22}_{-0.26} \times 10^{12}\,\mathrm{M}_{\odot}$ ($\log_{10}(\mathrm{M}_{\mathrm{vir}}/\mathrm{M}_{\odot}) = 11.93^{+0.11}_{-0.16}$). These ensemble estimates are more precise than the masses inferred by any individual satellite and they narrow the mass range to less than a factor of two.

- Satellites with high specific orbital angular momentum like Leo II, as opposed to high speed satellites like Leo I or the LMC, now constrain the upper end of the MW's mass range. Satellites in the midst of disruption like the Sagittarius dSph have the lowest specific orbital angular momentum and therefore push the MW's mass to low values. As any one satellite alone can result in a biased MW mass estimate, satellite galaxies that are not undergoing disruption (evidenced by tidal tails or streams) are the most ideal candidates for this method.

- The 68% credible interval of the ensemble MW mass resulting from the momentum method when the Sagittarius dSph is excluded ranges from $0.67 - 1.25 \times 10^{12}\,\mathrm{M}_{\odot}$. This suggests Leo I could be bound to the MW if its true mass is in the upper half of this range (since $\mathrm{M}_{\mathrm{vir}} = 10^{12}\,\mathrm{M}_{\odot}$ corresponds to $\mathrm{R}_{\mathrm{vir}} \approx 260$ kpc). Our analysis only includes a fraction of the MW's satellite galaxy population, and while our MW mass estimates are not expected to change drastically as more satellites are included, these results are still preliminary.

- We find there is a linear relationship between host halo mass and the distribution of specific orbital angular momentum for subhalos at a given halo mass. This trend is independent of the presence of massive satellite analogs and their or-

bital histories (i.e. first infall versus multiple orbits). The presence of a massive satellite analog does, however, change the halo mass range in which low mass subhalos are likely to reside. For example, when we require all halos to harbor a massive satellite analog, subhalos are most abundant in halos with masses $\log_{10}(M_{vir}/M_{\odot}) \approx 11.8 - 12.3$. When massive satellites are not present, this range broadens and shifts down to $\log_{10}(M_{vir}/M_{\odot}) \approx 10.6 - 12.1$. The median specific orbital angular momentum of satellites in lower mass host halos is higher if massive satellite analogs are not present, suggesting a massive satellite that is a high fraction of the host halo mass can affect the kinematics of the low mass satellite population. While this trend brackets the orbital angular momenta distribution expected at a given host halo mass, our tests on the conditional independence assumption shows that the individual angular momentum vectors of satellites around a shared host are independent of one another.

- Upon comparing this trend to the distribution of specific orbital angular momenta for MW satellites with measured proper motions, we predict that ultra-faint MW dwarfs will have specific orbital angular momenta values between $5 \times 10^3 - 5 \times 10^4$ kpc km s^{-1}. Future proper motion measurements for MW dwarfs (HST-GO-14734, P.I. N. Kallivayalil) and specifically the ultra-faints residing at ~ 100 kpc (HST-GO-14236, P.I. S.T. Sohn) will allow us to test this hypothesis.

We have shown that combining a majority of the available satellite phase space information has already narrowed the plausible mass range for the MW, and eventually, the same can be done for M31 and other nearby galaxies in the era of JWST. As more satellite information becomes available, significant improvements to current cosmological simulations are crucial so a large prior sample of MW analogs, each hosting tens of satellites, can be selected. Together, a larger high precision data set for MW substructures and more advanced simulations will be powerful tools for converging on a precise and accurate MW mass.

CHAPTER 5

ΛCDM Predictions for the Satellite Population of M33

This chapter has been published previously as Patel, E., Carlin, J. L., Tollerud, E. J., Collins, M. L. M., Dooley, G. A., 2018, MNRAS, 480, 1883

Abstract

Triangulum (M33) is the most massive satellite galaxy of Andromeda (M31), with a stellar mass of about 3×10^9 $M_\odot$. Based on abundance matching techniques, M33's total mass at infall is estimated to be of order 10^{11} $M_\odot$. ΛCDM simulations predict that M33-mass halos host several of their own low mass satellite companions, yet only one candidate M33 satellite has been detected in deep photometric surveys to date. This 'satellites of satellites' hierarchy has recently been explored in the context of the dwarf galaxies discovered around the Milky Way's Magellanic Clouds in the Dark Energy Survey. Here we discuss the number of satellite galaxies predicted to reside within the virial radius (∼160 kpc) of M33 based on ΛCDM simulations. We also calculate the expected number of satellite detections in N fields of data using various ground–based imagers. Finally, we discuss how these satellite population predictions change as a function of M33's past orbital history. If M33 is on its first infall into M31's halo, its proposed satellites are expected to remain bound to M33 today. However, if M33 experienced a recent tidal interaction with M31, the number of surviving satellites depends strongly on the distance achieved at pericenter due to the effects of tidal stripping. We conclude that a survey extending to ∼100 kpc around M33 would be sufficient to constrain its orbital history and a majority of its satellite population. In the era of WFIRST, surveys of this size will be considered small observing programs.

5.1 Introduction

Until the last decade, satellite galaxies had only been discovered around host galaxies approximately the mass of the Milky Way (MW) and Andromeda (M31) or greater. More advanced instruments and improved techniques for extracting stellar overdensities have now extended our view of satellites around host galaxies down to dwarf galaxy masses. For example, tens of dwarf satellite galaxies have recently been discovered around the Magellanic Clouds, the MW's most massive satellites (Drlica-Wagner et al., 2015; Koposov et al., 2015; Martin et al., 2015; Bechtol et al., 2015; Kim et al., 2015; Kim and Jerjen, 2015). This provides evidence that dwarf galaxy halos also harbor satellite galaxies of their own, supporting predictions from Λ Cold Dark Matter (ΛCDM) numerical simulations (e.g., Moore et al., 1999; Gao et al., 2004; Kravtsov et al., 2004; Guo et al., 2011; Wang et al., 2012; Sales et al., 2011, 2013).

These discoveries have begun to fill in the faint end of the galaxy luminosity function, which is key to probing ΛCDM at small scales. ΛCDM is known for several challenges that arise upon comparing observations and ΛCDM simulations in the dwarf galaxy mass regime (i.e. core-cusp problem, missing satellites, too big to fail; see Bullock and Boylan-Kolchin, 2017, and references therein). Adding to the observed sample of low stellar mass galaxies within the Local Group (LG) and even the Local Volume (< 10 Mpc) will therefore improve our understanding of ΛCDM and help determine whether these challenges are truly setbacks to the standard cosmological paradigm.

As the third most massive member of the LG, M33's stellar mass is roughly the same as the Large Magellanic Cloud (LMC) (Guo et al., 2010; Corbelli, 2003). Its gravitational influence on both its host galaxy and less massive galaxies in the LG is therefore non-negligible. The LMC and M33 are estimated to have dark matter halo masses of order $10^{11}\,M_{\odot}$ at infall based on various abundance matching (hereafter AM) techniques (e.g., Guo et al., 2011). However, M33 likely resides in a more massive dark matter halo than the LMC as evidenced by a peak circular velocity

of 130 km s^{-1} at 15 kpc (Corbelli and Salucci, 2000) compared to the LMC's peak circular velocity of about 92 km s^{-1} (van der Marel and Kallivayalil, 2014). If the LMC hosts several satellite galaxies, M33 is also expected to host its own satellite galaxies and perhaps even more due to a larger halo mass. Since M33 does not have a 1:10 stellar mass ratio binary companion like the Small Magellanic Cloud (SMC) is to the LMC, it is easier to study the halo of M33 and thereby its satellite population in detail.

M33 can be considered an isolated analog of the LMC that resides at a close enough distance where even ultra-faint dwarf satellites ($M_* < 10^5\,M_\odot$ or $M_V > -7$; see Bullock and Boylan-Kolchin, 2017) can be detected. Observations of faint satellite galaxies around an M33 mass galaxy are crucial not only because of their importance to ΛCDM theory, but also because they may help us understand whether galaxies of this mass have a stellar halo. Stellar halos of MW mass galaxies are thought to be formed through the accretion of many satellite galaxies, but it is not yet clear whether this is true for less massive galaxies like the LMC and M33. Deep, wide-field observations at the distance of M33 may therefore provide insight on what the assembly histories for $M_{DM} \sim 10^{11}\,M_\odot$ galaxies are (i.e. whether they are dominated by accretion events or in situ star formation).

Several ongoing surveys are searching for ultra-faint dwarf galaxy companions around the Magellanic Clouds. For example, the Magellanic Satellites Survey (MagLiteS) is using the Dark Energy Camera data to identify potential galactic companions of the Magellanic Clouds (Drlica-Wagner et al., 2016; Pieres et al., 2017; Torrealba et al., 2018). The Survey of the MAgellanic Stellar History (SMASH; Nidever et al., 2017) aims to find low surface brightness features around the Magellanic Clouds and has already identified a globular cluster that is likely associated with the LMC. Beyond the Local Group, the Magellanic Analog Dwarf Companions And Stellar Halos (MADCASH; Carlin et al., 2016) survey is observing isolated galaxies with masses similar to the Magellanic Clouds to map their halos and search for any associated dwarf companions. An extended survey around M33 would provide an additional counterpart to these growing samples.

In this work, we predict the satellite population of M33 using the ΛCDM-based methodology of Dooley et al. (2017b,a, hereafter D17A and D17B) and provide observing strategies for two ground-based imagers to motivate a second search for the satellites of satellites phenomena in the LG. The main goal for predicting the M33 satellite population is to further constrain its orbital history and to explore alternative origins for its gaseous and stellar disk warps (Putman et al., 2009; McConnachie et al., 2009) in the event that they cannot be explained by its past orbital history, as suggested in Patel et al. (2017a). Since M33's past orbital history will directly affect the number of surviving satellites today, an extended survey around M33 can provide additional insight on M33's history. Finally, the orbital history of M33 is important to understanding the assembly of M31's halo, which appears to have had a very active recent accretion history (e.g., Fardal et al., 2006; Mackey et al., 2010; Ferguson and Mackey, 2016).

This paper is outlined as follows. In Section 5.2, we briefly discuss the mass of M33 and existing, deep observations of the M33 and M31 region. In Section 5.3, we describe the methods of D17A and D17B, which make predictions for the satellite populations of host galaxies ranging in mass from the SMC to the MW. We then apply these methods to M33 to tabulate the number of satellites expected to reside within its virial radius. We also determine the number of those satellites that can potentially be observed for various survey radii given two different wide field imagers. Section 5.4 discusses different M33 orbital histories and how each would affect the surviving population of satellite companions. In Section 5.5, we discuss the current morphology of M33, its potential origins in the context of satellite galaxy companions, and how M33 can improve our current understanding of ΛCDM at small scales. Finally, Section 5.6 presents our conclusions.

5.2 Observed Data

5.2.1 The Mass of M33

As the third most massive member of the Local Group (LG), M33's mass and gravitational influence are important to understanding the LG's history. While M33's baryonic mass is fairly well constrained via observations, the total mass is less well known since the dark matter halo cannot be measured directly. Halo mass is the determining factor for how many satellite companions M33 can harbor, so we briefly discuss M33 mass estimates from the literature below. See Section 2 of Patel et al. (2017a, hereafter P17A) for more detailed explanations.

HI mass: M33's extended gas disk was most recently observed by Putman et al. (2009, hereafter P09). It extends to 22 kpc from the galaxy's center and its total HI content has a mass of about $1.4 \times 10^9\,M_\odot$, approximately twice that of the LMC's HI disk. Most of the gas in the disk is located at radii beyond the extent of the star-forming disk. While it does not show any signs of significant truncation due to ram pressure, it does exhibit warps in both the north and south. These warps and their possible origin will be discussed further in Section 5.4.

M33's rotation curve was measured with 21-cm observations, illustrating that the circular velocity steadily rises out to 15 kpc (Corbelli and Salucci, 2000) where it is 130 km s^{-1}. This gives a dynamical mass ($V^2 = GM/r$) $\approx 5 \times 10^{10}\,M_\odot$. The continuous rise in the rotation curve may be linked to M33's warps at large radii.

Stellar mass: M33's stellar content has been estimated by Corbelli (2003) using rotation curve data and mass-to-light ratio arguments. This leads to a stellar mass range of $2.8 - 5.6 \times 10^9\,M_\odot$. Guo et al. (2010) used M33's $B - V$ color and stellar population models to estimate M33's mass-to-light ratio giving a stellar mass of $2.84 \pm 0.73 \times 10^9\,M_\odot$. Combining these estimates into one result gives $3.2 \pm 0.4 \times 10^9\,M_\odot$ (van der Marel et al., 2012a). We adopt this value for the remainder of this analysis, though our results are most sensitive to M33's adopted halo mass.

Halo mass: M33's baryonic mass content sums to approximately $6.4 \times 10^9\,M_\odot$

(Corbelli, 2003). Dividing this by the dynamical mass gives a baryon fraction of 12.8%. It has been shown that only a fraction of cosmic baryons condense to form stars in spiral galaxies, resulting in low baryon fractions between 3-5% (e.g., Trujillo-Gomez et al., 2015; Rodríguez-Puebla et al., 2012; Trujillo-Gomez et al., 2011; Leauthaud et al., 2011; Behroozi et al., 2010; Guo et al., 2010; Jiang and Kochanek, 2007; Mandelbaum et al., 2006; Fukugita et al., 1998). Applying this baryon fraction to M33 suggests its mass at infall could have been $1.3 - 2.1 \times 10^{11}\,M_{\odot}$. At this halo mass scale, M33 is approximately 10% of M31's mass. More importantly, ΛCDM predicts that all $10^{11}\,M_{\odot}$ halos host a few satellites with $M_{*} > 10^{3}\,M_{\odot}$ across independent AM techniques (see D17A). Details of M33's predicted satellite population will be discussed in Section 5.3.

5.2.2 Optical Observations of the M33-M31 Region

Numerous multi-wavelength observations have been taken of the M33-M31 region. Below we summarize one particular imaging survey of resolved stars in the M31 system that has led to many discoveries of new dwarf galaxies, globular clusters, and stellar streams in M31's extended halo.

The Pan-Andromeda Archaeological Survey (PAndAS) used the 1 square degree field of view of MegaPrime/MegaCam on the 3.6m Canada-France-Hawaii Telescope (CFHT, McConnachie et al., 2009, hereafter M09). The survey footprint is illustrated in black in Fig. 5.1. The survey covers more than 300 square degrees (equivalent to 70,000 kpc^2) spanning the region extending to 150 projected kpc (10.5°) from the center of M31 and 50 projected kpc (3.5°) from the center of M33. Stars in M31 are resolved down to $g = 26.5$ and $i = 25.5$.

These data have led to the discovery of new M31 stellar structures in the northwest and southwest, which both extend to 100 kpc, and the extension of a previously known stream in the east. Sixteen additional dwarf galaxies (see Martin et al., 2016, and references therein, hereafter M16) and 59 globular clusters (Huxor et al., 2014) were also identified in the PAndAS data. PAndAS and preceding surveys have greatly increased our view of substructures in M31's inner and outer halo. While

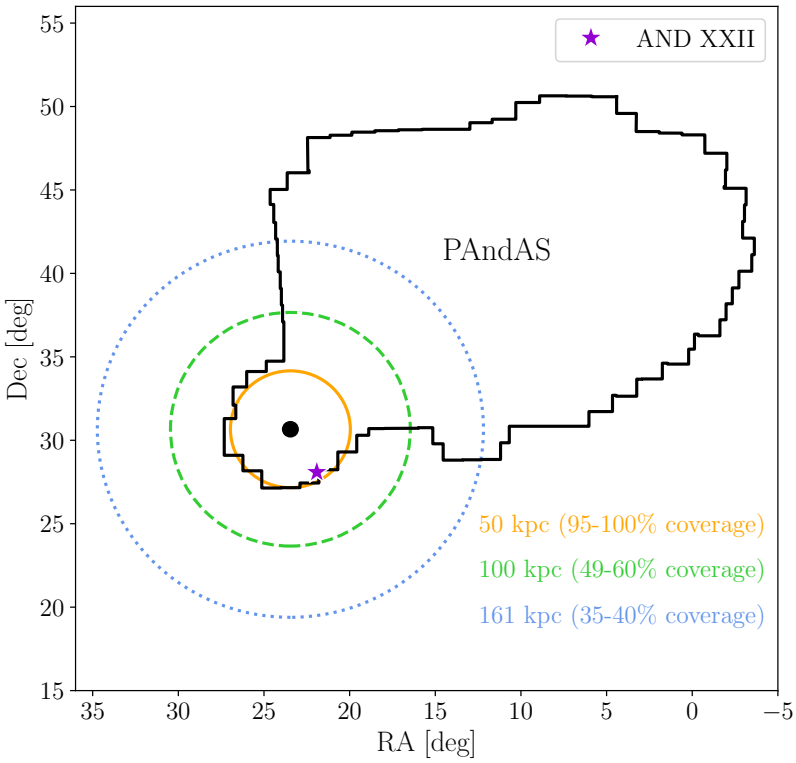

Figure 5.1: The PAndAS footprint (black) compared to the virial radius of M33 (dotted blue circle), a 100 kpc region around M33 (dashed green circle), and a 50 kpc region around M33 (orange). All circles assume as distance of 794 kpc to M33. The closed black circle indicates three scale lengths of M33's stellar disk using a scale length of approximately 0.15°. The fraction of the virial volume associated with each circle that is encompassed by the PAndAS footprint is listed on the bottom right. The lower limit comes from a distance of 794 kpc to M33 and the upper limit assumes a distance of 968 kpc to M33. The position of And XXII, the only potential M33 satellite known to date is indicated with a purple star.

the faintest and most diffuse structures within this survey may fall below the completeness limits, PAndAS has revolutionized our view of the M31 system thus far.

Of the dwarf galaxies discovered in the PAndAS survey, only one is considered a candidate satellite of M33 rather than M31. And XXII lies to the southeast of M33 on the sky and its relative systemic velocity, angular separation from M33, and distance all indicate that it may be a satellite of M33 instead of M31 (Tollerud et al., 2012; Chapman et al., 2013; Martin et al., 2009). The position of And XXII is denoted by a purple star in Fig. 5.1.

Chapman et al. (2013) present the results of an N-body simulation of M33 and M31 from which they conclude that during a close pericentric passage, only M33 halo particles at large distances from M33 would be stripped. Assuming that bound satellites follow the dark matter distribution of their host, And XXII would remain bound to M33 during such an encounter based on these simulations. These results strongly depend on the adopted M33 orbital history and other potential orbits may not yield the same conclusion for And XXII.

The absolute magnitude of And XXII is $M_V = -6.5$[1] and M33's $M_V = -18.8$ (McConnachie, 2012). Using these values, a rough approximation for the stellar mass content of And XXII can be derived. If we adopt an M33 stellar mass of $3.2 \times 10^9\, M_\odot$ and assume that the stellar mass-to-light ratio is unity for ultra-faint dwarfs as in McConnachie (2012)[2], then And XXII has a stellar mass $M_* \approx 3.8 \times 10^4\, M_\odot$. This means the PAndAS survey is sensitive to galaxies near the upper end of the ultra-faint dwarf regime (see Bullock and Boylan-Kolchin, 2017). This stellar mass matches to a virial mass of $\gtrsim 5 \times 10^8\, M_\odot$ according to the Moster et al. (2013) AM technique.

Satellites of M31 have been discovered in the Sloan Digital Sky Survey (SDSS) (Zucker et al., 2004, 2007), which reaches a limiting magnitude of $M_V = -8$ at best for a distance of 800-1000 kpc (Tollerud et al., 2008). The SDSS photometry

[1]M16 report $M_V = -6.7$ for And XXII, resulting in $M_* \approx 4.6 \times 10^4\, M_\odot$. Our conclusions are unaffected by this incremental difference in And XXII's approximate stellar mass.

[2]A ratio of unity allows one to easily scale to any preferred stellar mass-to-light ratio.

is roughly sensitive to galaxies with stellar mass $M_* \gtrsim 1.5 \times 10^5\, M_\odot$ assuming a mass-to-light ratio of unity. The stellar mass limits quoted in this work should be considered lower limits as a function of survey depth because the stellar mass-to-light ratios of the ultra-faint dwarfs are more consistent with ratios between one and two (Kirby et al., 2013; McGaugh and Milgrom, 2013; McGaugh and Wolf, 2010; Tollerud et al., 2011b; Woo et al., 2008). For example, Kirby et al. (2013) assumes $M_*/L_V = 1.6 M_\odot/L_\odot$ based on the average values for dwarf spheroidals in Woo et al. (2008).

5.3 Methods and Results

In this section, we summarize the methods of D17A and D17B to derive the predicted satellite population of an M33-mass galaxy. Given that M33's virial radius is significantly larger than the area surveyed by PAndAS, we motivate the need to complete the search for satellites around M33 using available and upcoming wide field imagers. The average number of observed satellites that M33 is expected to host is reported for two different instruments and for a range of M33 distances following the analysis of D17A and D17B.

5.3.1 D17 Predictions for Luminous Satellites

In D17A , the *Caterpillar* simulation suite (Griffen et al., 2016) is used to predict the number of satellites expected to exist around MW mass halos and lower mass field halos in a ΛCDM paradigm. Since *Caterpillar* is a suite of dark matter only simulations, several additional steps are taken to include the effects of reionization and to assign stellar masses to dark matter subhalos. Here we briefly summarize the the *Caterpillar* simulation suite and the methods of D17A.

Caterpillar is a suite of 33 high particle resolution ($m_p = 3 \times 10^4\, M_\odot$) and high temporal resolution (5 Myr/snapshot) zoom-in simulations of MW mass galaxies. The suite was run with `P-GADGET3` and `GADGET4`, which are tree-based N-body codes derived from `GADGET2` (Springel, 2005b). *Caterpillar* adopts the *Planck* cosmology:

$\Omega_m = 0.32$, $\Omega_\Lambda = 0.68$, $\Omega_b = 0.05$, $n_s = 0.96$, $\sigma_8 = 0.83$, and Hubble constant $H_0 = 67.11$ km s^{-1} Mpc^{-1} (Planck Collaboration et al., 2014). Dark matter halos are identified using the `ROCKSTAR` (Behroozi et al., 2013b) algorithm and merger trees are created with `CONSISTENT-TREES` (Behroozi et al., 2013c). `ROCKSTAR` assigns virial masses to halos based on the Bryan and Norman (1998) definition.

Using the 33 simulated *Caterpillar* halos, subhalo mass functions (SHMFs) are computed for several AM methods explored in D17A. The SHMFs follow the general form

$$\frac{\mathrm{dN}}{\mathrm{dM_{sub}}} = \mathrm{K_0} \left(\frac{\mathrm{M_{sub}}}{\mathrm{M_\odot}} \right)^{-\alpha} \frac{\mathrm{M_{host}}}{\mathrm{M_\odot}}, \tag{5.1}$$

where K_0 and α depend on halo mass. For the Garrison-Kimmel et al. (2017a, hereafter GK17) AM model, $\alpha = 1.82$ and $K_0 = 0.000892$ for field halos and $\alpha = 1.87$ and $K_0 = 0.000188$ for MW analogs. This SHMF accounts for all self-bound subhalos within R_{vir} at z=0, however subhalos of subhalos are excluded. Ideally, these sub-subhalos will be included in this type of analysis in the future. We will use the D17A and D17B results for the GK17 AM method in the remainder of this analysis.

Given the SHMF, the mean number of dark matter subhalos predicted to exist within the virial radius of a host galaxy with mass $\mathrm{M_{host}}$ is calculated by integrating Eq. 5.1 from $\mathrm{M_{min}}$ to $\mathrm{M_{host}}$. This yields:

$$\bar{\mathrm{N}} = \frac{\mathrm{K_0 M_{host}}}{\alpha - 1} \left(\mathrm{M_{min}^{1-\alpha}} - \mathrm{M_{host}^{1-\alpha}} \right). \tag{5.2}$$

D17A chooses $\mathrm{M_{min}} = 10^{7.4}\,\mathrm{M_\odot}$ as a threshold below which no star formation occurs due to reionization. Using Eq. 5.2, they then generate random realizations of $\bar{N}$ according to a Poisson distribution and randomly assign halo masses based on the SHMF (Eq. 5.1). Once the halo masses are assigned, the reionization model is implemented.

Reionization is accounted for by randomly assigning whether simulated halos should host stars or remain dark according to Barber et al. (2014). This relation

depends on the host halo's mass. The fraction of halos that are luminous at z=0 is shown in D17A, Figure 3. Approximately 50% of halos with $\mathrm{M_{vir,peak}} > 10^9\,\mathrm{M_\odot}$ are luminous. This function is based on a semi-analytic model in which reionization occurs from $z = 15$ to $z = 11.5$ (Starkenburg et al., 2013). Since D17A considers several different AM methods, halos are determined to be dark or luminous halos with respect to the appropriate mass definition. In the GK17 AM method, stellar masses are assigned using the peak virial mass of halos. All mentions of virial quantities here also refer to the Bryan and Norman (1998) definition. In D17A, reionization is implemented as an instantaneous process at z=13.3.

Finally, halos are assigned stellar masses using the $M_* - M_{\rm halo}$ relation for the AM model of choice. For the GK17 AM model, the scatter in assigning stellar masses is explicitly taken into account. All simulated halos with galaxy stellar masses above $10^3\,M_\odot$ are included.

The mean predicted number of luminous satellites ($\bar{\mathrm{N}}_{\rm lum}$) around the LMC and the SMC are provided in Figure 1 of D17B as a function of satellite stellar mass. A stellar mass of $2.6\times10^9\,M_\odot$ is adopted for the LMC, which translates to $M_{\rm vir} = 2.3\times 10^{11}\,M_\odot$ using the GK17 AM method. This virial mass corresponds to a virial radius of $R_{\rm vir} = 156$ kpc. The stellar mass of M33 is approximately $3.2 \times 10^9\,M_\odot$, giving a virial mass $M_{\rm vir} = 2.5 \times 10^{11}\,M_\odot$ and $R_{\rm vir} = 161$ kpc. Throughout this analysis, we adopt this virial mass and radius for M33, however, other AM methods (Moster et al., 2013; Behroozi et al., 2013a; Brook et al., 2014; Garrison-Kimmel et al., 2014) yield slightly different masses, virial radii, and therefore different satellite populations as discussed in D17A. Since $M_{\rm vir,M33}/M_{\rm vir,LMC} \approx 1.09$ and $\frac{\mathrm{dN}}{\mathrm{dM_{sub}}} \propto \mathrm{M_{host}}$, one can take the results for the LMC in D17B and scale them up by ∼9% to acquire the predicted number of luminous satellites for M33. These results are represented by the solid gray line and shaded region in Fig. 5.2.

We will refer to the combined methodology of D17A and D17B as *D17 predictions* throughout the remainder of this work. This refers to the aggregate of ΛCDM predictions (from the *Caterpillar* suite of simulations), the GK17 AM method, and the reionization model described above.

5.3.2 Correcting for Geometric Effects

Thus far, we have described how D17A and D17B used ΛCDM simulations to compute the mean number of luminous satellites in the virial volume of isolated galaxies with masses similar to M33 and the LMC. However, these numbers do not directly translate into expectations for observations which depend on the field of view, distance to the target galaxy, and the virial radius of the target galaxy. These predictions must therefore be corrected (using a multiplicative scaling factor) for the number of satellites expected within the line of sight for a given survey radius. This scaling factor from D17A will be referred to as $K_{\rm los}(R)$.

$K_{\rm los}(R)$ is the fraction of satellites expected to exist within a cylinder along the line of sight centered on the host galaxy that includes the radial dependence of the satellite galaxy distribution. Therefore multiplying $K_{\rm los}(R)$ by the number of satellite galaxies predicted to reside within $R_{\rm vir}$ of a galaxy by the D17 predictions (i.e. the gray line in Fig. 5.2) yields the number of observed satellites expected in a given field of view (i.e. the colored lines in Fig. 5.2).

$K_{\rm los}(R)$ is derived as follows. Eq. 5.3 provides a fit to the radial distribution of satellites galaxies where satellite galaxies are the subhalos from the *Caterpillar* simulations that are determined to be luminous via the steps outlined in Section 5.3.1.

$$K(R) = \begin{cases} k_1 R + k_2 R^2 + k_3 R^3, & R < 0.2 \\ k_4 \arctan\left(\frac{R}{k_5} - k_6\right), & 0.2 \leq R \leq 1.5 \end{cases} \tag{5.3}$$

where $k_1 = -0.2615$, $k_2 = 6.888$, $k_3 = -7.035$, $k_4 = 0.9667$, $k_5 = 0.5298$, and $k_6 = 0.2055$.

Physically, the volume we are interested in considering is a cylinder of radius R and half-depth Z inscribed within a sphere of radius $R_{\rm vir}$ given the D17 formalism. $R \equiv r/R_{\rm vir}$ such that $R = 1$ corresponds to the virial radius of a galaxy's halo, which is approximated as a sphere. In practice, r would be the field of view radius of a survey, $\rm R_{FoV}$. The function $\frac{1}{4\pi R^2}\frac{dK}{dR}$ then describes the density of satellite galaxies as a function of R (or r in spherical coordinates). Integrating this density function in

spherical coordinates over a cylinder gives the scaling factor, $K_{\rm los}(R)$. The density function should be integrated using bounds corresponding to a cylinder with a radius of R and a half-depth of $Z \equiv z/R_{\rm vir}$. $K_{\rm los}(R)$ is plotted for values of $Z = 1$ and $Z = 1.5$ in Figure 11 of D17A.

For our calculations, we follow the conventions of D17A and adopt $Z = 1.5$, which corresponds to approximately the splashback radius of the target host galaxy, or the distance at which bound satellites will reach their first apocenter (More et al., 2015). Beyond this radius, the density of satellites is expected to rapidly decrease to zero.

5.3.3 The Predicted Satellite Population of M33

Fig. 5.1 shows the PAndAS survey footprint in black along with three circles indicating survey regions of different radii centered on M33. The orange circle represents an area with a radius of 50 kpc, approximately the same as the PAndAS coverage around M33 if the bridge between M33 and M31 is excluded. The dashed green circle indicates the area spanned by a radius of 100 kpc. The PAndAS survey already observed ∼50% of this region. The dotted blue circle represents the area contained within the adopted virial radius of M33, or 161 kpc. Only ∼40% of this region is contained within the PAndAS survey. A comparison of the orange and blue areas reveals the drastic difference in area coverage of available data relative to the true extents of M33's full halo, thereby motivating the need to search for satellites in the outskirts of M33.

Table 5.1: Expectations for the number of satellites that could be observed with Hyper Suprime-Cam (HSC) in the area corresponding to N_{fields}, or the total number of fields observed. The first row shows the D17 predictions for the number of satellites within R_{vir}. Column 3 lists R_{FoV} or the radius of the projected area observed by N_{fields} at the distance of M33. Columns 4-7 show the expected number of observed satellites at different limiting stellar masses using the scaling factor $K_{los}(R)$. HSC's field of view has a diameter of 1.5°. The corresponding physical radius for a single field is approximately 10.4, 11.5, and 12.7 kpc at M33 distances of 794, 880, 968 kpc respectively. All calculations assume a 100% observational efficiency rate.

			$\bar{N}_{lum}$ ($M_* > 10^3 M_\odot$)	$\bar{N}_{lum}$ ($M_* > 10^4 M_\odot$)	$\bar{N}_{lum}$ ($M_* > 10^5 M_\odot$)	$\bar{N}_{lum}$ ($M_* > 10^6 M_\odot$)
D17 predictions ($R_{survey} = R_{vir}$)			$11.42^{+3.86}_{-3.82}$	$8.07^{+3.16}_{-3.18}$	$4.04^{+2.13}_{-2.20}$	$1.45^{+1.27}_{-1.28}$
D_{M33} = 794 kpc	N_{fields}	R_{FoV} (kpc)	$\bar{N}_{obs}$ ($M_* > 10^3 M_\odot$)	$\bar{N}_{obs}$ ($M_* > 10^4 M_\odot$)	$\bar{N}_{obs}$ ($M_* > 10^5 M_\odot$)	$\bar{N}_{obs}$ ($M_* > 10^6 M_\odot$)
	1	10.4	0.53	0.37	0.19	0.07
	10	32.9	3.59	2.53	1.27	0.46
	23	49.8	5.86	4.14	2.07	0.74
	50	73.5	8.25	5.83	2.92	1.05
	100	103.9	10.32	7.29	3.65	1.31
	154	129.0	11.42	8.07	4.04	1.45
D_{M33} = 880 kpc	N_{fields}	R_{FoV} (kpc)	$\bar{N}_{obs}$ ($M_* > 10^3 M_\odot$)	$\bar{N}_{obs}$ ($M_* > 10^4 M_\odot$)	$\bar{N}_{obs}$ ($M_* > 10^5 M_\odot$)	$\bar{N}_{obs}$ ($M_* > 10^6 M_\odot$)
	1	11.5	0.64	0.45	0.23	0.08
	10	36.4	4.11	2.90	1.45	0.52
	23	55.2	6.48	4.58	2.29	0.82
	50	81.4	8.88	6.28	3.14	1.13
	100	115.2	10.88	7.69	3.85	1.38
	125	128.8	11.42	8.07	4.04	1.45
D_{M33} = 968 kpc	N_{fields}	R_{FoV} (kpc)	$\bar{N}_{obs}$ ($M_* > 10^3 M_\odot$)	$\bar{N}_{obs}$ ($M_* > 10^4 M_\odot$)	$\bar{N}_{obs}$ ($M_* > 10^5 M_\odot$)	$\bar{N}_{obs}$ ($M_* > 10^6 M_\odot$)
	1	12.7	0.77	0.54	0.27	0.10
	10	40.1	4.61	3.26	1.63	0.59
	23	60.8	7.07	4.99	2.50	0.90
	50	89.6	9.46	6.68	3.35	1.20
	103	128.6	11.42	8.07	4.04	1.45

Table 5.2: Similar to Table 5.1 for the MegaCam/MegaPrime (MC) imager. MC has a square field of view with a 1° diameter. We have approximated it as a circular field of view with the same area (or a 1.13° diameter). $R_{\rm FoV}$ for a single field corresponds to 7.8, 8.7, and 9.5 kpc at M33 distances of 794, 880, 968 kpc respectively.

			$\bar{\rm N}_{\rm lum}$ ($\rm M_* > 10^3 M_\odot$)	$\bar{\rm N}_{\rm lum}$ ($\rm M_* > 10^4 M_\odot$)	$\bar{\rm N}_{\rm lum}$ ($\rm M_* > 10^5 M_\odot$)	$\bar{\rm N}_{\rm lum}$ ($\rm M_* > 10^6 M_\odot$)
D17 predictions ($R_{\rm survey} = R_{\rm vir}$)			$11.42^{+3.86}_{-3.82}$	$8.07^{+3.16}_{-3.18}$	$4.04^{+2.13}_{-2.20}$	$1.45^{+1.27}_{-1.28}$
$\rm D_{M33}$ = 794 kpc	$\rm N_{fields}$	$\rm R_{FoV}$ (kpc)	$\bar{\rm N}_{\rm obs}$ ($\rm M_* > 10^3 M_\odot$)	$\bar{\rm N}_{\rm obs}$ ($\rm M_* > 10^4 M_\odot$)	$\bar{\rm N}_{\rm obs}$ ($\rm M_* > 10^5 M_\odot$)	$\bar{\rm N}_{\rm obs}$ ($\rm M_* > 10^6 M_\odot$)
	10	24.8	2.38	1.68	0.84	0.30
	41	50.1	5.90	4.17	2.09	0.75
	100	78.3	8.64	6.11	3.06	1.10
	200	110.7	10.67	7.54	3.77	1.35
	254	128.9	11.42	8.07	4.04	1.45
$\rm D_{M33}$ = 880 kpc	$\rm N_{fields}$	$\rm R_{FoV}$ (kpc)	$\bar{\rm N}_{\rm obs}$ ($\rm M_* > 10^3 M_\odot$)	$\bar{\rm N}_{\rm obs}$ ($\rm M_* > 10^4 M_\odot$)	$\bar{\rm N}_{\rm obs}$ ($\rm M_* > 10^5 M_\odot$)	$\bar{\rm N}_{\rm obs}$ ($\rm M_* > 10^6 M_\odot$)
	10	27.4	2.77	1.96	0.98	0.35
	41	55.6	6.52	4.61	2.31	0.83
	100	86.8	9.27	6.55	3.28	1.18
	200	122.7	11.20	7.92	3.96	1.42
	207	128.7	11.42	8.07	4.04	1.45
$\rm D_{M33}$ = 968 kpc	$\rm N_{fields}$	$\rm R_{FoV}$ (kpc)	$\bar{\rm N}_{\rm obs}$ ($\rm M_* > 10^3 M_\odot$)	$\bar{\rm N}_{\rm obs}$ ($\rm M_* > 10^4 M_\odot$)	$\bar{\rm N}_{\rm obs}$ ($\rm M_* > 10^5 M_\odot$)	$\bar{\rm N}_{\rm obs}$ ($\rm M_* > 10^6 M_\odot$)
	10	30.2	3.18	2.25	1.13	0.40
	41	61.1	7.10	5.02	2.51	0.90
	100	95.4	9.83	6.95	3.48	1.25
	171	128.8	11.42	8.07	4.04	1.45

The PAndAS survey used MegaCam/MegaPrime (MC) on the CFHT, which has a $1^\circ \times 1^\circ$ square field of view. For our calculations, we have approximated it as a circular field of view with a 1.13° diameter or a circular field with the same area. Hyper Suprime-Cam (HSC) on the 8.2m Subaru telescope has a field of view with a 1.5° diameter. Other imagers, such as the Dark Energy Camera on the Blanco telescope and LSST would be ideal for surveys around M33; however, they are located in the South and will not observe the M31 region.

In Tables 5.1 and 5.2, we tabulate how many luminous satellites are expected to exist around M33 for various satellite mass (or limiting magnitude) thresholds. Each table corresponds to a different instrument (HSC or MC). The first row in both tables lists the mean number of luminous satellites, $\bar{\mathrm{N}}_{\mathrm{lum}}$, M33 is expected to host within its virial radius from the D17 predictions. We list the corrected number of satellites, $\bar{N}_{\mathrm{obs}}$ in the following rows as a function of the number of observed fields, $\mathrm{N_{fields}}$. The values in these rows are calculated by multiplying the predicted number of luminous satellites $\bar{\mathrm{N}}_{\mathrm{lum}}$ by the scaling factor $K_{\mathrm{los}}(R)$, which is calculated using $\mathrm{R} = (\mathrm{N_{fields}} \times \mathrm{R}^2_{\mathrm{FoV}}/\mathrm{R}^2_{\mathrm{vir}})^{1/2}$ and Z=1.5. $\mathrm{R_{FoV}}$ is the physical radius (in kpc) that corresponds to the radius observed by $\mathrm{N_{fields}}$ at the distance of M33 for each imager and $\mathrm{R_{vir}} = 161$ kpc. Several rows are included from $\mathrm{N_{fields}} = 1$ to the maximum number of fields needed to detect all potential satellites using HSC or MC.

Distance measurements to M33 in the literature range from 794 kpc (McConnachie et al., 2004) to 968 kpc (U et al., 2009); thus we repeat all calculations for M33 distances of 794 kpc, 880 kpc, and 968 kpc. For M33 distances $>$ 794 kpc, fewer fields are required for both HSC and MC. Note that all results assume a ΛCDM cosmology and that the observational efficiency rate for any number of fields is 100% (i.e. if 10 HSC fields are taken, then two satellites with $M_* > 10^3\,M_\odot$ are guaranteed at a distance of 794 kpc). The number of fields, $\mathrm{N_{fields}}$, listed are approximate and do not account for the fact that off-axis fields probe a smaller volume than on-axis fields. They also do not account for the overlapping regions between fields.

Since $K_{\mathrm{los}}(R)$ is approximately zero at $R \equiv R_{\mathrm{fov}}/R_{\mathrm{vir}} \lesssim 0.05$, Table 5.2 excludes

$N_{\rm fields} = 1$. The smaller field of view of MC requires significantly more fields to probe the area around M33, thus, it is not surprising that the PAndAS survey did not extend to larger radii. The satellite stellar mass thresholds range from $10^3 - 10^6\,M_\odot$, or from the ultra-faint dwarf regime to the classical dwarf satellite regime. According to D17A, the probability that an M33-stellar mass galaxy hosts a satellite with $M_* > 10^3, 10^4$, and $10^5\,M_\odot$ is unanimously $> 95\%$ for the GK17 AM method.

Fig. 5.2 summarizes the results in Tables 5.1 and 5.2, illustrating the number of expected satellites not only as a function of satellite stellar mass, but also by visual magnitude assuming a mass-to-light ratio of unity. Given the D17 predictions (gray line and shaded region), M33 could host up to 15 satellites with stellar masses $> 10^3\,M_\odot$ within the expected errors. All solid colored lines correspond to HSC and all dot dashed colored lines correspond to MC.

The number of satellites expected to reside roughly within the 50 kpc area observed around M33 by PAndAS is provided by the rows indicating $N_{\rm fields} = 23$ in Table 5.1 and $N_{\rm fields} = 41$ in Table 5.2. These limits are also indicated by the intersection of the orange curves and dotted vertical orange line in Fig. 5.2. At the stellar mass of And XXII, M33 is expected to host about three satellites within this area on average. Therefore the discovery of only one potential satellite companion of M33 by PAndAS is lower than the number of luminous satellites calculated to exist within 50 kpc of M33 using the adopted methodology.

PAndAS surveyed about one-third of M33's virial radius (see Fig. 5.1). Naively, one would expect that roughly $(50\text{ kpc})^2/(161\text{ kpc})^2$ (or 9.6%) of the satellites predicted in M33's full virial volume to be detected within this area on the sky. However, the number of satellites expected using $K_{\rm los}(50/161)$ is $\sim$53% of the total expected satellites. Similarly, for a survey radius of 100 kpc, one would naively expect $(100\text{ kpc})^2/(161\text{ kpc})^2$ (or 38.6%) of the total satellites to be detected, but $\sim$92% of the total expected satellites are predicted to be observed in that survey area.

The discrepancy between naive expectations and our results is a combination

of effects associated with the geometry of proposed observations and the radial distribution of subhalos. Geometrically, a 50 kpc survey radius corresponds to a 50 kpc cylinder cut out of a sphere with a radius of R_{vir} = 161 kpc (also known as a spherical ring), which is about 14% of the sphere's volume compared to the 9.6% expectation when two cylinders of different radii are considered. Furthermore, the radial distribution of subhalos is not uniform. Generally subhalos follow the radial dark matter density profile of their primary host halo in ΛCDM. The radial distribution of satellites labeled as luminous owing to reionization tend to be even more centrally concentrated. In other words, the density of satellites per unit volume is highest near the center of a host halo, resulting in more predicted satellites within smaller survey radii than expected for a uniform distribution.

5.3.4 An Extended Survey of M33's Virial Volume

The PAndAS survey footprint is approximately 35% of M33's virial volume (if D_{M33} = 794 kpc) when the full footprint is accounted for, so while we calculate that 154 fields and 254 fields with HSC and MC, respectively, are required to survey the full projected area of M33's virial volume, only 100 fields with HSC and 165 fields with MC would be necessary to fill in this region. We acknowledge that this number of fields is not trivial to acquire, observe, and process. If one were to survey a radius of only 100 kpc around M33 rather than extending to its virial radius, approximately 50 (HSC) and 100 (MC) new fields of data would be necessary since the PAndAS area is about 50% of this region. About 90% of the total M33 satellite population is expected to reside within 100 kpc.

Fig. 5.3 shows the number of resolved stars in a single M33 satellite at various depths in the g-band. These calculations are for an [Fe/H] = -2.0 stellar population with an age of 12 Gyr and a power law initial mass function with a slope of -2.0. Predictions for satellites of various stellar masses (and M_V) at the distance of M33 are shown in the black lines and gray shaded regions, where the shaded regions span the various M33 distances discussed in this work. The blue lines and hashed area show how many stars are expected at various g-band magnitude limits for an

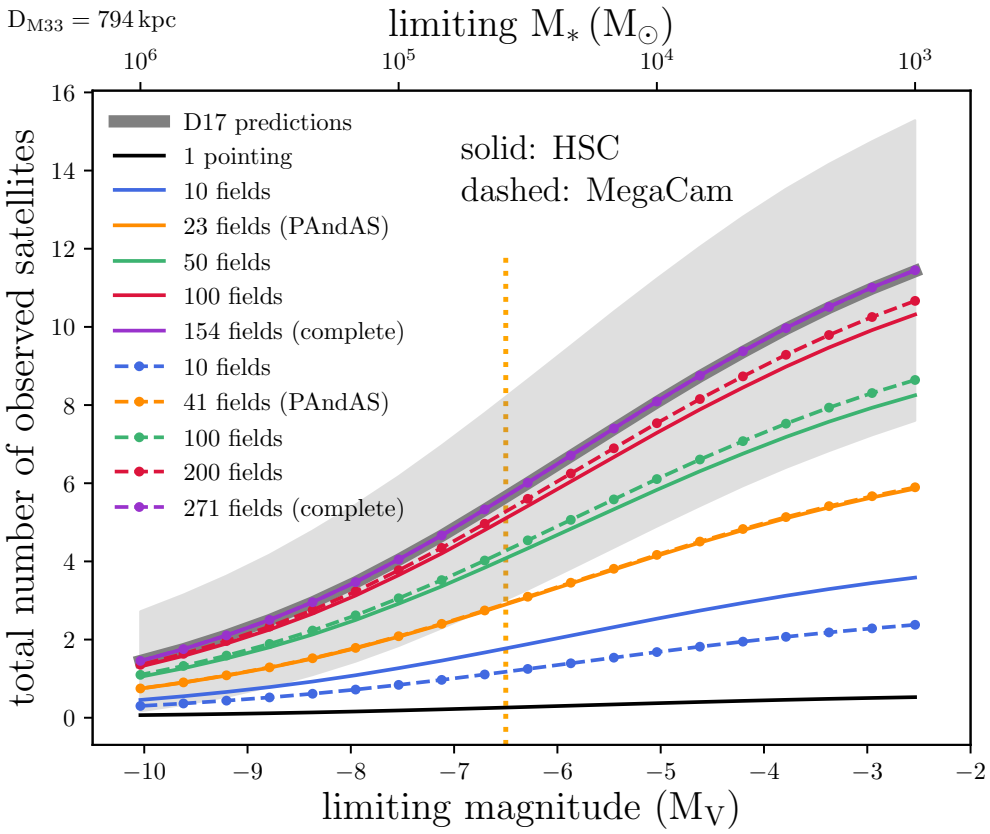

Figure 5.2: The total number of predicted M33 satellites as a function of limiting visual magnitude and limiting stellar mass. A mass-to-light ratio of unity is used to convert from M_V to M_*. The gray solid line and shaded region represent the D17 predictions. All colored lines refer to the D17 predictions corrected using the K_{los} scaling factor. Each line corresponds to N fields observed with HSC (solid lines) or MC (dot dashed lines). The PAndAS area is represented by 23 fields using HSC (solid orange line) and 41 fields using MC (dot dashed orange line). These two lines are coincident since they correspond to the same area. These results are exclusively for an M33 distance of 794 kpc. The dotted vertical orange line indicates the faintest object detected in the PAndAS survey.

$M_V = -6.7$ satellite corrected for the PAndAS completeness limits (see M16).

The black diamond indicates the resolved red giant branch stars in And XXII from M16. Our predictions for And XXII are in agreement with this simple luminosity function analysis. The vertical dashed gray lines represent the PAndAS 50% completeness limit, PAndAS limiting g-band magnitude and the HSC Subaru Strategic Program (SSP)[3] limiting g-band magnitude, respectively. When we change the default age of 12 Gyr and [Fe/H]=-2.0 to luminosity functions with the same age and [Fe/H]=-1.0, or with the same metallicity and an age of 5 Gyr, the predicted number of stars changes by 20 per cent at most.

With HSC on the 8.2m Subaru Telescope, reaching the PAndAS magnitude limit of $g \sim 26$ requires only $\sim$ 4-minute exposures, and $i \sim 25.5$ can be achieved in $\sim$ 12.5-min exposure time. Based on these exposure times, we estimate that a survey with Subaru/HSC covering 100 fields to PAndAS depth would require only $\sim$ 4 nights of observing time. As illustrated in Figure 5.3, observations extending to the depth of the HSC-SSP Deep fields ($g \sim 27.5$) could enable detection of ~ 20 stars in satellites as faint as $M_* = 10^3\ M_\odot$. HSC-SSP has required exposures of 1.4/2.1 hours per field in g/i to reach these depths. This is technically feasible, and could increase the expected number of M33 satellites by a factor of ~ 3 compared to the PAndAS depth. However, more reasonable exposure times of $\sim$ 25 and 55 minutes would reach depths of $g \sim 27$ and $i \sim 26.3$, enabling detection of most satellites to a few times $10^3\ M_\odot$. Such a survey would likely require $\sim 12-14$ nights to cover 100 HSC fields. The fainter satellites would make the model comparisons more statistically robust, and in addition these faintest galaxies could be the relics of the reionization era and the first populations of stars.

The imagers discussed thus far are both on ground-based telescopes, but upcoming space observatories will be far better equipped to tackle the region surrounding M33. WFIRST is expected to have a wide field imager with a field of view nearly 100 times that of the Hubble Space Telescope's IR channel. With a 0.28 square degree field of view, a region of 125 square deg (or a 160 projected kpc radius around M33)

[3]See `http://hsc.mtk.nao.ac.jp/ssp/survey/`.

would require 448 fields. The 2.4m aperture of WFIRST will be able to reach the same depths as HST in similar exposure times. For example, to reach $M_V = -7$ (or $\sim$17.5 in the V-band), short exposures of only 36 seconds could reach 6 magnitudes deeper than this in a total of $\sim$4 hours. Of course, this does not account for the additional overheard and slew time. Regardless, this would still be a small observing program for an observatory with the capabilities of WFIRST. A survey around M33 may also be suitable for proposed missions such as the Habitable Exoplanet Imaging Mission (HabEx), which will be able to observe resolved stellar populations in nearby galaxies.

The predictions listed in Tables 5.1 and 5.2 only consider the satellites that are bound to M33. The total number of galaxies observed around M33 would actually be a combination of M33 satellites and M31 satellites that happen to be near M33 since M33's halo is encompassed by M31's halo. These background M31 satellites are not included in our predictions but may be observed in extended surveys around M33. Adopting a mass of $1.5 - 2 \times 10^{12}\, M_\odot$ for M31, at a distance of about 200 kpc away, approximately a dozen M31 satellites with stellar mass $\geq 10^3\, M_\odot$ may coincide with the virial area of M33. If new satellites are detected around M33, additional kinematic information will be necessary to determine which host galaxy the satellites are bound to, similar to the case of And XXII.

Our results also assume that M33 has evolved in isolation and that its potential satellites have not endured strong tides from the larger environment surrounding M33. However, the past orbital history of M33 is not well-constrained, so these results are subject to change if M33 had any recent interactions with other galaxies, such as its host, M31. In the next section, we discuss plausible M33 orbital histories from the literature and the implications of such histories for its predicted satellite population.

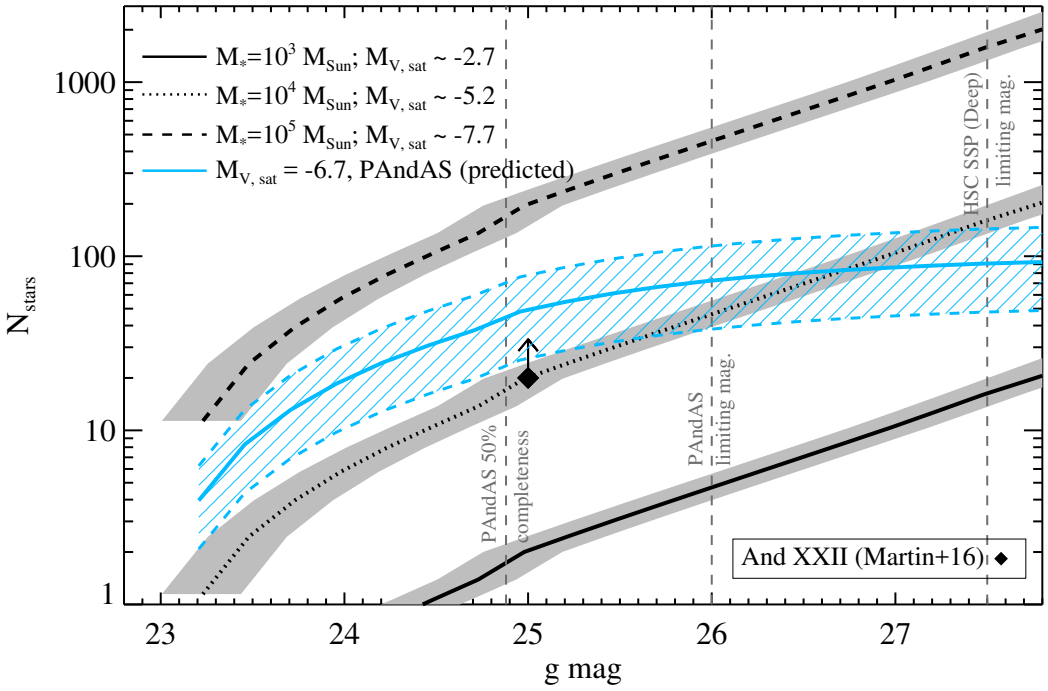

Figure 5.3: The predicted number of resolved stars per M33 satellite as a function of g-band magnitude. The black lines and gray shaded regions show the number of resolved stars for satellites of different masses or M_V across the range of M33 distances considered in this work. The blue line and hashed region indicates the number of resolved stars expected for a satellite of $M_V = -6.7$, the measured magnitude of And XXII (M16), corrected for the PAndAS completeness limits. These calculations assume a [Fe/H]=-2.0 stellar population with an age of 12 Gyr and an IMF power-law slope of -2.0. The black diamond shows the actual number of red giant branch stars observed in the PAndAS survey (M16). The observed number of And XXII stars is approximately consistent with the luminosity function predictions.

5.4 The Orbital History of M33

While the results in Section 5.3.3 are applicable to M33 at the time it first fell into M31's halo, the number of surviving M33 satellites is highly sensitive to M33's recent orbital history. In P17A, cosmological analogs of M33-mass subhalos around M31-mass hosts strongly favored more recent infall times with about 70% of all M33 analogs exhibiting infall times in the last 4 Gyr. Infall time was defined as the first time a subhalo crossed into the virial radius of its host while moving inwards. The trajectory after infall, however, can vary significantly. Constraining the orbital history of M33 is therefore key to understanding and predicting its surviving satellite population.

Computing the orbital history of halo substructures requires knowledge of several basic parameters. To start, the distance to both the host and satellite are crucial initial conditions (for analytic integrations) or as consistency checks (for the output of an N-body simulation). M31's distance is constrained to 785 ± 25 kpc (McConnachie et al., 2005) and estimates preceding this do not stray far from this range. M33's distance, however, spans a wider range of values from about 794 to 968 kpc (McConnachie et al., 2004; U et al., 2009) and can alter solutions for the past trajectory of M33.

In addition to distance, the 3D velocity of both the host and satellite are necessary. The proper motion of M33 was measured by tracking the motion of water masers using the *Very Long Baseline Array* (VLBA) (Brunthaler et al., 2005). M31's transverse motion has only been measured recently with the Hubble Space Telescope (HST) and *Gaia* (Sohn et al., 2012; van der Marel et al., 2012a, 2019). Prior to that, calculations of M33's orbit around M31 explored a wide range of plausible M31 tangential velocities. In Section 5.4.1, we discuss two studies that calculate M33's orbit without a measured value for M31's tangential velocity. In Section 5.4.2, we discuss studies that use directly measured and estimated values for M31's tangential motion to do the same. We also discuss the implications of these orbital histories on M33's satellite population and argue that the number of satellites discovered around

M33 can narrow the potential solutions for M33's orbital history.

5.4.1 M33's Morphologically Motivated Orbital History

Two recent studies have used the past orbit of M33 to find an explanation for its current morphology. Here we are only referring to the morphology in the outer regions of M33's disks. Knowledge of a warp in the outer HI disk of M33 was first reported in Rogstad et al. (1976) and later by Corbelli and Schneider (1997); Putman et al. (2009); Corbelli et al. (2014); Kam et al. (2017). While Rogstad et al. (1976); Corbelli and Schneider (1997) both concluded that the tidal force from M31 was not strong enough to induce this warp, more recent studies have revisited these claims.

For example, P09 showed that the gaseous M33 warp extends to nearly 22 kpc from the galaxy's center. As a result, they explore the possibility of a tidal interaction between M33 and M31 to explain such features by integrating orbits backwards in time. In the absence of a measurement for M31's tangential velocity components, they explore a range between -200 km s^{-1} and 200 km s^{-1}. For distances to M31 and M33, they adopt 770 kpc and 794 kpc, respectively. An M31 virial mass $> 2.5 \times 10^{12}\, M_{\odot}$ at $z = 0$ that decreases exponentially as a function of redshift is used throughout the P09 analysis. M33 is treated as a point mass of $\sim 10^{10}\, M_{\odot}$ that evolves in the presence of M31 and the MW, where the MW is also modeled as a point mass of $10^{12}\, M_{\odot}$. P09 concludes there is a 60% probability that M33 and M31 did reach within 100 kpc of each other about 3 Gyr ago, which yields an M33 tidal radius of 15 kpc. As a result, the tidal and ram pressure forces acting on M33 as it moves through M31 at a close distance are proposed to give rise to the asymmetries in M33's gaseous disk.

A warp in the stellar disk of M33 was discovered by the PAndAS survey (M09). The stellar warp has a similar orientation to the gaseous warp and extends about 30 kpc from its center. In an effort to reproduce the stellar morphological features observed in the PAndAS survey, M09 created a suite of N-body simulations of the M33-M31 system to search for an orbital history that leads to a tidal interaction.

These simulations aim to reproduce the stellar morphologies of M33 and M31, so they do not follow the evolution of neutral gas in either galaxy.

Using over 6 million particles, M33 and M31 are each modeled with a halo, disk and bulge component. The simulations use total masses of $2.56 \times 10^{12}\,M_{\odot}$ and $8.27 \times 10^{10}\,M_{\odot}$ for M31 and M33 respectively. The tangential velocity of M31 had yet to be measured, so a range of plausible velocities were explored to match the present day position and velocity of M33 in addition to the morphological features (see also Chapman et al., 2013). M09 finds several representative orbits of an M33-M31 encounter, one of which suggests that a pericentric passage at 55 kpc about 3 Gyr ago achieves the desired kinematics and observed features. Both the gaseous and stellar M33 warps can be accounted for by M09 and P09's proposed orbits, which together suggest M33 completed a pericentric passage at < 100 kpc in the last 3 Gyr.

Interestingly, a pericentric approach as close as 50 kpc could strongly truncate or perhaps destroy the gaseous disk of M33 (see Salem et al., 2015, for a study of the LMC's disk as it moves through the MW's circumgalactic medium), but this is not evident in HI observations of M33. Dobbs et al. (2018) have also shown that M33's flocculent spiral pattern and velocity field as seen in HI are reproducible in simulations through gravitational instabilities in the stars and gas alone, further supporting that an interaction is not required.

Implications for M33's Predicted Satellite Population

If M33 has already completed a pericentric passage about M31 in the last 3 Gyr, M31 could have tidally stripped satellites from M33's halo. These stripped satellites may appear to be satellites of M31 today. The strength of tidal forces depends directly on the distance between the two galaxies when M33 is at pericenter. In this section we explore how many satellites would survive a pericentric passage at a range of pericenter distances. Note that these calculations assume that all satellites outside of the calculated tidal radius are completely stripped from M33 and more detailed simulations of these scenarios should be explored.

Table 5.3: The tidal radius of M33 at three different pericentric distances: 50 kpc, 100 kpc, and 150 kpc from M31. All tidal radii are calculated assuming a virial mass of $2.5 \times 10^{11}\ M_\odot$ and scale length of 20 kpc for M33 where M33 is represented as a Plummer sphere. M31 is modeled as an NFW halo with masses of $1.5 \times 10^{12}\ M_\odot$ ($2 \times 10^{12}\ M_\odot$) and concentrations of 9.56 (9.36). The final row gives the fraction of the tidal radius volume relative to the virial volume of M33, suggesting that if satellites outside of $r_{\rm tidal}$ are stripped, very few are expected to remain bound to M33.

$\mathrm{r_{peri}}$ [kpc]	$\mathrm{M_{M31}(r_{peri})}$ [$10^{11}\ M_\odot$]	$\mathrm{r_{tidal}}$ [kpc]	$\frac{\mathrm{V(r_{tidal})}}{\mathrm{V(r_{vir})}}$
50	3.6 (4.2)	29.2 (26.9)	0.05
100	7.0 (8.6)	52.6 (48.8)	0.16
150	9.7 (12)	73.1 (67.8)	0.30

The tidal radius is computed following Eq. 3 of van den Bosch et al. (2018), which models both the host and satellite galaxy as extended objects:

$$\mathrm{r_t} = \mathrm{r_{peri}} \left[\frac{\mathrm{m(r_t)/M_{host}(r_{peri})}}{2 - \frac{\mathrm{dlnM}}{\mathrm{dlnR}}|_{\mathrm{R}}} \right]^{1/3} . \tag{5.4}$$

M33 is approximated as a Plummer sphere (Plummer, 1911) with a total mass of $2.5 \times 10^{11}\ M_\odot$ and a scale length of 20 kpc. M31 has been approximated as an NFW halo (Navarro et al., 1996) and we consider two different masses: $1.5 \times 10^{12}\ M_\odot$ with concentration $c_{\rm vir} \equiv r_{\rm vir}/r_s = 9.56$ and $2 \times 10^{12}\ M_\odot$ with $c_{\rm vir} = 9.36$. For pericentric distances of 50 kpc, 100 kpc, and 150 kpc, we have listed the corresponding tidal radii in Table 5.3 along with M31's mass enclosed at that distance and the fraction of the volume within the tidal radius relative to the virial radius.

For a pericentric approach at 50 kpc, only satellites in the inner 5% of M33's virial volume are expected to remain bound after such an encounter[4]. This yields a tidal radius of 27-29 kpc depending on the mass of M31. From the results in Tables 5.1 and 5.2 only one to two satellites on average are expected to be in a survey radius of ∼30 kpc that reaches the same photometric depth as PAndAS ($M_V \sim -6.5$; $M_* = 10^4 - 10^5\ M_\odot$). PAndAS surveyed a larger area but only one

[4]In this section, "bound" refers to whether a satellite can escape the influence of M33's gravitational potential due to M31's tidal forces.

potential M33 companion was identified.

At a pericentric passage of 100 kpc, only satellites within 49-53 kpc (16% of the virial volume) of M33 are estimated to be bound today. This yields two to four satellites with M_* between $10^4\,M_\odot$ and $10^5\,M_\odot$ in a circular area with a radius of $\sim$50 kpc. For a wider pericentric approach of 150 kpc, a tidal radius of 68-73 kpc yields an average of three to six satellites at these detection limits. Fainter M33 satellites ($M_* \sim 10^3\,M_\odot$) are also predicted to exist within these proposed survey radii, but deeper observations would be necessary to robustly detect such faint objects.

If a total of approximately four or more satellites ($M_* \gtrsim 10^4\,M_\odot$) are discovered and furthermore confirmed as true M33 satellites (i.e. through proper motion analysis), a recent, close (< 100 kpc) tidal encounter (M09, P09, Semczuk et al., 2018) is unlikely under the assumption that the D17 predictions are correct since only one or two satellites are estimated to survive such a close interaction.

5.4.2 M33's Orbital History Using its Current Space Motion

Orbits Using Direct M31 Proper Motion Measurement

Section 5.4.1 summarizes M33 orbital histories that aimed to reconstruct the observed morphological structure of the M31-M33 system. P17A computed the orbital history for M33 around M31 using only the current space motion of both galaxies. Such calculations still require assumptions for the mass of both galaxies, however, the focus is shifted to the most statistically common orbital histories for M33. These calculations are made possible by direct measurement of M31's proper motion using the HST (Sohn et al., 2012; van der Marel et al., 2012a). Sohn et al. (2012) presents the direct measurement from three fields of data. van der Marel et al. (2012a) corrects the HST measurement for the internal motion of M31, viewing perspective, and weights this measurement with several indirect methods discussed in van der Marel and Guhathakurta (2008). Both HST derived measurements yield similar M33 orbits (see P17A for more details).

P17A follows a similar methodology to P09 to compute M33's orbit. A three

component analytic potential is adopted for M31 but M33 is approximated by a Plummer sphere rather than a point mass. The latter is necessary to approximate the effects of dynamical friction accurately. Rather than choosing just one mass for either galaxy, a range of masses is explored resulting in six different M31-M33 mass combinations. M33's mass range is set by the dynamical mass estimate on the low end and extends up to masses predicted by AM relations. This results in a range from $5-25\times10^{10}\,M_{\odot}$ (Corbelli and Salucci, 2000; Guo et al., 2011). For M31, virial masses of $1.5-2\times10^{12}\,M_{\odot}$ are considered, similar to our tidal radius calculations. Note that these M31 masses are lower than those adopted in both M09 and P09.

Using the 6D phase space information derived from proper motions of both galaxies, 10,000 orbits are calculated for each mass combination. The 10,000 orbits encompass measurements errors in the distances to M33 and M31, their proper motions, and the measurement errors in the solar quantities, which are used to correct for a galactocentric reference frame (van der Marel et al., 2012a). Less than 1% of all orbits achieve a pericentric passage within 100 kpc of M31 during the last 3 Gyr, regardless of M33 mass. If the mass of M31 is increased to $> 2\times10^{12}\,M_{\odot}$, this increases to a few percent of orbits. Instead, most orbital solutions favor a scenario where M33 is on its first infall into M31's halo (like the Magellanic Clouds in the Milky Way; Besla et al., 2007), or it is on a long period orbit where its last pericentric passage was about 6 Gyr ago at a distance of $\sim$ 100 kpc from M31. These solutions are in agreement with other dynamical studies of LG galaxies (Shaya and Tully, 2013; van der Marel et al., 2012b).

All calculations assume a distance of $\sim$ 800 kpc to M33, which corresponds to a separation of about 200 kpc between M33 and M31. Higher M33 distance (U et al., 2009) measurements would suggest larger separations between M33 and M31 (in excess of 220 kpc). Larger separations provide further support for a first infall scenario. In the event of a long period orbit, higher M33 distances suggest that the pericenter occurred closer to 5.5 Gyr ago or that their separation at pericenter was $>$ 100 kpc. The orbits of cosmological M33 analogs in P17A that completed a pericentric passage about their host ($\sim$77% of the sample) exhibited average infall

times $t_{\rm inf} = 3.9 \pm 2.1$ Gyr and a wide range of average distances at pericenter where $r_{\rm peri} = 89.8 \pm 60.2$ kpc.

Orbits Using M31 Proper Motion Estimates

The P17A models use the M31 proper motion measurement from van der Marel et al. (2012a), but other values have also been reported through indirect methods. Salomon et al. (2016, hereafter S16) inferred M31's proper motion using the one-dimensional kinematics of its satellites. This yields an M33 orbital history in which it makes a pericentric approach in the last 2-3 Gyr, but only at distances of 140-175 kpc on average (P17A). At these separations, it is not likely that M31 can induce any strong tidal features such as the warps seen in M33's disks.

More recently, Semczuk et al. (2018) has explored the range of relative velocity vectors derived from the S16 M31 proper motion estimates. Similar to our P17A analysis, Semczuk et al. (2018) conclude that the van der Marel et al. (2012a) M31 proper motion measurement does not favor a recent tidal interaction between M33 and M31. They instead focus on the S16 results, which are more likely to result in a recent encounter between the galaxies within the estimated error space. By varying the initial magnitude and direction of the S16 velocity vector, Semczuk et al. (2018) recovers orbits with pericentric distances < 100 kpc in the last 2 Gyr, settling on a fiducial orbit with a pericentric distance of 37 kpc at 2.7 Gyr from the start of their simulation. Note that this distance at pericenter is even smaller than that suggested by both P09 and M09. It is also closer than the predicted pericentric distance for the LMC relative to the MW (Besla et al., 2007).

Using this fiducial orbit, Semczuk et al. (2018) run an additional N-body/SPH simulation of the M33-M31 system and reproduce features similar to the gaseous warps and stellar streams in M33 only when an M31 hot halo is included. While Semczuk et al. (2018) perform a thorough analysis of the S16 M31 proper motion error space, the S16 errors are about twice as large as those in van der Marel et al. (2012a). The relative velocity vector corresponding to the best match projection in neutral hydrogen is 1-2σ in each component from the average S16 results and up to

4-5σ from the van der Marel et al. (2012a) values. Such discrepancies in the orbital history of M33 clearly demonstrate the need for additional direct measurements of M31's proper motion. Third epoch measurements with HST may be able to provide a factor of two to three improvement for M31's tangential velocity.

Independent proper motions for M33 and M31 have already been measured with *Gaia* DR2 (Gaia Collaboration et al., 2018a; van der Marel et al., 2019). These results agree with the van der Marel et al. (2012a) M31 results at $< 1\sigma$. For M33, the Gaia DR2 proper motion is in agreement with the VLBA Brunthaler et al. (2005) proper motion at the 1σ level. The Gaia DR2 proper motions are an independent consistency check that the previously measured M33 and M31 proper motions are accurate. When the M31 DR2+HST weighted average and the M33 DR2+VLBA weighted average are used to compute the orbital history of M33 similar to P17A, a first infall scenario is unanimously preferred.

Implications for M33's Predicted Satellite Population

In Section 5.4.1, we conclude that the discovery of four or more confirmed satellites could suggest a close tidal interaction between M33 and M31 (M09, P09, Semczuk et al., 2018) is unlikely, leaving only a long-period orbit or first infall scenario (P17A).

If M33 made its closest approach to M31 around 6 Gyr ago at a distance of 100 kpc, some tidal stripping would be expected and this could reduce the number of bound M33 satellites observed today (see Section 5.4.1). Only two to four surviving satellites are predicted to remain bound to M33 in such circumstances. Recall that the interaction history between M33 and M31 is typically used to explain M33's morphology. If M33 experienced a pericentric passage at larger distances (> 100 kpc) as suggested in P17A, tidal interactions alone are unlikely to be the origin of M33's warps. Interactions between satellites of M33 and M33 must therefore be invoked. Our calculations confirm that M33 would retain a fraction of its satellite population in these orbital scenarios and subsequently that tidal forces owing to M31 plus interactions with satellites could lead to its current morphological asymmetries. These conclusions do not account for the potential relaxation of the gaseous and

stellar disk after this type of tidal interaction, thus simulations should be carried out to determine how long-lived such features are on average relative to a 6 Gyr orbital period.

If M33 is on first infall and has evolved in isolation for a majority of its lifetime, its satellite population is expected to be almost fully intact. A full virial volume survey could result in four to eight satellite galaxies with $M_* = 10^4 - 10^5\,M_\odot$ if the D17 predictions hold. Up to seven additional, fainter satellites ($M_* < 10^4\,M_\odot$) may also be detected with a survey reaching greater photometric depth than PAndAS. Due to the higher concentration of satellites in the inner region of M33's halo, even a 100 kpc survey radius (twice that of the PAndAS survey) is expected to yield $\gtrsim 90\%$ of the predicted M33 satellite population.

Greater than four M33 satellite candidates would provide further evidence for a first infall scenario. On the other hand, a deficiency of satellites may confirm a recent, pericentric approach of M33 around M31. Alternatively, it could suggest that the D17B methodology needs revision. Recall that the determination of luminous satellites from dark subhalos is sensitive to the $M_* - M_{\rm halo}$ relationship and the effects of suppressed star formation due to reionization. Different AM models or a modification of the reionization implementation may alter the resulting satellite population. Finally, the ΛCDM cosmology itself could be flawed and perhaps other types of dark matter (i.e. warm, hot, self-interacting) may need to be considered.

5.5 Discussion

The predictions provided in this work represent the number of satellites expected around an LMC or M33-mass host at $z = 0$ after accounting for the accretion history and the potential group pre-processing that may have taken place prior to infall (see Wetzel et al., 2015). M33 could have up to 15 satellites down to a limiting magnitude of $\mathrm{M_V} = -3$ today according to the GK17 AM model in D17B. A more recent study suggests that LMC-mass hosts could have $\sim$25 surviving satellites down to $\mathrm{M_V} = -3$ if reionization occurred at $z \sim 6$ (Bose et al., 2018), indicating that these predictions

strongly depend on the choice of AM method and the time of reionization.

Simulations are also known for the over-disruption of subhalos owing to numerical effects associated with simulation softening length choices in cosmological simulations (van den Bosch and Ogiya, 2018) and tidal effects due to the presence of a galactic disk (Garrison-Kimmel et al., 2017b). AM techniques are calibrated against simulations to match with observations and incorporate such inaccuracies in the $M_* - M_{\rm halo}$ relationship itself. These processes are not expected to underestimate the satellite population for a single AM technique, but may add additional variation to this type of analysis across many AM methods.

Additionally, the cosmological zoom simulations used in the D17 formalism and Bose et al. (2018) do not include baryonic physics, but the co-evolution of baryons and dark matter is known to impact the abundance and properties of dark matter substructures (e.g. Garrison-Kimmel et al., 2017b; Dolag et al., 2009; Brooks and Zolotov, 2014; Wetzel et al., 2016; Sawala et al., 2017). For example, Garrison-Kimmel et al. (2017b) and Sawala et al. (2017) have recently studied the impact of baryons in cosmological zoom simulations of MW-like halos using different prescriptions for star formation and feedback and both studies conclude that the dark matter only simulations overpredict the number of subhalos within 300 kpc of the simulated MW-like halos by factors of 1.2-1.5 relative to the full hydrodynamical simulation counterparts. This difference is largely attributed to the gravitational influence of the host galaxy's disk. Within 50 kpc of the host, subhalos counts are overpredicted by a factor of 1.75-2 (Sawala et al., 2017) or 3-4 (Garrison-Kimmel et al., 2017b).

If the same disparity holds for halo masses an order of magnitude less massive ($\sim 10^{11}\,M_\odot$), the subhalo populations for galaxies like M33 would also be overpredicted by similar amounts. The subhalo counts themselves determine the SHMF and are important for establishing abundance matching relations between observations and simulations, but the time of reionization and how it is implemented also plays a key role in determining which of the subhalos host luminous satellites. As a result, an overabundance of subhalos in dark matter only simulations does not directly

correlate to an overprediction of luminous halos. While the combination of these effects may affect the number of predicted satellites around galaxies like M33, it is unclear by exactly how much once both numerical effects and contributions from baryonic physics are reconciled and this should be studied in further detail.

Regardless of these phenomena, if M33 is just now reaching the closest distance to M31 ever, it is likely to have been host to more satellites prior to infall than these studies suggest. Below, we discuss the satellites of satellites hierarchy, its implications for the merger history and morphological evolution of an M33-mass galaxy, and the mass function of the predicted M33 satellite population.

5.5.1 Implications for Satellites of Satellites

If the M33 orbital history presented in Section 5.4.2 is correct and M33 did not have a recent, close tidal interaction with M31, alternate explanations for M33's gas and stellar disk warps are required. One potential solution is that satellites themselves could induce such warping through close interactions, high speed flybys, collisions, or mergers.

Simulations of discy dwarf galaxy hosts with $M_{vir} = 5.6 \times 10^{10} M_{\odot}$ and dark subhalos with 5-20% of the host mass have illustrated that subhalos can alter the kinematics and structure of the dwarf hosts during interactions (Starkenburg et al., 2016). They find that dark satellites on radial orbits can especially cause structural changes in the host galaxy that manifest as asymmetries in both the gas and stars. For slightly higher mass host halos like M33, similar processes between dark matter dominated dwarfs or dark satellites may also lead to morphological features that mimic those produced by tidal interactions. The mass ratios of such encounters, however, would have to be low (i.e. halo mass ratios $\lesssim 1/100$) and at distances that would not perturb the innermost regions of M33's gaseous and stellar disks.

For example, Semczuk et al. (2018) provides a basic analysis of whether And XXII could provide the tidal impact necessary to induce M33's warps. They conclude that And XXII would have to reach very close distances ($\sim$5 kpc) to induce such features at which point M33's disk may be affected. We emphasize that while one

close interaction between M33 and a satellite may not be enough to induce the warps and debris in and around M33, several interactions with one or more satellites could amount to its current morphology.

Following ΛCDM hierarchical assembly, M33 should have experienced several mergers already. The cumulative merger histories of ∼100 massive satellite galaxy analogs ($M_{halo} > 10^{11} M_\odot$, P17A) residing in M31-mass halos ($0.7 - 3 \times 10^{12} M_\odot$) in the lllustris-1 cosmological simulation (Vogelsberger et al., 2014a; Nelson et al., 2015) show that the median number of galaxy-galaxy mergers throughout a massive satellite galaxy's lifetime is 3 ± 1.5 (Rodriguez-Gomez et al., 2015). This excludes any mergers between galaxies that cannot be traced back to two different friends-of-friends groups, but it does include all mergers with stellar mass ratios $> 1/10$. A floor of ten stellar particles ($M_* \sim 10^7 M_\odot$) for the smallest progenitor in each merger is imposed, thus these estimates will not include merger events involving ultra-faint dwarf galaxies, for example.

Recent work on dwarf-dwarf mergers has shown that merger remnants are biased towards larger distances in host galaxy halos since mergers typically occur before infall thereby resulting in more recent accretion times (Deason et al., 2014). If M33 is indeed on its first infall into M31's halo with an accretion time of 2-4 Gyr ago as suggested in P17A, this picture is consistent with M33's current morphology and separation of about 200 kpc from M31, or beyond half of the virial radius of M31.

Jethwa et al. (2016) have suggested that a total of 70^{+30}_{-40} satellites between $-7 < M_V < -1$ could have evolved within the virial radii of either of the Magellanic Clouds prior to infall into the MW's halo (see also Drlica-Wagner et al., 2015). If M33 has a similar or greater halo mass than the LMC, it has likely been host to tens of satellites throughout its lifetime as well (once the contribution of satellites associated with an SMC-mass companion are subtracted). The number of mergers predicted using Illustris-1 plus the number of surviving satellites expected to reside around an LMC-mass galaxy today (D17B, Bose et al., 2018) are roughly consistent with the lower limit presented in Jethwa et al. (2016).

5.5.2 The Lack of Bright M33 Companions

Much of our analysis focuses on satellites in the ultra-faint dwarf galaxy regime. However, ΛCDM suggests that even host galaxies with stellar masses comparable to the LMC or M33 should have fairly smooth satellite mass functions such that they host at least one $M_* \sim 10^6\,M_\odot$ satellite, resulting in a three orders of magnitude difference between host and satellite stellar masses at most. This gap is often referred to as the stellar mass gap statistic (see Deason et al., 2013).

An M33 satellite of this mass and brightness ($M_* \gtrsim 10^6\,M_\odot$ and $-9 > M_V > -10$) would have been detected in surveys such as SDSS, yet none have been found. If we assume that And XXII or another satellite of roughly the same stellar mass is M33's next most massive satellite, this leads to a four or five orders of magnitude difference between the stellar mass of M33 and its brightest satellite, suggesting that this is possibly a small-scale ΛCDM problem.

Recently discovered dwarfs around the Large Magellanic Cloud also lead to a fairly substantial stellar mass gap for the LMC. There, the difference in the LMC's stellar mass and that of its next most massive satellite is almost six orders of magnitude (see D17B and references within). Unfortunately, the complex orbital history of the LMC and SMC (i.e. their binary nature and recent infall into the MW's halo; see Besla et al., 2007, 2012; Kallivayalil et al., 2013; Diaz and Bekki, 2011) makes it difficult to determine whether this stellar mass gap is long-lived or if interactions between the Magellanic Clouds have changed their total satellite populations and therefore the stellar mass gap characteristic over time.

First results from the MADCASH survey have yielded one satellite galaxy around NGC 2403, a dwarf spiral at 3.2 Mpc with about twice the LMC's stellar mass (Carlin et al., 2016). The dwarf companion (MADCASH J074238+652501-dw) is estimated to have a stellar mass of $\sim 10^5\,M_\odot$ and a previously known satellite, DDO 44 has a stellar mass of approximately $6 \times 10^7\,M_\odot$ (Karachentsev et al., 2013). The presence of DDO 44 leads to only a two orders of magnitude stellar mass gap for this system, which is more consistent with ΛCDM expectations. However, Besla et

al. 2018 (submitted) find that less than 1% of isolated dwarf pairs in both SDSS and cosmological mock catalogs are stellar mass analogs of the Magellanic Clouds, suggesting that mass gaps of about one order of magnitude are very uncommon. Further results from the MADCASH survey will increase the sample of LMC stellar mass hosts and their satellite populations, helping to decipher whether stellar mass gaps are truly in contention with ΛCDM. A larger sample may also inform our knowledge of how host environment may affect the properties and number of satellite companions around LMC/M33 stellar mass galaxies.

5.6 Conclusions

We have tabulated the number of satellites expected to reside within the virial radius of M33 following the D17 framework to motivate a concentrated search for M33 satellites beyond the existing PAndAS survey region. To date, there is only one potential M33 candidate satellite, And XXII, but it is unclear based on its one-dimensional kinematics whether And XXII is bound to M31 or M33. A proper motion measurement for And XXII would make it possible to derive a full orbital history in the combined M31+M33 gravitational potential and possibly determine if it is a true satellite of M33 or just another member of the larger M31 system.

The discovery of additional M33 satellites or the lack thereof could further constrain the orbital history of M33. The common orbital histories in the literature have different implications for the M33 satellite system as one (M09, P09, Semczuk et al., 2018) suggests it had a recent tidal interaction with M31 that occurred at close enough separations to induce warps in M33's stellar and gaseous disk and potentially strip satellites away from M33's halo. On the other hand, the current space motions of M33 and M31 favor a scenario where M33 was only recently accreted into M31's halo and is moving towards its first pericenter or a scenario in which M33 already completed its first pericentric passage around M31 at about 6 Gyr ago and at separations $\gtrsim$100 kpc (P17A, van der Marel et al., 2019). If M33 is on its first infall, its satellites are expected to remain bound and the satellites

themselves may explain M33's morphology. A wide pericentric passage may strip away some outer M33 satellites but a majority of the satellites are still expected to remain dynamically stable.

While a survey encompassing the full virial area of M33 on the sky that reaches the same depth as the PAndAS survey would provide the most complete picture of the M33 satellite population, a survey of this magnitude would not be trivial. A survey extending to 100 kpc in projection from the center of M33 (or twice the PAndAS survey radius), however, would yield up to eleven M33 satellites on average with $M_* \geq 10^3\,M_\odot$ (or about five satellites at the PAndAS photometric limits) if the D17 predictions are correct. This is approximately $\sim$90% of the total predicted M33 satellite population. The PAndAS survey area already observed about 50% of this region, so a ground-based imager like HSC with a 1.5° field of view diameter would need to observe about 50 fields of new data. In the era of WFIRST, this proposed survey would be a small program requiring about 224 fields and short exposure times of about 36 seconds each.

We conclude that the discovery of four or more new M33 satellites would strongly disfavor the recent, close tidal interaction scenario. Greater numbers of satellites would provide further evidence of a first infall scenario or a long-period orbit at larger pericentric distances. Upwards of about six M33 candidate satellites would permit only a first infall scenario for M33 given the measured positions and velocities of M33 and M31.

In addition to dwarf satellite galaxies, extending the PAndAS survey region may also result in the discovery of additional globular clusters. Studies of the inner (< 10 kpc; San Roman et al., 2010) and outer (10-50 kpc; Cockcroft et al., 2011) regions of M33 concluded M33 has a much lower globular cluster surface density than M31, especially in its outermost regions. These results suggest that some M33 globular clusters may have been accreted by M31 through recent tidal interactions or that M33's accretion history is calmer than M31's, which could mean it evolved in a more isolated, low density environment. The latter would also support a first infall scenario for M33.

The disparity between the orbital histories presented in M09, P09, and Semczuk et al. (2018) compared to P17A and van der Marel et al. (2019) leads to further discussions on the history of the larger M31 system. For example, a first infall scenario for M33 suggests that it entered M31's halo around the same time that the progenitor of M31's Giant Southern Steam was moving towards the center of M31 for the first time (Ibata et al., 2004; Font et al., 2006; Fardal et al., 2006). The implications of two massive satellites entering the halo of an M31-mass galaxy have yet to be explored and will be the topic of future work.

Additional deep surveys of M33 and LMC stellar mass analogs residing within the halos of intermediate mass galaxies like the MW and M31 will further our understanding of satellite populations around low mass host galaxies in the era of WFIRST and LSST. These data will also allow us to comment further on whether the lack of bright companions around M33 is a true obstacle for ΛCDM. Since approximately one-third of all MW-mass halos host a massive satellite like the LMC or M33 (P17A, Boylan-Kolchin et al., 2011a; Tollerud et al., 2011a; Robotham et al., 2012), the 'satellites of satellites' phenomena is an intriguing way to increase our understanding of the faint end of the galaxy luminosity function overall.

CHAPTER 6

First *Gaia* Dynamics of the Andromeda System: DR2 Proper Motions, Orbits, and Rotation of M31 and M33

This chapter is an excerpt from a paper which has been published previously as van der Marel, R. P., Fardal, M. A., Sohn, S. T., Patel, E., Besla, G., del Pino, A., Sahlmann, J., Watkins, L. L., 2019, ApJ, 872, 24. I was responsible for the calculations in the Discussion section and co-wrote the Introduction and Discussion text. The original abstract, introduction, discussion, and conclusions sections are included. An abridged section titled "Data Samples and Proper Motion Analysis" has been added in place of original text to provide context for the results presented.

Abstract

The 3D velocities of M31 and M33 are important for understanding the evolution and cosmological context of the Local Group. Their most massive stars are detected by *Gaia*, and we use Data Release 2 (DR2) to determine the galaxy proper motions (PMs). We select galaxy members based on, e.g., parallax, PM, color-magnitude-diagram location, and local stellar density. The PM rotation of both galaxies is confidently detected, consistent with the known line-of-sight rotation curves: $V_{\rm rot} = -206 \pm 86$ km s^{-1} (counter-clockwise) for M31, and $V_{\rm rot} = 80 \pm 52$ km s^{-1} (clockwise) for M33. We measure the center-of-mass PM of each galaxy relative to surrounding background quasars in DR2. This yields that $(\mu_{\alpha*}, \mu_\delta)$ equals $(65 \pm 18, -57 \pm 15)$ μas yr^{-1} for M31, and $(31 \pm 19, -29 \pm 16)$ μas yr^{-1} for M33. In addition to the listed random errors, each component has an additional residual systematic error of 16 μas yr^{-1}. These results are consistent at 0.8σ and 1.0σ with the (2 and 3 times higher-accuracy) measurements already available from *Hubble Space Telescope* (*HST*) optical imaging and VLBA water maser observations, respectively. This lends confidence that all these measurements are robust. The new results imply

that the M31 orbit towards the Milky Way is somewhat less radial than previously inferred, $V_{\rm tan,DR2+HST} = 57^{+35}_{-31}$ km s^{-1} , and strengthen arguments that M33 may be on its first infall into M31. The results highlight the future potential of *Gaia* for PM studies beyond the Milky Way satellite system.

6.1 Introduction

The Milky Way (MW), Andromeda (M31) and Triangulum (M33) galaxies are the three most massive members of the small group of galaxies commonly referred to as the Local Group (LG). Together these spiral galaxies make up the majority of the mass in the LG, which has been estimated to weigh approximately 3–5 $\times$ 10^{12}M$_{\odot}$ (e.g., González et al., 2014; van der Marel et al., 2012a, hereafter vdM12a).

As our nearest laboratory for testing theories of galaxy formation and evolution, the LG and its constituents are the best examples of hierarchical structure formation and large-scale structure. Studies of galactic archaeology and near-field cosmology have made tremendous progress in recent decades, and this has placed the LG in a proper cosmological context. However, much of this work was carried out without detailed knowledge of the three-dimensional (3D) velocity vectors of LG objects. At the distances of these objects, the proper motions (PMs) are small and hard to measure with traditional techniques. As a result, the relative motion of M31 with respect to the MW has been a matter of debate. This motion is central to our understanding of both the assembly and current state of the LG (e.g., Forero-Romero et al., 2013; Peebles and Tully, 2013) and its future evolution (Cox and Loeb, 2008; van der Marel et al., 2012b, hereafter vdM12b).

PM measurements are also an essential ingredient for a better understanding of the dynamics of satellite galaxies and tidal streams. This has been successfully explored in the halo of the MW system (e.g., Pawlowski and Kroupa, 2013; Sohn et al., 2015), but measurements for the halo of the Andromeda system are still lacking. Also, PM measurements can reveal the internal rotation and structure of galaxies. Reports of this date back a century with the (discredited) work of van Maanen

(reviewed in Hetherington, 1972). This has now become possible, but to date the technique has only been realized for the Large (LMC) and Small (SMC) Magellanic Clouds (van der Marel and Kallivayalil, 2014; van der Marel and Sahlmann, 2016b; Niederhofer et al., 2018; Zivick et al., 2018). Among other things, this makes it possible to obtain kinematic distance estimates when combined with LOS velocity data (Olling and Peterson, 2000).

The line-of-sight (LOS) velocity of M31 was first determined by Slipher using observations performed in 1912 (Slipher, 1913). Exactly one century later, observations with the *Hubble Space Telescope* (*HST*) were used to report for the first time the absolute PM (Sohn et al., 2012, vdM12a). *HST* observed three fields of stars in M31 over a 5–7 year baseline to obtain a measurement with an accuracy per coordinate of 12 μas yr^{-1} ($\sim$ 45 km s^{-1}).

Alternatively, the transverse velocity $V_{\rm tan}$ of M31 can be estimated by indirect dynamical methods based on modeling the LOS velocities of M31 or LG satellites. A collection of methods was presented in van der Marel and Guhathakurta (2008), and their implications were subsequently refined with more recent data in vdM12a. These methods assume little more than non-rotating equilibrium. Salomon et al. (2016, hereafter S16) used a variation on one of these methods and applied it to a larger sample of satellite galaxies with more precise distance measurements. Their method makes more specific assumptions about the dynamical equilibrium of the satellites, but was verified using cosmological simulations. All methods yield a fairly consistent $V_{\rm tan}$, with a method-dependent uncertainty of $\sim$ 60–90 km s^{-1} per coordinate.

The PM measured with *HST* differs from the $V_{\rm tan}$ implied by the indirect dynamical methods. In case the of the S16 values, the difference is 130–140 km s^{-1} in each coordinate, with an uncertainty of $\sim$ 80 km s^{-1}. This is significant at the 1.9σ level. vdM12a posited that different methods probably have different systematics, so that the most accurate estimate is obtained by averaging the direct PM measurement with the indirect dynamical results. Either with or without this averaging, the resulting velocity is statistically consistent with a direct radial (head-on collision)

orbit for M31 towards the MW, implying a future collision and merging of the two galaxies (vdM12b). By contrast, S16 adopted their indirect dynamical estimate as the preferred one, and hence argued that $V_{\rm tan}$ is in fact 165 ± 62 km s^{-1}, in which case the LG may not be a bound system. These discrepancies clearly impact our understanding of the dynamics of the LG.

The situation is different for M33. The PM of M33 was determined using VLBA water maser observations by Brunthaler et al. (2005). VLBA has very high intrinsic spatial resolution, unlike *HST*, which has the ability to measure PMs at levels below one-hundredth of a pixel. The VLBA determination is therefore likely to be robust. However, the motion of M33 relative to M31 is less well-constrained, due to the uncertainties in the PM of M31.

The M33-M31 orbit is interesting for multiple reasons. Observations of M33 have provided evidence for warps in its outer stellar and gaseous disks (Rogstad et al., 1976; Corbelli and Schneider, 1997; Putman et al., 2009; Corbelli et al., 2014; Kam et al., 2017). Tidal streams have been detected as well (McConnachie et al., 2009). By aiming to match these morphological features in M33 via simulations, it is possible to constrain the allowed M33 orbits and M31 PM values (Loeb et al., 2005; van der Marel and Guhathakurta, 2008). McConnachie et al. (2009) find that the stellar debris around M33 can be formed through a recent (< 3 Gyr ago), close (< 55 kpc) tidal interaction with M31. Semczuk et al. (2018) argue that the S16 estimate of M31's $V_{\rm tan}$ is more consistent with this scenario than the *HST* PM measurement, but they did not explore the full space of orbits allowed within the uncertainties.

The M31 *HST* and M33 VLBA PM measurements can be combined to determine both the future orbital evolution (vdM12b) and past orbital history of the M33-M31 system. Patel et al. (2017a, hereafter P17) calculated the plausible orbital histories for M33 to determine which orbital solutions are allowed within the observational uncertainties. They concluded that M33 is either on its first infall into the halo of M31 or that it is on a long-period orbit (~ 6 Gyr) where it completed a pericentric approach at a distance of $\sim$100 kpc. First infall orbits are in fact cosmologically expected for satellites in this mass range at the present epoch (Boylan-Kolchin et al.,

2011a, P17).

New observational evidence for the PMs of M31 and M33 is highly desirable to discriminate between the various scenarios discussed above. The Data Release 2 (DR2) (Gaia Collaboration et al., 2018a) of the *Gaia* mission (Gaia Collaboration et al., 2016) provides an opportunity for progress. The *Gaia* mission is optimized for studies of the MW (Gaia Collaboration et al., 2018c) and its satellite system (Simon, 2018; Fritz et al., 2018; Kallivayalil et al., 2018; Massari and Helmi, 2018; Gaia Collaboration et al., 2018b, hereafter H18). However, rare supergiant stars in star-forming regions can be bright enough to be detected by *Gaia* even at the distance of the Andromeda system. We therefore present here the first *Gaia* study of the dynamics of the Andromeda system, focusing on the PMs of M31 and M33 as revealed by the DR2.

The available accuracies with DR2 are not yet competitive with either *HST* or VLBA, but they are close. So by themselves, they cannot yet resolve most of the aforementioned questions. However, they have the potential to discriminate some opposing models and scenarios, and they provide an independent consistency check. For example, both the M31 measurement with *HST* and the M33 measurement with VLBA use small areas within these galaxies, and must correct for the internal kinematics within these galaxies which is a potential source of systematic error. *Gaia* observes the entire disk of each galaxy and thus is more robust in this respect. *Gaia* can also help check for purely instrumental biases in the other measurements. Moreover, it is possible to measure the PM rotation of both galaxy disks. The present study derives the current constraints from *Gaia* in these areas, and highlights the potential for further progress with future *Gaia* data releases.

6.2 Data Samples and Proper Motion Analysis

6.2.1 M31 and M33 Sample Selection

At the distance of M31 (D = 770 kpc) and M33 (D = 794 kpc), *Gaia* can easily pick out bright, young stars in the most actively star-forming regions across the

disks of both galaxies. In a pre-release assessment using DR1 data, we confirmed that sources in the *Gaia* DR1 catalog were true point sources rather than patches of nebular emission by cross checking with sources from the LGGS catalog (Massey et al., 2016) and comparing to images from SDSS. These sources show evidence for a color-magnitude diagram (CMD) that is consistent with supergiants at the distance of the M31 system, confirming that *Gaia* provides reliable sources for astrometric analysis of the M31 system.

To extract the stellar sources necessary for this analysis, all *Gaia* DR2 sources within circular regions of 1.8° and 1° around M31 and M33, respectively were initially selected. All sources within these regions without PMs were removed and several additional sample cuts designed to rule out bad astrometric measurements and contaminants were then imposed. These criteria are described below:

- Remove sources with parallax values that are inconsistent with the M31 system at the 2σ level.
- Remove sources outside of an initial color-magnitude box defined by $-1.0 < G_{BP} - G_{RP} < 4$ and $G > 16$.
- Only retain sources with PM values defined by the following loose criteria: $|\mu_{\alpha*}| < 0.2\,\mathrm{mas\,yr^{-1}} + 2.0\sigma_{\mu_{\alpha*}}$ and $|\mu_{\delta}| < 0.2\,\mathrm{mas\,yr^{-1}} + 2.0\sigma_{\mu_{\delta}}$. This ensures that all sources with velocities that differ by $\gtrsim 500$ km s^{-1} from M31 and M33 are excluded.
- Following Eq. C.1 in Lindegren et al. (2018), remove sources with bad astrometric fits from the sample.
- Only keep sources falling within an ellipse on the sky outlining the star forming regions of each galaxy, where the ellipses are aligned with the viewing angle of each disk and span 1.8° for M31 and 0.6° for M33.

Following the criteria above, the CMDs of remaining sources form two plumes representing the blue and red supergiants with a few blue main sequence stars.

However, this pattern becomes difficult to distinguish towards the center of the galaxies and the flux excess factor $E \equiv$ `phot_bp_rp_excess_factor` reaches higher than expected values for stars in the centermost regions. Thus, a few additional cuts are applied to ensure that the CMD cuts described above are still representative of the remaining sample.

Sources that satisfy $1 + 0.015(G_{BP} - G_{RP})^2 < E < 1.5[1.3 + 0.06(G_{BP} - G_{RP})^2]$ remain and this includes only sources that have reliable G_{RP} and G_{BP} photometry. When these cuts are applied, most of the sources close to the center are removed from the sample. To avoid foreground contamination, which takes the shape of a vertical plume between the red and blue plumes, only sources that fall within either the red ($22.1 < G + 2.50(G_{BP} - G_{RP}) < 25.9$ and $14.586 < G - 1.071(G_{BP} - G_{RP}) < 17.886$) or blue region ($-0.4 < G_{BP} - G_{RP} < 0.70$ and $16 < G < 20$) of the CMD remain. Applying these criteria, any remaining contaminants should not be associated with the star-forming regions of the galaxies. The final step of sample selection is to apply a kernel density estimate to remove any lingering contaminants. Smoothing lengths are set independently for each galaxy and those sources that satisfy a certain density threshold (also set separately for each galaxy) are kept for the final astrometric analysis (see Appendix C of van der Marel et al., 2019, for full details). These criteria result in 1084 sources for M31 and 1518 sources for M33. The locations of these sources are illustrated with red points in Fig. 6.1. The final samples clearly illuminate the star-forming regions in M31 and M33.

The brightest stars in these samples are at $G \sim 16$ and their PM uncertainties are $\sim 100\,\mu\mathrm{as\,yr^{-1}}$. The median sample brightness is $G \sim 19$ the PM uncertainty at this magnitude is $\sim 600\mu\mathrm{as\,yr^{-1}}$. At the distance of M31 and M33, $1\mu\mathrm{as\,yr^{-1}}$ corresponds to 3.65 and 3.76km $\mathrm{s^{-1}}$, respectively. Thus, the *individual* PM uncertainties are too large to assess the galaxy's kinematics using individual source measurements. However, by averaging or model fitting, we are able to reduce these uncertainties to levels that are useful for analyzing the motion and internal kinematics of M31 and M33.

By binning the sources in each galaxy into four (M33) to six (M31) bins in

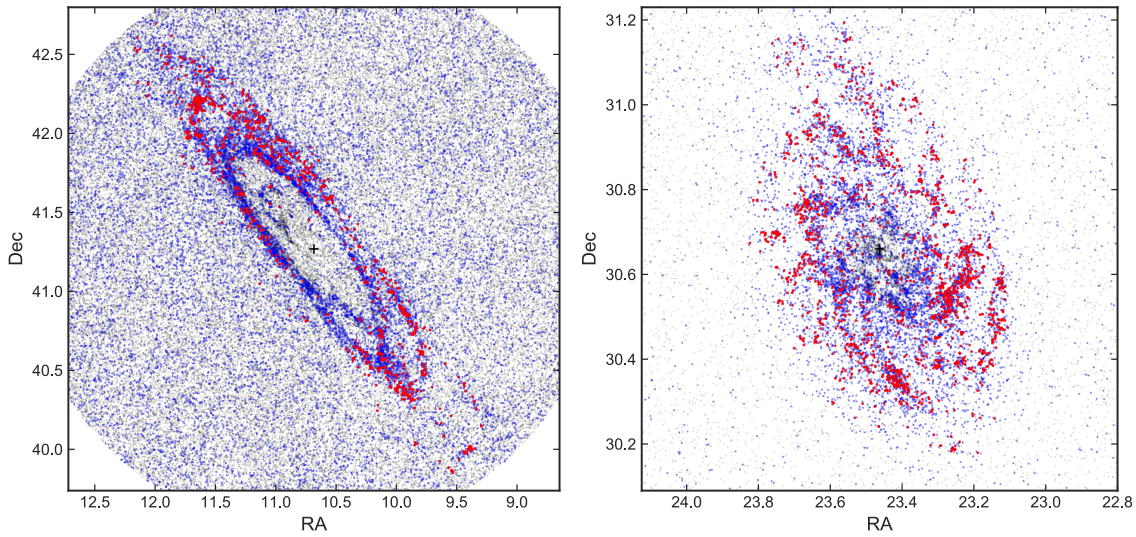

Figure 6.1: Spatial distribution of the *Gaia* DR2 sources selected for this analysis. Gray points show all *Gaia* DR2 sources within the circular extraction region with valid proper motions. Blue points show sources also passing the parallax and loose proper motion cuts discussed in the text. Red points show sources that also pass the cuts on astrometric fit quality, photometry, elliptical galaxy boundary, local spatial density, and CMD position for membership in the final sample. The left panel subtends a linear size that is ~ 3 times larger than the right panel.

position angle with equal numbers of stars in each bin, the weighted-average PMs are calculated. When the center of mass (COM) PMs are subtracted from the weighted-average PMs, the rotation of the galaxies becomes apparent.

As the zero-point of the *Gaia* DR2 PM reference frame varies over the sky, we also measured the PMs for a sample of quasars to assess and correct for PM systematics in DR2. More details on the process are outlined in Section 2.2 and Appendix A of van der Marel et al. (2019). This analysis shows that expected systematic proper errors are only $\ll 15\,\mu\mathrm{as\,yr}^{-1}$ due to color or magnitude dependencies. This is below the known systematic and statistical errors quantified in this work, so we neglect these errors.

6.2.2 Proper Motion Analysis

The PM fields are fit by following the methodology used for the LMC in van der Marel and Kallivayalil (2014) and van der Marel and Sahlmann (2016a). This method assumes all stars in the disk lie in flat plane and move on circular orbits around the COM. Disk orientation depends only on the inclination angle i and the position angle Θ of the line of nodes, and is assumed to be fixed with time (i.e., no precession or nutation of the spin axis). Viewing perspective is taken into account using full spherical geometry. COM position, LOS velocity of the COM, distance, and viewing angles all remain fixed at previously quantified values as *Gaia* is not sufficient to remeasure these quantities reliably. For M31, the COM position (RA,Dec) = $(10.68333, 41.26917)$ deg, $v_{\rm LOS} = -301$ km s^{-1}, $i = 77.5$ deg, and $\Theta = 37.5$ deg; for M33 we use (RA,Dec) = $(23.46250, 30.6602)$ deg, $v_{\rm LOS} = -180$ km s^{-1}, $i = 49.0$ deg, and $\Theta = 21.1$ deg (vdM12a; vdM12b, and references therein). The rotation curves of both galaxies are also assumed to be flat since *Gaia* cannot reliably constrain their shape.

In this model, there are only three free parameters: the PM $(\mu_{\alpha*}, \mu_\delta)$ of the COM, and the constant rotation velocity $V_{\rm rot}$ in the disk. The model is varied to minimize the χ^2 of the fit to the data while also taking into account any correlations between the PM components for each source. Using outlier rejection, about 4% of

the data are removed, thus the final χ^2 is slightly below the number of degrees of freedom.

Monte Carlo pseudo-data sets are created by adding deviates drawn at random from the measurement uncertainties. These data are used to estimate the uncertainties on the three model parameters. Small and large-scale spatially correlated PM errors are reported in the *Gaia* DR2 catalog (Lindegren et al., 2018; Gaia Collaboration et al., 2018b). The small-scale errors are expected to average out and any remaining errors are explored in Appendix B of van der Marel et al. (2019). The PMs of quasars are used to correct for the large-scale component. Our tests show that the measurement uncertainties are robust against any major changes to the underlying assumptions. Even if $V_{\rm rot}$ is held constant rather than as a free parameter in the model, we find that the COM PM does not change significantly. The weighted-average PMs alone with no disk model also yield COM PM estimates that are consistent with the disk model fits because the sources in each galaxy are distributed approximately symmetrically around the COM.

Results for M31 and Comparison to Literature

The best-fit model for the M31 sample has $V_{\rm rot} = -206 \pm 86$ km s^{-1}. This is consistent with the rotation curve inferred from LOS velocity studies, which reaches a maximum at $V_{\rm rot} \approx 250$ km s^{-1} at the radii where most of the DR2 sources in M31 are located (e.g. Corbelli et al., 2010). The minus sign represents counterclockwise rotation on the sky. This is consistent with expectations, given that: (a) LOS velocities are approaching on the South-West side of the disk; and (b) the morphology of the dust lane implies that the near side of the disk is on the North-West side (vdM12b, Table 1, and references therein).

The best-fit model has COM PM $\vec{\mu}_{\rm obs} \equiv (\mu_{\alpha*}, \mu_\delta) = (60 \pm 14, -24 \pm 12)\,\mu{\rm as\,yr}^{-1}$. The average PM of the quasar sample is $\vec{\mu}_{\rm qso} = (-6 \pm 12, 35 \pm 8)\,\mu{\rm as\,yr}^{-1}$. Hence,

the corrected PM of M31 after subtracting the quasar PM is:

$$\vec{\mu}_{\rm M31,DR2} = (65 \pm 18[\rm rand] \pm 16[\rm syst], \\ -57 \pm 15[\rm rand] \pm 16[\rm syst])\ \mu\rm as\,yr^{-1}. \quad (6.1)$$

The weighted-average PM measured by *HST* for three fields in M31, corrected for internal kinematics in vdM12 gives[1]:

$$\vec{\mu}_{\rm M31,HST} = (45 \pm 13, -32 \pm 12)\ \mu\rm as\,yr^{-1} \quad (6.2)$$

Therefore, the *Gaia* DR2 and *HST* measurements are statistically consistent at 0.8σ (the equivalent probability for a 1D Gaussian). Since the measurements are consistent, a weighted average is taken to obtain the improved estimate

$$\vec{\mu}_{\rm M31,DR2+HST} = (49 \pm 11, -38 \pm 11)\ \mu\rm as\,yr^{-1}. \quad (6.3)$$

This is closer to the *HST* results than the DR2 measurement because the uncertainties of the former are ~ 2 times smaller. To obtain the PM in the Galactocentric rest frame and correct for the solar reflex motion, one must subtract the PM

$$\vec{\mu}_{\rm M31,rad} = (39, -22)\ \mu\rm as\,yr^{-1} \quad (6.4)$$

corresponding to a purely radial approach for M31 towards the MW. This implies

$$\vec{V}_{\rm M31,DR2+HST} = (38 \pm 41, -61 \pm 39)\rm km\,s^{-1}. \quad (6.5)$$

Following van der Marel and Guhathakurta (2008), if a flat prior is assumed in the tangential Galactocentric velocity $V_{\rm tan}$, , the median and 68% confidence region are $V_{\rm tan,DR2+HST} = 57^{+35}_{-31}$ km s^{-1} . For comparison, the *HST*-only measurement yields $V_{\rm tan,HST} = 36^{+39}_{-26}$ km s^{-1} and the *Gaia* measurement implies $V_{\rm tan,DR2} = 133^{+70}_{-68}$ km s^{-1} .

[1] As noted in van der Marel et al. (2019), observed proper motions from Gaia, HST, and VLBA pertain to different tracer objects in different fields, and these should therefore not be compared directly. To enable a fair comparison, we consider only the implied COM PMs of each galaxy. These were obtained in each case (by us or previous authors) upon correcting the observed PMs using a model for the internal kinematics that is appropriate for the given tracer objects.

S16 used an indirect dynamical method to estimate the proper motion velocity of M31 as

$$\vec{V}_{\rm M31,S16} = (-112 \pm 70, 99 \pm 60) {\rm km\,s^{-1}}. \quad (6.6)$$

This differs from DR2+*HST* weighted average by 2.4σ and by 2.5σ from the DR2 measurement itself. Figure 6.3 compares the various measurements in heliocentric (RA,Dec) velocities (i.e., transforming μas yr^{-1} to km s^{-1} , but *not* correcting for the solar reflex motion). The *HST* measurement is shown with a red triangle; the DR2 and DR2+*HST* results are shown as open and closed black pentagons, respectively; the S16 result is shown as a green square.

The Galactocentric velocity $\vec{v} = (V_X, V_Y, V_Z)$ of M31 implied by the DR2 measurement is

$$\vec{v}_{\rm M31,DR2} = (0 \pm 75, -176 \pm 51, -84 \pm 73) {\rm km\,s^{-1}}. \quad (6.7)$$

The velocity implied by DR2+*HST* weighted average is

$$\vec{v}_{\rm M31,DR2+HST} = (34 \pm 36, -123 \pm 25, -19 \pm 37) {\rm km\,s^{-1}}. \quad (6.8)$$

These velocities are expressed in the Galactocentric (X, Y, Z) coordinate system defined in vdM12a, and make the same assumptions about the solar position and velocity. Eq. 6.8 is used to calculate the relative orbital history of M33 and in future orbital calculations of the MW and M31 in Section 6.3.

Results for M33 and Comparison to Literature

The M33 best-fit model has $V_{\rm rot} = +80 \pm 52$km s^{-1} , which is also in agreement with the rotation curve inferred from LOS velocity studies. These studies show that the rotation curve reaches $V_{\rm rot} \approx 100$km s^{-1} over the region where the DR2 sources in M33 are located (e.g. Corbelli and Salucci, 2000). The plus sign now indicates clockwise rotation on the sky. This is consistent with expectation, given that: (a) LOS velocities are approaching on the North side of the disk; and (b) morphologies of the dust lane imply that the near side of the disk is in the West (vdM12b, Table 1, and references therein). These values are also consistent with the rotation inferred by Brunthaler et al. (2005) from the PMs of two water maser regions in M33.

The best-fit model has COM PM $\vec{\mu}_{\rm obs} = (73 \pm 14, 32 \pm 12)\,\mu{\rm as\,yr^{-1}}$. The average PM of the quasar sample is $\vec{\mu}_{\rm qso} = (45 \pm 13, 66 \pm 11)\,\mu{\rm as\,yr^{-1}}$, so the corrected M33 PM is

$$\begin{aligned}\vec{\mu}_{\rm M33,DR2} = (&31 \pm 19[{\rm rand}] \pm 16[{\rm syst}],\\ &-29 \pm 16[{\rm rand}] \pm 16[{\rm syst}])\,\mu{\rm as\,yr^{-1}}.\end{aligned} \tag{6.9}$$

Existing measurements from water masers using the VLBA, corrected for internal M33 kinematics, in Brunthaler et al. (2005) yield

$$\vec{\mu}_{\rm M33,VLBA} = (23 \pm 7, 8 \pm 9)\,\mu{\rm as\,yr^{-1}}. \tag{6.10}$$

The *Gaia* DR2 and VLBA measurements are statistically consistent at the 1.0σ level. Since these measurements are consistent, one can take a weighted average to obtain the improved estimate of

$$\vec{\mu}_{\rm M33,DR2+VLBA} = (24 \pm 7, 3 \pm 8)\,\mu{\rm as\,yr^{-1}}. \tag{6.11}$$

As with M31 and *HST*, this weighted average differs very little from the VLBA measurement because it has uncertainties that are ~ 3 times smaller than the DR2 measurement.

The Galactocentric velocity resulting from the DR2 measurement alone is

$$\vec{v}_{\rm M33,DR2} = (49 \pm 74, 14 \pm 70, 28 \pm 73){\rm km\,s^{-1}}. \tag{6.12}$$

The velocity implied by the DR2+VLBA weighted average is

$$\vec{v}_{\rm M33,DR2+VLBA} = (45 \pm 20, 91 \pm 22, 124 \pm 26){\rm km\,s^{-1}}. \tag{6.13}$$

If we use the weighted average values of DR2 with VLBA and *HST* respectively, then the velocity vector of M33 relative to M31 has a radial component of $V_{\rm rad,DR2+VLBA+HST} = -225$ km s^{-1} and a tangential component of $V_{\rm tan,DR2+VLBA+HST} = 126$ km s^{-1}. If instead we use only the new DR2 measurements, then $V_{\rm rad,DR2} = -209$ km s^{-1} and $V_{\rm tan,DR2} = 85$ km s^{-1}. The velocity provided in Eq. 6.13 is used in Section 6.3 to calculate the orbit of M33 relative to M31 to calculate the future orbits for the MW, LMC, M31, and M33.

6.3 Discussion

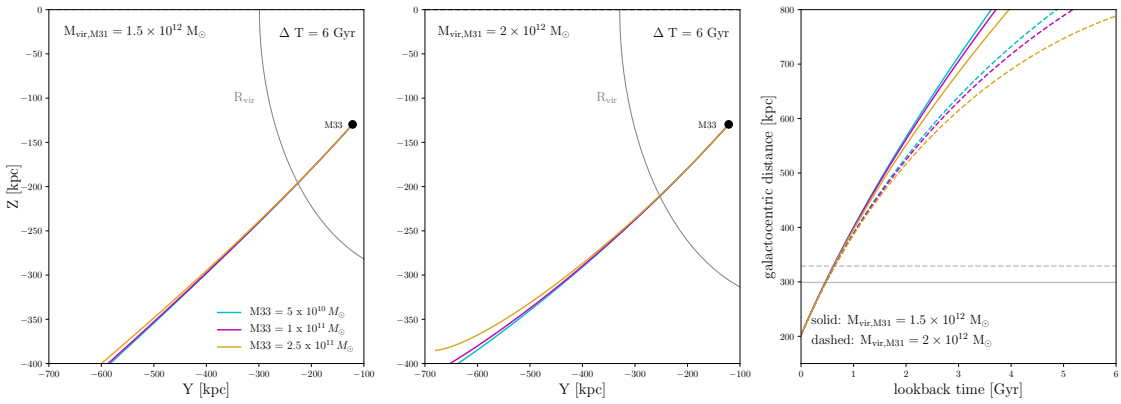

Figure 6.2: Numerically integrated orbits for M33 over the past 6 Gyr using three masses for M33 and two masses for M31. The left and middle panels show the Y-Z orbital cross section for the two different M31 virial mass models. The orbits have been integrated backwards using the mean position and velocity vectors (Eq. 6.13 for the initial conditions. The gray solid curves indicate the extents of the virial radius of M31 in each model. The right panel shows the orbits for each of the two M31 models in time versus galactocentric distance. The colored solid lines indicate the lower M31 mass, while the dashed colored lines show the resulting orbits in the higher M31 mass model. The dashed and solid gray lines represent the virial radius in the high and low virial mass models of M31. In all mass combinations for M31 and M33, M33 unanimously prefers a first infall orbit, entering the halo of M31 in the last 2 Gyr using the *Gaia* DR2 PMs. (Note: This figure was not included in original publication.)

6.3.1 The Orbit of M33

P17 performed orbital calculations for M33. Their models spanned M33 halo masses between $5 - 25 \times 10^{10}$ $M_\odot$. Two values for M31's virial mass (high mass: 2×10^{12} $M_\odot$ and low mass: 1.5×10^{12} $M_\odot$) were considered. M33 was modeled as an extended body and a three-component potential was adopted for M31. The present-day velocities were chosen in accordance with the vdM12a PM value for M31 and with the VLBA PM value for M33, and their respective uncertainty ranges. The vdM12a PM value is a weighted average of the PM measured with *HST*, and several indirect dynamical estimates based on satellite LOS velocities. It is shown

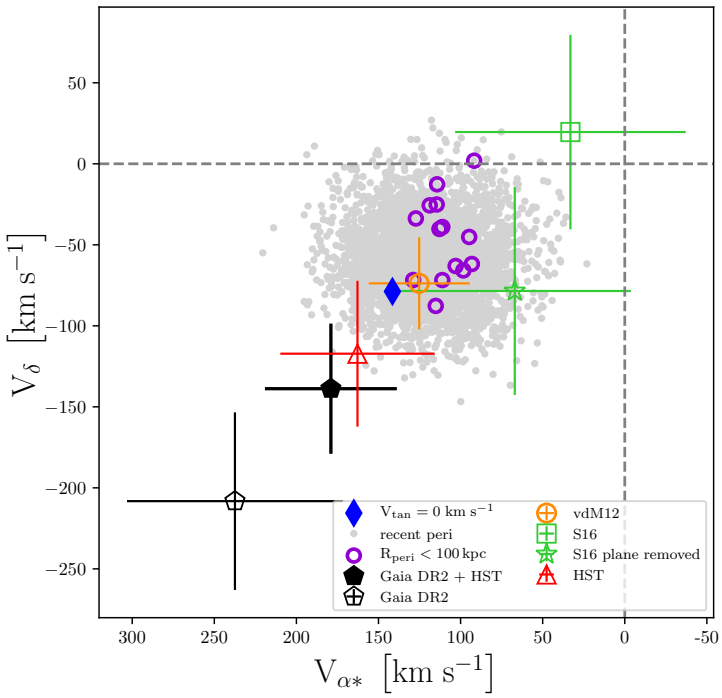

Figure 6.3: Heliocentric M31 transverse velocity measurements $(V_{\alpha*}, V_\delta)$ (i.e., PMs in the (RA,Dec) directions transformed from μas yr^{-1} to km s^{-1}). The blue diamond marks the transverse velocity that corresponds to a purely radial orbit for M31 towards the MW (subtraction of this velocity vector yields Galactocentric transverse velocities). Points with error bars mark the following measurements: *Gaia* DR2 (open black pentagon); average *HST* measurement from observations of 3 distinct fields (open red triangle; from vdM12a); average of the *Gaia* DR2 and *HST* measurements (closed black pentagon); indirect dynamical estimates from LOS velocities of M31 satellite galaxies, with (open green square) or without (open green star) the members of M31's plane of satellites (both from S16); average of *HST* and other indirect dynamical estimates (open orange circle; vdM12a). P17 numerically calculated M33 orbits relative to M31 for velocities inside the 4σ uncertainty region for the latter average, as described in the text. The gray points indicate orbits where M33 had a pericentric approach to M31 (smaller than their current separation) in the past 6 Gyr (the ARP sample from P17). The purple circles indicate a further subset, where the distance at pericenter was < 100 kpc and the latter occurred within the last 3 Gyr (the RP100T sample from P17). The *Gaia* DR2 PM exclusively supports orbits where M33 is on first infall into M31.

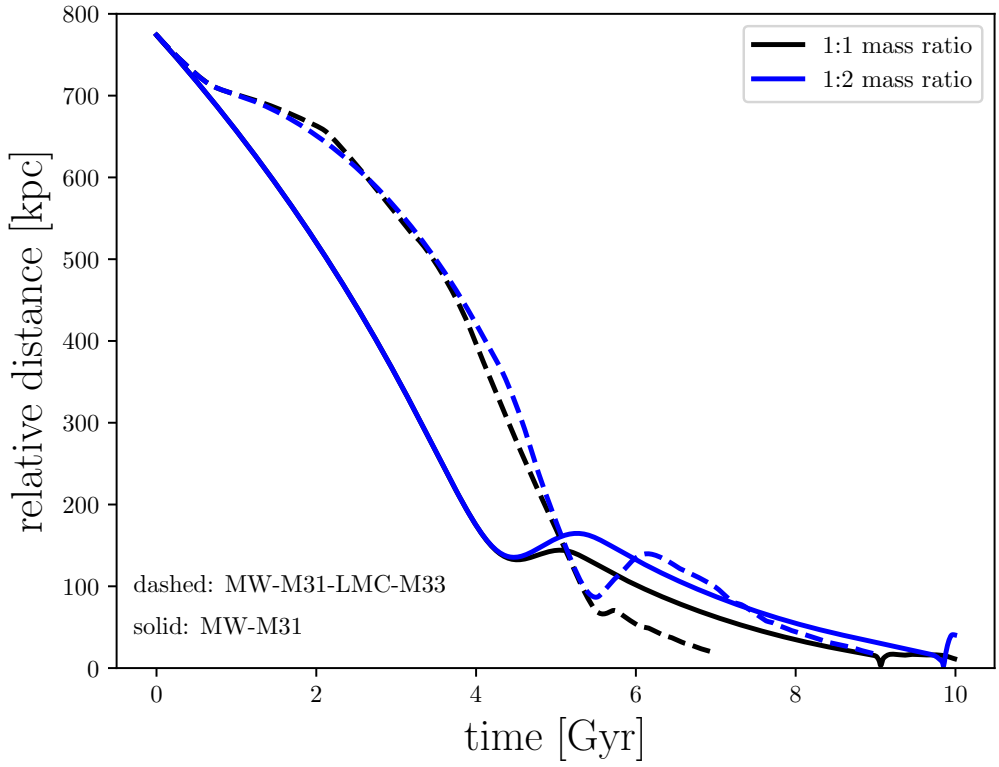

Figure 6.4: The relative distance between the MW and M31 as a function of time. The blue lines (1:2 mass ratio) indicate orbits where the masses of the MW and M31 are assumed to be $1 \times 10^{12}\,M_\odot$ and $2 \times 10^{12}\,M_\odot$, respectively. For the black lines (1:1 mass ratio), the mass of the MW and M31 are set to be equal at $1.5 \times 10^{12}\,M_\odot$. The solid lines show the resulting orbit when only the gravitational influence of the MW and M31 are considered and the dashed lines additionally include the influence of the LMC and M33 (i.e. a 4-body encounter) assuming masses of $1 \times 10^{11}\,M_\odot$ and $2.5 \times 10^{11}\,M_\odot$, respectively. The MW and M31 are expected to first collide around 4.5 Gyr from now at a separation of approximately 130 kpc. Including the influence of the LMC and M33 in this calculation delays the first collision to 5.5 Gyr and reduces the impact parameter to $\sim$75 kpc. Varying the mass ratio between the MW and M31 results in negligible changes to these results. (Note: This figure was not included in original publication.)

in Figure 6.3 as an open orange circle with error bars (roughly midway between the *HST* PM measurement and the S16 indirect dynamical estimates). P17 calculated M33 orbits within the 4σ error ellipse for this velocity, and found that the two most likely orbital solutions are: 1) M33 is on first infall (low mass M31 model); or 2) M33 completed a long-period orbit where it made a pericentric approach around ~ 6 Gyr ago at a distance of $\sim$100 kpc from a high mass M31. Gray points in Figure 6.3 show orbits that allow for a more recent (< 6 Gyr ago) pericentric passage, while open purple circles show those that additionally reach within 100 kpc in the last 3 Gyr. The latter sample generally has a high mass M33 (2.5×10^{11} $M_{\odot}$) and M31 (2×10^{12} $M_{\odot}$), a mass combination that increases the odds of retrieving such an orbital solution. Both P17 and Semczuk et al. (2018) show that the mean S16 velocity vector does allow for a recent pericentric passage of M33 around M31, but only at distances > 100 kpc.

Using the new DR2+*HST* weighted average velocity for M31 (Eq. 6.8) and the DR2+VLBA weighted average velocity for M33 (Eq. 6.13), we numerically integrated the orbit of M33 around M31 backwards in time, following the same methodology of P17. For the six M31-M33 mass combinations explored in P17, the new velocities unanimously prefer a first infall orbit for M33; a long-period orbit is no longer a plausible orbital solution (see Fig. 6.2). The reason for this is evident from Figure 6.3, since the *Gaia* DR2 results move the M31 PM further away from the gray points (and open purple circles) that designate a previous and recent pericenter passage. Such a first infall scenario is further supported by a study by Shaya and Tully (2013) of the formation of planes of satellites in the Local Group, which concluded that M33's closest approach to M31 is happening now, also ruling out a possible recent tidal interaction.

6.3.2 The Future Fate of the Local Group

We next assess the impact of the new measurements on the future fate of the four most massive members of the LG: M31, the MW, M33 and LMC. We first follow the methodology outlined in P17 to model and integrate the orbits of the MW

and M31 into the future, ignoring their massive satellites. We used the average DR2+*HST* PM, and adopt two different mass ratios for the encounter: a high mass ratio encounter ($M_{vir,MW} = 10^{12}$ $M_\odot$ and $M_{vir,M31} = 2 \times 10^{12}$ $M_\odot$) and an equal mass ratio encounter ($M_{vir,MW} = 1.5 \times 10^{12}$ $M_\odot = M_{vir,M31}$; compare Watkins et al., 2019). In both scenarios, the increased tangential velocity, relative to vdM12a, is not sufficient to unbind the LG. The MW and M31 are still destined to merge. However, both the timing and the impact parameter of the first encounter have increased relative to vdM12b, from T_{peri} =∼3.9 Gyr to ∼4.5 Gyr and $R_{peri} \sim 31$ kpc to ∼130 kpc (see Fig. 6.4). The larger tangential velocity implied by the average DR2+*HST* PM means that a future direct collision between the MW and M31 is less likely.

We then included the dynamical influence of the LMC ($M_{vir,LMC} = 10^{11}$ $M_\odot$) and M33 ($M_{vir,M33} = 2.5 \times 10^{11}$ $M_\odot$) in the orbit calculations, using the Kallivayalil et al. (2013) PM for the LMC and the DR2+VLBA PM for M33. This further delays the MW-M31 encounter time by ∼1 Gyr, but decreases the impact parameter by half (∼75 kpc; see Fig. 6.4). All these calculations assume the mean 3D velocity vectors and static halo models. A more detailed analysis, searching the full PM error space, coupled with full N-body simulations of the 4-body encounter are needed to fully describe the future dynamics and merger of the MW-M31 system.

6.3.3 Cosmological Context

The aforementioned results are broadly consistent with cosmological expectations. Using the Bolshoi dark matter only cosmological simulation, Forero-Romero et al. (2013) find $V_{tan} = 50 \pm 10$ km/s as the most probable relative tangential velocity for MW-M31 mass analogs (isolated pairs of halos with masses ranging from 7×10^{11} $M_\odot$ to 7×10^{12} $M_\odot$ and negative relative radial velocities). In contrast, they found that only 8-12% of cosmological MW-M31 analogs have $V_{tan}/V_{rad} < 0.32$, as was implied by the tangential velocity advocated by vdM12a. Similar conclusions were reported by vdM12a, Garrison-Kimmel et al. (2014), and Carlesi et al. (2017). Therefore, the increase in M31's tangential motion to $V_{tan,DR2+HST} = 57^{+35}_{-31}$ km s^{-1} better aligns the

observational evidence with cosmological expectations. The increased tangential velocity is not sufficient to significantly increase the LG mass inferred from the Timing Argument (González et al., 2014).

Also, the implied first infall orbit for M33 is consistent with cosmological expectations. P17 showed that mass analogs of M33 residing around M31-mass halos preferentially exhibit recent infall times (i.e. < 4 Gyr ago). The orbits of 22% of cosmological analogs never complete a pericentric passage about their host. Of the remaining 78%, 32% are able to achieve a pericentric passage at distances < 55 kpc in the last 3 Gyr and the remaining 46% complete pericentric passages but only at distances > 55 kpc. At pericentric distances $\gtrsim 55$ kpc, tidal forces can partially induce the tidal features observed in M33, but these are likely not strong enough to be the sole cause of the asymmetries in its stellar and gaseous disks.

The main implication for a first infall M33 orbit is that its stellar and gaseous warps cannot be the result of tidal forces via a close encounter with M31. This also supports the assertions in P17 that M33 must have a significant satellite population of its own, similar to the LMC (Jethwa et al., 2016; Kallivayalil et al., 2018). Patel et al. (2018b) provides details on the predicted satellite population of M33. Multiple satellite encounters (fly-bys, collisions, mergers, e.g., Starkenburg et al., 2016) could then have given rise to M33's warps. Other possibilities include long range tides due to M31 (rather than invoking a strong tidal encounter as in McConnachie et al., 2009) or that the features may be related to asymmetric gas accretion or inflows (e.g., Debattista and Sellwood, 1999; López-Corredoira et al., 2002). Moreover, it has been shown that M33's floccuent spiral pattern and velocity field are reproducible in simulations through gravitational instabilities in the stars and gas alone (Dobbs et al., 2018), so it is conceivable that purely internal drivers may have contributed to the warp as well.

6.3.4 Structure of the M31 Satellite System

We have found good agreement between the *Gaia* DR2 and *HST* PMs of M31, but both measurements disagree with indirect dynamical estimates of M31's PM

using LOS velocities of satellite galaxies (van der Marel and Guhathakurta (2008), updated in vdM12a, and S16). This could be due to non-equilibrium in the M31 satellite system.

A significant number of satellites of M31 are purportedly aligned in a kinematically coherent plane (Ibata et al., 2013). This coherent motion suggests that this system of satellites may not be in equilibrium with M31's dark matter halo. By contrast, for the Milky Way, *Gaia* DR2 has confirmed that while a significant number of MW satellites are on polar orbital configurations, they may not be moving coherently (H18). Also, a large number of satellites are found to be counter-rotating (Fritz et al., 2018). Furthermore, *Gaia* DR2 PMs strongly suggest that some ultra-faint satellites have been accreted as satellites of the LMC (Kallivayalil et al., 2018). It is possible that such processes may have occurred in M31 as well, at different intervals in time (e.g. multiple group infall events). This may result in less pronounced satellite associations today, but nonetheless, could invalidate the assumption of dynamical equilibrium.

The analysis presented in S16 provides direct support for this hypothesis. S16 repeated their analysis for the entire satellite system (open green square in Figure 6.3), using only the non-plane members (open green star). The result for the latter subsample, while statistically consistent with that for the full sample, is noticeably closer to the available M31 PM measurements. In fact, it agrees with the average DR2+*HST* measurement at an equivalent 1D-Gaussian confidence of 1.0σ, and with the *Gaia* DR2 measurement by itself at an equivalent 1D-Gaussian confidence of 1.5σ. It is possible that the (currently unknown) dynamical influences that created the M31 satellite plane (e.g. group infall, torques from large-scale structure, influence of prior massive accretion events) may have also distorted the kinematics of the current non-plane members. This could plausibly explain the residual differences, which are in fact barely statistically significant.

6.4 Conclusions

We have used the *Gaia* DR2 to study the PMs of M31 and M33. We carefully selected samples of sources in the target galaxies with a minimum of contamination, and then analyzed their PMs using a simple rotating disk model. We used background quasars to limit the impact of residual systematics. The PM rotation of both galaxies is confidently detected, at values consistent with the known line-of-sight rotation curves.

The inferred COM motions are consistent at 0.8σ and 1.0σ with the (2 and 3 times higher-accuracy) measurements already available from *HST* optical imaging and VLBA water maser observations, respectively. This lends confidence that all these measurements are robust. This is further supported by the finding that the *Gaia* DR2 PM of the distant Milky Way dwarf galaxy Leo I, as determined by H18 and Simon (2018), is consistent with the *HST* measurement of Sohn et al. (2013) that used the same techniques as for M31.

We used the new *Gaia* PM measurements, combined with the existing measurements, to perform numerical orbit integrations. Doing this backward in time for M33 with respect to M31, implies that M33 must be on its first infall. This is consistent with cosmological expectations, and is similar to what has been found for the LMC orbit with respect to the MW (Kallivayalil et al., 2013). One corollary of such an orbit is that M33's stellar and gaseous warps and tails cannot be the result of tidal forces via a close encounter with M31.

The new measurements imply that the M31 orbit towards the Milky Way is less radial than implied by the *HST* measurement alone, $V_{\rm tan,DR2+HST} = 57^{+35}_{-31}$ km s^{-1}. This too is in good agreement with cosmological expectations. This implies that the future collision with the Milky Way will happen somewhat later, and with larger pericenter, than previously inferred by vdM12b.

The Gaia DR2 and HST PM measurements for M31 both differ from estimates inferred using indirect dynamical methods based on the LOS velocities of satellite galaxies. However, the agreement improves considerably when the satellites that

reside in a planar configuration are removed from the sample. This suggests that non-equilibrium features in the satellite kinematics may be responsible for this discrepancy.

The results highlight the potential of *Gaia* for PM studies beyond the Milky Way satellite system, especially with future data releases. The random PM uncertainties, and many kinds of systematic uncertainties as well, decrease as the 1.5th power of the time-baseline. Therefore, the *Gaia* PMs should be a factor 4.5 more accurate after the nominal mission, and a factor 12 more accurate after a possible extended mission. This will not only shed more light on the questions already addressed in the present paper, but it will also help address new questions. For example, the PMs of M31 dwarf satellite galaxies that are too faint for *Gaia* can be measured with other telescopes such as *HST* or the James Webb Space Telescope. Projects for such measurements are already underway or in planning. When combined with an accurate M31 PM determination from *Gaia*, it then becomes possible to determine how the satellites move in 3D with respect to their parent galaxy.

CHAPTER 7

Summary and Future Prospects

7.1 Summary

This dissertation is a compilation of five chapters that focus on the dynamics and orbital evolution of satellite galaxies in the Local Group (LG) and their counterparts in cosmological simulations. In particular, two primary over-arching questions are addressed in this work: What are the orbital histories of the most massive satellite galaxies of the Milky Way (MW) and M31, namely the Large Magellanic Cloud (LMC) and M33, and how common are these orbits in a cosmological context? How can the dynamics of a population of satellite galaxies be used to constrain properties of their host galaxy (i.e. total halo mass)? In this section, I summarize the key points presented in these five chapters, which address these questions using the confluence of high precision astrometric data and high resolution cosmological simulations.

M33 is the most massive satellite galaxy of M31 ($\sim$10% the mass of M31) and the 3rd most massive galaxy in the LG, therefore constraining its orbital history is important for piecing together M31's accretion history, the history of the LG, and for interpreting the star formation history of M33. M33 has a complex morphology including a vast gaseous disk with an S-shaped warp extending to 22 kpc from its center (Fig. 7.1, Panel A). The Pan-Andromeda Archaeological Survey (PAndAS; McConnachie et al., 2009) also revealed comparable stellar warps, which have conventionally been explained by a recent ($t_{peri} < 3$ Gyr ago), close ($r_{peri} < 100$ kpc) encounter between M33 and M31 (see inset on Panel B, Fig. 7.1; McConnachie et al., 2009; Putman et al., 2009; Semczuk et al., 2018). However prior to 2012, M31's PM was not known, so these orbital solutions were constrained only by radial velocity data.

In Chapter 2, I used the HST PM measurement of M31 (Sohn et al., 2012; van der Marel et al., 2012a) to calculate the past orbital trajectory of M33 and surprisingly concluded that it is improbable ($< 1\%$) that M33 obeys the conventional orbit. Instead, a first infall scenario is the most likely orbital history ($> 90\%$) with a 6% probability of a long period orbit ($r_{peri} > 100$ kpc at $t_{peri} \leq 6$ Gyr ago; gold lines in Panel B, Fig. 7.1), requiring an alternative explanation for M33's current morphology. Similar orbital histores were recovered for the LMC, where a low mass MW leads to a first infall scenario and a high mass MW puts the LMC on a long-period orbital history.

Using a dark-matter-only cosmological simulation, I further demonstrated that a first infall scenario is cosmologically expected for LMC/M33 analogs in MW/M31-mass halos at z=0 (70% have been captured in the last 2-4 Gyr). Recently, I used the PMs of M33 and M31 measured with *Gaia* DR2 to show that these independent PMs unanimously prefer a first infall scenario (magenta lines in Panel B, Fig. 7.1) for M33 (van der Marel et al., 2019, see Chapter 6). This result is consistent with several other studies (Shaya and Tully, 2013; van der Marel et al., 2012a), such as Dobbs et al. (2018) who show that the flocculent spiral pattern can be produced without invoking a tidal interaction with M31. Furthermore, observations of M33's HI disk show no signs of ram pressure truncation, which is inconsistent with a pericentric passage of 50 kpc (Panel A, Fig. 7.1).

In a first infall scenario, M33 retains its cosmological infall mass of $\sim 10^{11}\,M_{\odot}$ and the structure of its dark matter halo (i.e. no truncation). ΛCDM theory predicts that M33 should host a handful of very low mass "ultra-faint" satellite galaxies, as relics of its own accretion history. Such satellites could explain M33's warps through interactions, mergers, and fly-bys. Yet PAndAS has found just one potential M33 satellite candidate to date.

In Chapter 5, I quantified M33's expected satellite galaxy population in ΛCDM as a function of satellite absolute magnitude. I showed that M33 is expected to host an average of three satellites in an area equivalent to the PAndAS survey down to $M_V \approx -6.5$ (PAndAS completeness limit). However, the PAndAS footprint only

covers 40% of M33's virial volume. An average of six satellites are expected to reside within its full virial volume (R_{vir}=161 kpc) down to $M_V \approx -6.5$, and ∼90% should reside within a circular area of 100 kpc in radius. Thus, there should be more M33 satellites to find. In Chapter 5, I also determined that observations of a 50-100 kpc annulus in projection around M33 are feasible using ∼50 fields of Hyper Suprime-Cam, which has a field of view diameter of 1.5°. In addition to testing ΛCDM predictions, establishing the existence or absence of M33 satellites will further constrain the orbital history of M33. If M33's closest approach to M31 occurs today, satellites should still be bound to it, whereas a recent tidal interaction with M31 would have stripped away satellites. Based on tidal radius calculations, I argued that the discovery of four or more M33 satellites strongly disfavors an orbital history with $r_{peri} \leq 100$ kpc, providing further support that M33 is on first infall and a test case for ΛCDM at the low-mass end.

Constraining the history and future fate of the LG relies on precise total mass estimates for its two most massive members, the MW and M31. However, current values for each galaxy range from approximately $M_{vir} = 0.7-2.5\times10^{12}\,M_\odot$ (see Patel et al., 2018a). As our closest laboratories for testing theories of galaxy formation, precise mass measurements are necessary. In Chapter 3, I extended a Bayesian framework designed to statistically estimate the mass of a galaxy by comparing observed properties of satellite galaxies to those of cosmologically simulated analogs. By shifting the focus of this method away from instantaneous properties, such as satellite position and velocity, and towards specific orbital angular momentum, I showed that the latter is a more reliable mass indicator as a function of time because it is well-conserved, independent of orbital phase, and does not rely on whether a satellite is bound to its host. The properties of the most massive satellites of the MW and M31 (the LMC, M33 respectively) yield masses of $1.02^{+0.77}_{-0.55}\times10^{12}\,M_\odot$ and $1.37^{+1.39}_{-0.75}\times10^{12}\,M_\odot$, respectively. This is the first time the 6D space motions of M33 were used to constrain the mass of M31.

Given the recent influx of MW satellite galaxy PMs, I enhanced the methods in Chapter 3 to accommodate the properties of multiple satellite galaxies simulta-

neously in Chapter 4. Using 6D phase space information for eight classical MW satellite galaxies, I inferred an ensemble MW mass estimate of $0.96^{+0.29}_{-0.28} \times 10^{12}\,\mathrm{M}_{\odot}$, narrowing the current factor of two uncertainty in the MW's mass by ∼25%. This method will be extended to include additional satellite galaxies (i.e. ultra-faint dwarfs) in the near future to further constrain the allowed mass range of the MW, M31, and eventually other galaxies with measured satellite PMs from HST, JWST, and WFIRST.

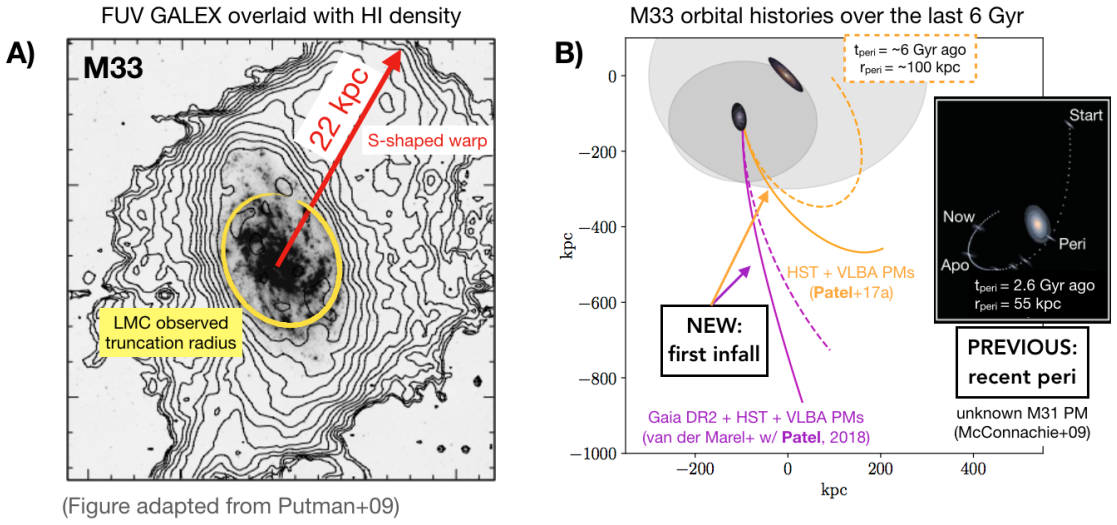

Figure 7.1: *(A)*: The HI density overlaid on the FUV GALEX image of M33 clearly indicates the S-shaped warp extending to 22 kpc from the galaxy's center (Putman et al., 2009). M33 shows no signs of truncation associated with a 50 kpc distance at pericenter when compared to the LMC's truncation radius (yellow ellipse). *(B)*: The inset indicates the previous orbital history presented in (McConnachie et al., 2009) compared to the new orbital histories presented in Chapter 2 (gold lines) and Chapter 6 (magenta lines). Orbits are calculated for a low ($1.5 \times 10^{12}\,M_{\odot}$; solid) and a high ($2 \times 10^{12}\,M_{\odot}$; dashed) M31 mass. The gray shaded regions indicate the virial extents of the two galaxies. New M31 PMs from HST and *Gaia* prefer a first infall orbit for M33.

Together, these projects demonstrate how new tools, techniques, and high precision observational data sets can lead to revisions of and improvements on conventional theories of our LG of galaxies. As more high precision astrometric data and the next generation of state-of-the-art simulations become available, the method-

ologies and results presented in this dissertation will be key to further analysis of LG galaxies and for testing the ΛCDM paradigm. There are several projects that naturally stem from the studies included in this dissertation. In Sections 7.2, 7.3, and 7.4, I will briefly describe several avenues of further exploration.

7.2 Future Surveys of M33: Obtaining Deep Imaging of M33's Halo with Hyper-Suprime Cam

As discussed in Chapter 5, M33 and the LMC are the only galaxies in the LG with halo masses of order $10^{11}\,M_{\odot}$. At this mass scale, ΛCDM implies that these galaxies should host a population of very low mass "ultra-faint" satellite galaxies, stellar streams, and a stellar halo as relics of their own accretion histories. While the LMC is being intensely targeted observationally to test hierarchical structure formation (e.g., Gaia, DES, SMASH, MagLiteS), the M33 system remains relatively unexplored. Only the inner halo of M33 (to $\sim$ 50 kpc in projection) has been imaged with relatively deep observations by PAndAS (50% completeness limits of $(g, i) \sim (24.9, 23.9)$; Martin et al., 2016), encompassing only a small fraction of M33's virial radius of $\sim$ 160 kpc (Fig. 7.2). In this limited region, there is also no definitive evidence of a stellar halo or streams (McConnachie, 2016).

Given the close proximity of M33 ($D = 809 \pm 24$ kpc; McConnachie et al., 2005), searching for faint dwarf galaxies, stellar streams, and a smooth stellar halo component is possible down to surface brightnesses as low as $\mu_g \approx 34$ mag arcsec^{-2}. Hyper Suprime-Cam (HSC) on the 8m Subaru Telescope on Mauna Kea is the ideal instrument for a survey of M33's halo given its 1.5° field of view (see Section 7.2). Using the exquisite image quality possible with HSC to depths of $g = 26.5$ and $i = 25.5$ enables detections of dwarf satellites to stellar mass limits of $M_* \approx 10^3\,M_{\odot}$, a gain of nearly two orders of magnitude in mass compared to satellite searches around M33-mass systems outside the LG (i.e., MADCASH; Carlin et al., 2016) and a one order of magnitude gain over the PAndAS coverage of M33. In addition to searching for faint stellar systems, deep HSC data resolving individual stars will

enable a full characterization of the southern portion of M33's stellar disk warp and an improved distance to And XXII using horizontal branch stars.

A full survey of the unmapped M33 halo out to 100 kpc in projection requires ∼8.5 nights (∼ 50 HSC fields); we have proposed a pilot program to observe the first ∼ 20% of this region, equivalent to 2 nights of HSC (see Fig. 7.2). The goals of this survey are outlined below.

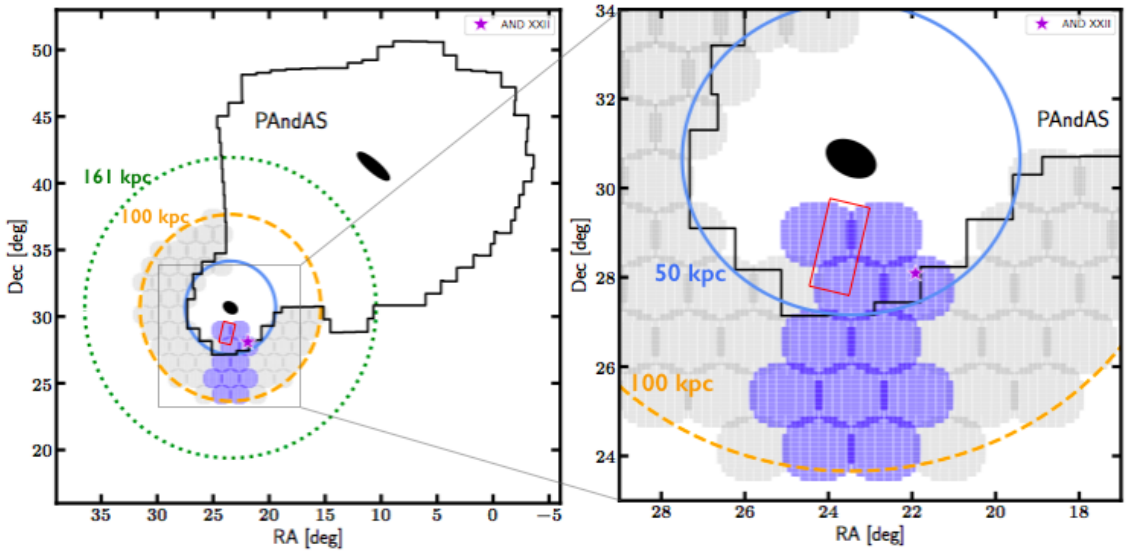

Figure 7.2: **Left:** The 11 fields proposed as a pilot HSC survey in Semester 2019B (blue HSC footprints) vs. our full survey plan (gray HSC footprints) overlaid on the PAndAS survey footprint (black outline). The filled black ovals represent the optical disks of M33 and M31; And XXII is marked with a purple star. Blue/orange/green circles indicate radii of 50/100/161 kpc from M33. The red rectangle is the approximate location of M33's southern stellar disk warp. **Right:** A zoomed-in view of our proposed HSC fields. (Figure credit: Jeff Carlin)

Satellites of M33: Given the predictions in Chapter 5, ∼ 6-12 low mass satellites are expected to reside within the full survey area, or the volume enclosed by 100 kpc in projection (solid red line, Fig. 5.2), with 2 ± 2 satellites in the volume of our pilot observations. At these depths, between 10-100 resolved red giant branch (RGB) stars are predicted for each satellite (see Fig. 5.3). A clear detection of satellites around M33 would provide strong support for hierarchical structure for-

mation and a unique opportunity to study satellites of a low-mass galaxy in detail. In Chapter 5, I motivated several reasons for searching for satellites around M33. In line with these goals, the number of newly detected M33 satellites will provide a test of ΛCDM predictions at the low-mass end in addition to providing independent constraints on M33's orbital history.

The Elusive Stellar Halo of M33: Stellar halos are the fossil records of galaxy accretion histories. Detected ubiquitously around MW-mass systems, such structures are expected hierarchically around less massive galaxies, albeit fainter and with lower total luminosities. Yet, no M33 stellar halo has been identified due to surface brightness limits (McMonigal et al., 2016). Our proposed survey will also us to confidently determine whether M33 hosts a stellar halo using deeper data (i.e., $\mu_g \sim 34$ mag arcsec^{-2} vs. $\mu_V \sim 32$ mag arcsec^{-2} in PAndAS), over a larger volume, and in a region less impacted by M31 contamination. Simulating stellar halos is still challenging since they are computationally expensive, require high resolution, and depend on an accurate description of galaxy formation and evolution processes, including feedback. Even a non-detection will provide a unique constraint to simulations on the assembly of low-mass galaxies.

Characterizing the stellar warp (red rectangle, Fig. 7.2): The proposed observations will provide a deeper view of M33's southern stellar disk warp with higher stellar counts. This warp is purported to be a byproduct of a close interaction between M33 and M31 (see Chapter 5), so it is included as one of the target regions in the proposed pilot program. Paired with spectroscopic follow-up from Keck+DEIMOS (accessed through collaborators), we will disentangle whether the warp is coherent with the orbital motion of M33 and potentially uncover the true origin scenario of the stellar warp.

And XXII (purple star, Fig. 7.2): And XXII is currently a *candidate* M33 satellite as its sparsely populated RGB prohibits a robust TRGB distance and its 1D kinematics do not provide sufficient information to determine its gravitational host. Our imaging would reach the horizontal branch enabling an improved distance measurement that may help distinguish whether And XXII (and any newly detected

satellites) belong to M33 or M31 (Chapman et al., 2013).

Discovery space for stellar streams: At large distances in galaxy halos, dynamical timescales are longer so any past accretion events will more likely have spatial coherence and appear as a stream (possibly with associated globular clusters as seen in M31 by Mackey et al., 2019) rather than a smooth stellar halo. If such a stream exists in the survey area it would be detected by our survey limits, thereby providing yet another probe of M33's accretion history and the build-up of a $10^{11}\,M_{\odot}$ halo.

Other than HSC, there are no existing wide-field imagers capable of such a survey of M33's halo. We would have to wait until the mid-2020s (or longer) for upcoming observatories, such as WFIRST and 30m-class telescopes to tackle this area (see Section 5.3.4). Given the wealth of information that a detailed study of M33's outer disk and halo can provide, it would act as a critical data point in our understanding of the assembly of $10^{11}\,M_{\odot}$ halos, providing constraints for both theory and observations of similar-mass galaxies beyond the LG.

7.3 M31 as the Next Frontier for Detailed Studies of Hierarchical Galaxy Evolution in the Local Group and Beyond

Accurate 6D phase space information for halo substructures in the MW enables the reconstruction of its accretion history and the characterization of its dark matter halo. Together, these increase our knowledge of the complex physical processes that govern galaxy evolution and they provide a local test of ΛCDM cosmology. In the era of HST and soon JWST, placing the MW in the broader context of low redshift galaxies requires a close examination of other analogous galactic ecosystems. As our Galaxy provides just one laboratory for detailed studies of galaxy evolution, the MW's comparably massive neighbor M31 is naturally the next frontier for exploring the global assembly history of $10^{12}\,M_{\odot}$ halos.

While M31 is a galactic twin of the MW in many respects, M31's recent accretion history is markedly more active. A particularly striking feature of this history is

the Giant Southern Stream (GSS), the remnant of a recent (major or minor) merger event that spans 100 kpc of M31's halo (e.g. Fardal et al., 2006, 2009; Hammer et al., 2018; D'Souza and Bell, 2018). Additionally, M31 hosts a massive satellite galaxy, M33. Conventional models suggest that M33 is a long-term companion to M31, however, I concluded that M33 is only making its first close approach to M31 today (Chapter 2). This further implies that M33 and the galaxy that formed the GSS, which together sum to $\gtrsim$1/5th of M31's current mass, entered M31's halo at similar times about 2 Gyr ago. These dynamical events have been studied separately but addressing both at once is critical for accurately rewinding the clock on the assembly of M31's satellite system.

Furthermore, roughly half of M31's satellites are purported to be in a thin, co-rotating plane (Fig. 7.3; Ibata et al., 2013). These coherent, planar structures are rare in ΛCDM cosmological simulations (Ibata et al., 2013), thus direct cosmological analogs of the M31 satellite system do not currently exist. In light of M31's violent recent history, the question of whether a dynamically stable, rotating plane exists is currently a major concern. Quantifying the perturbations that two massive satellites exert on M31's dark matter halo (see Garavito-Camargo et al., 2019, for details on the MW-LMC system) and the orbital planes of its $\sim$30 other satellites is therefore key to a full reconstruction of M31's recent dynamical history.

As a postdoctoral fellow, I plan to simulate the global dynamical history of M31's satellite system and place it in a cosmological context using an original suite of N-body simulations coupled with analogs identified in a cosmological simulation. The goals of this project will be to: 1) quantify the gravitational potential and mass profiles of M31 and M33, and 2) answer fundamental questions surrounding the physics of M31's complex plane of satellite galaxies. This program will aid in interpreting existing and upcoming measurements of star formation histories (SFHs) and PMs for both MW and M31 satellite galaxies, and it will further set the stage for understanding galaxy assembly beyond the MW (see Gilbert et al., 2019).

To date, 6D phase space information (derived from PMs) and detailed SFHs are only available for two of M31's 35 known satellite galaxies (M33, IC 10). HST

and JWST will create a huge influx of observations for M31 satellite galaxies over the next 5-10 years and PMs for at least six galaxies in M31's plane of satellites are already guaranteed (see Fig. 7.3). I, as a member of the HSTPROMO collaboration, am leading the orbital analysis for two of these: NGC 145/187 (dwarf ellipticals in the outer halo) using PMs from HST GO-14769 (PI: T. Sohn). When JWST launches, our collaboration will receive PMs for four more satellites (And I, III, XIV, XVII) through GTO-1305 (PI: R. van der Marel).

There is a also an ongoing effort in the community to obtain PMs and SFHs of all M31 satellite galaxies (< 300 kpc) using HST (PI: D. Weisz, Co-I: E. Patel). Such data would enable us to calculate the 3D orbital histories for these satellites, including the influence of M33, to trace out the dark halo and mass profile of M31. However, these calculations invoke static halos for M31 and M33 and therefore only provide first order satellite orbital histories. To capture the complex, time evolving dark matter distributions of both galaxies, which are critical to the assembly of the M31 satellite system, high-resolution N-body simulations of this system are also necessary (Garavito-Camargo et al., 2019).

To this end, I plan to develop a suite of high-resolution (10^8 particles) N-body simulations using Gadget-3 to model the resulting disturbances in M31's dark matter halo caused by the recent accretion of both M33 and the GSS progenitor. The goals of this suite are to: a) quantify the influence of M33 on the orbits of low mass M31 satellites, b) determine the effects of a disrupted massive satellite galaxy (GSS progenitor) on M31's halo, and c) assess the combined effects of these two major dynamical events in shaping the current properties of the M31 satellite system.

The proposed simulations will describe the orbital conditions under which massive satellite galaxies can induce or destroy coherent planes of satellites, if at all. Using this information, I will identify M31-mass analogs from the *IllustrisTNG* cosmological simulation to quantify the frequency that M31-like galaxies host satellite planes. While cosmological simulations, such as *IllustrisTNG*, are unlikely to resolve extremely low mass satellites (i.e. ultra-faint dwarfs), massive satellite analogs and their orbital properties are well-resolved (as demonstrated in Chapter 2). Satis-

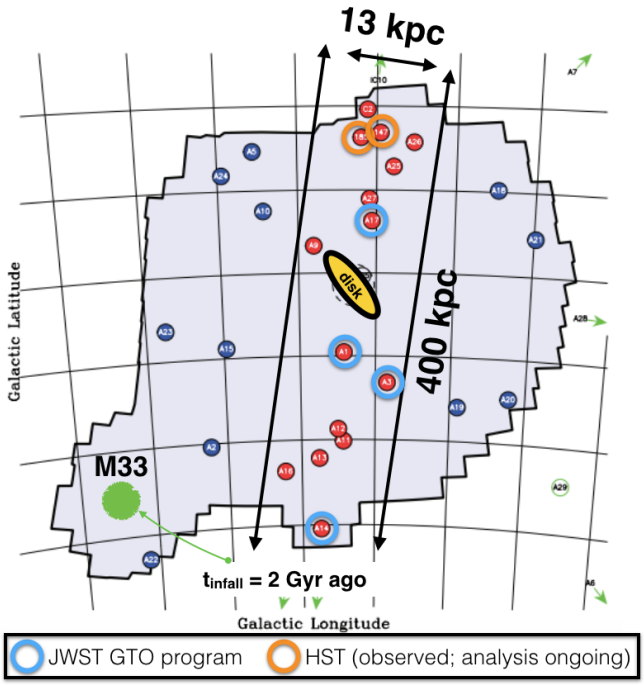

Figure 7.3: The planar distribution of satellites in M31's halo (adapted from Ibata et al., 2013) where satellites in the plane are denoted with red filled circles and others are denoted with blue filled circles. Not pictured is the Giant Southern Stream (GSS) which extends 100 kpc along the line segment connecting M31's disk and M33. Planes of satellites are rare in ΛCDM cosmological simulations and therefore their origin is not well understood. In my proposed suite of N-body simulations, two sets of initial conditions (randomly distributed satellites vs. satellites initialized in a planar structure) will be tested to investigate whether the dynamical influence of two massive satellite galaxies (M33 and the GSS progenitor) evolving in M31's halo plays a role in the formation of planar structures. Blue circles encompass satellites whose PMs are guaranteed through a JWST GTO program and orange circles outline the satellites who PMs have been measured with HST.

factory M31 analogs will be chosen to have a massive satellite galaxy at z=0 (i.e. M33) and a recent (< 4 Gyr ago) merger event involving a galaxy with a progenitor mass $\gtrsim 10^{11}\,M_\odot$. Applying these constraints, I will determine the most probable mass for M31 as a function of its accretion history. Furthermore, the confluence of high-precision 6D phase space for a large sample of M31 satellites and satellite analogs from *IllustrisTNG* will enable a more precise statistical mass estimate for M31 following the method presented in Chapter 5.

This three-pronged approach to study the complex history of M31 combines the kinematic and dynamical information derived from precision astrometry with high-resolution simulations to reconstruct the assembly history of M31. Massive satellite galaxies ($10^{11}\,M_\odot$) are the building blocks of M31-mass halos and approximately 35% of M31-mass halos host one at z=0 (Chapter 2), thus the data generated through this program will be widely applicable to other galaxy systems of similar mass. Centaurus A ($D \sim 3.4$ Mpc) is an obvious choice for studies beyond the LG as it has also been reported to host planes of satellites (Müller et al., 2018). Furthermore, the Satellites Around Galactic Analogs (SAGA) survey (Geha et al., 2017) is measuring the satellite luminosity function of 100 MW stellar mass galaxies, providing a statistical comparison for the MW and M31's classical satellite populations. The next decade(s) will yield a wealth of high precision phase space information and resolved stellar population data for M31's halo and for galaxies beyond the LG (i.e. WFIRST, JWST, ELTs). Thus, building a complete picture of M31's accretion history is imperative as it will be the foundation on which interpretations for these more distant galaxies are built (Gilbert et al., 2019).

7.4 Orbital Histories of Magellanic Satellites Using Gaia DR2

As shown in Chapter 1 and Fig. 1.1, satellite galaxies around the MW have been discovered at a rapid rate in the last two decades thanks to wide-field surveys like the *Sloan Digital Sky Survey* (SDSS) and the *Dark Energy Survey* (DES). Many of these recently detected satellites, especially those found within the DES footprint

are spatially located in close proximity to the Magellanic Clouds (MCs). Significant efforts have also been made by the theoretical community to predict exactly how many satellite galaxies the MCs should host (e.g. Sales et al., 2013; D'Onghia and Lake, 2008; Dooley et al., 2017b,a; Wetzel et al., 2015). Furthermore, using M33, we have already demonstrated that a substantial population of low mass satellite galaxies is expected to orbit around massive satellite galaxies in a ΛCDM paradigm (Chapter 5). The MCs are the first such example where observations are now able to directly test these predictions. A natural extension of the work presented in this dissertation is to use astrometric measurements of these satellites to investigate which ones are dynamically associated with the MCs (see also Kallivayalil et al., 2018).

Using PM measurements of the MCs from Kallivayalil et al. (2006a,b), Besla et al. (2007) showed that the MCs are likely on their first infall into the halo of the MW. If any of the recently discovered satellites around the MCs are truly of a Magellanic origin, they should share common orbital properties with the MCs. Revised PM estimates for the MCs were presented in Kallivayalil et al. (2013), where third epoch measurements showed that the total velocities of the Clouds relative to the MW decreased substantially, but the LMC-SMC relative velocity stayed about the same. Using these revised PMs, Gómez et al. (2015) recalculated the orbital history of the LMC where the MW also experienced the gravitational influence of the LMC's approach. These results are also consistent with a first infall scenario for the LMC. In Chapter 2 I also recalculated the orbital history of the LMC, implementing a more modern dynamical friction term calibrated to match simulations of a 1:10 mass ratio host-satellite pair, and the data still statistically prefer an orbital history where the LMC is on first infall having made a pericentric passage about 50 Myr ago (unless the mass of the MW is higher than $1.5 \times 10^{12}\,\mathrm{M}_{\odot}$).

With several lines of evidence that point to the MCs being on first infall, one way to confirm that satellites in the halo of the MW are actually of a Magellanic origin is to compute their 3D orbits. These orbits should be calculated including the influence of the MW's tidal field plus the gravitational influences of both of the Clouds to

distinguish between those satellites whose orbits mimic a similar orbital history as the MCs versus those that do not. 6D phase space information also allows for the computation of satellite angular momenta vectors, orbital energies, comparisons of total velocities relative to the escape speed of the LMC, and comparisons of 3D positions with the equivalent properties for the MCs[1].

There are currently 32 satellite galaxies in the literature that are more likely to be satellites of the MCs than the MW based on their proximity alone. Of these 32, 15 satellite galaxies have existing proper motion measurements (e.g. Fritz et al., 2018; Kallivayalil et al., 2018; Simon, 2018) thanks to the *Gaia* mission's second data release (Gaia Collaboration et al., 2018a,b). In future work, I will use 6D phase space information derived from these proper motions to calculate the orbital histories of candidate MC satellites to determine whether they are dynamically associated with the MCs. Preliminary calculations in Fig. 7.4 show that 5 of these 15 satellites are likely to be associated with the MCs given their similar orbital histories (in agreement with Kallivayalil et al., 2018). Note that these calculations do not explore the uncertainties on the PMs, which amount to velocity errors between 100-200 km s^{-1} for galaxies beyond 150 kpc from the Galactic Center and 10-60 km s^{-1} for the remainder of the sample[2]. They also do not consider the range of masses in the literature for the MW, LMC, or SMC. Therefore, a thorough analysis is required to truly confirm whether this group of satellites entered the halo of the

[1]Alternative methods to determine associations between satellites and the MCs include comparing their metallicity information, where similar amounts of metals are expected assuming that these galaxies all formed within the same environment. However, these properties should be interpreted with caution as the shallow gravitational potential wells of these low mass galaxies ($M_{\rm tot} \leq 10^9\,{\rm M}_\odot$) may cause them to be strongly affected by various feedback processes, and therefore may not provide the most accurate point of comparison. SFHs can sometimes be telling for these satellites as well, however the many processes at play (i.e. host environment, reionization, group pre-processing) make it difficult to draw connections between SFHs and orbital dynamics. Ideally, a combination of both dynamical and baryonic properties is the most powerful way to place constraints on these satellites.

[2]By the end of the planned *Gaia* mission, these uncertainties are expected to reach uncertainties equivalent to those resulting from measurements with *HST* ($\lesssim 50$ km s^{-1}) or better.

MW simultaneously as a dynamically bound group.

In addition to testing the dynamical associations of the MC satellite candidates and comparing these to theoretical predictions, there are several additional questions of interest that can be explored through this analysis. Some of these include: How do the orbits of low mass satellites differ when they enter with a massive satellite companion like the LMC versus when they fall into a MW-mass galaxy alone? What LMC mass is necessary to keep all of these satellites bound to the LMC between the time of the MCs' infall and today? Can any connections be drawn between the SFHs of the MC satellites and the formation timeline of the Magellanic Stream?

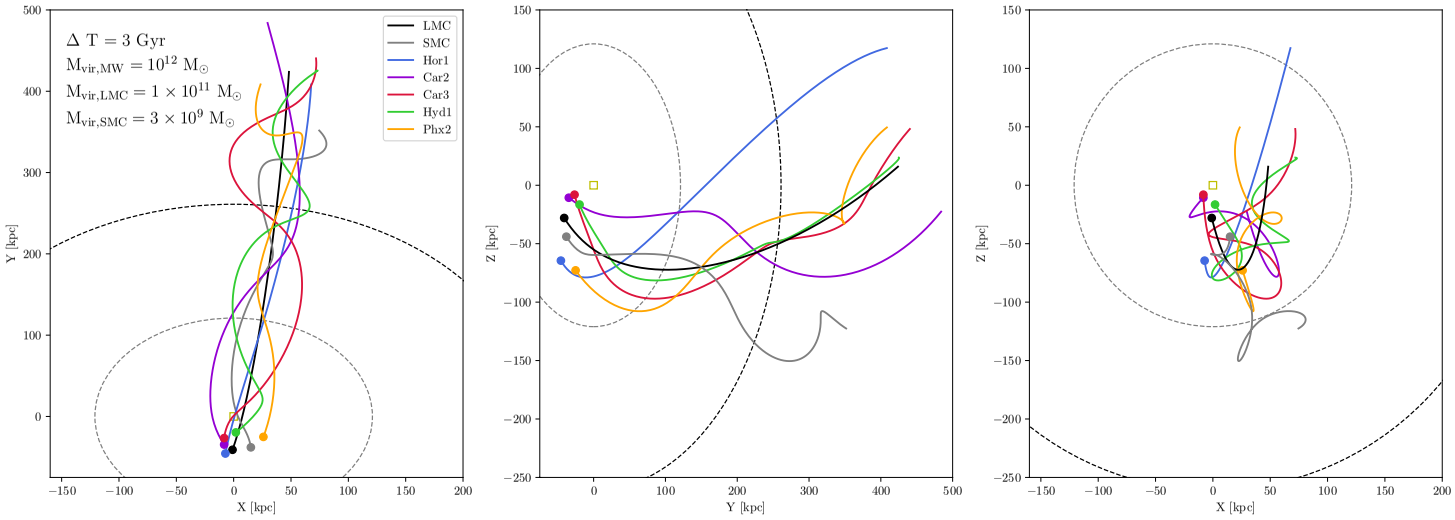

Figure 7.4: Preliminary orbital histories for five (of the 15) candidate MC satellite galaxies ($M = 10^9\,\mathrm{M}_\odot$) relative to the MW over the last 3 Gyr. The black dashed circle indicates the virial radius of the MW and the gray dashed circle represents the virial radius of the LMC. These five satellites are shown here as their orbits indicate they are highly likely to be members of the Magellanic group (i.e. they entered the halo of the MW together) given the similarity between the orbits of the LMC (black), SMC (gray), and these satellites. The satellite orbital histories plus the SMC's orbit are calculated such that they feel the gravitational influence of both the MW and the LMC. Future improvements include orbital calculations that simultaneously account for the gravitational potential of the MW, LMC, and SMC. Multiple mass combinations and dynamical friction prescriptions will be considered for each pair of galaxies as well.

7.5 The Future of Theory and Simulations for Studies of the Local Group

The results presented in this dissertation have utilized three main tools and techniques, namely high resolution cosmological simulations, numerical orbit modeling, and Bayesian inference methods to explore the dynamical histories of LG satellite galaxies and to estimate the precise masses of the MW and M31. However, even these advanced tools have opportunities for improvement as our understanding of the LG changes. Here, I will describe some of their limitations and discuss potential areas of growth.

Next Generation High Resolution Cosmological Simulations

Cosmological simulations such as Illustris-Dark include a few thousand mass analogs of the MW and M31. However, reliably identifying halos that host galaxies less massive than the classical dwarf spheroidals ($M_{halo} < 10^{10}\,M_\odot$) rapidly becomes difficult due to resolution limits (see Chapter 4). Several suites of cosmological zoom simulations have been created over the last decade to extend detailed studies down to dwarf and ultra-faint dwarf (UFD) galaxy masses ($M_{halo} \leq 10^{9}\,M_\odot$) in isolation and in MW-like environments. One such example is the *Caterpillar* simulation suite upon which the foundation of the work in Chapter 5 is built. However, these suites of cosmological-zoom simulations typically contain between 10-30 runs and focus on halos of similar mass (i.e. MW-mass halos, or $\approx 10^{12}\,M_\odot$). As such, there is a need for a higher resolution, large volume (i.e. $(100\text{ Mpc})^3$ box with $m_{DM} = 10^4 - 10^5\,M_\odot$ particle mass resolution) simulation in which UFDs and globular clusters can be resolved[3].

A simulation of this volume and resolution would be particularly useful in the context of this dissertation since one of the limitations of the methodology in Chapter 4 is the absence of a statistically significant population of MW-mass halos in Illustris-

[3]Alternatively, a suite of cosmological zoom simulations with > 100 runs focusing on a broader range of halo masses (i.e. $10^{11} - 10^{13}\,M_\odot$) may allow for similar advancements.

Dark that each host ~ 10 satellites in the classical dwarf spheroidal regime. At the requested resolution for a next generation simulation, it is expected that many hundreds of analogous systems would be resolved, making it possible to rigorously apply the mass estimation techniques in Chapter 4 to the classical MW satellites galaxies. It would also enable an extension of this method to the full population of known MW satellites, including the few dozen UFDs orbiting around the MW for which measured 6D phase space information already exists (Fritz et al., 2018; Simon, 2018; Kallivayalil et al., 2018, see). Not only will this allow for better constraints on the MW's total mass, it will also help constrain the concentration and mass profile of the MW to the virial radius.

Considerations for Orbital Modeling

The numerical orbit models used to calculate the orbital histories of M33 and the LMC (Chapters 2 and 6) and the future fate of the MW-M31 collision (Chapter 6) all consider static halo potentials, ignoring the mass growth of host halos over time and their time-evolving potentials. In Appendix A, I show that numerically integrated orbits for cosmological analogs of massive satellite galaxies provide good matches compared to the orbits extracted from Illustris-Dark over the last 6 Gyr, especially for recent, first infall scenarios. Beyond this time frame, fully cosmological models are necessary to account for the effects of large scale structure.

Most numerical orbits are calculated using an approximation for dynamical friction (DF), which does not capture the full complexity of perturbations and resonances that are introduced when a massive satellite galaxy passes through its host halo. The DF approximation adopted in this work (see Eq. 2.5) relies on several parameters, including the density of the matter that the satellite passes through, the Coulomb logarithm ($\ln \Lambda$), the mass of the satellite, and the relation between the velocity of the satellite and that of the surrounding matter.

Garavito-Camargo et al. (2019) showed that the LMC significantly perturbs the dark matter halo of the MW as it enters and orbits within the halo of the MW, introducing regions of over- and underdensities at distances of 50-200 kpc. One

of these overdense regions is a wake of matter trailing behind the LMC with an increased acceleration. Lux et al. (2010) further demonstrate that analytic DF prescriptions are only approximate and a full treatment of the halo's response to the motion of satellites is necessary. Given these prominent perturbations that arise owing to the motion of the LMC, future work on orbital models for the MW's satellite galaxies must use the full analytic solution for the time-evolving potential of the MW+LMC (Garavito-Camargo et al., in prep.) to properly account for DF and the influence of the LMC over time. Mass growth of host halos like the MW over the last 5-6 Gyr is minimally significant for the massive satellite galaxies considered in this work, but this may become important for satellites where the ratio of host to satellite mass is $> 10:1$.

For calculations of M33's orbit, I adopted a dynamical friction approximation that is calibrated against N-body simulations of the M31-M33 system (see van der Marel et al., 2012b), alleviating some of the uncertainties in the DF approximation, such as the appropriate value of the Coulomb logarithm ($\ln \Lambda$). However, a time-evolving potential for M31 combined with the presence of a massive satellite galaxy (M33) and the imprint of a massive satellite progenitor (the GSS progenitor) is still necessary to gain a more thorough understanding of the dynamics of the entire system of satellite galaxies orbiting around M31.

Systematics of Statistical Mass Estimation Techniques

The Bayesian framework developed in Chapters 3 and 4 focuses on the total specific orbital angular momenta of satellite galaxies and how that information can be used to constrain the precise masses of their host galaxy. There are several systematics involved in this Bayesian inference technique that should be considered as this method is broadened to include larger satellite populations and additional satellite properties that can further constrain their host halo masses and additional halo properties.

Currently, this method yields estimates for the *virial mass* of the MW and M31. The classical dwarf galaxies I used to estimate the mass of the MW are located

at varying radial distances from the Galactic Center. This raises the question of whether the inner or outer satellites bias the resulting ensemble virial MW mass as a function of their location relative to the MW's center. Moving forward, it should be tested whether these tracers adequately recover the actual virial mass of the MW (using simulated MW-mass analogs) or just the mass enclosed within the subset of orbits considered (i.e. if more inner (outer) tracers are used, does this bias the virial mass to lower (higher) values?). This will become especially important as additional MW satellite galaxies are added to the ensemble since the radial distribution of satellite galaxies in observations and simulations is typically non-linear.

When applying a statistical method like the one used in this work to compare observational data to simulations, it is also important to understand the systematics that are introduced under the assumption that the simulations are an accurate representation of reality. For example, whether or not the MW has had a major merger since $z \sim 2$ could affect the overall angular momenta distribution of MW satellites. Alternatively, satellites could be disrupted too early or too late in a way that systematically depends on the value of their angular momenta. The angular momenta of true MW satellites may also be affected by the influence of the LMC since it has made a close pericentric passage about the MW recently, introducing perturbations to the halo of the MW. Thus, the measured properties of the MW's satellites may be intrinsically biased relative to simulated satellites in the prior samples from Chapter 4. While we require that all halos in the prior sample from Illustris-Dark host a massive satellite analog, most do not reflect the current kinematics and orbital history of the LMC.

Finally, correlated satellites affect the statistical significance of inference techniques and they are not yet accounted for in a rigorous fashion in our Bayesian framework. Typically, each satellite's properties are treated as an independent measurement, whereas satellites are likely to be correlated in reality. The covariance between their properties must therefore be included unless it can be shown that the covariance is negligible (see Busha et al. (2011) on the covariance of the properties

of the MCs). This will be particularly important for groups of satellites that have entered their host's halo at similar times (i.e. the Magellanic satellites in the MW's halo) and requires thorough testing of the technique.

Together, these improvements will not only provide more comprehensive results that build on the conclusions presented in this dissertation, but they also have the potential to address open questions in LG dynamics, small-scale ΛCDM, and fundamental physics on the origin of our galactic neighborhood.

APPENDIX A

Appendix to Chapter 2

A.1 Forward Orbit Integrations

For the massive satellite analogs which do not contain a pericentre and/or apocentre between their crossing time and $z = 0$ in the Illustris-Dark merger tree data, we integrate their orbits forward in time for 6 Gyr. The host haloes are modeled as NFW dark matter haloes (Equation 2.1) and the satellites are modeled by Plummer spheres (Equation 2.4). We aim to match the orbits from the Illustris-Dark simulation, which contains only dark matter, so we do not model the baryons in the host galaxies unlike the analytic constructions in Section 2.3. Consequently, the NFW host haloes are not adiabatically contracted. We do, however, implement dynamical friction (Equation 2.5) and allow the host haloes to move as a result of the gravitational force exerted by the satellites.

The satellite gravitational softening lengths, $\mathrm{k_{sat}}$, for the massive satellite analogs are computed by fitting the following equation:

$$\mathrm{M(r_{half})} = \frac{\mathrm{M_{tot} r_{half}^3}}{(\mathrm{r_{half}^2} + \mathrm{k_{sat}^2})^{3/2}}. \tag{A.1}$$

$\mathrm{M_{tot}}$ is the subhalo mass at $z = 0$, $\mathrm{M(r_{half})}$ is half of the subhalo mass, and $\mathrm{r_{half}}$ is the radius at which half of the subhalo mass is enclosed. $\mathrm{r_{half}}$ is provided in the Illustris-Dark halo catalogs. With these quantities, $\mathrm{k_{sat}}$ is calculated to match the mass enclosed within $\mathrm{r_{half}}$, given $\mathrm{M_{tot}}$.

All forward orbits are calculated for 6 Gyr, except in Section 2.7.1 where we integrate forward for 3 Gyr to recover only recently accreted satellites. The future orbital trajectories are then analysed to find a true pericentre/and or apocentre as described in Section 2.6.3. In the event that a pericentre exists in the merger tree data, it is used in combination with the next apocentre from the forward orbit.

Therefore, the merger trees and forward orbits are used in unison and act as a complete past and future orbital history.

For 19 (4 per cent) of the massive satellite analogs, the forward orbit integration fails to find a pericentre and apocentre. We suspect these are fly by satellites that only remain in the vicinity of their host halo's R_{vir} for a short period of time. Upon inspecting these 19 analogs further, we find that all satellites which are energetically unbound in Figs 2.9 and 2.10 are members of this population, providing a nice consistency check within our data sample.

While analytic orbits are often questioned as suitable matches to the true orbits in a cosmological volume, we show here that our backwards orbit integration methods result in acceptable solutions, especially for recent, first infall scenarios. Fig. A.1 shows the merger tree data (solid lines) and corresponding numerical orbits (dashed lines) for ten randomly chosen massive satellite analogs in our Illustris sample. The top panel separates the six massive satellite analogs whose orbits exhibit a recent, first infall scenario. For these satellites, the orbital trajectories are recovered very well by the numerical integrations.

The bottom panel of Fig. A.1 indicates the remaining four orbits which are either accreted early and make multiple pericentric passages (purple and gray) or are on first infall with no recent pericentre (light blue and green). The latter are the analogs whose forward orbit integrations are important to our analysis, and they show good agreement between the merger tree data and backwards orbit integration. Therefore, integrating their orbits forward in time using their $z = 0$ properties to recover their first pericentre is justified.

The numerical integrations are least effective at reproducing the orbits of massive satellite analogs that were accreted early and make several pericentric passages in the last 6 Gyr (Lux et al., 2010), but these are scarce in our massive satellite analogs population. Furthermore, we can recover orbital histories for them in the merger tree data, so there is no need to integrate their orbits forward in time. There is little concern with regards to cosmology in the future orbits since large scale structure is changing minimally at $z = 0$ and therefore in the future. Furthermore,

the sample is chosen such that there is only one massive host in the vicinity of each satellite analog. These numerical orbit integrations also confirm that the new implementation of dynamical friction used in this work (which allows for varying softening lengths based on mass) is efficient at predicting the orbital decay of massive satellites accurately. Finally, we relax our assumption that host haloes are truncated at their R_{vir} and allow dynamical friction to continue to larger radii. By doing so, we find that there is little to no difference in our ability to match analytic orbits of massive satellites to their cosmological counterparts within $\sim$500 kpc of their hosts.

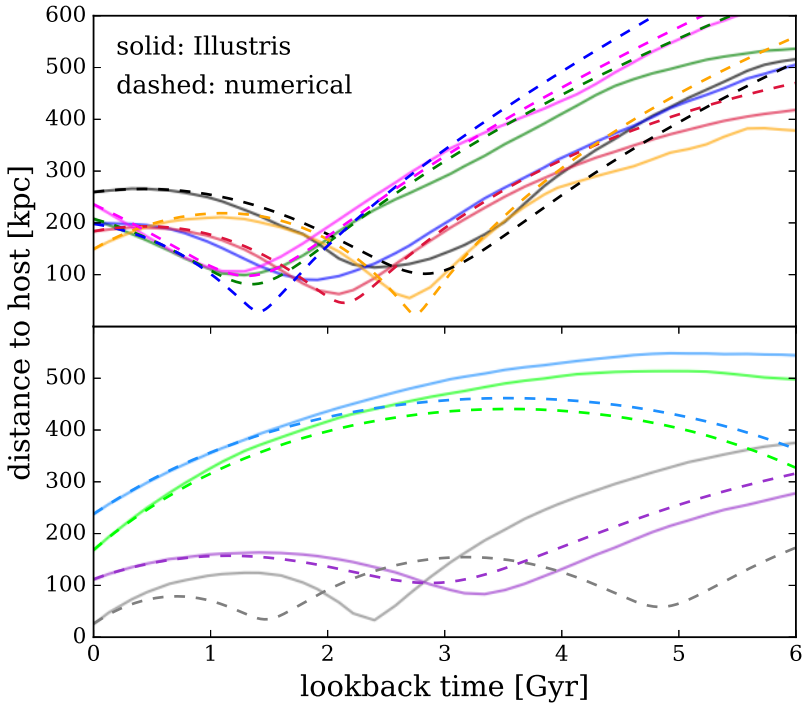

Figure A.1: Orbital histories for ten randomly chosen massive satellite analogs. The solid lines indicate the true distance of each analog relative to its host as a function of time from the Illustris-Dark merger tree data. The dashed lines indicate the corresponding numerical orbit integration using the $z = 0$ properties of each host-satellite system. The hosts are modeled as NFW dark matter haloes and the satellites are approximated by Plummer spheres. The top panel shows the subset of orbits on first infall which reach a pericentric distance $\lesssim 100$ kpc from their hosts in the last 3 Gyr, while the bottom panel shows the remaining orbits. There is good agreement for the first infall scenarios with a close pericentric passage (top) and first infall with no pericentric passage (bottom–light blue and green), which are the orbits relevant to our analysis. Therefore, numerical orbit integrations are a reasonable approximation to the future orbits of massive satellite analogs from Illustris-Dark.

APPENDIX B

Appendix to Chapter 3

B.1 The Stability of Maximum Circular Velocity

The maximum circular velocity of a dark matter halo is generally more stable than the subhalo mass (typically defined as the sum of bound particle masses) as a function of time. It is well known from numerical simulations that dark matter haloes lose mass from their periphery rather than their most central region due to tidal disruptions (Klypin et al., 1999). Secondly, much of the fluctuation in subhalo mass history is caused by the numerical effects of halo finding algorithms themselves. The friends of friends (FoF, Davis et al., 1985) algorithm and `SUBFIND`, the substructure identification code used in Illustris-Dark are both sources of mass bias for subhaloes. The identification of haloes and assignment of substructures within individual haloes therefore raises concerns for analyses using several, consecutive simulation snapshots.

Our Bayesian inference methods consider all subhaloes in a window of $z = 0 - 0.26$, or 20 snapshots of the Illustris-Dark output. For this study, we choose v_{max} as a proxy for subhalo mass and identify analogs of the LMC and M33 purely based on v_{max}. Both galaxies have well-defined rotation curves (van der Marel and Kallivayalil, 2014; Corbelli, 2003), motivating our choice to move away from subhalo mass and its related uncertainties. This choice is also justified from evidence in Paper I, which shows that at least 49.36 per cent of the massive satellite sample in Illustris-Dark make one pericentric passage within 100 kpc of its host's centre of mass recently (within the last 3 Gyr). At such separations, tidal stripping will remove material (the tidal radius of the LMC for example is expected to be between 20-30 kpc) and will likely cause significant mass and radius fluctuation for massive satellite analogs.

Fig. B.1 compares the change in circular velocity and subhalo mass at two epochs

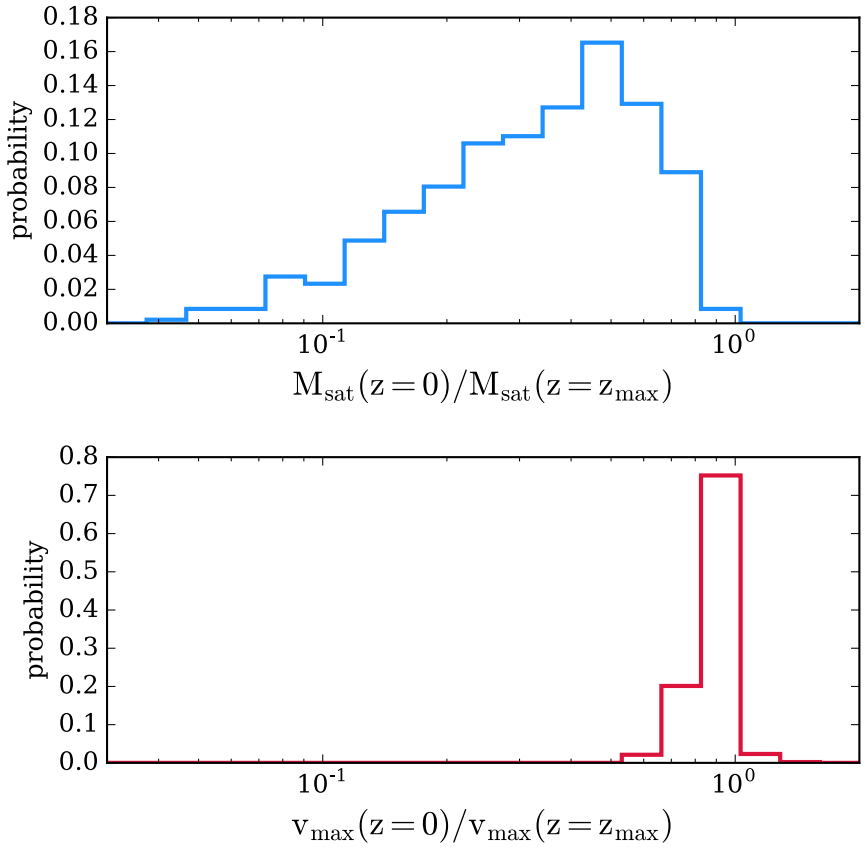

Figure B.1: *Top:* The distribution of the ratio of satellite mass at $z = 0$ to satellite mass at maximal mass for the Illustris-Dark control sample of massive satellite analogs. *Bottom:* The distribution of the ratio of satellite maximal circular velocity at $z = 0$ to satellite maximal circular velocity at the time of maximal mass, z_{max}. The latter shows much less variation for the overall massive satellites analog sample when the quantities are binned over the same range and with a fixed bin width. The y-axis denotes the probability of a specific ratio.

in the lifetime of the Illustris-Dark massive satellite analogs control sample (see Section 3.2.2). The ratio is computed using the $z = 0$ properties compared to the epoch at which the satellites reach their maximal mass, z_{max}. This epoch is identified using the `SUBLINK` merger trees (Rodriguez-Gomez et al., 2015). Fig. B.1 illustrates that v_{max} is generally constant over a few Gyr timescale while M_{sat} is more variable. The distributions are plotted for a fixed bin width to emphasize the range of each distribution. In a fixed period of time, the subhalo mass can decrease by up to a factor of 10, whereas the circular velocity remains consistent within a factor of a few at most. The subhaloes with highest mass loss ratios generally have a time of maximal mass ≥ 3 Gyr ago, which is about half of an average orbital period.

Note that in Paper I and prior to Section 3.3 in this work, massive satellite analogs are chosen primarily based on mass provided that they survive until $z = 0$ within the virial radius of their hosts. Since Paper I tracks the dynamical histories of massive satellite analogs, the evolution of subhalo mass across time did not affect our conclusions. In this work, v_{max} allows us to choose a consistent sample of massive analogs across 20 snapshots in Illustris-Dark.

B.2 Kernel Density Estimation for Bayesian Inference

Histograms are a common way to represent posterior probability distributions. This process typically goes as follows: choose a mass bin for which to compute the posterior of the sample at that mass range and repeat for multiple, contiguous mass bins until you have computed enough data points to form an informative distribution. This method yields one point per mass bin where the point represents the total probability for the set of samples only in that host mass range. However, calculating the posterior for a finite number of bins will not finely sample the posterior well and can be computationally expensive. Consequently, the summary statistics (i.e. mean and credible intervals) over the set of samples become difficult to compare directly with a coarsely sampled host halo mass probability distribution.

One way to sample the posterior more finely is to compute the probability of

the target parameter (i.e. host halo mass) by taking bins in the mass range of interest through a gaussian kernel density estimation (KDE) technique. Kernel density estimation allows us to smooth over the posterior PDF to avoid harsh edges caused by a coarse sampling of the grid over the target parameter range, as found in the histogram method.

In the KDE method, we create a uniformly spaced grid over a reasonable range for the host halo mass exhibited by the haloes in the prior. Each halo in the prior is represented on this mass grid by a Gaussian distribution centered at the halo's mass with a standard deviation given by the optimal bandwidth determined by the whole sample. We scale each halo's Gaussian by its normalised importance weight, and then sum these distributions over all the halos. This results in a smooth representation of the posterior PDF in mass, as we have shown in Figs. 3.3 and 3.4. The rule of thumb for choosing the optimal bandwidth, h, is determined by Silverman (1986) as

$$\mathrm{h} = \left(\frac{4\sigma^5}{3\mathrm{n}}\right)^{1/5} \approx 1.06\sigma\mathrm{n}^{-1/5}. \tag{B.1}$$

Here, σ is the posterior standard deviation estimated from the importance-weighted halo masses and n is the sample size where each of the values is typically given a weight (w_i) of one. However, in importance sampling, each sample is not given an equal weight, thus n must be substituted with the effective sample size (Kong, 1992, ESS),

$$\mathrm{ESS} = \frac{(\sum_{\mathrm{i}=1}^{\mathrm{m}} \mathrm{w_i})^2}{\sum_{\mathrm{i}=1}^{\mathrm{m}} \mathrm{w_i^2}}. \tag{B.2}$$

To preserve the machine precision of the importance sampling technique, all weights should be calculated and stored as $log(w_i)$ and exponentiated when used in the calculations of bandwidth, ESS, and summary statistics. It should be noted that regardless of technique, mean values and credible intervals should always be calculated over the full set of samples, not from the binned or KDE results.

APPENDIX C

Appendix to Chapter 4

C.1 The Halo Mass-Specific Angular Momenta Relation in the Presence of a Galactic Disk

The presence of a galactic disk is known to cause a depletion of subhalos in the inner regions of MW-like halos (e.g. D'Onghia et al., 2010). More specifically, recent work shows that subhalos on radial orbits are most susceptible to this phenomena (Garrison-Kimmel et al., 2017c). Here we use the Illustris-1 N-body+hydrodynamical simulation to examine whether there are any significant changes to the intrinsic relationship seen between host halo virial mass and the specific orbital angular momenta of subhalos discussed in Section 2.7 when baryons are considered. By comparing the results from the two versions of the Illustris simulation, we can also demonstrate whether the resulting MW mass estimates change significantly when both dark matter and baryons are taken into account.

To this end, a new sample of low mass satellite analogs are chosen from the final 20 snapshots of Illustris-1 that satisfy the same exact selection criteria described in Section 4.3.1. This sample contains 59,156 subhalos residing in 18,858 unique host halos. Notice that one-third fewer subhalos satisfy our selection criteria in Illustris-1 compared to Illustris-Dark, indicating that there is a general depletion of low mass subhalos when disks and other hydrodynamic processes, such as feedback, are included.

Fig. C.1 shows the distribution of specific orbital angular momenta for subhalos in Illustris-1 binned by host halo virial mass. The gray shaded region is identical to the previous figures and represents the distribution of specific orbital angular momenta for the classical MW satellites. Fig. C.1 is generally in good agreement with Figs. 4.4 and 4.5, as indicated by the consistency between the data points and the black solid line (the line of best fit from the dark-matter-only counterpart

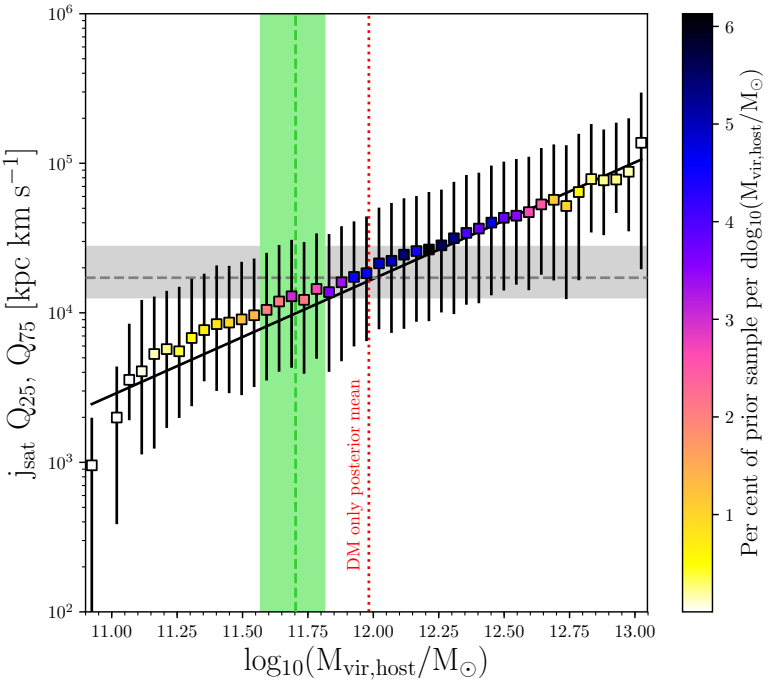

Figure C.1: Similar to Fig. 4.4 but the data shown here are selected from the Illustris-1 simulation, which includes baryonic physics. This sample includes 59,156 subhalos residing in 18,858 unique host halos, just two-thirds of the subhalos found in Illustris-Dark. The black solid line is the line of best fit from Fig. 4.4. The green shaded region indicates the ensemble MW mass estimate ($\log_{10}(M_{vir}/M_\odot = 11.70^{+0.12}_{-0.14}$) using the Illustris-1 data and the observed properties of 8 satellites. The Illustris-Dark results are indicated by the dotted red line. The overall trend between host halo mass and the distribution of specific orbital angular momenta is in agreement with the dark-matter-only sample analysis beyond halo masses of $\log_{10}(M_{vir}/M_\odot) = 11.75$. In host halos of lower mass, the kinematics of low mass subhalos may be more strongly affected by the co-evolution of dark matter and baryons, potentially causing the deviation from the line of best fit. The ensemble MW mass inferred with the Illustris-1 data is lower than that resulting from the dark-matter-only analysis, but they are consistent within 2σ of each other, suggesting that our technique is robust across simulations.

sample) for host halo masses above $\log_{10}(M_{vir}/M_{\odot}) = 11.75$. The deviation from the line of best fit at host halo masses $\log_{10}(M_{vir}/M_{\odot}) < 11.75$ is likely due to the depletion of the lowest specific orbital angular momenta satellites and suggests there is a difference in subhalo kinematics between the simulations. The green shaded region indicates the ensemble MW mass estimate when the Illustris-1 data is used. Notice that the latter is lower than that predicted by the dark-matter-only subhalos, indicated by the red dotted line.

We have also split the prior sample from Illustris-1 into subsets based on the time of their most recent major merger where this is defined as the last time there was a 1:4 stellar mass ratio collision such that the Illustris halo finding algorithm can no longer distinguish between two distinct halos. Hosts with major mergers greater than 6 Gyr ago make up 79% of the sample and the halo mass-specific orbital angular momentum trend for this subset is in good agreement with Fig. C.1. The scatter associated with various formation histories is therefore implicitly included in our mass estimates even though our prior selection criteria do no explicitly require any specific formation history. Complementary work by Li et al. (2017) suggest that this scatter can contribute to up to 20% uncertainty to the MW mass estimates.

We conclude that on average, the addition of baryonic physics and other hydrodynamical processes results in lower MW halo mass values. However, the posterior mean MW halo masses using each individual satellite and all satellites simultaneously are still within 2σ of their counterpart MW posterior mean halo masses predicted by the dark-matter-only analysis. It appears that such discrepancy could arise from the depletion of low mass subhalos, which may consequently change the correlation between subhalo properties and their host halo properties. However, a new generation of cosmological simulations with revised feedback formulae and perhaps higher particle mass resolution may be able to address such concerns more confidently.

Since the subhalos considered here all have subhalo masses $\geq 10^9\,M_{\odot}$ and most have a typical $v_{max} = 20 - 45$ km s^{-1}, their overall depletion is less drastic than expected. At this mass, subhalos are less susceptible to rapid tidal disruption by

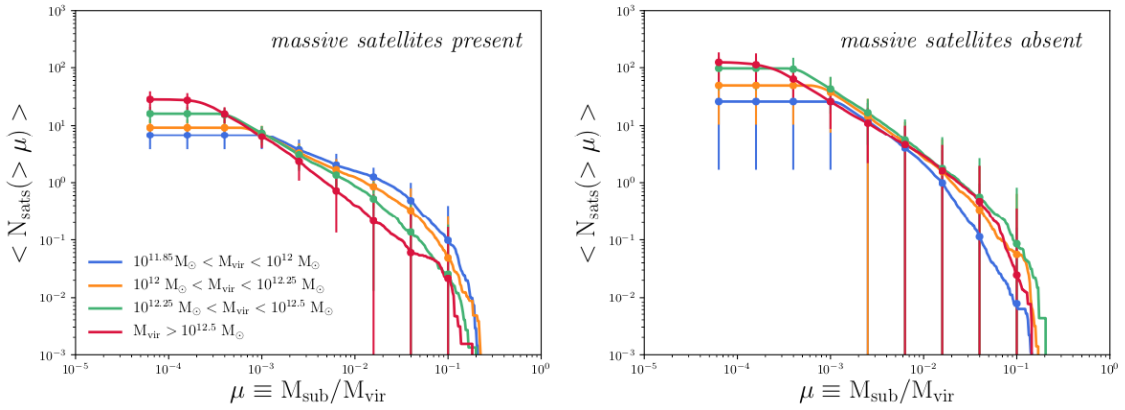

Figure C.2: *Left*: Subhalo abundance functions for the 3,153 unique host halos in Prior 2 with halo masses $< 10^{11.85}\,M_\odot$ from the final 5 snapshots of Illustris-Dark. These hosts all have a massive satellite companion. All low mass subhalos around these hosts with a mass $\geq 10^9\,M_\odot$ or 133 dark matter particles and that reside within the virial radius of their hosts are included. Abundances are plotted as a function of μ where μ is the ratio between subhalo mass and host virial mass (M_{sub}/M_{vir}). The data points with error bars indicate the standard deviation in each bin. Host halos with approximately 10 subhalos analogous to the classical MW satellites favor halo masses $10^{11.85} - 10^{12.25}\,M_\odot$, in agreement with our analysis results. *Right:* The subhalo abundance function for the 104,362 host halos that harbor low mass satellites analogs, but no massive satellite analog. This data is also taken from the final 5 snapshots of Illustris-Dark and all subhalos $\geq 10^9\,M_\odot$ and within their host's virial radius are included. When massive satellite analogs are absent, on average, there are more low mass satellites about host halos with masses $> 10^{11.85}\,M_\odot$.

their hosts. Those subhalos that tend to experience significant depletion due to baryons are generally lower in mass and v_{max}, such as in the simulation data studied by Garrison-Kimmel et al. (2017c). If our method is extended to ultra-faint dwarf galaxies, these issues will need to be reconsidered.

C.2 Subhalo Abundance Functions With and Without Massive Satellite Analogs

In this analysis, all host halos with a massive satellite analog and one or more low mass satellite analogs were used to infer the halo mass of the MW (see Section 3.4).

The latter constraint, that there should be one or more low mass satellite analogs, rather than ten per host like the classical satellites around the MW, is necessary due to the current state of cosmological simulations and specifically their resolution limits. Here, we calculate the subhalo abundance functions around the host halos used for the MW halo mass calculations presented in Section 3.4 to demonstrate that on average, there are 10-20 subhalos with masses $\geq 10^9$ in the vicinity of their host's center of mass. However, the general properties of these subhalos, such as their $v_{\rm max}$ and current distances from their respective hosts, are not all representative of the classical MW satellites and were therefore omitted from Prior 2. In the left panel of Fig. C.2, we show the cumulative subhalo abundance function for all host halos in Prior 2 that were selected from the final 5 Illustris-Dark snapshots. These halos host exactly one massive satellite analog and at least one or more low mass satellite analogs (see Sections 4.3.1 and 4.3.1 for definitions).

In Section 2.7, we note that the trend between host halo mass and the distribution of satellite specific orbital angular momenta in the presence and absence of a massive satellite analog differs at host halo masses $< 10^{11.5}\,{\rm M}_\odot$. Below this host halo mass, the median orbital angular momentum is higher when massive satellites are not present. However, inferred MW masses resulting from the ensemble of classical satellites are still in good agreement with each other, independent of this difference. Here, we examine the cumulative subhalo abundance for host halos that do not have a massive satellite analog since 33% of $\sim 10^{12}\,{\rm M}_\odot$ halos typically host an LMC mass companion (Patel et al., 2017a).

To create the abundance functions, all subhalos belonging to host halos in Prior 2, regardless of whether they satisfy our selection criteria in Sections 4.3.1 and 4.3.1, with a subhalo mass $\geq 10^9\,{\rm M}_\odot$ and that reside within their host's virial radius are considered. All included subhalos are not necessarily members of the Prior 2 sample, but this sample encompasses all subhalos above our imposed ~ 133 dark matter particle resolution limit. The abundances are plotted as a function of $\mu \equiv M_{\rm sub}/M_{\rm vir}$, or the ratio between subhalo mass and host virial mass. The error bars on the data points indicate the standard deviations in each μ bin. Host halos

less massive than $10^{11.85}\,M_\odot$ are excluded, as this is beyond the range of MW masses in the literature.

The curves in the left panel of Fig. C.2 all exhibit an increase near $\mu = 10^{-2}$ due to the strict one massive satellite criterion (see Section 4.3.1). This is most obvious in the lowest host halo masses (blue curve) where the massive satellites are a significant fraction of their host's mass. The highest mass host halos ($> 10^{12.5}\,M_\odot$, red line) are expected to host the greatest number of subhalos, but the strict one massive satellite criterion causes this trend to drop off more quickly around $\mu = 10^{-3}$. Notice that at $\mu = 10^{-3}$, all host halos harbor 8-10 subhalos on average. While the results presented in Section 3.4 use halos that have a massive satellite and one or more low mass satellite analogs, the abundance of subhalos around hosts in Prior 2 are generally in agreement with the observed MW satellite population.

In the right panel of Fig. C.2, the cumulative abundance functions are shown for all host halos that do not host a massive satellite analog. Notice there is no longer a peak near $\mu = 10^{-2}$ as the requirement for exactly one massive satellite analog is eliminated. Overall, the shape of the abundance functions changes most significantly at $\mu > 10^{-3}$ and the abundance of subhalos is higher when a massive satellite analog is absent. At $\mu = 10^{-3}$, hosts tend to have 20-40 subhalos, compared to only 8-10 subhalos when massive satellites are present. The exact cause for the higher subhalo abundance in host halos $> 10^{11.85}\,M_\odot$ is unknown and will be explored in future work. While the overall subhalo abundances differ for these host halo samples, the distribution of satellite specific orbital angular momentum for specifically the low mass satellite analogs in each sample generally remains the same and therefore yields similar MW masses.

Cumulative subhalo abundance functions for the Illustris simulations have been presented by Chua et al. (2016), where they have not imposed any selection criteria on their host halos as we have implemented here. Their samples are chosen from the Illustris-1 simulation, which includes baryons and hydrodynamical processes, so the abundance of subhalos with masses $\sim 10^9\,M_\odot$ is immediately lower (see Appendix C.1). Using the sample chosen from Illustris-1, they find equivalent matches for

each Illustris-1 halo in the Illustris-Dark simulation and formulate their cumulative abundances based on those halo populations. Our Fig. C.2 data is chosen directly from the Illustris-Dark simulation and does not suffer these depletion effects, leading to higher subhalo abundances overall.

REFERENCES

al Sufi, A. a.-R. (964). *Kitab suwar al-kawakib al-thabita (Book of the Images of the Fixed Stars)*.

Barber, C., E. Starkenburg, J. F. Navarro, A. W. McConnachie, and A. Fattahi (2014). The orbital ellipticity of satellite galaxies and the mass of the Milky Way. *MNRAS*, **437**, pp. 959–967. doi:10.1093/mnras/stt1959.

Battaglia, G., A. Helmi, H. Morrison, P. Harding, E. W. Olszewski, M. Mateo, K. C. Freeman, J. Norris, and S. A. Shectman (2005). The radial velocity dispersion profile of the Galactic halo: constraining the density profile of the dark halo of the Milky Way. *MNRAS*, **364**, pp. 433–442. doi:10.1111/j.1365-2966.2005.09367.x.

Bechtol, K., A. Drlica-Wagner, E. Balbinot, A. Pieres, J. D. Simon, B. Yanny, B. Santiago, R. H. Wechsler, J. Frieman, A. R. Walker, P. Williams, E. Rozo, E. S. Rykoff, A. Queiroz, E. Luque, A. Benoit-Lévy, D. Tucker, I. Sevilla, R. A. Gruendl, L. N. da Costa, A. Fausti Neto, M. A. G. Maia, T. Abbott, S. Allam, R. Armstrong, A. H. Bauer, G. M. Bernstein, R. A. Bernstein, E. Bertin, D. Brooks, E. Buckley-Geer, D. L. Burke, A. Carnero Rosell, F. J. Castander, R. Covarrubias, C. B. D'Andrea, D. L. DePoy, S. Desai, H. T. Diehl, T. F. Eifler, J. Estrada, A. E. Evrard, E. Fernandez, D. A. Finley, B. Flaugher, E. Gaztanaga, D. Gerdes, L. Girardi, M. Gladders, D. Gruen, G. Gutierrez, J. Hao, K. Honscheid, B. Jain, D. James, S. Kent, R. Kron, K. Kuehn, N. Kuropatkin, O. Lahav, T. S. Li, H. Lin, M. Makler, M. March, J. Marshall, P. Martini, K. W. Merritt, C. Miller, R. Miquel, J. Mohr, E. Neilsen, R. Nichol, B. Nord, R. Ogando, J. Peoples, D. Petravick, A. A. Plazas, A. K. Romer, A. Roodman, M. Sako, E. Sanchez, V. Scarpine, M. Schubnell, R. C. Smith, M. Soares-Santos, F. Sobreira, E. Suchyta, M. E. C. Swanson, G. Tarle, J. Thaler, D. Thomas, W. Wester, J. Zuntz, and DES Collaboration (2015). Eight New Milky Way Companions Discovered in First-year Dark Energy Survey Data. *ApJ*, **807**, 50. doi:10.1088/0004-637X/807/1/50.

Behroozi, P. S., C. Conroy, and R. H. Wechsler (2010). A Comprehensive Analysis of Uncertainties Affecting the Stellar Mass-Halo Mass Relation for $0 < z < 4$. *ApJ*, **717**, pp. 379–403. doi:10.1088/0004-637X/717/1/379.

Behroozi, P. S., R. H. Wechsler, and C. Conroy (2013a). The Average Star Formation Histories of Galaxies in Dark Matter Halos from z = 0-8. *ApJ*, **770**, 57. doi:10.1088/0004-637X/770/1/57.

Behroozi, P. S., R. H. Wechsler, and H.-Y. Wu (2013b). The ROCKSTAR Phase-space Temporal Halo Finder and the Velocity Offsets of Cluster Cores. *ApJ*, **762**, 109. doi:10.1088/0004-637X/762/2/109.

Behroozi, P. S., R. H. Wechsler, H.-Y. Wu, M. T. Busha, A. A. Klypin, and J. R. Primack (2013c). Gravitationally Consistent Halo Catalogs and Merger Trees for Precision Cosmology. *ApJ*, **763**, 18. doi:10.1088/0004-637X/763/1/18.

Belokurov, V., S. E. Koposov, N. W. Evans, J. Peñarrubia, M. J. Irwin, M. C. Smith, G. F. Lewis, M. Gieles, M. I. Wilkinson, G. Gilmore, E. W. Olszewski, and M. Niederste-Ostholt (2014). Precession of the Sagittarius stream. *MNRAS*, **437**, pp. 116–131. doi:10.1093/mnras/stt1862.

Benson, A. J. (2005). Orbital parameters of infalling dark matter substructures. *MNRAS*, **358**, pp. 551–562. doi:10.1111/j.1365-2966.2005.08788.x.

Berentzen, I., E. Athanassoula, C. H. Heller, and K. J. Fricke (2003). Numerical simulations of interacting gas-rich barred galaxies: vertical impact of small companions. *MNRAS*, **341**, pp. 343–360. doi:10.1046/j.1365-8711.2003.06417.x.

Besla, G. (2015). The Orbits and Total Mass of the Magellanic Clouds. *ArXiv e-prints*.

Besla, G., N. Kallivayalil, L. Hernquist, B. Robertson, T. J. Cox, R. P. van der Marel, and C. Alcock (2007). Are the Magellanic Clouds on Their First Passage about the Milky Way? *ApJ*, **668**, pp. 949–967. doi:10.1086/521385.

Besla, G., N. Kallivayalil, L. Hernquist, R. P. van der Marel, T. J. Cox, and D. Kereš (2010). Simulations of the Magellanic Stream in a First Infall Scenario. *The Astrophysical Journal Letters*, **721**(2), p. L97.

Besla, G., N. Kallivayalil, L. Hernquist, R. P. van der Marel, T. J. Cox, and D. Kereš (2012). The role of dwarf galaxy interactions in shaping the Magellanic System and implications for Magellanic Irregulars. *MNRAS*, **421**, pp. 2109–2138. doi: 10.1111/j.1365-2966.2012.20466.x.

Besla, G., D. Martínez-Delgado, R. P. van der Marel, Y. Beletsky, M. Seibert, E. F. Schlafly, E. K. Grebel, and F. Neyer (2016). Low Surface Brightness Imaging of the Magellanic System: Imprints of Tidal Interactions between the Clouds in the Stellar Periphery. *ApJ*, **825**, 20. doi:10.3847/0004-637X/825/1/20.

Binney, J. and S. Tremaine (2008). *Galactic Dynamics: Second Edition*. Princeton University Press.

Binney, J. J. and N. W. Evans (2001). Cuspy dark matter haloes and the Galaxy. *MNRAS*, **327**, pp. L27–L31. doi:10.1046/j.1365-8711.2001.04968.x.

Bland-Hawthorn, J. and O. Gerhard (2016). The Galaxy in Context: Structural, Kinematic, and Integrated Properties. *Annual Review of Astronomy and Astrophysics*, **54**, pp. 529–596. doi:10.1146/annurev-astro-081915-023441.

Bland-Hawthorn, J., R. Sutherland, O. Agertz, and B. Moore (2007). The Source of Ionization along the Magellanic Stream. *ApJL*, **670**, pp. L109–L112. doi:10.1086/524657.

Block, D. L., F. Bournaud, F. Combes, R. Groess, P. Barmby, M. L. N. Ashby, G. G. Fazio, M. A. Pahre, and S. P. Willner (2006). An almost head-on collision as the origin of two off-centre rings in the Andromeda galaxy. *Nature*, **443**, pp. 832–834. doi:10.1038/nature05184.

Bonanos, A. Z., K. Z. Stanek, R. P. Kudritzki, L. M. Macri, D. D. Sasselov, J. Kaluzny, P. B. Stetson, D. Bersier, F. Bresolin, T. Matheson, B. J. Mochejska, N. Przybilla, A. H. Szentgyorgyi, J. Tonry, and G. Torres (2006). The First DIRECT Distance Determination to a Detached Eclipsing Binary in M33. *ApJ*, **652**, pp. 313–322. doi:10.1086/508140.

Bose, S., A. J. Deason, and C. S. Frenk (2018). The Imprint of Cosmic Reionization on the Luminosity Function of Galaxies. *ApJ*, **863**, 123. doi:10.3847/1538-4357/aacbc4.

Bovy, J. (2014). Dynamical Modeling of Tidal Streams. *ApJ*, **795**, 95. doi:10.1088/0004-637X/795/1/95.

Boylan-Kolchin, M., G. Besla, and L. Hernquist (2011a). Dynamics of the Magellanic Clouds in a Lambda cold dark matter universe. *MNRAS*, **414**, pp. 1560–1572. doi:10.1111/j.1365-2966.2011.18495.x.

Boylan-Kolchin, M., J. S. Bullock, and M. Kaplinghat (2011b). Too big to fail? The puzzling darkness of massive Milky Way subhaloes. *MNRAS*, **415**, pp. L40–L44. doi:10.1111/j.1745-3933.2011.01074.x.

Boylan-Kolchin, M., J. S. Bullock, and M. Kaplinghat (2012). The Milky Way's bright satellites as an apparent failure of ΛCDM. *MNRAS*, **422**, pp. 1203–1218. doi:10.1111/j.1365-2966.2012.20695.x.

Boylan-Kolchin, M., J. S. Bullock, S. T. Sohn, G. Besla, and R. P. van der Marel (2013). The Space Motion of Leo I: The Mass of the Milky Way's Dark Matter Halo. *ApJ*, **768**, 140. doi:10.1088/0004-637X/768/2/140.

Boylan-Kolchin, M., V. Springel, S. D. M. White, A. Jenkins, and G. Lemson (2009). Resolving cosmic structure formation with the Millennium-II Simulation. *MNRAS*, **398**, pp. 1150–1164. doi:10.1111/j.1365-2966.2009.15191.x.

Brook, C. B., A. Di Cintio, A. Knebe, S. Gottlöber, Y. Hoffman, G. Yepes, and S. Garrison-Kimmel (2014). The Stellar-to-halo Mass Relation for Local Group Galaxies. *ApJL*, **784**, L14. doi:10.1088/2041-8205/784/1/L14.

Brooks, A. M. and A. Zolotov (2014). Why Baryons Matter: The Kinematics of Dwarf Spheroidal Satellites. *ApJ*, **786**, 87. doi:10.1088/0004-637X/786/2/87.

Brown, W. R., M. J. Geller, S. J. Kenyon, and M. J. Kurtz (2006). Hypervelocity Stars. I. The Spectroscopic Survey. *ApJ*, **647**, pp. 303–311. doi:10.1086/505165.

Brüns, C. and J. Kerp (2004). The Magellanic System in H I. *Astronomische Nachrichten Supplement*, **325**, p. 61.

Brüns, C., J. Kerp, L. Staveley-Smith, U. Mebold, M. E. Putman, R. F. Haynes, P. M. W. Kalberla, E. Muller, and M. D. Filipovic (2005). The Parkes H I Survey of the Magellanic System. *A&A*, **432**, pp. 45–67. doi:10.1051/0004-6361:20040321.

Brunthaler, A., M. J. Reid, H. Falcke, L. J. Greenhill, and C. Henkel (2005). The Geometric Distance and Proper Motion of the Triangulum Galaxy (M33). *Science*, **307**, pp. 1440–1443. doi:10.1126/science.1108342.

Bryan, G. L. and M. L. Norman (1998). Statistical Properties of X-Ray Clusters: Analytic and Numerical Comparisons. *ApJ*, **495**, pp. 80–99. doi:10.1086/305262.

Bullock, J. S. and M. Boylan-Kolchin (2017). Small-Scale Challenges to the ΛCDM Paradigm. *ARA&A*, **55**, pp. 343–387. doi:10.1146/annurev-astro-091916-055313.

Busha, M. T., P. J. Marshall, R. H. Wechsler, A. Klypin, and J. Primack (2011). The Mass Distribution and Assembly of the Milky Way from the Properties of the Magellanic Clouds. *ApJ*, **743**, 40. doi:10.1088/0004-637X/743/1/40.

Callingham, T. M., M. Cautun, A. J. Deason, C. S. Frenk, W. Wang, F. A. Gómez, R. J. J. Grand, F. Marinacci, and R. Pakmor (2019). The mass of the Milky Way from satellite dynamics. *MNRAS*, **484**(4), pp. 5453–5467. doi:10.1093/mnras/stz365.

Carlesi, E., Y. Hoffman, J. G. Sorce, and S. Gottlöber (2017). Constraining the mass of the Local Group. *MNRAS*, **465**, pp. 4886–4894. doi:10.1093/mnras/stw3073.

Carlin, J. L., D. J. Sand, P. Price, B. Willman, A. Karunakaran, K. Spekkens, E. F. Bell, J. P. Brodie, D. Crnojević, D. A. Forbes, J. Hargis, E. Kirby, R. Lupton, A. H. G. Peter, A. J. Romanowsky, and J. Strader (2016). First Results from the MADCASH Survey: A Faint Dwarf Galaxy Companion to the Low-mass Spiral Galaxy NGC 2403 at 3.2 Mpc. *ApJL*, **828**, L5. doi:10.3847/2041-8205/828/1/L5.

Casetti-Dinescu, D. I., T. M. Girard, and M. Schriefer (2018). Proper motion of the Sextans dwarf galaxy from Subaru Suprime-Cam data. *MNRAS*, **473**, pp. 4064–4076. doi:10.1093/mnras/stx2645.

Chandrasekhar, S. (1943). Dynamical Friction. I. General Considerations: the Coefficient of Dynamical Friction. *ApJ*, **97**, p. 255. doi:10.1086/144517.

Chapman, S. C., L. Widrow, M. L. M. Collins, J. Dubinski, R. A. Ibata, M. Rich, A. M. N. Ferguson, M. J. Irwin, G. F. Lewis, N. Martin, A. McConnachie, J. Peñarrubia, and N. Tanvir (2013). Dynamics in the satellite system of Triangulum: is And XXII a dwarf satellite of M33? *MNRAS*, **430**, pp. 37–49. doi:10.1093/mnras/sts392.

Chua, K. T. E., A. Pillepich, V. Rodriguez-Gomez, M. Vogelsberger, S. Bird, and L. Hernquist (2016). Subhalo Demographics in the Illustris Simulation: Effects of Baryons and Halo-to-Halo Variation. *ArXiv e-prints*.

Cockcroft, R., W. E. Harris, A. M. N. Ferguson, A. Huxor, R. Ibata, M. J. Irwin, A. W. McConnachie, K. A. Woodley, S. C. Chapman, G. F. Lewis, and T. H. Puzia (2011). The M33 Globular Cluster System with PAndAS Data: the Last Outer Halo Cluster? *ApJ*, **730**, 112. doi:10.1088/0004-637X/730/2/112.

Connors, T. W., D. Kawata, and B. K. Gibson (2006). N-body simulations of the Magellanic stream. *MNRAS*, **371**, pp. 108–120. doi:10.1111/j.1365-2966.2006.10659.x.

Corbelli, E. (2003). Dark matter and visible baryons in M33. *MNRAS*, **342**, pp. 199–207. doi:10.1046/j.1365-8711.2003.06531.x.

Corbelli, E., S. Lorenzoni, R. Walterbos, R. Braun, and D. Thilker (2010). A wide-field H I mosaic of Messier 31. II. The disk warp, rotation, and the dark matter halo. *A&A*, **511**, A89. doi:10.1051/0004-6361/200913297.

Corbelli, E. and P. Salucci (2000). The extended rotation curve and the dark matter halo of M33. *MNRAS*, **311**, pp. 441–447. doi:10.1046/j.1365-8711.2000.03075.x.

Corbelli, E. and S. E. Schneider (1997). A Warped Disk Model for M33 and the 21 Centimeter Line Width in Spiral Galaxies. *ApJ*, **479**, pp. 244–257. doi:10.1086/303849.

Corbelli, E., D. Thilker, S. Zibetti, C. Giovanardi, and P. Salucci (2014). Dynamical signatures of a ΛCDM-halo and the distribution of the baryons in M 33. *A&A*, **572**, A23. doi:10.1051/0004-6361/201424033.

Courteau, S., M. Cappellari, R. S. de Jong, A. A. Dutton, E. Emsellem, H. Hoekstra, L. V. E. Koopmans, G. A. Mamon, C. Maraston, T. Treu, and L. M. Widrow (2014). Galaxy masses. *Reviews of Modern Physics*, **86**(1), pp. 47–119. doi: 10.1103/RevModPhys.86.47.

Cox, T. J. and A. Loeb (2008). The collision between the Milky Way and Andromeda. *MNRAS*, **386**, pp. 461–474. doi:10.1111/j.1365-2966.2008.13048.x.

Cunningham, E. C., A. J. Deason, R. E. Sanderson, S. T. Sohn, J. Anderson, P. Guhathakurta, C. M. Rockosi, R. P. van der Marel, S. R. Loebman, and A. Wetzel (2018). HALO7D II: The Halo Velocity Ellipsoid and Velocity Anisotropy with Distant Main Sequence Stars. *arXiv e-prints*, arXiv:1810.12201.

Davis, M., G. Efstathiou, C. S. Frenk, and S. D. M. White (1985). The evolution of large-scale structure in a universe dominated by cold dark matter. *ApJ*, **292**, pp. 371–394. doi:10.1086/163168.

Deason, A., A. Wetzel, and S. Garrison-Kimmel (2014). Satellite Dwarf Galaxies in a Hierarchical Universe: The Prevalence of Dwarf-Dwarf Major Mergers. *ApJ*, **794**, 115. doi:10.1088/0004-637X/794/2/115.

Deason, A. J., C. Conroy, A. R. Wetzel, and J. L. Tinker (2013). Stellar Mass-gap as a Probe of Halo Assembly History and Concentration: Youth Hidden among Old Fossils. *ApJ*, **777**, 154. doi:10.1088/0004-637X/777/2/154.

Deason, A. J., A. R. Wetzel, S. Garrison-Kimmel, and V. Belokurov (2015). Satellites of LMC-mass dwarfs: close friendships ruined by Milky Way mass haloes. *MNRAS*, **453**, pp. 3568–3574. doi:10.1093/mnras/stv1939.

Debattista, V. P. and J. A. Sellwood (1999). Warped Galaxies from Misaligned Angular Momenta. *ApJL*, **513**, pp. L107–L110. doi:10.1086/311913.

Dehnen, W. and J. Binney (1998). Mass models of the Milky Way. *MNRAS*, **294**, p. 429. doi:10.1046/j.1365-8711.1998.01282.x.

Dehnen, W., D. E. McLaughlin, and J. Sachania (2006). The velocity dispersion and mass profile of the Milky Way. *MNRAS*, **369**, pp. 1688–1692. doi:10.1111/j.1365-2966.2006.10404.x.

Diaz, J. and K. Bekki (2011). Constraining the orbital history of the Magellanic Clouds: a new bound scenario suggested by the tidal origin of the Magellanic Stream. *MNRAS*, **413**, pp. 2015–2020. doi:10.1111/j.1365-2966.2011.18289.x.

Diaz, J. D. and K. Bekki (2012). The Tidal Origin of the Magellanic Stream and the Possibility of a Stellar Counterpart. *ApJ*, **750**, 36. doi:10.1088/0004-637X/750/1/36.

Dierickx, M. I. P. and A. Loeb (2017a). Predicted Extension of the Sagittarius Stream to the Milky Way Virial Radius. *ApJ*, **836**, 92. doi:10.3847/1538-4357/836/1/92.

Dierickx, M. I. P. and A. Loeb (2017b). Upper Limit on the Milky Way Mass from the Orbit of the Sagittarius Dwarf Satellite. *ArXiv e-prints*.

Dinescu, D. I., W. F. van Altena, T. M. Girard, and C. E. López (1999). Space Velocities of Southern Globular Clusters. II. New Results for 10 Clusters. *AJ*, **117**(1), pp. 277–285. doi:10.1086/300699.

Dobbs, C. L., A. R. Pettitt, E. Corbelli, and J. E. Pringle (2018). Simulations of the flocculent spiral M33: what drives the spiral structure? *ArXiv e-prints*.

Dolag, K., S. Borgani, G. Murante, and V. Springel (2009). Substructures in hydrodynamical cluster simulations. *MNRAS*, **399**, pp. 497–514. doi:10.1111/j.1365-2966.2009.15034.x.

D'Onghia, E. and G. Lake (2008). Small Dwarf Galaxies within Larger Dwarfs: Why Some Are Luminous while Most Go Dark. *ApJ*, **686**, p. L61. doi:10.1086/592995.

D'Onghia, E., V. Springel, L. Hernquist, and D. Keres (2010). Substructure Depletion in the Milky Way Halo by the Disk. *ApJ*, **709**, pp. 1138–1147. doi:10.1088/0004-637X/709/2/1138.

Dooley, G. A., A. H. G. Peter, J. L. Carlin, A. Frebel, K. Bechtol, and B. Willman (2017a). The predicted luminous satellite populations around SMC- and LMC-mass galaxies - a missing satellite problem around the LMC? *MNRAS*, **472**, pp. 1060–1073. doi:10.1093/mnras/stx2001.

Dooley, G. A., A. H. G. Peter, T. Yang, B. Willman, B. F. Griffen, and A. Frebel (2017b). An observer's guide to the (Local Group) dwarf galaxies: predictions for their own dwarf satellite populations. *MNRAS*, **471**, pp. 4894–4909. doi:10.1093/mnras/stx1900.

Drlica-Wagner, A., K. Bechtol, S. Allam, D. L. Tucker, R. A. Gruendl, M. D. Johnson, A. R. Walker, D. J. James, D. L. Nidever, K. A. G. Olsen, R. H. Wechsler, M. R. L. Cioni, B. C. Conn, K. Kuehn, T. S. Li, Y.-Y. Mao, N. F. Martin, E. Neilsen, N. E. D. Noel, A. Pieres, J. D. Simon, G. S. Stringfellow, R. P. van der Marel, and B. Yanny (2016). An Ultra-faint Galaxy Candidate Discovered in Early Data from the Magellanic Satellites Survey. *ApJL*, **833**, L5. doi:10.3847/2041-8205/833/1/L5.

Drlica-Wagner, A., K. Bechtol, E. S. Rykoff, E. Luque, A. Queiroz, Y.-Y. Mao, R. H. Wechsler, J. D. Simon, B. Santiago, B. Yanny, E. Balbinot, S. Dodelson,

A. Fausti Neto, D. J. James, T. S. Li, M. A. G. Maia, J. L. Marshall, A. Pieres, K. Stringer, A. R. Walker, T. M. C. Abbott, F. B. Abdalla, S. Allam, A. Benoit-Lévy, G. M. Bernstein, E. Bertin, D. Brooks, E. Buckley-Geer, D. L. Burke, A. Carnero Rosell, M. Carrasco Kind, J. Carretero, M. Crocce, L. N. da Costa, S. Desai, H. T. Diehl, J. P. Dietrich, P. Doel, T. F. Eifler, A. E. Evrard, D. A. Finley, B. Flaugher, P. Fosalba, J. Frieman, E. Gaztanaga, D. W. Gerdes, D. Gruen, R. A. Gruendl, G. Gutierrez, K. Honscheid, K. Kuehn, N. Kuropatkin, O. Lahav, P. Martini, R. Miquel, B. Nord, R. Ogando, A. A. Plazas, K. Reil, A. Roodman, M. Sako, E. Sanchez, V. Scarpine, M. Schubnell, I. Sevilla-Noarbe, R. C. Smith, M. Soares-Santos, F. Sobreira, E. Suchyta, M. E. C. Swanson, G. Tarle, D. Tucker, V. Vikram, W. Wester, Y. Zhang, J. Zuntz, and DES Collaboration (2015). Eight Ultra-faint Galaxy Candidates Discovered in Year Two of the Dark Energy Survey. *ApJ*, **813**, 109. doi:10.1088/0004-637X/813/2/109.

D'Souza, R. and E. F. Bell (2018). The Andromeda galaxy's most important merger about 2 billion years ago as M32's likely progenitor. *Nature Astronomy*, **2**, pp. 737–743. doi:10.1038/s41550-018-0533-x.

Eadie, G. M., A. Springford, and W. E. Harris (2017). Bayesian Mass Estimates of the Milky Way: Including Measurement Uncertainties with Hierarchical Bayes. *ApJ*, **835**, 167. doi:10.3847/1538-4357/835/2/167.

Evans, N. W., M. I. Wilkinson, P. Guhathakurta, E. K. Grebel, and S. S. Vogt (2000). Dynamical Mass Estimates for the Halo of M31 from Keck Spectroscopy. *ApJL*, **540**, pp. L9–L12. doi:10.1086/312861.

Fardal, M., P. Guhathakurta, K. Gilbert, A. Babul, C. Dodge, M. D. Weinberg, and Y. Lu (2009). M31's Giant Southern Stream: Constraints on the Progenitor's Mass Phase, and Rotation. In Jogee, S., I. Marinova, L. Hao, and G. A. Blanc (eds.) *Galaxy Evolution: Emerging Insights and Future Challenges*, volume 419 of *Astronomical Society of the Pacific Conference Series*, p. 118.

Fardal, M. A., A. Babul, J. J. Geehan, and P. Guhathakurta (2006). Investigating the Andromeda stream - II. Orbital fits and properties of the progenitor. *MNRAS*, **366**, pp. 1012–1028. doi:10.1111/j.1365-2966.2005.09864.x.

Fardal, M. A., M. D. Weinberg, A. Babul, M. J. Irwin, P. Guhathakurta, K. M. Gilbert, A. M. N. Ferguson, R. A. Ibata, G. F. Lewis, N. R. Tanvir, and A. P. Huxor (2013). Inferring the Andromeda Galaxy's mass from its giant southern stream with Bayesian simulation sampling. *MNRAS*, **434**, pp. 2779–2802. doi:10.1093/mnras/stt1121.

Ferguson, A. M. N. and A. D. Mackey (2016). Substructure and Tidal Streams in the Andromeda Galaxy and its Satellites. In Newberg, H. J. and J. L. Carlin

(eds.) *Tidal Streams in the Local Group and Beyond*, volume 420 of *Astrophysics and Space Science Library*, p. 191. doi:10.1007/978-3-319-19336-6_8.

Fich, M. and S. Tremaine (1991). The mass of the Galaxy. *ARA&A*, **29**, pp. 409–445. doi:10.1146/annurev.aa.29.090191.002205.

Font, A. S., K. V. Johnston, P. Guhathakurta, S. R. Majewski, and R. M. Rich (2006). Dynamics and Stellar Content of the Giant Southern Stream in M31. II. Interpretation. *AJ*, **131**, pp. 1436–1444. doi:10.1086/499564.

Forero-Romero, J. E., Y. Hoffman, S. Bustamante, S. Gottlöber, and G. Yepes (2013). The Kinematics of the Local Group in a Cosmological Context. *ApJL*, **767**, L5. doi:10.1088/2041-8205/767/1/L5.

Fritz, T. K., G. Battaglia, M. S. Pawlowski, N. Kallivayalil, R. van der Marel, S. T. Sohn, C. Brook, and G. Besla (2018). Gaia DR2 proper motions of dwarf galaxies within 420 kpc. Orbits, Milky Way mass, tidal influences, planar alignments, and group infall. *A&A*, **619**, A103. doi:10.1051/0004-6361/201833343.

Fritz, T. K., S. T. Linden, P. Zivick, N. Kallivayalil, R. L. Beaton, J. Bovy, L. V. Sales, T. Sohn, D. Angell, M. Boylan-Kolchin, E. R. Carrasco, G. Damke, R. Davies, S. Majewski, B. Neichel, and R. van der Marel (2017). The Proper Motion of Pyxis: The First Use of Adaptive Optics in Tandem with HST on a Faint Halo Object. *ApJ*, **840**(1), 30. doi:10.3847/1538-4357/aa6b5a.

Fukugita, M., C. J. Hogan, and P. J. E. Peebles (1998). The Cosmic Baryon Budget. *ApJ*, **503**, pp. 518–530. doi:10.1086/306025.

Gaia Collaboration, A. G. A. Brown, A. Vallenari, T. Prusti, J. H. J. de Bruijne, C. Babusiaux, C. A. L. Bailer-Jones, M. Biermann, D. W. Evans, L. Eyer, F. Jansen, C. Jordi, S. A. Klioner, U. Lammers, L. Lindegren, X. Luri, F. Mignard, C. Panem, D. Pourbaix, S. Randich, P. Sartoretti, H. I. Siddiqui, C. Soubiran, F. van Leeuwen, N. A. Walton, F. Arenou, U. Bastian, M. Cropper, R. Drimmel, D. Katz, M. G. Lattanzi, J. Bakker, C. Cacciari, J. Castañeda, L. Chaoul, N. Cheek, F. De Angeli, C. Fabricius, R. Guerra, B. Holl, E. Masana, R. Messineo, N. Mowlavi, K. Nienartowicz, P. Panuzzo, J. Portell, M. Riello, G. M. Seabroke, P. Tanga, F. Thévenin, G. Gracia-Abril, G. Comoretto, M. Garcia-Reinaldos, D. Teyssier, M. Altmann, R. Andrae, M. Audard, I. Bellas-Velidis, K. Benson, J. Berthier, R. Blomme, P. Burgess, G. Busso, B. Carry, A. Cellino, G. Clementini, M. Clotet, O. Creevey, M. Davidson, J. De Ridder, L. Delchambre, A. Dell'Oro, C. Ducourant, J. Fernández-Hernández, M. Fouesneau, Y. Frémat, L. Galluccio, M. García-Torres, J. González-Núñez, J. J. González-Vidal, E. Gosset, L. P. Guy, J. L. Halbwachs, N. C. Hambly, D. L. Harrison, J. Hernández, D. Hestroffer, S. T. Hodgkin, A. Hutton, G. Jasniewicz, A. Jean-Antoine-Piccolo, S. Jordan, A. J.

Korn, A. Krone-Martins, A. C. Lanzafame, T. Lebzelter, W. Löffler, M. Manteiga, P. M. Marrese, J. M. Martín-Fleitas, A. Moitinho, A. Mora, K. Muinonen, J. Osinde, E. Pancino, T. Pauwels, J. M. Petit, A. Recio-Blanco, P. J. Richards, L. Rimoldini, A. C. Robin, L. M. Sarro, C. Siopis, M. Smith, A. Sozzetti, M. Süveges, J. Torra, W. van Reeven, U. Abbas, A. Abreu Aramburu, S. Accart, C. Aerts, G. Altavilla, M. A. Álvarez, R. Alvarez, J. Alves, R. I. Anderson, A. H. Andrei, E. Anglada Varela, E. Antiche, T. Antoja, B. Arcay, T. L. Astraatmadja, N. Bach, S. G. Baker, L. Balaguer-Núñez, P. Balm, C. Barache, C. Barata, D. Barbato, F. Barblan, P. S. Barklem, D. Barrado, M. Barros, M. A. Barstow, S. Bartholomé Muñoz, J. L. Bassilana, U. Becciani, M. Bellazzini, A. Berihuete, S. Bertone, L. Bianchi, O. Bienaymé, S. Blanco-Cuaresma, T. Boch, C. Boeche, A. Bombrun, R. Borrachero, D. Bossini, S. Bouquillon, G. Bourda, A. Bragaglia, L. Bramante, M. A. Breddels, A. Bressan, N. Brouillet, T. Brüsemeister, E. Brugaletta, B. Bucciarelli, A. Burlacu, D. Busonero, A. G. Butkevich, R. Buzzi, E. Caffau, R. Cancelliere, G. Cannizzaro, T. Cantat-Gaudin, R. Carballo, T. Carlucci, J. M. Carrasco, L. Casamiquela, M. Castellani, A. Castro-Ginard, P. Charlot, L. Chemin, A. Chiavassa, G. Cocozza, G. Costigan, S. Cowell, F. Crifo, M. Crosta, C. Crowley, J. Cuypers, C. Dafonte, Y. Damerdji, A. Dapergolas, P. David, M. David, P. de Laverny, F. De Luise, R. De March, D. de Martino, R. de Souza, A. de Torres, J. Debosscher, E. del Pozo, M. Delbo, A. Delgado, H. E. Delgado, P. Di Matteo, S. Diakite, C. Diener, E. Distefano, C. Dolding, P. Drazinos, J. Durán, B. Edvardsson, H. Enke, K. Eriksson, P. Esquej, G. Eynard Bontemps, C. Fabre, M. Fabrizio, S. Faigler, A. J. Falcão, M. Farràs Casas, L. Federici, G. Fedorets, P. Fernique, F. Figueras, F. Filippi, K. Findeisen, A. Fonti, E. Fraile, M. Fraser, B. Frézouls, M. Gai, S. Galleti, D. Garabato, F. García-Sedano, A. Garofalo, N. Garralda, A. Gavel, P. Gavras, J. Gerssen, R. Geyer, P. Giacobbe, G. Gilmore, S. Girona, G. Giuffrida, F. Glass, M. Gomes, M. Granvik, A. Gueguen, A. Guerrier, J. Guiraud, R. Gutiérrez-Sánchez, R. Haigron, D. Hatzidimitriou, M. Hauser, M. Haywood, U. Heiter, A. Helmi, J. Heu, T. Hilger, D. Hobbs, W. Hofmann, G. Holland, H. E. Huckle, A. Hypki, V. Icardi, K. Janßen, G. Jevardat de Fombelle, P. G. Jonker, Á. L. Juhász, F. Julbe, A. Karampelas, A. Kewley, J. Klar, A. Kochoska, R. Kohley, K. Kolenberg, M. Kontizas, E. Kontizas, S. E. Koposov, G. Kordopatis, Z. Kostrzewa-Rutkowska, P. Koubsky, S. Lambert, A. F. Lanza, Y. Lasne, J. B. Lavigne, Y. Le Fustec, C. Le Poncin-Lafitte, Y. Lebreton, S. Leccia, N. Leclerc, I. Lecoeur-Taibi, H. Lenhardt, F. Leroux, S. Liao, E. Licata, H. E. P. Lindstrøm, T. A. Lister, E. Livanou, A. Lobel, M. López, S. Managau, R. G. Mann, G. Mantelet, O. Marchal, J. M. Marchant, M. Marconi, S. Marinoni, G. Marschalkó, D. J. Marshall, M. Martino, G. Marton, N. Mary, D. Massari, G. Matijevič, T. Mazeh, P. J. McMillan, S. Messina, D. Michalik, N. R. Millar, D. Molina, R. Molinaro, L. Molnár, P. Montegriffo, R. Mor, R. Morbidelli, T. Morel, D. Morris, A. F. Mulone, T. Muraveva, I. Musella, G. Nelemans, L. Nicastro, L. Noval, W. O'Mullane,

C. Ordénovic, D. Ordóñez-Blanco, P. Osborne, C. Pagani, I. Pagano, F. Pailler, H. Palacin, L. Palaversa, A. Panahi, M. Pawlak, A. M. Piersimoni, F. X. Pineau, E. Plachy, G. Plum, E. Poggio, E. Poujoulet, A. Prša, L. Pulone, E. Racero, S. Ragaini, N. Rambaux, M. Ramos-Lerate, S. Regibo, C. Reylé, F. Riclet, V. Ripepi, A. Riva, A. Rivard, G. Rixon, T. Roegiers, M. Roelens, M. Romero-Gómez, N. Rowell, F. Royer, L. Ruiz-Dern, G. Sadowski, T. Sagristà Sellés, J. Sahlmann, J. Salgado, E. Salguero, N. Sanna, T. Santana-Ros, M. Sarasso, H. Savietto, M. Schultheis, E. Sciacca, M. Segol, J. C. Segovia, D. Ségransan, I. C. Shih, L. Siltala, A. F. Silva, R. L. Smart, K. W. Smith, E. Solano, F. Solitro, R. Sordo, S. Soria Nieto, J. Souchay, A. Spagna, F. Spoto, U. Stampa, I. A. Steele, H. Steidelmüller, C. A. Stephenson, H. Stoev, F. F. Suess, J. Surdej, L. Szabados, E. Szegedi-Elek, D. Tapiador, F. Taris, G. Tauran, M. B. Taylor, R. Teixeira, D. Terrett, P. Teyssand ier, W. Thuillot, A. Titarenko, F. Torra Clotet, C. Turon, A. Ulla, E. Utrilla, S. Uzzi, M. Vaillant, G. Valentini, V. Valette, A. van Elteren, E. Van Hemelryck, M. van Leeuwen, M. Vaschetto, A. Vecchiato, J. Veljanoski, Y. Viala, D. Vicente, S. Vogt, C. von Essen, H. Voss, V. Votruba, S. Voutsinas, G. Walmsley, M. Weiler, O. Wertz, T. Wevers, Ł. Wyrzykowski, A. Yoldas, M. Žerjal, H. Ziaeepour, J. Zorec, S. Zschocke, S. Zucker, C. Zurbach, and T. Zwitter (2018a). Gaia Data Release 2. Summary of the contents and survey properties. *A&A*, **616**, A1. doi:10.1051/0004-6361/201833051.

Gaia Collaboration, A. G. A. Brown, A. Vallenari, T. Prusti, J. H. J. de Bruijne, F. Mignard, R. Drimmel, C. Babusiaux, C. A. L. Bailer-Jones, U. Bastian, M. Biermann, D. W. Evans, L. Eyer, F. Jansen, C. Jordi, D. Katz, S. A. Klioner, U. Lammers, L. Lindegren, X. Luri, W. O'Mullane, C. Panem, D. Pourbaix, S. Randich, P. Sartoretti, H. I. Siddiqui, C. Soubiran, V. Valette, F. van Leeuwen, N. A. Walton, C. Aerts, F. Arenou, M. Cropper, E. Høg, M. G. Lattanzi, E. K. Grebel, A. D. Holland, C. Huc, X. Passot, M. Perryman, L. Bramante, C. Cacciari, J. Castañeda, L. Chaoul, N. Cheek, F. De Angeli, C. Fabricius, R. Guerra, J. Hernández, A. Jean-Antoine-Piccolo, E. Masana, R. Messineo, N. Mowlavi, K. Nienartowicz, D. Ordóñez-Blanco, P. Panuzzo, J. Portell, P. J. Richards, M. Riello, G. M. Seabroke, P. Tanga, F. Thévenin, J. Torra, S. G. Els, G. Gracia-Abril, G. Comoretto, M. Garcia-Reinaldos, T. Lock, E. Mercier, M. Altmann, R. Andrae, T. L. Astraatmadja, I. Bellas-Velidis, K. Benson, J. Berthier, R. Blomme, G. Busso, B. Carry, A. Cellino, G. Clementini, S. Cowell, O. Creevey, J. Cuypers, M. Davidson, J. De Ridder, A. de Torres, L. Delchambre, A. Dell'Oro, C. Ducourant, Y. Frémat, M. García-Torres, E. Gosset, J. L. Halbwachs, N. C. Hambly, D. L. Harrison, M. Hauser, D. Hestroffer, S. T. Hodgkin, H. E. Huckle, A. Hutton, G. Jasniewicz, S. Jordan, M. Kontizas, A. J. Korn, A. C. Lanzafame, M. Manteiga, A. Moitinho, K. Muinonen, J. Osinde, E. Pancino, T. Pauwels, J. M. Petit, A. Recio-Blanco, A. C. Robin, L. M. Sarro, C. Siopis, M. Smith, K. W. Smith, A. Sozzetti, W. Thuillot, W. van Reeven, Y. Viala, U. Abbas, A. Abreu

Aramburu, S. Accart, J. J. Aguado, P. M. Allan, W. Allasia, G. Altavilla, M. A. Álvarez, J. Alves, R. I. Anderson, A. H. Andrei, E. Anglada Varela, E. Antiche, T. Antoja, S. Antón, B. Arcay, N. Bach, S. G. Baker, L. Balaguer-Núñez, C. Barache, C. Barata, A. Barbier, F. Barblan, D. Barrado y Navascués, M. Barros, M. A. Barstow, U. Becciani, M. Bellazzini, A. Bello García, V. Belokurov, P. Bendjoya, A. Berihuete, L. Bianchi, O. Bienaymé, F. Billebaud, N. Blagorodnova, S. Blanco-Cuaresma, T. Boch, A. Bombrun, R. Borrachero, S. Bouquillon, G. Bourda, H. Bouy, A. Bragaglia, M. A. Breddels, N. Brouillet, T. Brüsemeister, B. Bucciarelli, P. Burgess, R. Burgon, A. Burlacu, D. Busonero, R. Buzzi, E. Caffau, J. Cambras, H. Campbell, R. Cancelliere, T. Cantat-Gaudin, T. Carlucci, J. M. Carrasco, M. Castellani, P. Charlot, J. Charnas, A. Chiavassa, M. Clotet, G. Cocozza, R. S. Collins, G. Costigan, F. Crifo, N. J. G. Cross, M. Crosta, C. Crowley, C. Dafonte, Y. Damerdji, A. Dapergolas, P. David, M. David, P. De Cat, F. de Felice, P. de Laverny, F. De Luise, R. De March, D. de Martino, R. de Souza, J. Debosscher, E. del Pozo, M. Delbo, A. Delgado, H. E. Delgado, P. Di Matteo, S. Diakite, E. Distefano, C. Dolding, S. Dos Anjos, P. Drazinos, J. Duran, Y. Dzigan, B. Edvardsson, H. Enke, N. W. Evans, G. Eynard Bontemps, C. Fabre, M. Fabrizio, S. Faigler, A. J. Falcão, M. Farràs Casas, L. Federici, G. Fedorets, J. Fernández-Hernández, P. Fernique, A. Fienga, F. Figueras, F. Filippi, K. Findeisen, A. Fonti, M. Fouesneau, E. Fraile, M. Fraser, J. Fuchs, M. Gai, S. Galleti, L. Galluccio, D. Garabato, F. García-Sedano, A. Garofalo, N. Garralda, P. Gavras, J. Gerssen, R. Geyer, G. Gilmore, S. Girona, G. Giuffrida, M. Gomes, A. González-Marcos, J. González-Núñez, J. J. González-Vidal, M. Granvik, A. Guerrier, P. Guillout, J. Guiraud, A. Gúrpide, R. Gutiérrez-Sánchez, L. P. Guy, R. Haigron, D. Hatzidimitriou, M. Haywood, U. Heiter, A. Helmi, D. Hobbs, W. Hofmann, B. Holl, G. Holland , J. A. S. Hunt, A. Hypki, V. Icardi, M. Irwin, G. Jevardat de Fombelle, P. Jofré, P. G. Jonker, A. Jorissen, F. Julbe, A. Karampelas, A. Kochoska, R. Kohley, K. Kolenberg, E. Kontizas, S. E. Koposov, G. Kordopatis, P. Koubsky, A. Krone-Martins, M. Kudryashova, I. Kull, R. K. Bachchan, F. Lacoste-Seris, A. F. Lanza, J. B. Lavigne, C. Le Poncin-Lafitte, Y. Lebreton, T. Lebzelter, S. Leccia, N. Leclerc, I. Lecoeur-Taibi, V. Lemaitre, H. Lenhardt, F. Leroux, S. Liao, E. Licata, H. E. P. Lindstrøm, T. A. Lister, E. Livanou, A. Lobel, W. Löffler, M. López, D. Lorenz, I. MacDonald, T. Magalhães Fernandes, S. Managau, R. G. Mann, G. Mantelet, O. Marchal, J. M. Marchant, M. Marconi, S. Marinoni, P. M. Marrese, G. Marschalkó, D. J. Marshall, J. M. Martín-Fleitas, M. Martino, N. Mary, G. Matijevič, T. Mazeh, P. J. McMillan, S. Messina, D. Michalik, N. R. Millar, B. M. H. Mirand a, D. Molina, R. Molinaro, M. Molinaro, L. Molnár, M. Moniez, P. Montegriffo, R. Mor, A. Mora, R. Morbidelli, T. Morel, S. Morgenthaler, D. Morris, A. F. Mulone, T. Muraveva, I. Musella, J. Narbonne, G. Nelemans, L. Nicastro, L. Noval, C. Ordénovic, J. Ordieres-Meré, P. Osborne, C. Pagani, I. Pagano, F. Pailler, H. Palacin, L. Palaversa, P. Parsons, M. Pecoraro, R. Pedrosa, H. Pentikäinen,

B. Pichon, A. M. Piersimoni, F. X. Pineau, E. Plachy, G. Plum, E. Poujoulet, A. Prša, L. Pulone, S. Ragaini, S. Rago, N. Rambaux, M. Ramos-Lerate, P. Ranalli, G. Rauw, A. Read, S. Regibo, C. Reylé, R. A. Ribeiro, L. Rimoldini, V. Ripepi, A. Riva, G. Rixon, M. Roelens, M. Romero-Gómez, N. Rowell, F. Royer, L. Ruiz-Dern, G. Sadowski, T. Sagristà Sellés, J. Sahlmann, J. Salgado, E. Salguero, M. Sarasso, H. Savietto, M. Schultheis, E. Sciacca, M. Segol, J. C. Segovia, D. Segransan, I. C. Shih, R. Smareglia, R. L. Smart, E. Solano, F. Solitro, R. Sordo, S. Soria Nieto, J. Souchay, A. Spagna, F. Spoto, U. Stampa, I. A. Steele, H. Steidelmüller, C. A. Stephenson, H. Stoev, F. F. Suess, M. Süveges, J. Surdej, L. Szabados, E. Szegedi-Elek, D. Tapiador, F. Taris, G. Tauran, M. B. Taylor, R. Teixeira, D. Terrett, B. Tingley, S. C. Trager, C. Turon, A. Ulla, E. Utrilla, G. Valentini, A. van Elteren, E. Van Hemelryck, M. van Leeuwen, M. Varadi, A. Vecchiato, J. Veljanoski, T. Via, D. Vicente, S. Vogt, H. Voss, V. Votruba, S. Voutsinas, G. Walmsley, M. Weiler, K. Weingrill, T. Wevers, Ł. Wyrzykowski, A. Yoldas, M. Žerjal, S. Zucker, C. Zurbach, T. Zwitter, A. Alecu, M. Allen, C. Allende Prieto, A. Amorim, G. Anglada-Escudé, V. Arsenijevic, S. Azaz, P. Balm, M. Beck, H. H. Bernstein, L. Bigot, A. Bijaoui, C. Blasco, M. Bonfigli, G. Bono, S. Boudreault, A. Bressan, S. Brown, P. M. Brunet, P. Bunclark, R. Buonanno, A. G. Butkevich, C. Carret, C. Carrion, L. Chemin, F. Chéreau, L. Corcione, E. Darmigny, K. S. de Boer, P. de Teodoro, P. T. de Zeeuw, C. Delle Luche, C. D. Domingues, P. Dubath, F. Fodor, B. Frézouls, A. Fries, D. Fustes, D. Fyfe, E. Gallardo, J. Gallegos, D. Gardiol, M. Gebran, A. Gomboc, A. Gómez, E. Grux, A. Gueguen, A. Heyrovsky, J. Hoar, G. Iannicola, Y. Isasi Parache, A. M. Janotto, E. Joliet, A. Jonckheere, R. Keil, D. W. Kim, P. Klagyivik, J. Klar, J. Knude, O. Kochukhov, I. Kolka, J. Kos, A. Kutka, V. Lainey, D. LeBouquin, C. Liu, D. Loreggia, V. V. Makarov, M. G. Marseille, C. Martayan, O. Martinez-Rubi, B. Massart, F. Meynadier, S. Mignot, U. Munari, A. T. Nguyen, T. Nordlander, P. Ocvirk, K. S. O'Flaherty, A. Olias Sanz, P. Ortiz, J. Osorio, D. Oszkiewicz, A. Ouzounis, M. Palmer, P. Park, E. Pasquato, C. Peltzer, J. Peralta, F. Péturaud, T. Pieniluoma, E. Pigozzi, J. Poels, G. Prat, T. Prod'homme, F. Raison, J. M. Rebordao, D. Risquez, B. Rocca-Volmerange, S. Rosen, M. I. Ruiz-Fuertes, F. Russo, S. Sembay, I. Serraller Vizcaino, A. Short, A. Siebert, H. Silva, D. Sinachopoulos, E. Slezak, M. Soffel, D. Sosnowska, V. Straižys, M. ter Linden, D. Terrell, S. Theil, C. Tiede, L. Troisi, P. Tsalmantza, D. Tur, M. Vaccari, F. Vachier, P. Valles, W. Van Hamme, L. Veltz, J. Virtanen, J. M. Wallut, R. Wichmann, M. I. Wilkinson, H. Ziaeepour, and S. Zschocke (2016). Gaia Data Release 1. Summary of the astrometric, photometric, and survey properties. *A&A*, **595**, A2. doi:10.1051/0004-6361/201629512.

Gaia Collaboration, A. Helmi, F. van Leeuwen, P. J. McMillan, D. Massari, T. Antoja, A. C. Robin, L. Lindegren, U. Bastian, F. Arenou, and et al. (2018b). Gaia Data Release 2. Kinematics of globular clusters and dwarf galaxies around the

Milky Way. *A&A*, **616**, A12. doi:10.1051/0004-6361/201832698.

Gaia Collaboration, D. Katz, T. Antoja, M. Romero-Gómez, R. Drimmel, C. Reylé, G. M. Seabroke, C. Soubiran, C. Babusiaux, P. Di Matteo, and et al. (2018c). Gaia Data Release 2. Mapping the Milky Way disc kinematics. *A&A*, **616**, A11. doi:10.1051/0004-6361/201832865.

Gao, L. and S. D. M. White (2007). Assembly bias in the clustering of dark matter haloes. *MNRAS*, **377**, pp. L5–L9. doi:10.1111/j.1745-3933.2007.00292.x.

Gao, L., S. D. M. White, A. Jenkins, F. Stoehr, and V. Springel (2004). The subhalo populations of ΛCDM dark haloes. *MNRAS*, **355**, pp. 819–834. doi:10.1111/j.1365-2966.2004.08360.x.

Garavito-Camargo, N., G. Besla, C. F. P. Laporte, K. V. Johnston, F. A. Gómez, and L. L. Watkins (2019). Hunting for the Dark Matter Wake Induced by the Large Magellanic Cloud. *arXiv e-prints*, arXiv:1902.05089.

Gardiner, L. T. and M. Noguchi (1996). N-body simulations of the Small Magellanic Cloud and the Magellanic Stream. *MNRAS*, **278**, pp. 191–208. doi:10.1093/mnras/278.1.191.

Garrison-Kimmel, S., M. Boylan-Kolchin, J. S. Bullock, and K. Lee (2014). ELVIS: Exploring the Local Volume in Simulations. *MNRAS*, **438**, pp. 2578–2596. doi:10.1093/mnras/stt2377.

Garrison-Kimmel, S., J. S. Bullock, M. Boylan-Kolchin, and E. Bardwell (2017a). Organized chaos: scatter in the relation between stellar mass and halo mass in small galaxies. *MNRAS*, **464**, pp. 3108–3120. doi:10.1093/mnras/stw2564.

Garrison-Kimmel, S., A. Wetzel, J. S. Bullock, P. F. Hopkins, M. Boylan-Kolchin, C.-A. Faucher-Giguère, D. Kereš, E. Quataert, R. E. Sanderson, A. S. Graus, and T. Kelley (2017b). Not so lumpy after all: modelling the depletion of dark matter subhaloes by Milky Way-like galaxies. *MNRAS*, **471**, pp. 1709–1727. doi:10.1093/mnras/stx1710.

Garrison-Kimmel, S., A. R. Wetzel, J. S. Bullock, P. F. Hopkins, M. Boylan-Kolchin, C.-A. Faucher-Giguere, D. Keres, E. Quataert, R. E. Sanderson, A. S. Graus, and T. Kelley (2017c). Not so lumpy after all: modeling the depletion of dark matter subhalos by Milky Way-like galaxies. *ArXiv e-prints*.

Geha, M., R. H. Wechsler, Y.-Y. Mao, E. J. Tollerud, B. Weiner, R. Bernstein, B. Hoyle, S. Marchi, P. J. Marshall, R. Munoz, and Y. Lu (2017). The SAGA Survey: I. Satellite Galaxy Populations Around Eight Milky Way Analogs. *ArXiv e-prints*.

Genel, S., M. Vogelsberger, V. Springel, D. Sijacki, D. Nelson, G. Snyder, V. Rodriguez-Gomez, P. Torrey, and L. Hernquist (2014). Introducing the Illustris project: the evolution of galaxy populations across cosmic time. *MNRAS*, **445**, pp. 175–200. doi:10.1093/mnras/stu1654.

Gibbons, S. L. J., V. Belokurov, and N. W. Evans (2014). 'Skinny Milky Way please', says Sagittarius. *MNRAS*, **445**, pp. 3788–3802. doi:10.1093/mnras/stu1986.

Gilbert, K. M., E. J. Tollerud, J. Anderson, R. L. Beaton, E. F. Bell, A. Brooks, T. M. Brown, J. Bullock, J. L. Carlin, M. Collins, A. Cooper, D. Crnojevic, J. Dalcanton, A. del Pino, R. D'Souza, I. Escala, M. Fardal, A. Font, M. Geha, P. Guhathakurta, E. Kirby, G. F. Lewis, J. L. Marshall, N. F. Martin, K. McQuinn, A. Monachesi, E. Patel, M. S. Peeples, A. Pillepich, A. C. N. Quirk, R. M. Rich, S. T. Sohn, Y.-S. Ting, R. P. van der Marel, A. Wetzel, B. F. Williams, and J. Wojno (2019). Astro2020 Science White Paper: Construction of an L* Galaxy: the Transformative Power of Wide Fields for Revealing the Past, Present and Future of the Great Andromeda System. *arXiv e-prints*, arXiv:1904.01074.

Gnedin, O. Y., W. R. Brown, M. J. Geller, and S. J. Kenyon (2010). The Mass Profile of the Galaxy to 80 kpc. *ApJL*, **720**, pp. L108–L112. doi:10.1088/2041-8205/720/1/L108.

Gnedin, O. Y., A. V. Kravtsov, A. A. Klypin, and D. Nagai (2004). Response of Dark Matter Halos to Condensation of Baryons: Cosmological Simulations and Improved Adiabatic Contraction Model. *ApJ*, **616**, pp. 16–26. doi:10.1086/424914.

Gómez, F. A., G. Besla, D. D. Carpintero, Á. Villalobos, B. W. O'Shea, and E. F. Bell (2015). And Yet it Moves: The Dangers of Artificially Fixing the Milky Way Center of Mass in the Presence of a Massive Large Magellanic Cloud. *ApJ*, **802**, 128. doi:10.1088/0004-637X/802/2/128.

Gómez, F. A., I. Minchev, B. W. O'Shea, T. C. Beers, J. S. Bullock, and C. W. Purcell (2013). Vertical density waves in the Milky Way disc induced by the Sagittarius dwarf galaxy. *MNRAS*, **429**, pp. 159–164. doi:10.1093/mnras/sts327.

González, R. E., A. V. Kravtsov, and N. Y. Gnedin (2013). Satellites in Milky-Way-like Hosts: Environment Dependence and Close Pairs. *ApJ*, **770**, 96. doi:10.1088/0004-637X/770/2/96.

González, R. E., A. V. Kravtsov, and N. Y. Gnedin (2014). On the Mass of the Local Group. *ApJ*, **793**, 91. doi:10.1088/0004-637X/793/2/91.

Griffen, B. F., A. P. Ji, G. A. Dooley, F. A. Gómez, M. Vogelsberger, B. W. O'Shea, and A. Frebel (2016). The Caterpillar Project: A Large Suite of Milky Way Sized Halos. *ApJ*, **818**, 10. doi:10.3847/0004-637X/818/1/10.

Grillmair, C. J. (2006). Detection of a 60°-long Dwarf Galaxy Debris Stream. *ApJ*, **645**, pp. L37–L40. doi:10.1086/505863.

Guglielmo, M., G. F. Lewis, and J. Bland-Hawthorn (2014). A genetic approach to the history of the Magellanic Clouds. *MNRAS*, **444**, pp. 1759–1774. doi:10.1093/mnras/stu1549.

Guo, Q., S. White, M. Boylan-Kolchin, G. De Lucia, G. Kauffmann, G. Lemson, C. Li, V. Springel, and S. Weinmann (2011). From dwarf spheroidals to cD galaxies: simulating the galaxy population in a ΛCDM cosmology. *MNRAS*, **413**, pp. 101–131. doi:10.1111/j.1365-2966.2010.18114.x.

Guo, Q., S. White, C. Li, and M. Boylan-Kolchin (2010). How do galaxies populate dark matter haloes? *MNRAS*, **404**, pp. 1111–1120. doi:10.1111/j.1365-2966.2010.16341.x.

Hammer, F., Y. B. Yang, J. L. Wang, R. Ibata, H. Flores, and M. Puech (2018). A 2-3 billion year old major merger paradigm for the Andromeda galaxy and its outskirts. *MNRAS*, **475**, pp. 2754–2767. doi:10.1093/mnras/stx3343.

Hashimoto, Y., Y. Funato, and J. Makino (2003). To Circularize or Not To Circularize?-Orbital Evolution of Satellite Galaxies. *ApJ*, **582**, pp. 196–201. doi:10.1086/344260.

Helmi, A. and H. H. Koppelman (2016). The Time Evolution of Gaps in Tidal Streams. *ApJL*, **828**, L10. doi:10.3847/2041-8205/828/1/L10.

Helmi, A. and S. D. M. White (1999). Building up the stellar halo of the Galaxy. *MNRAS*, **307**, pp. 495–517. doi:10.1046/j.1365-8711.1999.02616.x.

Hernquist, L. (1990). An analytical model for spherical galaxies and bulges. *ApJ*, **356**, pp. 359–364. doi:10.1086/168845.

Hetherington, N. S. (1972). Adrian van Maanen and Internal Motions in Spiral Nebulae: a Historical Review. *QJRAS*, **13**, p. 25.

Hinshaw, G., D. Larson, E. Komatsu, D. N. Spergel, C. L. Bennett, J. Dunkley, M. R. Nolta, M. Halpern, R. S. Hill, N. Odegard, L. Page, K. M. Smith, J. L. Weiland, B. Gold, N. Jarosik, A. Kogut, M. Limon, S. S. Meyer, G. S. Tucker, E. Wollack, and E. L. Wright (2013). Nine-year Wilkinson Microwave Anisotropy Probe (WMAP) Observations: Cosmological Parameter Results. *ApJS*, **208**, 19. doi:10.1088/0067-0049/208/2/19.

Huxor, A. P., A. D. Mackey, A. M. N. Ferguson, M. J. Irwin, N. F. Martin, N. R. Tanvir, J. Veljanoski, A. McConnachie, C. K. Fishlock, R. Ibata, and G. F. Lewis (2014). The outer halo globular cluster system of M31 - I. The final PAndAS catalogue. *MNRAS*, **442**, pp. 2165–2187. doi:10.1093/mnras/stu771.

Ibata, R., S. Chapman, A. M. N. Ferguson, M. Irwin, G. Lewis, and A. McConnachie (2004). Taking measure of the Andromeda halo: a kinematic analysis of the giant stream surrounding M31. *MNRAS*, **351**, pp. 117–124. doi:10.1111/j.1365-2966.2004.07759.x.

Ibata, R. A. and G. F. Lewis (1998). Galactic Indigestion: Numerical Simulations of the Milky Way's Closest Neighbor. *ApJ*, **500**, pp. 575–590. doi:10.1086/305773.

Ibata, R. A., G. F. Lewis, A. R. Conn, M. J. Irwin, A. W. McConnachie, S. C. Chapman, M. L. Collins, M. Fardal, A. M. N. Ferguson, N. G. Ibata, A. D. Mackey, N. F. Martin, J. Navarro, R. M. Rich, D. Valls-Gabaud, and L. M. Widrow (2013). A vast, thin plane of corotating dwarf galaxies orbiting the Andromeda galaxy. *Nature*, **493**, pp. 62–65. doi:10.1038/nature11717.

Irwin, M. J., V. Belokurov, N. W. Evans, E. V. Ryan-Weber, J. T. A. de Jong, S. Koposov, D. B. Zucker, S. T. Hodgkin, G. Gilmore, P. Prema, L. Hebb, A. Begum, M. Fellhauer, P. C. Hewett, J. Kennicutt, R. C., M. I. Wilkinson, D. M. Bramich, S. Vidrih, H. W. Rix, T. C. Beers, J. C. Barentine, H. Brewington, M. Harvanek, J. Krzesinski, D. Long, A. Nitta, and S. A. Snedden (2007). Discovery of an Unusual Dwarf Galaxy in the Outskirts of the Milky Way. *ApJ*, **656**, pp. L13–L16. doi:10.1086/512183.

Jethwa, P., D. Erkal, and V. Belokurov (2016). A Magellanic origin of the DES dwarfs. *MNRAS*, **461**, pp. 2212–2233. doi:10.1093/mnras/stw1343.

Jiang, G. and C. S. Kochanek (2007). The Baryon Fractions and Mass-to-Light Ratios of Early-Type Galaxies. *ApJ*, **671**, pp. 1568–1578. doi:10.1086/522580.

Kafle, P. R., S. Sharma, G. F. Lewis, and J. Bland-Hawthorn (2012). Kinematics of the Stellar Halo and the Mass Distribution of the Milky Way Using Blue Horizontal Branch Stars. *ApJ*, **761**, 98. doi:10.1088/0004-637X/761/2/98.

Kafle, P. R., S. Sharma, G. F. Lewis, and J. Bland-Hawthorn (2014). On the Shoulders of Giants: Properties of the Stellar Halo and the Milky Way Mass Distribution. *ApJ*, **794**, 59. doi:10.1088/0004-637X/794/1/59.

Kallivayalil, N., G. Besla, R. Sanderson, and C. Alcock (2009). Revisiting the Role of M31 in the Dynamical History of the Magellanic Clouds. *ApJ*, **700**, pp. 924–930. doi:10.1088/0004-637X/700/2/924.

Kallivayalil, N., L. V. Sales, P. Zivick, T. K. Fritz, A. Del Pino, S. T. Sohn, G. Besla, R. P. van der Marel, J. F. Navarro, and E. Sacchi (2018). The Missing Satellites of the Magellanic Clouds? Gaia Proper Motions of the Recently Discovered Ultra-faint Galaxies. *ApJ*, **867**, 19. doi:10.3847/1538-4357/aadfee.

Kallivayalil, N., R. P. van der Marel, and C. Alcock (2006b). Is the SMC Bound to the LMC? The Hubble Space Telescope Proper Motion of the SMC. *ApJ*, **652**, pp. 1213–1229. doi:10.1086/508014.

Kallivayalil, N., R. P. van der Marel, C. Alcock, T. Axelrod, K. H. Cook, A. J. Drake, and M. Geha (2006a). The Proper Motion of the Large Magellanic Cloud Using HST. *ApJ*, **638**, pp. 772–785. doi:10.1086/498972.

Kallivayalil, N., R. P. van der Marel, G. Besla, J. Anderson, and C. Alcock (2013). Third-epoch Magellanic Cloud Proper Motions. I. Hubble Space Telescope/WFC3 Data and Orbit Implications. *ApJ*, **764**, 161. doi:10.1088/0004-637X/764/2/161.

Kam, S. Z., C. Carignan, L. Chemin, T. Foster, E. Elson, and T. H. Jarrett (2017). H I Kinematics and Mass Distribution of Messier 33. *AJ*, **154**, 41. doi:10.3847/1538-3881/aa79f3.

Karachentsev, I. D., D. I. Makarov, and E. I. Kaisina (2013). Updated Nearby Galaxy Catalog. *AJ*, **145**, 101. doi:10.1088/0004-6256/145/4/101.

Kim, D. and H. Jerjen (2015). Horologium II: A Second Ultra-faint Milky Way Satellite in the Horologium Constellation. *ApJL*, **808**, L39. doi:10.1088/2041-8205/808/2/L39.

Kim, D., H. Jerjen, D. Mackey, G. S. Da Costa, and A. P. Milone (2015). A Hero's Dark Horse: Discovery of an Ultra-faint Milky Way Satellite in Pegasus. *ApJL*, **804**, L44. doi:10.1088/2041-8205/804/2/L44.

Kim, S., L. Staveley-Smith, M. A. Dopita, K. C. Freeman, R. J. Sault, M. J. Kesteven, and D. McConnell (1998). An H I Aperture Synthesis Mosaic of the Large Magellanic Cloud. *ApJ*, **503**, pp. 674–688. doi:10.1086/306030.

Kirby, E. N., J. G. Cohen, P. Guhathakurta, L. Cheng, J. S. Bullock, and A. Gallazzi (2013). The Universal Stellar Mass-Stellar Metallicity Relation for Dwarf Galaxies. *ApJ*, **779**, 102. doi:10.1088/0004-637X/779/2/102.

Klypin, A., S. Gottlöber, A. V. Kravtsov, and A. M. Khokhlov (1999). Galaxies in N-Body Simulations: Overcoming the Overmerging Problem. *ApJ*, **516**, pp. 530–551. doi:10.1086/307122.

Klypin, A., H. Zhao, and R. S. Somerville (2002). ΛCDM-based Models for the Milky Way and M31. I. Dynamical Models. *ApJ*, **573**, pp. 597–613. doi:10.1086/340656.

Klypin, A. A., S. Trujillo-Gomez, and J. Primack (2011). Dark Matter Halos in the Standard Cosmological Model: Results from the Bolshoi Simulation. *ApJ*, **740**, 102. doi:10.1088/0004-637X/740/2/102.

Kochanek, C. S. (1996). The Mass of the Milky Way. *ApJ*, **457**, p. 228. doi:10.1086/176724.

Kong, A. (1992). A Note on Importance Sampling using Standardized Weights. Technical report, University of Chicago, Department of Statistics.

Koposov, S. E., V. Belokurov, G. Torrealba, and N. W. Evans (2015). Beasts of the Southern Wild : Discovery of nine Ultra Faint satellites in the vicinity of the Magellanic Clouds. *ApJ*, **805**, 130. doi:10.1088/0004-637X/805/2/130.

Kravtsov, A. V., A. A. Berlind, R. H. Wechsler, A. A. Klypin, S. Gottlöber, B. Allgood, and J. R. Primack (2004). The Dark Side of the Halo Occupation Distribution. *ApJ*, **609**, pp. 35–49. doi:10.1086/420959.

Laporte, C. F. P., F. A. Gómez, G. Besla, K. V. Johnston, and N. Garavito-Camargo (2018). Response of the Milky Way's disc to the Large Magellanic Cloud in a first infall scenario. *MNRAS*, **473**, pp. 1218–1230. doi:10.1093/mnras/stx2146.

Leauthaud, A., J. Tinker, P. S. Behroozi, M. T. Busha, and R. H. Wechsler (2011). A Theoretical Framework for Combining Techniques that Probe the Link Between Galaxies and Dark Matter. *ApJ*, **738**, 45. doi:10.1088/0004-637X/738/1/45.

Lehner, N., J. C. Howk, and B. P. Wakker (2015). Evidence for a Massive, Extended Circumgalactic Medium Around the Andromeda Galaxy. *ApJ*, **804**, 79. doi:10.1088/0004-637X/804/2/79.

Lewis, G. F., R. Braun, A. W. McConnachie, M. J. Irwin, R. A. Ibata, S. C. Chapman, A. M. N. Ferguson, N. F. Martin, M. Fardal, J. Dubinski, L. Widrow, A. D. Mackey, A. Babul, N. R. Tanvir, and M. Rich (2013). PAndAS in the Mist: The Stellar and Gaseous Mass within the Halos of M31 and M33. *ApJ*, **763**, 4. doi:10.1088/0004-637X/763/1/4.

Li, Y.-S. and S. D. M. White (2008). Masses for the Local Group and the Milky Way. *MNRAS*, **384**, pp. 1459–1468. doi:10.1111/j.1365-2966.2007.12748.x.

Li, Z.-Z., Y. P. Jing, Y.-Z. Qian, Z. Yuan, and D.-H. Zhao (2017). Determination of Dark Matter Halo Mass from Dynamics of Satellite Galaxies. *ApJ*, **850**, 116. doi:10.3847/1538-4357/aa94c0.

Lindegren, L., J. Hernández, A. Bombrun, S. Klioner, U. Bastian, M. Ramos-Lerate, A. de Torres, H. Steidelmüller, C. Stephenson, D. Hobbs, U. Lammers, M. Biermann, R. Geyer, T. Hilger, D. Michalik, U. Stampa, P. J. McMillan, J. Castañeda,

M. Clotet, G. Comoretto, M. Davidson, C. Fabricius, G. Gracia, N. C. Hambly, A. Hutton, A. Mora, J. Portell, F. van Leeuwen, U. Abbas, A. Abreu, M. Altmann, A. Andrei, E. Anglada, L. Balaguer-Núñez, C. Barache, U. Becciani, S. Bertone, L. Bianchi, S. Bouquillon, G. Bourda, T. Brüsemeister, B. Bucciarelli, D. Busonero, R. Buzzi, R. Cancelliere, T. Carlucci, P. Charlot, N. Cheek, M. Crosta, C. Crowley, J. de Bruijne, F. de Felice, R. Drimmel, P. Esquej, A. Fienga, E. Fraile, M. Gai, N. Garralda, J. J. González-Vidal, R. Guerra, M. Hauser, W. Hofmann, B. Holl, S. Jordan, M. G. Lattanzi, H. Lenhardt, S. Liao, E. Licata, T. Lister, W. Löffler, J. Marchant, J.-M. Martin-Fleitas, R. Messineo, F. Mignard, R. Morbidelli, E. Poggio, A. Riva, N. Rowell, E. Salguero, M. Sarasso, E. Sciacca, H. Siddiqui, R. L. Smart, A. Spagna, I. Steele, F. Taris, J. Torra, A. van Elteren, W. van Reeven, and A. Vecchiato (2018). Gaia Data Release 2. The astrometric solution. *A&A*, **616**, A2. doi:10.1051/0004-6361/201832727.

Liu, L., B. F. Gerke, R. H. Wechsler, P. S. Behroozi, and M. T. Busha (2011). How Common are the Magellanic Clouds? *ApJ*, **733**, 62. doi:10.1088/0004-637X/733/1/62.

Loeb, A., M. J. Reid, A. Brunthaler, and H. Falcke (2005). Constraints on the Proper Motion of the Andromeda Galaxy Based on the Survival of Its Satellite M33. *ApJ*, **633**, pp. 894–898. doi:10.1086/491644.

López-Corredoira, M., J. Betancort-Rijo, and J. E. Beckman (2002). Generation of galactic disc warps due to intergalactic accretion flows onto the disc. *A&A*, **386**, pp. 169–186. doi:10.1051/0004-6361:20020229.

Lu, Y., A. Benson, Y.-Y. Mao, S. Tonnesen, A. H. G. Peter, A. R. Wetzel, M. Boylan-Kolchin, and R. H. Wechsler (2016). The Connection between the Host Halo and the Satellite Galaxies of the Milky Way. *ApJ*, **830**(2), 59. doi:10.3847/0004-637X/830/2/59.

Lux, H., J. I. Read, and G. Lake (2010). Determining orbits for the Milky Way's dwarfs. *MNRAS*, **406**, pp. 2312–2324. doi:10.1111/j.1365-2966.2010.16877.x.

Mackey, A. D., A. M. N. Ferguson, A. P. Huxor, J. Veljanoski, G. F. Lewis, A. W. McConnachie, N. F. Martin, R. A. Ibata, M. J. Irwin, P. Côté, M. L. M. Collins, N. R. Tanvir, and N. F. Bate (2019). The outer halo globular cluster system of M31 - III. Relationship to the stellar halo. *MNRAS*, **484**, pp. 1756–1789. doi:10.1093/mnras/stz072.

Mackey, A. D., A. P. Huxor, A. M. N. Ferguson, M. J. Irwin, N. R. Tanvir, A. W. McConnachie, R. A. Ibata, S. C. Chapman, and G. F. Lewis (2010). Evidence for an Accretion Origin for the Outer Halo Globular Cluster System of M31. *ApJL*, **717**, pp. L11–L16. doi:10.1088/2041-8205/717/1/L11.

Mackey, A. D., S. E. Koposov, D. Erkal, V. Belokurov, G. S. Da Costa, and F. A. Gómez (2016). A 10 kpc stellar substructure at the edge of the Large Magellanic Cloud: perturbed outer disc or evidence for tidal stripping? *MNRAS*, **459**, pp. 239–255. doi:10.1093/mnras/stw497.

Majewski, S. R., D. L. Nidever, R. R. Muñoz, R. J. Patterson, W. E. Kunkel, and J. L. Carlin (2009). Discovery of an extended, halo-like stellar population around the Large Magellanic Cloud. In Van Loon, J. T. and J. M. Oliveira (eds.) *The Magellanic System: Stars, Gas, and Galaxies*, volume 256 of *IAU Symposium*, pp. 51–56. doi:10.1017/S1743921308028251.

Mandelbaum, R., U. Seljak, G. Kauffmann, C. M. Hirata, and J. Brinkmann (2006). Galaxy halo masses and satellite fractions from galaxy-galaxy lensing in the Sloan Digital Sky Survey: stellar mass, luminosity, morphology and environment dependencies. *MNRAS*, **368**, pp. 715–731. doi:10.1111/j.1365-2966.2006.10156.x.

Martin, N. F., R. A. Ibata, G. F. Lewis, A. McConnachie, A. Babul, N. F. Bate, E. Bernard, S. C. Chapman, M. M. L. Collins, A. R. Conn, D. Crnojević, M. A. Fardal, A. M. N. Ferguson, M. Irwin, A. D. Mackey, B. McMonigal, J. F. Navarro, and R. M. Rich (2016). The PAndAS View of the Andromeda Satellite System. II. Detailed Properties of 23 M31 Dwarf Spheroidal Galaxies. *ApJ*, **833**, 167. doi:10.3847/1538-4357/833/2/167.

Martin, N. F., A. W. McConnachie, M. Irwin, L. M. Widrow, A. M. N. Ferguson, R. A. Ibata, J. Dubinski, A. Babul, S. Chapman, M. Fardal, G. F. Lewis, J. Navarro, and R. M. Rich (2009). PAndAS' CUBS: Discovery of Two New Dwarf Galaxies in the Surroundings of the Andromeda and Triangulum Galaxies. *ApJ*, **705**, pp. 758–765. doi:10.1088/0004-637X/705/1/758.

Martin, N. F., D. L. Nidever, G. Besla, K. Olsen, A. R. Walker, A. K. Vivas, R. A. Gruendl, C. C. Kaleida, R. R. Muñoz, R. D. Blum, A. Saha, B. C. Conn, E. F. Bell, Y.-H. Chu, M.-R. L. Cioni, T. J. L. de Boer, C. Gallart, S. Jin, A. Kunder, S. R. Majewski, D. Martinez-Delgado, A. Monachesi, M. Monelli, L. Monteagudo, N. E. D. Noël, E. W. Olszewski, G. S. Stringfellow, R. P. van der Marel, and D. Zaritsky (2015). Hydra II: A Faint and Compact Milky Way Dwarf Galaxy Found in the Survey of the Magellanic Stellar History. *ApJL*, **804**, L5. doi:10.1088/2041-8205/804/1/L5.

Martin, N. F., E. F. Schlafly, C. T. Slater, E. J. Bernard, H.-W. Rix, E. F. Bell, A. M. N. Ferguson, D. P. Finkbeiner, B. P. M. Laevens, W. S. Burgett, K. C. Chambers, P. W. Draper, K. W. Hodapp, N. Kaiser, R.-P. Kudritzki, E. A. Magnier, N. Metcalfe, J. S. Morgan, P. A. Price, J. L. Tonry, R. J. Wainscoat, and C. Waters (2013b). Perseus I: A Distant Satellite Dwarf Galaxy of Andromeda. *ApJ*, **779**(1), L10. doi:10.1088/2041-8205/779/1/L10.

Martin, N. F., C. T. Slater, E. F. Schlafly, E. Morganson, H.-W. Rix, E. F. Bell, B. P. M. Laevens, E. J. Bernard, A. M. N. Ferguson, D. P. Finkbeiner, W. S. Burgett, K. C. Chambers, K. W. Hodapp, N. Kaiser, R.-P. Kudritzki, E. A. Magnier, J. S. Morgan, P. A. Price, J. L. Tonry, and R. J. Wainscoat (2013a). Lacerta I and Cassiopeia III. Two Luminous and Distant Andromeda Satellite Dwarf Galaxies Found in the 3π Pan-STARRS1 Survey. *ApJ*, **772**(1), 15. doi: 10.1088/0004-637X/772/1/15.

Massari, D., A. Bellini, F. R. Ferraro, R. P. van der Marel, J. Anderson, E. Dalessandro, and B. Lanzoni (2013). Hubble Space Telescope Absolute Proper Motions Of NGC 6681 (M70) and the Sagittarius Dwarf Spheroidal Galaxy. *ApJ*, **779**, 81. doi:10.1088/0004-637X/779/1/81.

Massari, D. and A. Helmi (2018). With and without spectroscopy: Gaia DR2 proper motions of seven ultra-faint dwarf galaxies. *A&A*, **620**, A155. doi:10.1051/0004-6361/201833367.

Massey, P., K. F. Neugent, and B. M. Smart (2016). VizieR Online Data Catalog: Revised LGGS UBVRI photometry of M31 and M33 stars (Massey+, 2016). *VizieR Online Data Catalog*, **515**.

Mathewson, D. S., M. P. Schwarz, and J. D. Murray (1977). The Magellanic stream - The turbulent wake of the Magellanic clouds in the halo of the Galaxy. *ApJL*, **217**, pp. L5–L8. doi:10.1086/182527.

McAlpine, S., J. C. Helly, M. Schaller, J. W. Trayford, Y. Qu, M. Furlong, R. G. Bower, R. A. Crain, J. Schaye, T. Theuns, C. Dalla Vecchia, C. S. Frenk, I. G. McCarthy, A. Jenkins, Y. Rosas-Guevara, S. D. M. White, M. Baes, P. Camps, and G. Lemson (2016). The EAGLE simulations of galaxy formation: Public release of halo and galaxy catalogues. *Astronomy and Computing*, **15**, pp. 72–89. doi:10.1016/j.ascom.2016.02.004.

McConnachie, A. W. (2012). The Observed Properties of Dwarf Galaxies in and around the Local Group. *AJ*, **144**, 4. doi:10.1088/0004-6256/144/1/4.

McConnachie, A. W. (2016). Stellar halos around Local Group galaxies. In Bragaglia, A., M. Arnaboldi, M. Rejkuba, and D. Romano (eds.) *The General Assembly of Galaxy Halos: Structure, Origin and Evolution*, volume 317 of *IAU Symposium*, pp. 15–20. doi:10.1017/S1743921316000090.

McConnachie, A. W., R. Ibata, N. Martin, A. M. N. Ferguson, M. Collins, S. Gwyn, M. Irwin, G. F. Lewis, A. D. Mackey, T. Davidge, V. Arias, A. Conn, P. Côté, D. Crnojevic, A. Huxor, J. Penarrubia, C. Spengler, N. Tanvir, D. Valls-Gabaud, A. Babul, P. Barmby, N. F. Bate, E. Bernard, S. Chapman, A. Dotter, W. Harris,

B. McMonigal, J. Navarro, T. H. Puzia, R. M. Rich, G. Thomas, and L. M. Widrow (2018). The Large-scale Structure of the Halo of the Andromeda Galaxy. II. Hierarchical Structure in the Pan-Andromeda Archaeological Survey. *ApJ*, **868**(1), 55. doi:10.3847/1538-4357/aae8e7.

McConnachie, A. W., M. J. Irwin, A. M. N. Ferguson, R. A. Ibata, G. F. Lewis, and N. Tanvir (2004). Determining the location of the tip of the red giant branch in old stellar populations: M33, Andromeda I and II. *MNRAS*, **350**, pp. 243–252. doi:10.1111/j.1365-2966.2004.07637.x.

McConnachie, A. W., M. J. Irwin, A. M. N. Ferguson, R. A. Ibata, G. F. Lewis, and N. Tanvir (2005). Distances and metallicities for 17 Local Group galaxies. *MNRAS*, **356**, pp. 979–997. doi:10.1111/j.1365-2966.2004.08514.x.

McConnachie, A. W., M. J. Irwin, R. A. Ibata, J. Dubinski, L. M. Widrow, N. F. Martin, P. Côté, A. L. Dotter, J. F. Navarro, A. M. N. Ferguson, T. H. Puzia, G. F. Lewis, A. Babul, P. Barmby, O. Bienaymé, S. C. Chapman, R. Cockcroft, M. L. M. Collins, M. A. Fardal, W. E. Harris, A. Huxor, A. D. Mackey, J. Peñarrubia, R. M. Rich, H. B. Richer, A. Siebert, N. Tanvir, D. Valls-Gabaud, and K. A. Venn (2009). The remnants of galaxy formation from a panoramic survey of the region around M31. *Nature*, **461**, pp. 66–69. doi:10.1038/nature08327.

McGaugh, S. and M. Milgrom (2013). Andromeda Dwarfs in Light of MOND. II. Testing Prior Predictions. *ApJ*, **775**, 139. doi:10.1088/0004-637X/775/2/139.

McGaugh, S. S. and J. Wolf (2010). Local Group Dwarf Spheroidals: Correlated Deviations from the Baryonic Tully-Fisher Relation. *ApJ*, **722**, pp. 248–261. doi:10.1088/0004-637X/722/1/248.

McMillan, P. J. (2011). The solar neighbourhood in angle coordinates: the Hyades moving group. *MNRAS*, **418**, pp. 1565–1574. doi:10.1111/j.1365-2966.2011.19520.x.

McMonigal, B., G. F. Lewis, B. J. Brewer, M. J. Irwin, N. F. Martin, A. W. McConnachie, R. A. Ibata, A. M. N. Ferguson, A. D. Mackey, and S. C. Chapman (2016). The elusive stellar halo of the Triangulum galaxy. *MNRAS*, **461**, pp. 4374–4388. doi:10.1093/mnras/stw1657.

Miyamoto, M. and R. Nagai (1975). Three-dimensional models for the distribution of mass in galaxies. *PASJ*, **27**, pp. 533–543.

Moore, B. and M. Davis (1994). The Origin of the Magellanic Stream. *MNRAS*, **270**, p. 209. doi:10.1093/mnras/270.2.209.

Moore, B., S. Ghigna, F. Governato, G. Lake, T. Quinn, J. Stadel, and P. Tozzi (1999). Dark Matter Substructure within Galactic Halos. *ApJL*, **524**, pp. L19–L22. doi:10.1086/312287.

More, S., B. Diemer, and A. V. Kravtsov (2015). The Splashback Radius as a Physical Halo Boundary and the Growth of Halo Mass. *ApJ*, **810**, 36. doi:10.1088/0004-637X/810/1/36.

Moster, B. P., T. Naab, and S. D. M. White (2013). Galactic star formation and accretion histories from matching galaxies to dark matter haloes. *MNRAS*, **428**, pp. 3121–3138. doi:10.1093/mnras/sts261.

Müller, O., M. S. Pawlowski, H. Jerjen, and F. Lelli (2018). A whirling plane of satellite galaxies around Centaurus A challenges cold dark matter cosmology. *Science*, **359**(6375), pp. 534–537. doi:10.1126/science.aao1858.

Murai, T. and M. Fujimoto (1980). The Magellanic Stream and the Galaxy with a Massive Halo. *PASJ*, **32**, p. 581.

Murali, C. (2000). The Magellanic Stream and the Density of Coronal Gas in the Galactic Halo. *ApJL*, **529**, pp. L81–L84. doi:10.1086/312462.

Navarro, J. F., C. S. Frenk, and S. D. M. White (1996). The Structure of Cold Dark Matter Halos. *ApJ*, **462**, p. 563. doi:10.1086/177173.

Nelson, D., A. Pillepich, S. Genel, M. Vogelsberger, V. Springel, P. Torrey, V. Rodriguez-Gomez, D. Sijacki, G. F. Snyder, B. Griffen, F. Marinacci, L. Blecha, L. Sales, D. Xu, and L. Hernquist (2015). The illustris simulation: Public data release. *Astronomy and Computing*, **13**, pp. 12–37. doi:10.1016/j.ascom.2015.09.003.

Newton, K. and D. T. Emerson (1977). Neutral hydrogen in the outer regions of M31. *MNRAS*, **181**, pp. 573–590. doi:10.1093/mnras/181.3.573.

Newton, O., M. Cautun, A. Jenkins, C. S. Frenk, and J. C. Helly (2018). The total satellite population of the Milky Way. *MNRAS*, **479**, pp. 2853–2870. doi:10.1093/mnras/sty1085.

Nidever, D. L., S. R. Majewski, and W. Butler Burton (2008). The Origin of the Magellanic Stream and Its Leading Arm. *ApJ*, **679**, 432-459. doi:10.1086/587042.

Nidever, D. L., S. R. Majewski, W. Butler Burton, and L. Nigra (2010). The 200deg Long Magellanic Stream System Long Magellanic Stream System. *ApJ*, **723**, pp. 1618–1631. doi:10.1088/0004-637X/723/2/1618.

Nidever, D. L., K. Olsen, A. R. Walker, A. K. Vivas, R. D. Blum, C. Kaleida, Y. Choi, B. C. Conn, R. A. Gruendl, E. F. Bell, G. Besla, R. R. Muñoz, C. Gallart, N. F. Martin, E. W. Olszewski, A. Saha, A. Monachesi, M. Monelli, T. J. L. de Boer, L. C. Johnson, D. Zaritsky, G. S. Stringfellow, R. P. van der Marel, M.-R. L. Cioni, S. Jin, S. R. Majewski, D. Martinez-Delgado, L. Monteagudo, N. E. D. Noël, E. J. Bernard, A. Kunder, Y.-H. Chu, C. P. M. Bell, F. Santana, J. Frechem, G. E. Medina, V. Parkash, J. C. Serón Navarrete, and C. Hayes (2017). SMASH: Survey of the MAgellanic Stellar History. *AJ*, **154**, 199. doi: 10.3847/1538-3881/aa8d1c.

Niederhofer, F., M.-R. L. Cioni, S. Rubele, T. Schmidt, K. Bekki, R. d. Grijs, J. Emerson, V. D. Ivanov, M. Marconi, J. M. Oliveira, M. G. Petr-Gotzens, V. Ripepi, J. T. van Loon, and S. Zaggia (2018). The VMC survey. XXX. Stellar proper motions in the central parts of the Small Magellanic Cloud. *A&A*, **613**, L8. doi:10.1051/0004-6361/201833144.

Olling, R. P. and D. M. Peterson (2000). Galaxy Distances via Rotational Parallaxes. *ArXiv Astrophysics e-prints*.

Oort, J. H., F. J. Kerr, and G. Westerhout (1958). The galactic system as a spiral nebula (Council Note). *MNRAS*, **118**, p. 379. doi:10.1093/mnras/118.4.379.

Pasetto, S., E. K. Grebel, P. Berczik, C. Chiosi, and R. Spurzem (2011). Orbital evolution of the Carina dwarf galaxy and self-consistent determination of star formation history. *A&A*, **525**, A99. doi:10.1051/0004-6361/200913415.

Patel, E., G. Besla, and K. Mandel (2017b). Orbits of massive satellite galaxies - II. Bayesian estimates of the Milky Way and Andromeda masses using high-precision astrometry and cosmological simulations. *MNRAS*, **468**, pp. 3428–3449. doi:10.1093/mnras/stx698.

Patel, E., G. Besla, K. Mandel, and S. T. Sohn (2018a). Estimating the Mass of the Milky Way Using the Ensemble of Classical Satellite Galaxies. *ApJ*, **857**, 78. doi:10.3847/1538-4357/aab78f.

Patel, E., G. Besla, and S. T. Sohn (2017a). Orbits of massive satellite galaxies - I. A close look at the Large Magellanic Cloud and a new orbital history for M33. *MNRAS*, **464**, pp. 3825–3849. doi:10.1093/mnras/stw2616.

Patel, E., J. L. Carlin, E. J. Tollerud, M. L. M. Collins, and G. A. Dooley (2018b). ΛCDM predictions for the satellite population of M33. *MNRAS*, **480**, pp. 1883–1897. doi:10.1093/mnras/sty1946.

Pawlowski, M. S. and P. Kroupa (2013). The rotationally stabilized VPOS and predicted proper motions of the Milky Way satellite galaxies. *MNRAS*, **435**, pp. 2116–2131. doi:10.1093/mnras/stt1429.

Peebles, P. J. E. (1996). Dynamics of the Relative Motions of the Galaxies in and Near the Local Group. In Lahav, O., E. Terlevich, and R. J. Terlevich (eds.) *Gravitational dynamics*, p. 219.

Peebles, P. J. E. and R. B. Tully (2013). A Primeval Magellanic Stream and Others. *ApJ*, **778**, 137. doi:10.1088/0004-637X/778/2/137.

Piatek, S., C. Pryor, P. Bristow, E. W. Olszewski, H. C. Harris, M. Mateo, D. Minniti, and C. G. Tinney (2005). Proper Motions of Dwarf Spheroidal Galaxies from Hubble Space Telescope Imaging. III. Measurement for Ursa Minor. *AJ*, **130**, pp. 95–115. doi:10.1086/430532.

Piatek, S., C. Pryor, P. Bristow, E. W. Olszewski, H. C. Harris, M. Mateo, D. Minniti, and C. G. Tinney (2006). Proper Motions of Dwarf Spheroidal Galaxies from Hubble Space Telescope Imaging. IV. Measurement for Sculptor. *AJ*, **131**, pp. 1445–1460. doi:10.1086/499526.

Piatek, S., C. Pryor, P. Bristow, E. W. Olszewski, H. C. Harris, M. Mateo, D. Minniti, and C. G. Tinney (2007). Proper Motions of Dwarf Spheroidal Galaxies from Hubble Space Telescope Imaging. V. Final Measurement for Fornax. *AJ*, **133**, pp. 818–844. doi:10.1086/510456.

Piatek, S., C. Pryor, and E. W. Olszewski (2008). Proper Motions of the Large Magellanic Cloud and Small Magellanic Cloud: Re-Analysis of Hubble Space Telescope Data. *AJ*, **135**, pp. 1024–1038. doi:10.1088/0004-6256/135/3/1024.

Piatek, S., C. Pryor, and E. W. Olszewski (2016). Proper Motion of the Leo II Dwarf Galaxy Based On Hubble Space Telescope Imaging. *AJ*, **152**, 166. doi:10.3847/0004-6256/152/6/166.

Piatek, S., C. Pryor, E. W. Olszewski, H. C. Harris, M. Mateo, D. Minniti, D. G. Monet, H. Morrison, and C. G. Tinney (2002). Proper Motions of Dwarf Spheroidal Galaxies from Hubble Space Telescope Imaging. I. Method and a Preliminary Measurement for Fornax. *AJ*, **124**, pp. 3198–3221. doi:10.1086/344767.

Piatek, S., C. Pryor, E. W. Olszewski, H. C. Harris, M. Mateo, D. Minniti, and C. G. Tinney (2003). Proper Motions of Dwarf Spheroidal Galaxies from Hubble Space Telescope Imaging. II. Measurement for Carina. *AJ*, **126**, pp. 2346–2361. doi:10.1086/378713.

Pieres, A., B. X. Santiago, A. Drlica-Wagner, K. Bechtol, R. P. v. d. Marel, G. Besla, N. F. Martin, V. Belokurov, C. Gallart, D. Martinez-Delgado, J. Marshall, N. E. D. Nöel, S. R. Majewski, M.-R. L. Cioni, T. S. Li, W. Hartley, E. Luque, B. C. Conn, A. R. Walker, E. Balbinot, G. S. Stringfellow, K. A. G. Olsen, D. Nidever, L. N. da Costa, R. Ogando, M. Maia, A. F. Neto, T. M. C. Abbott, F. B. Abdalla, S. Allam, J. Annis, A. Benoit-Lévy, A. C. Rosell, M. C. Kind, J. Carretero, C. E. Cunha, C. B. D'Andrea, S. Desai, H. T. Diehl, P. Doel, B. Flaugher, P. Fosalba, J. García-Bellido, D. Gruen, R. A. Gruendl, J. Gschwend, G. Gutierrez, K. Honscheid, D. James, K. Kuehn, N. Kuropatkin, F. Menanteau, R. Miquel, A. A. Plazas, A. K. Romer, M. Sako, E. Sanchez, V. Scarpine, M. Schubnell, I. Sevilla-Noarbe, R. C. Smith, M. Soares-Santos, F. Sobreira, E. Suchyta, M. E. C. Swanson, G. Tarle, D. L. Tucker, and W. Wester (2017). A stellar overdensity associated with the Small Magellanic Cloud. *MNRAS*, **468**, pp. 1349–1360. doi:10.1093/mnras/stx507.

Planck Collaboration, P. A. R. Ade, N. Aghanim, C. Armitage-Caplan, M. Arnaud, M. Ashdown, F. Atrio-Barandela, J. Aumont, C. Baccigalupi, A. J. Banday, and et al. (2014). Planck 2013 results. XVI. Cosmological parameters. *A&A*, **571**, A16. doi:10.1051/0004-6361/201321591.

Plummer, H. C. (1911). On the problem of distribution in globular star clusters. *MNRAS*, **71**, pp. 460–470. doi:10.1093/mnras/71.5.460.

Putman, M. E., B. K. Gibson, L. Staveley-Smith, G. Banks, D. G. Barnes, R. Bhatal, M. J. Disney, R. D. Ekers, K. C. Freeman, R. F. Haynes, P. Henning, H. Jerjen, V. Kilborn, B. Koribalski, P. Knezek, D. F. Malin, J. R. Mould, T. Oosterloo, R. M. Price, S. D. Ryder, E. M. Sadler, I. Stewart, F. Stootman, R. A. Vaile, R. L. Webster, and A. E. Wright (1998). Tidal disruption of the Magellanic Clouds by the Milky Way. *Nature*, **394**, pp. 752–754. doi:10.1038/29466.

Putman, M. E., J. E. G. Peek, A. Muratov, O. Y. Gnedin, W. Hsu, K. A. Douglas, C. Heiles, S. Stanimirovic, E. J. Korpela, and S. J. Gibson (2009). The Disruption and Fueling of M33. *ApJ*, **703**, pp. 1486–1501. doi:10.1088/0004-637X/703/2/1486.

Putman, M. E., L. Staveley-Smith, K. C. Freeman, B. K. Gibson, and D. G. Barnes (2003). The Magellanic Stream, High-Velocity Clouds, and the Sculptor Group. *ApJ*, **586**, pp. 170–194. doi:10.1086/344477.

Rasmussen, J. and K. Pedersen (2001). Constraints on a Local Group X-Ray Halo. *ApJ*, **559**, pp. 892–902. doi:10.1086/322380.

Roberts, M. S. and R. N. Whitehurst (1975). The rotation curve and geometry of M31 at large galactocentric distances. *ApJ*, **201**, pp. 327–346. doi:10.1086/153889.

Robotham, A. S. G., I. K. Baldry, J. Bland-Hawthorn, S. P. Driver, J. Loveday, P. Norberg, A. E. Bauer, K. Bekki, S. Brough, M. Brown, A. Graham, A. M. Hopkins, S. Phillipps, C. Power, A. Sansom, and L. Staveley-Smith (2012). Galaxy And Mass Assembly (GAMA): in search of Milky Way Magellanic Cloud analogues. *MNRAS*, **424**, pp. 1448–1453. doi:10.1111/j.1365-2966.2012.21332.x.

Rodriguez-Gomez, V., S. Genel, M. Vogelsberger, D. Sijacki, A. Pillepich, L. V. Sales, P. Torrey, G. Snyder, D. Nelson, V. Springel, C.-P. Ma, and L. Hernquist (2015). The merger rate of galaxies in the Illustris simulation: a comparison with observations and semi-empirical models. *MNRAS*, **449**, pp. 49–64. doi:10.1093/mnras/stv264.

Rodríguez-Puebla, A., N. Drory, and V. Avila-Reese (2012). The Stellar-Subhalo Mass Relation of Satellite Galaxies. *ApJ*, **756**, 2. doi:10.1088/0004-637X/756/1/2.

Rogstad, D. H., M. C. H. Wright, and I. A. Lockhart (1976). Aperture synthesis of neutral hydrogen in the galaxy M33. *ApJ*, **204**, pp. 703–711. doi:10.1086/154219.

Růžička, A., C. Theis, and J. Palouš (2009). Spatial Motion of The Magellanic Clouds: Tidal Models Ruled Out? *ApJ*, **691**, pp. 1807–1815. doi:10.1088/0004-637X/691/2/1807.

Saha, A., E. W. Olszewski, B. Brondel, K. Olsen, P. Knezek, J. Harris, C. Smith, A. Subramaniam, J. Claver, A. Rest, P. Seitzer, K. H. Cook, D. Minniti, and N. B. Suntzeff (2010). First Results from the NOAO Survey of the Outer Limits of the Magellanic Clouds. *AJ*, **140**, pp. 1719–1738. doi:10.1088/0004-6256/140/6/1719.

Sakamoto, T., M. Chiba, and T. C. Beers (2003). The mass of the Milky Way: Limits from a newly assembled set of halo objects. *A&A*, **397**, pp. 899–911. doi:10.1051/0004-6361:20021499.

Salem, M., G. Besla, G. Bryan, M. Putman, R. P. van der Marel, and S. Tonnesen (2015). Ram Pressure Stripping of the Large Magellanic Cloud's Disk as a Probe of the Milky Way's Circumgalactic Medium. *ApJ*, **815**, 77. doi:10.1088/0004-637X/815/1/77.

Sales, L. V., J. F. Navarro, M. G. Abadi, and M. Steinmetz (2007). Cosmic ménage à trois: the origin of satellite galaxies on extreme orbits. *MNRAS*, **379**, pp. 1475–1483. doi:10.1111/j.1365-2966.2007.12026.x.

Sales, L. V., J. F. Navarro, A. P. Cooper, S. D. M. White, C. S. Frenk, and A. Helmi (2011). Clues to the 'Magellanic Galaxy' from cosmological simulations. *MNRAS*, **418**, pp. 648–658. doi:10.1111/j.1365-2966.2011.19514.x.

Sales, L. V., W. Wang, S. D. M. White, and J. F. Navarro (2013). Satellites and haloes of dwarf galaxies. *MNRAS*, **428**, pp. 573–578. doi:10.1093/mnras/sts054.

Salomon, J.-B., R. A. Ibata, B. Famaey, N. F. Martin, and G. F. Lewis (2016). The transverse velocity of the Andromeda system, derived from the M31 satellite population. *MNRAS*, **456**, pp. 4432–4440. doi:10.1093/mnras/stv2865.

San Roman, I., A. Sarajedini, and A. Aparicio (2010). Photometric Properties of the M33 Star Cluster System. *ApJ*, **720**, pp. 1674–1683. doi:10.1088/0004-637X/720/2/1674.

Sanders, J. L. and J. Binney (2014). Actions, angles and frequencies for numerically integrated orbits. *MNRAS*, **441**, pp. 3284–3295. doi:10.1093/mnras/stu796.

Sawala, T., P. Pihajoki, P. H. Johansson, C. S. Frenk, J. F. Navarro, K. A. Oman, and S. D. M. White (2017). Shaken and stirred: the Milky Way's dark substructures. *MNRAS*, **467**, pp. 4383–4400. doi:10.1093/mnras/stx360.

Scholz, R.-D. and M. J. Irwin (1994). Absolute Proper Motions of the Dwarf Spheroidal Galaxies in Draco and Ursa Minor. In MacGillivray, H. T. (ed.) *Astronomy from Wide-Field Imaging*, volume 161 of *IAU Symposium*, p. 535.

Schönrich, R., J. Binney, and W. Dehnen (2010). Local kinematics and the local standard of rest. *MNRAS*, **403**, pp. 1829–1833. doi:10.1111/j.1365-2966.2010.16253.x.

Semczuk, M., E. L. Łokas, J.-B. Salomon, E. Athanassoula, and E. D'Onghia (2018). Tidally Induced Morphology of M33 in Hydrodynamical Simulations of Its Recent Interaction with M31. *ApJ*, **864**, 34. doi:10.3847/1538-4357/aad4ae.

Shaya, E. J. and R. B. Tully (2013). The formation of Local Group planes of galaxies. *MNRAS*, **436**, pp. 2096–2119. doi:10.1093/mnras/stt1714.

Silverman, B. W. (1986). *Density Estimation for Statistics and Data Analysis*. Chapman and Hall, London.

Simon, J. D. (2018). Gaia Proper Motions and Orbits of the Ultra-faint Milky Way Satellites. *ApJ*, **863**, 89. doi:10.3847/1538-4357/aacdfb.

Slipher, V. M. (1913). The radial velocity of the Andromeda Nebula. *Lowell Observatory Bulletin*, **2**, pp. 56–57.

Smith, M. C., G. R. Ruchti, A. Helmi, R. F. G. Wyse, J. P. Fulbright, K. C. Freeman, J. F. Navarro, G. M. Seabroke, M. Steinmetz, M. Williams, O. Bienaymé, J. Binney, J. Bland-Hawthorn, W. Dehnen, B. K. Gibson, G. Gilmore, E. K. Grebel, U. Munari, Q. A. Parker, R.-D. Scholz, A. Siebert, F. G. Watson, and

T. Zwitter (2007). The RAVE survey: constraining the local Galactic escape speed. *MNRAS*, **379**, pp. 755–772. doi:10.1111/j.1365-2966.2007.11964.x.

Sohn, S. T., J. Anderson, and R. P. van der Marel (2012). The M31 Velocity Vector. I. Hubble Space Telescope Proper-motion Measurements. *ApJ*, **753**, 7. doi:10.1088/0004-637X/753/1/7.

Sohn, S. T., G. Besla, R. P. van der Marel, M. Boylan-Kolchin, S. R. Majewski, and J. S. Bullock (2013). The Space Motion of Leo I: Hubble Space Telescope Proper Motion and Implied Orbit. *ApJ*, **768**, 139. doi:10.1088/0004-637X/768/2/139.

Sohn, S. T., E. Patel, G. Besla, R. P. van der Marel, J. S. Bullock, L. E. Strigari, G. van de Ven, M. G. Walker, and A. Bellini (2017). Space Motions of the Dwarf Spheroidal Galaxies Draco and Sculptor Based on HST Proper Motions with a 10 yr Time Baseline. *ApJ*, **849**, 93. doi:10.3847/1538-4357/aa917b.

Sohn, S. T., R. P. van der Marel, J. L. Carlin, S. R. Majewski, N. Kallivayalil, D. R. Law, J. Anderson, and M. H. Siegel (2015). Hubble Space Telescope Proper Motions along the Sagittarius Stream. I. Observations and Results for Stars in Four Fields. *ApJ*, **803**, 56. doi:10.1088/0004-637X/803/2/56.

Sohn, S. T., L. L. Watkins, M. A. Fardal, R. P. van der Marel, A. J. Deason, G. Besla, and A. Bellini (2018). Absolute Hubble Space Telescope Proper Motion (HSTPROMO) of Distant Milky Way Globular Clusters: Galactocentric Space Velocities and the Milky Way Mass. *ApJ*, **862**(1), 52. doi:10.3847/1538-4357/aacd0b.

Springel, V. (2005b). The cosmological simulation code GADGET-2. *MNRAS*, **364**, pp. 1105–1134. doi:10.1111/j.1365-2966.2005.09655.x.

Springel, V. (2010). E pur si muove: Galilean-invariant cosmological hydrodynamical simulations on a moving mesh. *MNRAS*, **401**, pp. 791–851. doi:10.1111/j.1365-2966.2009.15715.x.

Springel, V., J. Wang, M. Vogelsberger, A. Ludlow, A. Jenkins, A. Helmi, J. F. Navarro, C. S. Frenk, and S. D. M. White (2008). The Aquarius Project: the subhaloes of galactic haloes. *MNRAS*, **391**, pp. 1685–1711. doi:10.1111/j.1365-2966.2008.14066.x.

Springel, V., S. D. M. White, A. Jenkins, C. S. Frenk, N. Yoshida, L. Gao, J. Navarro, R. Thacker, D. Croton, J. Helly, J. A. Peacock, S. Cole, P. Thomas, H. Couchman, A. Evrard, J. Colberg, and F. Pearce (2005a). Simulations of the formation, evolution and clustering of galaxies and quasars. *Nature*, **435**(7042), pp. 629–636. doi:10.1038/nature03597.

Springel, V., S. D. M. White, G. Tormen, and G. Kauffmann (2001a). Populating a cluster of galaxies - I. Results at [formmu2]z=0. *MNRAS*, **328**, pp. 726–750. doi:10.1046/j.1365-8711.2001.04912.x.

Springel, V., N. Yoshida, and S. D. M. White (2001b). GADGET: a code for collisionless and gasdynamical cosmological simulations. *NewA*, **6**, pp. 79–117. doi:10.1016/S1384-1076(01)00042-2.

Starkenburg, E., A. Helmi, G. De Lucia, Y.-S. Li, J. F. Navarro, A. S. Font, C. S. Frenk, V. Springel, C. A. Vera-Ciro, and S. D. M. White (2013). The satellites of the Milky Way - insights from semi-analytic modelling in a ΛCDM cosmology. *MNRAS*, **429**, pp. 725–743. doi:10.1093/mnras/sts367.

Starkenburg, T. K., A. Helmi, and L. V. Sales (2016). Dark influences. III. Structural characterization of minor mergers of dwarf galaxies with dark satellites. *A&A*, **595**, A56. doi:10.1051/0004-6361/201528066.

Staveley-Smith, L. (2002). The Large-Scale Structure of the Large Magellanic Cloud. In Taylor, A. R., T. L. Landecker, and A. G. Willis (eds.) *Seeing Through the Dust: The Detection of HI and the Exploration of the ISM in Galaxies*, volume 276 of *Astronomical Society of the Pacific Conference Series*, p. 391.

Staveley-Smith, L., S. Kim, M. R. Calabretta, R. F. Haynes, and M. J. Kesteven (2003). A new look at the large-scale HI structure of the Large Magellanic Cloud. *MNRAS*, **339**, pp. 87–104. doi:10.1046/j.1365-8711.2003.06146.x.

Stewart, K. R., J. S. Bullock, R. H. Wechsler, A. H. Maller, and A. R. Zentner (2008). Merger Histories of Galaxy Halos and Implications for Disk Survival. *ApJ*, **683**, 597-610. doi:10.1086/588579.

Tollerud, E. J., R. L. Beaton, M. C. Geha, J. S. Bullock, P. Guhathakurta, J. S. Kalirai, S. R. Majewski, E. N. Kirby, K. M. Gilbert, B. Yniguez, R. J. Patterson, J. C. Ostheimer, J. Cooke, C. E. Dorman, A. Choudhury, and M. C. Cooper (2012). The SPLASH Survey: Spectroscopy of 15 M31 Dwarf Spheroidal Satellite Galaxies. *ApJ*, **752**, 45. doi:10.1088/0004-637X/752/1/45.

Tollerud, E. J., M. Boylan-Kolchin, E. J. Barton, J. S. Bullock, and C. Q. Trinh (2011a). Small-scale Structure in the Sloan Digital Sky Survey and ΛCDM: Isolated ˜L $_*$ Galaxies with Bright Satellites. *ApJ*, **738**, 102. doi: 10.1088/0004-637X/738/1/102.

Tollerud, E. J., J. S. Bullock, G. J. Graves, and J. Wolf (2011b). From Galaxy Clusters to Ultra-faint Dwarf Spheroidals: A Fundamental Curve Connecting Dispersion-supported Galaxies to Their Dark Matter Halos. *ApJ*, **726**, 108. doi: 10.1088/0004-637X/726/2/108.

Tollerud, E. J., J. S. Bullock, L. E. Strigari, and B. Willman (2008). Hundreds of Milky Way Satellites? Luminosity Bias in the Satellite Luminosity Function. *ApJ*, **688**, 277-289. doi:10.1086/592102.

Torrealba, G., V. Belokurov, S. E. Koposov, K. Bechtol, A. Drlica-Wagner, K. A. G. Olsen, A. K. Vivas, B. Yanny, P. Jethwa, A. R. Walker, T. S. Li, S. Allam, B. C. Conn, C. Gallart, R. A. Gruendl, D. J. James, M. D. Johnson, K. Kuehn, N. Kuropatkin, N. F. Martin, D. Martinez-Delgado, D. L. Nidever, N. E. D. Noël, J. D. Simon, G. S. Stringfellow, and D. L. Tucker (2018). Discovery of two neighbouring satellites in the Carina constellation with MagLiteS. *MNRAS*, **475**, pp. 5085–5097. doi:10.1093/mnras/sty170.

Trujillo-Gomez, S., A. Klypin, P. Colín, D. Ceverino, K. S. Arraki, and J. Primack (2015). Low-mass galaxy assembly in simulations: regulation of early star formation by radiation from massive stars. *MNRAS*, **446**, pp. 1140–1162. doi:10.1093/mnras/stu2037.

Trujillo-Gomez, S., A. Klypin, J. Primack, and A. J. Romanowsky (2011). Galaxies in ΛCDM with Halo Abundance Matching: Luminosity-Velocity Relation, Baryonic Mass-Velocity Relation, Velocity Function, and Clustering. *ApJ*, **742**, 16. doi:10.1088/0004-637X/742/1/16.

Tsuchiya, T. (2002). Contribution of the Large Magellanic Cloud to the Galactic warp. *NewA*, **7**, pp. 293–315. doi:10.1016/S1384-1076(02)00138-0.

U, V., M. A. Urbaneja, R.-P. Kudritzki, B. A. Jacobs, F. Bresolin, and N. Przybilla (2009). A New Distance to M33 Using Blue Supergiants and the FGLR Method. *ApJ*, **704**, pp. 1120–1134. doi:10.1088/0004-637X/704/2/1120.

van den Bergh, S. (2006). The Dwarf Satellites of M31 and the Galaxy. *AJ*, **132**, pp. 1571–1574. doi:10.1086/507332.

van den Bosch, F. C. and G. Ogiya (2018). Dark Matter Substructure in Numerical Simulations: A Tale of Discreteness Noise, Runaway Instabilities, and Artificial Disruption. *MNRAS*. doi:10.1093/mnras/sty084.

van den Bosch, F. C., G. Ogiya, O. Hahn, and A. Burkert (2018). Disruption of dark matter substructure: fact or fiction? *MNRAS*, **474**, pp. 3043–3066. doi:10.1093/mnras/stx2956.

van der Marel, R. P. (2015). Local Group Proper Motion Dynamics. In Cappellari, M. and S. Courteau (eds.) *Galaxy Masses as Constraints of Formation Models*, volume 311 of *IAU Symposium*, pp. 1–10. doi:10.1017/S1743921315003294.

van der Marel, R. P., D. R. Alves, E. Hardy, and N. B. Suntzeff (2002). New Understanding of Large Magellanic Cloud Structure, Dynamics, and Orbit from Carbon Star Kinematics. *AJ*, **124**, pp. 2639–2663. doi:10.1086/343775.

van der Marel, R. P., G. Besla, T. J. Cox, S. T. Sohn, and J. Anderson (2012b). The M31 Velocity Vector. III. Future Milky Way M31-M33 Orbital Evolution, Merging, and Fate of the Sun. *ApJ*, **753**, 9. doi:10.1088/0004-637X/753/1/9.

van der Marel, R. P., M. Fardal, G. Besla, R. L. Beaton, S. T. Sohn, J. Anderson, T. Brown, and P. Guhathakurta (2012a). The M31 Velocity Vector. II. Radial Orbit toward the Milky Way and Implied Local Group Mass. *ApJ*, **753**, 8. doi:10.1088/0004-637X/753/1/8.

van der Marel, R. P., M. A. Fardal, S. T. Sohn, E. Patel, G. Besla, A. del Pino, J. Sahlmann, and L. L. Watkins (2019). First Gaia Dynamics of the Andromeda System: DR2 Proper Motions, Orbits, and Rotation of M31 and M33. *ApJ*, **872**, 24. doi:10.3847/1538-4357/ab001b.

van der Marel, R. P. and P. Guhathakurta (2008). M31 Transverse Velocity and Local Group Mass from Satellite Kinematics. *ApJ*, **678**, 187-199. doi:10.1086/533430.

van der Marel, R. P. and N. Kallivayalil (2014). Third-epoch Magellanic Cloud Proper Motions. II. The Large Magellanic Cloud Rotation Field in Three Dimensions. *ApJ*, **781**, 121. doi:10.1088/0004-637X/781/2/121.

van der Marel, R. P. and J. Sahlmann (2016a). First Gaia Local Group Dynamics: Magellanic Clouds Proper Motion and Rotation. *ApJL*, **832**, L23. doi:10.3847/2041-8205/832/2/L23.

van der Marel, R. P. and J. Sahlmann (2016b). First Gaia Local Group Dynamics: Magellanic Clouds Proper Motion and Rotation. *ApJ*, **832**, L23. doi:10.3847/2041-8205/832/2/L23.

Vieira, K., T. M. Girard, W. F. van Altena, N. Zacharias, D. I. Casetti-Dinescu, V. I. Korchagin, I. Platais, D. G. Monet, C. E. López, D. Herrera, and D. J. Castillo (2010). Proper-motion Study of the Magellanic Clouds Using SPM Material. *AJ*, **140**, pp. 1934–1950. doi:10.1088/0004-6256/140/6/1934.

Vogelsberger, M., S. Genel, V. Springel, P. Torrey, D. Sijacki, D. Xu, G. Snyder, S. Bird, D. Nelson, and L. Hernquist (2014a). Properties of galaxies reproduced by a hydrodynamic simulation. *Nature*, **509**, pp. 177–182. doi:10.1038/nature13316.

Vogelsberger, M., S. Genel, V. Springel, P. Torrey, D. Sijacki, D. Xu, G. Snyder, D. Nelson, and L. Hernquist (2014b). Introducing the Illustris Project: simulating

the coevolution of dark and visible matter in the Universe. *MNRAS*, **444**, pp. 1518–1547. doi:10.1093/mnras/stu1536.

Walker, M. G., M. Mateo, and E. W. Olszewski (2008). Systemic Proper Motions of Milky Way Satellites from Stellar Redshifts: The Carina, Fornax, Sculptor, and Sextans Dwarf Spheroidals. *ApJL*, **688**, L75. doi:10.1086/595586.

Wang, J., C. S. Frenk, J. F. Navarro, L. Gao, and T. Sawala (2012). The missing massive satellites of the Milky Way. *MNRAS*, **424**, pp. 2715–2721. doi:10.1111/j.1365-2966.2012.21357.x.

Wang, L., C. Li, G. Kauffmann, and G. De Lucia (2006). Modelling galaxy clustering in a high-resolution simulation of structure formation. *MNRAS*, **371**, pp. 537–547. doi:10.1111/j.1365-2966.2006.10669.x.

Wang, W., J. Han, S. Cole, C. Frenk, and T. Sawala (2017). What to expect from dynamical modelling of galactic haloes. *MNRAS*, **470**, pp. 2351–2366. doi:10.1093/mnras/stx1334.

Wang, W., J. Han, A. P. Cooper, S. Cole, C. Frenk, and B. Lowing (2015). Estimating the dark matter halo mass of our Milky Way using dynamical tracers. *MNRAS*, **453**(1), pp. 377–400. doi:10.1093/mnras/stv1647.

Watkins, L. L., N. W. Evans, and J. H. An (2010). The masses of the Milky Way and Andromeda galaxies. *MNRAS*, **406**, pp. 264–278. doi:10.1111/j.1365-2966.2010.16708.x.

Watkins, L. L., R. P. van der Marel, S. T. Sohn, and N. W. Evans (2019). Evidence for an Intermediate-mass Milky Way from Gaia DR2 Halo Globular Cluster Motions. *ApJ*, **873**, 118. doi:10.3847/1538-4357/ab089f.

Weinberg, M. D. (1998). Dynamics of an interacting luminous disc, dark halo and satellite companion. *MNRAS*, **299**, pp. 499–514. doi:10.1046/j.1365-8711.1998.01790.x.

Weinberg, M. D. and L. Blitz (2006). A Magellanic Origin for the Warp of the Galaxy. *ApJL*, **641**, pp. L33–L36. doi:10.1086/503607.

Weisz, D. R., J. J. Dalcanton, B. F. Williams, K. M. Gilbert, E. D. Skillman, A. C. Seth, A. E. Dolphin, K. B. W. McQuinn, S. M. Gogarten, J. Holtzman, K. Rosema, A. Cole, I. D. Karachentsev, and D. Zaritsky (2011). The ACS Nearby Galaxy Survey Treasury. VIII. The Global Star Formation Histories of 60 Dwarf Galaxies in the Local Volume. *ApJ*, **739**, 5. doi:10.1088/0004-637X/739/1/5.

Werk, J. K., J. X. Prochaska, J. Tumlinson, M. S. Peeples, T. M. Tripp, A. J. Fox, N. Lehner, C. Thom, J. M. O'Meara, A. B. Ford, R. Bordoloi, N. Katz, N. Tejos, B. D. Oppenheimer, R. Davé, and D. H. Weinberg (2014). The COS-Halos Survey: Physical Conditions and Baryonic Mass in the Low-redshift Circumgalactic Medium. *ApJ*, **792**, 8. doi:10.1088/0004-637X/792/1/8.

Wetzel, A. R. (2011). On the orbits of infalling satellite haloes. *MNRAS*, **412**, pp. 49–58. doi:10.1111/j.1365-2966.2010.17877.x.

Wetzel, A. R., A. J. Deason, and S. Garrison-Kimmel (2015). Satellite Dwarf Galaxies in a Hierarchical Universe: Infall Histories, Group Preprocessing, and Reionization. *The Astrophysical Journal*, **807**(1), p. 49.

Wetzel, A. R., P. F. Hopkins, J.-h. Kim, C.-A. Faucher-Giguère, D. Kereš, and E. Quataert (2016). Reconciling Dwarf Galaxies with ΛCDM Cosmology: Simulating a Realistic Population of Satellites around a Milky Way-mass Galaxy. *ApJL*, **827**, L23. doi:10.3847/2041-8205/827/2/L23.

Wetzel, A. R., J. L. Tinker, C. Conroy, and F. C. van den Bosch (2014). Galaxy evolution near groups and clusters: ejected satellites and the spatial extent of environmental quenching. *MNRAS*, **439**, pp. 2687–2700. doi:10.1093/mnras/stu122.

Wetzel, A. R., E. J. Tollerud, and D. R. Weisz (2015). Rapid Environmental Quenching of Satellite Dwarf Galaxies in the Local Group. *ApJL*, **808**, L27. doi:10.1088/2041-8205/808/1/L27.

Wilkinson, M. I. and N. W. Evans (1999). The present and future mass of the Milky Way halo. *MNRAS*, **310**, pp. 645–662. doi:10.1046/j.1365-8711.1999.02964.x.

Willman, B., M. R. Blanton, A. A. West, J. J. Dalcanton, D. W. Hogg, D. P. Schneider, N. Wherry, B. Yanny, and J. Brinkmann (2005). A New Milky Way Companion: Unusual Globular Cluster or Extreme Dwarf Satellite? *AJ*, **129**, pp. 2692–2700. doi:10.1086/430214.

Woo, J., S. Courteau, and A. Dekel (2008). Scaling relations and the fundamental line of the local group dwarf galaxies. *MNRAS*, **390**, pp. 1453–1469. doi:10.1111/j.1365-2966.2008.13770.x.

Zaritsky, D. and H. Courtois (2017). A dynamics-free lower bound on the mass of our Galaxy. *MNRAS*, **465**, pp. 3724–3728. doi:10.1093/mnras/stw2922.

Zaritsky, D., E. W. Olszewski, R. A. Schommer, R. C. Peterson, and M. Aaronson (1989). Velocities of stars in remote Galactic satellites and the mass of the Galaxy. *ApJ*, **345**, pp. 759–769. doi:10.1086/167947.

Zentner, A. R. and J. S. Bullock (2003). Halo Substructure and the Power Spectrum. *ApJ*, **598**, pp. 49–72. doi:10.1086/378797.

Zivick, P., N. Kallivayalil, R. P. van der Marel, G. Besla, S. T. Linden, S. Kozłowski, T. K. Fritz, C. S. Kochanek, J. Anderson, S. T. Sohn, M. C. Geha, and C. R. Alcock (2018). The Proper Motion Field of the Small Magellanic Cloud: Kinematic Evidence for Its Tidal Disruption. *ApJ*, **864**, 55. doi:10.3847/1538-4357/aad4b0.

Zucker, D. B., V. Belokurov, N. W. Evans, J. T. Kleyna, M. J. Irwin, M. I. Wilkinson, M. Fellhauer, D. M. Bramich, G. Gilmore, H. J. Newberg, B. Yanny, J. A. Smith, P. C. Hewett, E. F. Bell, H. W. Rix, O. Y. Gnedin, S. Vidrih, R. F. G. Wyse, B. Willman, E. K. Grebel, D. P. Schneider, T. C. Beers, A. Y. Kniazev, J. C. Barentine, H. Brewington, J. Brinkmann, M. Harvanek, S. J. Kleinman, J. Krzesinski, D. Long, A. Nitta, and S. A. Snedden (2006a). A Curious Milky Way Satellite in Ursa Major. *ApJ*, **650**, pp. L41–L44. doi:10.1086/508628.

Zucker, D. B., V. Belokurov, N. W. Evans, M. I. Wilkinson, M. J. Irwin, T. Sivarani, S. Hodgkin, D. M. Bramich, J. M. Irwin, G. Gilmore, B. Willman, S. Vidrih, M. Fellhauer, P. C. Hewett, T. C. Beers, E. F. Bell, E. K. Grebel, D. P. Schneider, H. J. Newberg, R. F. G. Wyse, C. M. Rockosi, B. Yanny, R. Lupton, J. A. Smith, J. C. Barentine, H. Brewington, J. Brinkmann, M. Harvanek, S. J. Kleinman, J. Krzesinski, D. Long, A. Nitta, and S. A. Snedden (2006b). A New Milky Way Dwarf Satellite in Canes Venatici. *ApJ*, **643**, pp. L103–L106. doi:10.1086/505216.

Zucker, D. B., A. Y. Kniazev, E. F. Bell, D. Martínez-Delgado, E. K. Grebel, H.-W. Rix, C. M. Rockosi, J. A. Holtzman, R. A. M. Walterbos, J. Annis, D. G. York, Ž. Ivezić, J. Brinkmann, H. Brewington, M. Harvanek, G. Hennessy, S. J. Kleinman, J. Krzesinski, D. Long, P. R. Newman, A. Nitta, and S. A. Snedden (2004). Andromeda IX: A New Dwarf Spheroidal Satellite of M31. *ApJL*, **612**, pp. L121–L124. doi:10.1086/424691.

Zucker, D. B., A. Y. Kniazev, D. Martínez-Delgado, E. F. Bell, H.-W. Rix, E. K. Grebel, J. A. Holtzman, R. A. M. Walterbos, C. M. Rockosi, D. G. York, J. C. Barentine, H. Brewington, J. Brinkmann, M. Harvanek, S. J. Kleinman, J. Krzesinski, D. Long, E. H. Neilsen, Jr., A. Nitta, and S. A. Snedden (2007). Andromeda X, a New Dwarf Spheroidal Satellite of M31: Photometry. *ApJL*, **659**, pp. L21–L24. doi:10.1086/516748.